# Ferromagnetic Ising Chains in Frustrated Magnetocaloric Frameworks

**Richard J.C. Dixey**

School of Physical Sciences

University of Kent

This thesis is submitted for the degree of

*Doctor of Philosophy*

April 2020

I would like to dedicate this thesis to my loving parents

# Declaration

I hereby declare that except where specific reference is made to the work of others, the contents of this dissertation are original and have not been submitted in whole or in part for consideration for any other degree or qualification in this, or any other university. This dissertation is my own work and contains nothing that is the outcome of work done in collaboration with others, except as specified in the text and acknowledgements.

Richard J.C. Dixey
April 2020

# Acknowledgements

# Abstract

Magnetic materials with strong local interactions, but lacking long range order, have long been a curiosity of physicists. Probing the magnetic interactions is crucial for understanding the unique properties they can exhibit. Framework materials have recently gathered more attention as they can produce more exotic structures, allowing for controlled design of magnetic properties not found in conventional metal-oxide materials. Probing the magnetic interactions, in functional magnetic materials, can reveal detailed insight into how to optimise the properties they possess while providing key understanding of the exotic phenomena they may host. Historically, magnetic diffuse scattering in such materials has been overlooked but has attracted greater attention recently, with advances in techniques. This thesis probes the short range magnetic order and long range magnetic structure of some highly efficient magnetocaloric frameworks containing heavier lanthanides. In particularly we aimed to identify the magneto-structural relationship that leads to an optimised magnetocaloric effect in low applied magnetic fields (<2 T) and at temperatures 2-10 K, where these materials could find use in adiabatic refrigeration applications as an energy efficient alternative for cooling to temperatures for which liquid helium has historically been used. The magnetic structure and correlations have been probed through neutron scattering, using reverse Monte Carlo refinements to establish the short range order they manifests, and Rietveld refinements to probe the long range order. A variety of physical property measurements have been used to provide additional information about the bulk properties of these materials.

This thesis begins with an introduction into magnetic materials, including the key aspects relevant to this thesis in Chapter one and a description of the experimental and analytical methods used in Chapter two. Chapter three then explores the crystal structure and magnetocaloric effect of the $Ln$OHCO$_3$ and $Ln$F$_3$ (where $Ln$ = Tb, Dy, Ho, and Er) phases. A combination of single crystal X-ray and neutron powder diffraction indicate that the $Ln$OHCO$_3$ materials solely adopt the $P2_12_12_1$ structure under these synthetic conditions and magnetic susceptibility measurements indicate they remain paramagnetic down to 2

K. We show that the magnetocaloric effect of $TbOHCO_3$ and $DyOHCO_3$ is significantly higher, above 4 K in moderate magnetic fields, than the promising $GdOHCO_3$ framework. Similarly, the $LnF_3$ also show impressive entropy changes, but less than that of $LnOHCO_3$. The entropy changes in $LnF_3$ are likely due to some persistent ferromagnetic correlations, and their high density. The peak magnetic entropy change of these frameworks exceeds that of $Gd_3Ga_5O_{12}$ in equivalent fields, making them suitable magnetic cooling materials for use at liquid helium temperatures using the low applied magnetic fields, required for practical for a low temperature cooling device.

Chapter four investigates the magnetic structure of metal-organic formate frameworks, using heat capacity, magnetic susceptibility and neutron diffraction. In $Tb(DCO_2)_3$ we observe emergent magnetic order at temperatures below 1.2 K, consisting of two $\mathbf{k}$-vectors. $Ho(DCO_2)_3$ shows diffuse scattering above 1.6 K, consistent with ferromagnetic chains packed in a frustrated antiferromagnetic triangular lattice, also observed in $Tb(DCO_2)_3$ above 1.2 K. $Ho(DCO_2)_3$ shows the same emergent charge ordered state below 0.7 K, but differs to $Tb(DCO_2)_3$ in that $\mathbf{k}_1$ and $\mathbf{k}_2$ become active simultaneously, and variable temperature measurements show how the peak width is due to disorder and not an artefact of small domain size. $Tb(DCO_2)_3$ also shows some interesting magnetic inelastic features which persist well above $T_N$, but can be described by Ising spins, for which the Hamiltonian has been deduced. The other lanthanides show no short or long range order down to 1.6 K, although at 50 mK $Er(DCO_2)_3$ shows order with antiferromagnetic coupling within the chains. The results suggest an Ising-like 1D magnetic order associated with frustration is responsible for the magnetocaloric properties, of some members in this family, improving at higher temperatures. However, the weak antiferromagnetic order in $Er(DCO_2)_3$ at 50 mK is likely responsible for the poor entropy changes seen, with applied magnetic fields.

Chapter five probes the short and long range magnetic order in the $LnODCO_3$ (where $Ln$ = Tb, Dy, Ho, and Er) framework magnetocalorics using variable-temperature neutron scattering measurements. Reverse Monte Carlo analysis of neutron scattering data shows that $TbODCO_3$, $DyODCO_3$ and $HoODCO_3$ develop short range Ising-like magnetic order between 1.5 and 20 K, consistent with dominant ferromagnetic correlations within chains along the $b$-axis. Through magnetic susceptibility measurements we identify long range magnetic order develops in $TbODCO_3$ and $HoODCO_3$ at 1.2 and 0.9 K, respectively. Neutron diffraction measurements were conducted on $HoODCO_3$ revealing incommensurate magnetic order develops between 1.2 and 0.9 K, before a commensurate magnetic phases emerges at 0.8 K with long-range ferromagnetic order in the chains. The results suggest

Ising-like ferromagnetic chains associated with frustration are responsible for the improved magnetocaloric properties, of some members in this family, at higher temperatures and low applied fields.

Chapter six investigates the magnetic structure of two key materials, $Tb(DCO_2)_3$ and $TbODCO_3$ in applied magnetic fields. By exploring the magnetic structure of these magnetocaloric materials, in situ, we have been able to understand the mechanism that leads to the efficient magnetocaloric effect. We find that the presence of short range ferromagnetic chains correlations develops into long range order upon increasing magnetic field. These persistent ferromagnetic chains allow for easy magnetisation of the materials in small magnetic fields, achieving high changes in entropy for moderate field changes.

This thesis provides insight into the fundamental magnetic properties and structure of lanthanide frameworks materials that have been shown to have excellent magnetocaloric behaviour. The results indicate that the presence of frustrated interactions preventing long range order, in combination with ferromagnetic Ising chains provide materials optimised for high entropy changes in low applied magnetic fields.

# List of Publications

Below are a list of publications that have been published, and were produced during the duration of the work contained within this thesis. Publications 2, 4 and 5 directly contributed to thesis chapters 3, 4 and 5 respectively.

1. "Three coordination frameworks with copper formate based low dimensional motifs: synthesis, structure and magnetic properties" S. M. Bovill, R. J. C. Dixey and P. J. Saines, *CrystEngComm*, 2017, **19**, 1831-1838.

2. "Optimization of the Magnetocaloric Effect in Low Applied Magnetic Fields in $Ln$OHCO$_3$ Frameworks" R. J. Dixey and P. J. Saines, *Inorganic Chemistry*, 2018, **57**, 12543-12551.

3. "Low dimensional and frustrated antiferromagnetic interactions in transition metal chloride complexes with simple amine ligands" J. E. Chalmers, A. K. Srivastava, R. J. Dixey, K. Sivakumaran and P. J. Saines, *CrystEngComm*, 2019, **21**, 1831-1838, 894–901.

4. "Emergent magnetic order and correlated disorder in formate metal-organic frameworks" R. J. C. Dixey, F. Orlandi, P. Manuel and S. E. Dutton, *Philosophical Transactions of the Royal Society A: Mathematical, Physical and Engineering Sciences*, 2019, **377**, 20190007.

5. "Ferromagnetic Ising Chains in Frustrated $Ln$ODCO$_3$: The Influence of Magnetic Structure in Magnetocaloric Frameworks" R. J. C. Dixey, G. Stenning, P. Manuel, F. Orlandi and P. Saines, *Journal of Materials Chemistry C*, 2019, **7**, 13111-13119

*"I am afraid neutrons will not be of any use to any one."*

– Sir James Chadwick

# Table of Contents

# List of Figures

# List of Tables

# Nomenclature

**Roman Symbols**

K             Kelvin

*sr*            Steradian

**Greek Symbols**

$\chi^2$           Goodness of fit squared

$\lambda$           Wavelength

$\pi$           $\simeq 3.14159$

$\theta$           Bragg Angle

$\theta_{CW}$        Curie-Weiss Temperature

$\varepsilon$           Correlation length

**Other Symbols**

Å            Angstrom, $1 \times 10^{-10}$ m

**Acronyms / Abbreviations**

AFM         Antiferromagnetic

ANSTO      Australian Nuclear Science and Technology Organisation

CIF          Crystallographic Information File

| | |
|---|---|
| CW | Constant Wavelength |
| DC | Direct Current |
| DSC | Differential Scanning Calorimetry |
| ECO | Emergent Charge Order |
| FC | Field Cooled |
| FTIR | Fourier Transform Infrared (Spectroscopy) |
| FWHM | Full Width Half Maximum |
| GGG | Gadolinium Gallium Garnet ($Gd_3Ga_5O_{12}$) |
| INS | Inelastic Neutron Spectroscopy |
| LET | Low Energy Transfer |
| *Ln* | Lanthanide or Y |
| LRO | Long Range Order |
| MCE | Magnetocaloric Effect |
| MC | Monte Carlo |
| meV | milli-electron Volts |
| M | Metal Cation |
| MOF | Metal-organic frameworks |
| MPMS | Magnetic Properties Measurement System |
| PND | Powder Neutron Diffraction |
| PPMS | Physical Properties Measurement System |
| $R_p$ | Profile factor |

| | |
|---|---|
| QSL | Quantum Spin Liquid |
| RMC | Reverse Monte Carlo |
| SQUID | Superconducting Quantum Interference Device |
| SRO | Short Range Order |
| $T_C$ | Curie Temperature |
| TGA | Thermo Gravimetric Analysis |
| TIA | Triangular Ising Antiferromagnet |
| $T_N$ | Néel Temperature |
| TOF | Time of Flight |
| WISH | Wide-angle In Single Histogram |
| $R_{wp}$ | Weighted profile factor |
| ZFC | Zero-field Cooled |

# 1

# General Introduction

## 1.1 Introduction

Magnetic materials have long been studied from a fundamental standpoint [1] and for their fascinating properties, including data storage and transfer, [2, 3] cooling devices [4, 5] and medical applications. [6] Ferromagnetism has been known about before modern science through the naturally occurring iron containing mineral, magnetite, [7] despite a lack of understanding of its underlying magnetic interactions. In 1907 Weiss published the first description of its origin [8] through studies of the temperature dependence of alloys and halides. Ferromagnetism was the only known type of magnetic order until 1948 when Néel proposed a new type of magnetism, the antiferromagnet [9] from which the interest in the fundamental understanding of magnetic materials grew. Traditionally, many of the studied magnetic materials are mineral-like compounds such as alloys, halides, and oxides, due to their strong magnetic interactions between magnetic centres. Therefore these materials have higher (and often more useful) ordering temperatures. Metal-oxides, such as materials with the general structure $ABX_3$ called perovskites, have enjoyed a long history of in depth studies, [10] and uses in functional devices. Studies go far beyond purely magnetic materials, for their ability to modify their properties through inclusion of characteristic A or B site cations, replacing oxygen for similar charged anions or creating layered perovskites.

Materials built from polyatomic components, such as hybrid perovskites which contain organic cations, have attracted much attention. Hybrid perovskites for example have been observed to exhibit properties that exceed the ability of traditional perovskites, such as in photovoltaic applications, [11] due to the inclusion of an organic cation allowing for

greater flexibility of the structure. [12] However, beyond modifying the composition of these materials, the knowledge required to tailor the underlying structure and interactions is not as well developed compared to metals oxides. Given the key role of structure-property relationships in optimising properties, this is the necessary avenue to investigate.

In general coordination frameworks containing polyatomic ligands, including metal-organic frameworks (MOFs), have attracted much attention in recent years for their ability to highly modify the structure and properties. This lends MOFs to gas storage [13, 14] because design and synthesis of highly porous frameworks, with extended connecting ligands between metal-centres, is possible. However, more recently, magnetic studies of coordination frameworks have emerged, highlighting the potential of such materials in functional magnetic materials. The ability for a greater flexibility in the design of the structure, allows for more specific topologies and magnetically isolated sheets and chains, opening up the means to low dimensional and frustrated magnetism, fundamentally interesting and useful when optimised through knowledge of structure-property relationships.

Frameworks have already been shown to feature a wide variety of the functionality found in oxides, with uses in chemical and magnetic sensors, [15] magnetocalorics [4, 5] and multiferroics that combine magnetism with ferroelectric order. [16] In frameworks, the magnetic interactions are facilitated through the connecting ligand, or a single atom within them and the strength and direction of these magnetic interactions depends on the precise nature of the linker. Magnetic interaction strength is typically inversely proportional to the size of the ligand, and therefore in magnetic frameworks, linkers must be kept short to allow for sufficient metal-metal magnetic interactions. Through meticulous design of magnetic frameworks we can build materials with properties such as low dimensional magnetism.

Frustration and low dimensional magnetism have recently been shown to improve the efficiency of magnetocaloric materials, in low applied magnetic fields. [4, 17] For example $Tb(HCO_2)_3$ shows larger changes in entropy for magnetic fields smaller than 2 T between 4-10 K, compared to $Gd(HCO_2)_3$ which shows higher changes in entropy at lower temperatures and in higher magnetic fields. This is suggested to arise from the 1D ferromagnetic correlations observed in the paramagnetic phase, which is allowed to stay paramagnetic through competing antiferromagnetic interactions. [18]

## 1.2 Crystallography

The aim of a solid state chemist or condensed matter physicist is to understand the structure of a solid material in order to optimise the properties. The most powerful framework for understanding the solid state structure of materials is crystallography. Great progress in the ease of calculations in crystallography has made the understanding of crystalline materials progress rapidly, and is now a key technique for modern chemistry and physics.

The perfect crystal consists of a regularly repeating structural unit, made of either a single atom or group of atoms. The regular repeating unit, known as the unit cell, can be translated in any direction to be perfectly mapped onto any other one. The unit cell is the smallest region with full symmetry, and can be thought of as the fundamental region from which the entire crystal may be constructed from purely translational displacement (see Figure 1.1). Therefore in order to understand the whole crystal, only the symmetry of a single unit cell has to be determined.
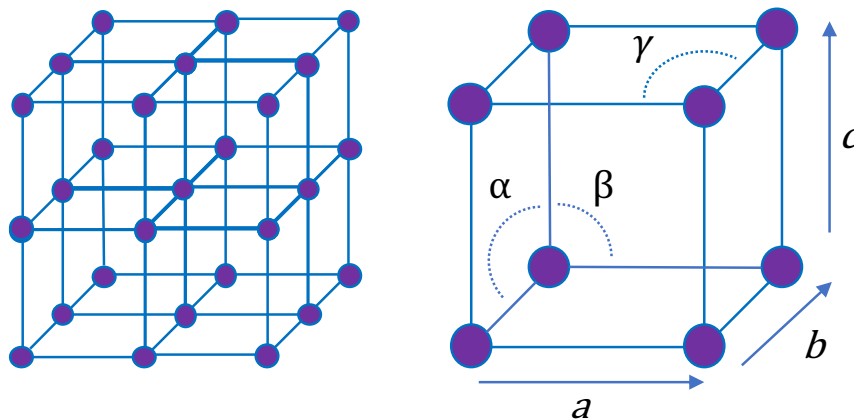
**Figure 1.1** A diagram showing a collection of regular repeating unit cells, and the lattice constants and the lattice angles of a simple cubic unit cell.

In real space the lengths of the unit cell are denoted as $a$, $b$ and $c$, with the angles between them labelled $\alpha$, $\beta$ and $\gamma$ as shown in Figure 1.1. The unit cells can be divided into seven crystal systems based on the rotational symmetry they have, Table 1.1 shows the essential symmetries the crystal must have to belong to the crystal system. [19].

The seven crystal system can then be further divided into fourteen Bravais lattices, dependent on the way atoms are packed into the unit cell. Taking into account all the symmetries, and constraints of the unit cells generates the 230 nuclear space groups, which is the basis of structural solution of crystals in crystallography.

**Table 1.1** The crystal systems. [20]

| System | Angles | Lengths | Rotational Symmetry |
|---|---|---|---|
| Triclinic | $\alpha \neq \beta \neq \gamma$ | $|a| \neq |b| \neq |c|$ | None |
| Monoclinic | $\alpha = \beta = 90° \neq \gamma$ | $|a| \neq |b| \neq |c|$ | One $C_2$ axis |
| Orthorhombic | $\alpha = \beta = \gamma = 90°$ | $|a| \neq |b| \neq |c|$ | Three Perpendicular $C_2$ axes |
| Tetragonal | $\alpha = \beta = \gamma = 90°$ | $|a| = |b| \neq |c|$ | One $C_4$ axis |
| Cubic | $\alpha = \beta = \gamma = 90°$ | $|a| = |b| = |c|$ | Four $C_4$ axes |
| Hexagonal | $\alpha = \beta = 90°, \gamma = 120°$ | $|a| = |b| \neq |c|$ | One $C_6$ axis |
| Trigonal | $\alpha = \beta = \gamma \neq 90°$ | $|a| = |b| = |c|$ | One $C_3$ axis |

## 1.3 Origin of magnetism

The electron is a fundamental spin 1/2 fermion particle ($s = \frac{1}{2}$), with a $-1$ electric charge and the particle of interest for chemists and condensed matter physicists. Organic chemists build their careers out of tracking the movement of the electron but as condensed matter and physical chemists we are concerned with how these particles are correlated within the electromagnetic mean field.

The Pauli-exclusion principle states: [21]

> "the total electron wavefunction is antisymmetric with respect to the interchange of any two electrons"

which simply means that no electron can have the same quantum numbers as another electron (same values of $n, l, m_l, m_s$ ), ie. no two electrons can occupy the same orbital with the same spin state. This lead to the German physicist Hund describing the lowest energy level for a partially filled orbital as one that maximises multiplicity (Figure 1.2). [22] Conveniently, for scientists interested in magnetic phenomena, this leads to the consequence of maximising the magnetic moment on an atom.
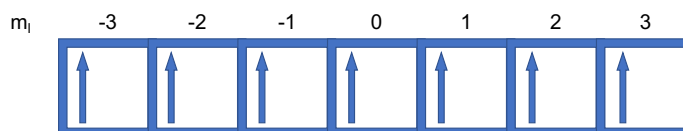


**Figure 1.2** A diagram demonstrating Hund's rule of maximum multiplicity in the $f$-orbitals, for $Gd^{3+}$

If we think of the electron as a rotating charged particle about an axis, then the magnetic moment of a single electron is given by: [23]

$$\mu_B = \frac{e\hbar}{2m_e}L = 9.274 \times 10^{-24} \text{J} \cdot \text{T}^{-1} \tag{1.1}$$

where $e$ is the charge of the electron, $\hbar$ is the reduced Planks constant, $m_e$ is the rest mass of an electron, and $L$ is the angular moment. The magnetic moment of a single electron is defined as 1 Bohr magneton ($\mu_B$).

In lanthanides the magnetic moment is given by the Russell-Saunders coupling scheme, which takes into account the number of spin contribution ($S$), the total orbital angular momentum ($L$) and the total angular momentum ($J$). [24] $J$ is calculated as $J = L - S$ for systems that have the $f$-orbitals less than half filled and $J = L + S$ for systems that are greater than half filled, caused by the coupling of spin moment to the orbital angular moment. The orbital angular momentum is determined by the sum of the quantum numbers ($m_l$) given by the occupation of electrons in the orbitals, as shown in Figure 1.2 for $Gd^{3+}$ , $L = 0$. [25] The magnetic moments, in units of Bohr magneton, are given by:

$$\mu_{eff} = g_j\sqrt{J(J+1)} \tag{1.2}$$

where the landé g-factor ($g_j$) for a lanthanide ion is given by:

$$g_j = \frac{3}{2} + \frac{S(S+1) - L(L+1)}{2J(J+1)} \tag{1.3}$$

The calculated values of $S$, $L$ and $J$ and the effective magnetic moments for systems containing unpaired electrons such as the lanthanides ($Ln$) are shown in Figure 1.3. Here we can see the the contributions of the spin only and orbital terms contributing to the total magnetic moment of the lanthanide ions.

## 1.4   Introduction to Magnetic Order and Disorder

The quantum mechanical origin of magnetism as discussed in Section 1.3, leads to the phenomenon of magnetic moments that can be considered classical vectors similar to that of a bar magnet. The moments are pictorially represented as arrows with arrows pointing up referred to as spin up, and pointing down as spin down. At high temperatures, the thermal energy of the lattice prevents the interactions between the moments cooperating with each other, and this state is referred to as a paramagnetic state. In the paramagnetic state, magnetic
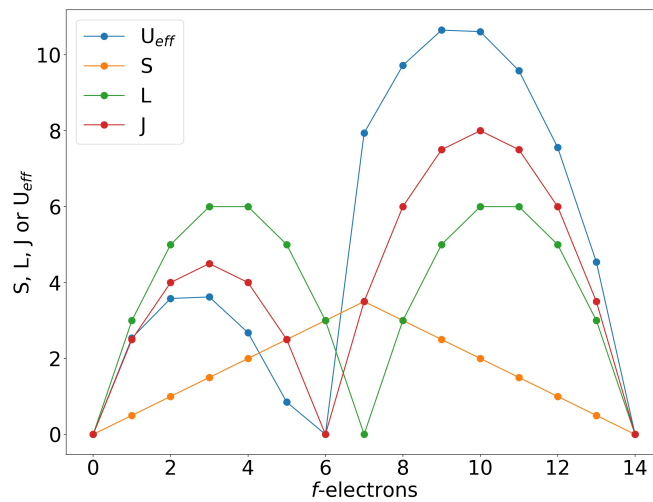
**Figure 1.3** The values of $S$, $J$, $L$ and $\mu_{eff}$ in the $Ln^{3+}$ ions

moments are not correlated to each other and fluctuate randomly with respect to each other, as shown in Figure 1.4a. Below some critical temperature where the strengths of the interactions between moments are sufficient to overcome thermal disturbances, the moments become strongly correlated with each another.
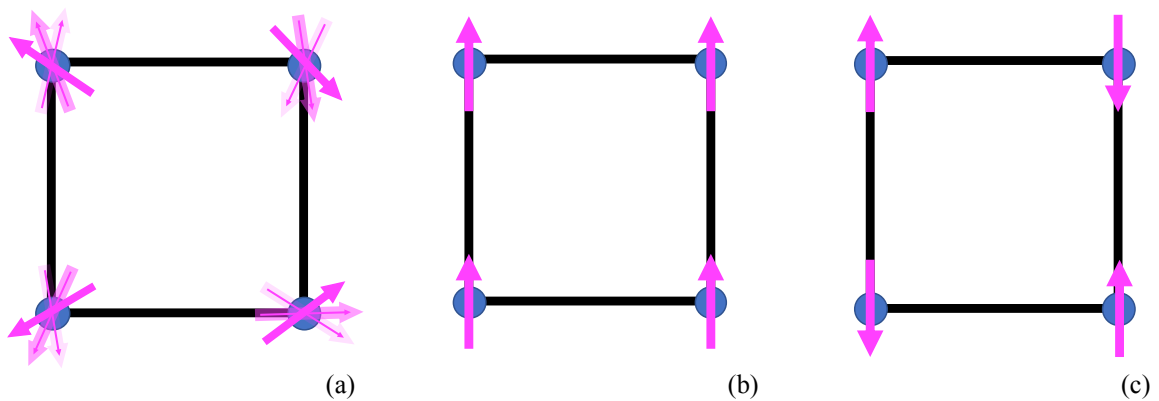


**Figure 1.4** Diagram of a (a) paramagnet showing the movement of the uncorrelated spins (b) Ferromagnet with static spins parallel with respect to the nearest neighbour and (c) an antiferromagnet with static spins antiparallel with respect to the nearest neighbour. All are shown on a square lattice, with atoms shown in blue and spin directions shown in pink.

In ferromagnetic substances the temperature at which the moments align with respect to its neighbours is known as the Curie temperature ($T_C$). In this arrangement the moments all align in the same direction over a range of thousands of atoms, within the magnetic domain. For a simple 2D lattice, ferromagnetism is shown in Figure 1.4b. The earliest known example

of this was magnetite, [7] but since then, many transition metals oxides and frameworks have been found to be ferromagnetic at low temperatures.

At low temperatures many materials undergo a transition to a state where the moments are antiparallel with respect to each other (Figure 1.4c). These materials are known as antiferromagnets and the ordering temperature is called the Néel temperature ($T_N$), after Néel who first predicted the state. [9] The first experimental evidence of an antiferromagnetic state came with advances in diffraction techniques, leading to the first experimentally observed antiferromagnetic state in MnO in 1949. [26] These simple magnetic structures can be considered to be commensurate magnetic order, because the magnetic order is contained within an integer number of unit cells, and can therefore be expressed using 3 hkl indices. However more complicated examples of magnetic order exist and are discussed in Section 1.8, where due to competing interactions the materials cannot form simple magnetic orders. Often the interactions are such that the materials form order over a non-integer number of unit cells, and are known as incommensurate magnetic structures. In incommensurate structures sharp Bragg reflection require >3 hkl indices so it is periodic in higher dimensional superspace, and the wavelength of the modulation is incommensurate with the average periodic lattice. An early example of an incommensurate structure is seen in metallic chromium, which shows a Néel temperature of 311 K, with early measurements suggesting a simple antiferromagnetic state. Chromium actually undergoes a transition to an incommensurate spin-density sine wave structure, with moments on the atoms subtly varying along the *a*-axis (Figure 1.5), resulting in a small shift in magnetic reflections that initially was overlooked. [27] Further examples of exotic magnetism are given in Section 1.8 and the theories explaining how this order forms is discussed further in Section 1.6.4.
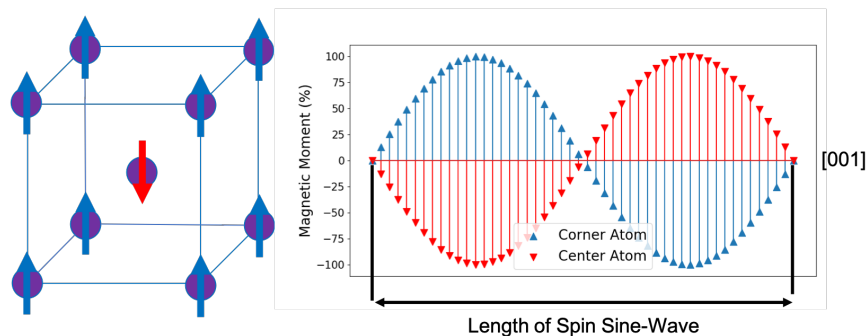


**Figure 1.5** Left image shows the magnetic structure of the first unit cell, in the sine wave of chromium, the plot on the right shows how the magnetic moment varies along each equivalent magnetic sites. A commensurate magnetic structure would consist of all unit cells identical to the first. The spin wave spans over a non-integer number of unit cell.

## 1.5 Magnetic Susceptibility and Behaviour in Field

When a material is exposed to an applied magnetic field $H$, a magnetic flux is induced in the sample, this is given by:

$$B = \mu_0 H + \mu_0 M \tag{1.4}$$

where $\mu_0$ is the permeability of free space, M is the magnetisation of the sample. $\mu_0 H$ is the magnetisation generated by the applied magnetic field and $\mu_0 M$ is the contribution from the material. The SI units for an applied magnetic field is the Tesla (T), but historically the centimetre-gram-second (CGS) unit system has been used and is still used today in magnetic measurements, where 1 T = 10000 Oe. [28] When a magnetic field is applied to a sample, the magnetic susceptibility $\chi$ is defined by the ratio of the magnetisation to the field where:

$$\chi = \frac{M}{H} \tag{1.5}$$

The magnetic susceptibility is the parameter that is often used to describe the response of a materials to an applied magnetic field. The magnetic susceptibility of a sample is strongly dependent on the sample temperature. As temperatures are lowered, the interactions between magnetic moments become relatively stronger compared to thermally induced disorder thereby effecting the behaviour of the susceptibility, as summarised in Table 1.2.

**Table 1.2** Magnetic susceptibilities of Different Magnetic Orders. SC = Superconductor. [28]

| Magnetic Behaviour | $\approx \chi_M$ (cm$^3$ mol$^{-1}$) | $\chi$ with Decreasing Temperature |
|---|---|---|
| Diamagnetism | $-8 \times 10^{-6}$, $-1$ for SC | None |
| Paramagnetism | 0.1-0.001 | Increases |
| Ferromagnetism | $5 \times 10^3$ | Increases |
| Antiferromagnetism | $0\text{-}10^{-2}$ | Decreases |

The different types of magnetism can be identified by the magnetic susceptibility of a material, including the effect of temperature. In diamagnetic samples, where there are no unpaired electrons and therefore no magnetic moments, a small negative susceptibility is present due to the exclusion of the magnetic flux from the sample. This diamagnetic effect is created by the orbital momentum of the electron, where a small moving electric field generates a magnetic field. The electron momentum is affected by the applied magnetic field, repelling it.

In paramagnets magnetic moments exist, typically from ions with unpaired electrons, but do not have sufficient interactions to order. In this paramagnetic state the application of a magnetic field aligns the moments with the field, producing a positive susceptibility, and as the temperature is lowered less thermal motion leads to an increase in magnetic susceptibility. As magnetic ordering emerges below $T_C$ or $T_N$ the susceptibility of a paramagnet changes. This thesis is concerned with the magnetic orders and interactions, so it is necessary to understand the effect of an applied magnetic field on materials with moments that can be ordered at low temperatures. At temperatures above the ordering temperature (Curie Temperature $T_C$ for a ferromagnetically ordering sample, Néel $T_N$ for an antiferromagnetically ordered sample) the material is paramagnetic. In ferromagnets, these parallel interactions allow for full alignment with a field and so the susceptibility increases rapidly. Where these interactions are anti-parallel this reduces the net moment, so susceptibility decreases (see Figure 1.6). Most materials have some sort of ordering transition, but there are exceptions. [29]
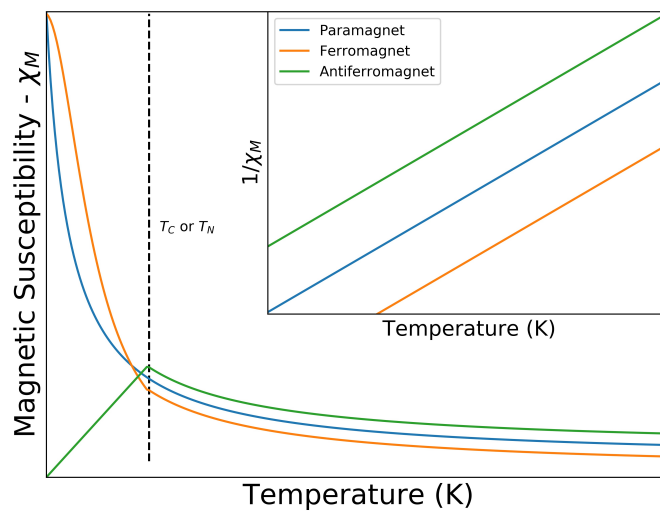


**Figure 1.6** Ideal magnetic susceptibility and reciprocal susceptibility, following Curie-Weiss law, as a function of temperature. Shown are the curves for a paramagnet, ferromagnet and antiferromagnet in blue, orange and green, respectively. The reciprocal susceptibility shows the x-intercept positive for a ferromagnet and negative for an antiferromagnet, known as the Curie temperature.

At $T_C$ and $T_N$ a order-disorder transition occurs, as the material goes from a disordered paramagnet to an ordered structure, evidence for this is shown within the magnetic susceptibility temperature dependence. A purely isolated paramagnet will obey the Curie-Law, which states that the magnetic susceptibility is inversely proportional to temperature, given by Equation 1.6. [28]

$$\chi = \frac{C}{T} \tag{1.6}$$

Where C is the Curie constant, and T is the temperature. Paramagnets with interactions between magnetic centres well obey a modification of the Curie law - the Curie-Weiss law, the application of which can aid with the identification of ferromagnets and antiferromagnets. [30] This is given by:

$$\chi = \frac{C}{T - \theta_{CW}} \tag{1.7}$$

where $\theta_{CW}$ is the Weiss constant. The insert in Figure 1.6 shows the effect that a positive or negative $\theta_{CW}$ has on the inverse magnetic susceptibility. A positive $\theta_{CW}$ indicates dominant ferromagnetic correlations within the materials, and conversely a negative value indicates dominant antiferromagnetic correlations, and in simple ferromagnets and antiferromagnets $\theta_{CW}$ is close to $T_C$ or $T_N$.

By fitting the inverse magnetic susceptibility in the paramagnetic region, and some simple maths, we are able to determine the Weiss and Curie constants of the sample. We can see that the Curie constant is equal to 1/slope and the Weiss constant is equal to −intercept/slope. In ideal cases the $|\theta_{CW}|$ determines the ordering temperature of the material and is equivalent to $T_N$ or $T_C$.

The observed magnetic moment can then be calculated from the Curie constant using:

$$\mu_{eff} = \sqrt{\frac{3k_B \cdot C}{N_A \cdot \mu_B^2}} \tag{1.8}$$

where $k_B$ is the Boltzmann constant, $N_A$ is Avogadro's constant and $\mu_B$ is a Bohr magneton.

For materials with significant competing interactions the actual long-range ordering temperatures may differ considerably from the Curie-Weiss temperature. In many cases the frustration index, $f_i$ therefore provides a way of measuring and comparing materials with high degrees of magnetic frustration, and is given by:

$$f_i = \frac{T_N}{\theta_{CW}} \tag{1.9}$$

This value must be considered tentatively in materials where low temperature effects become significant such that the orbital angular momentum is quenched, as in lanthanides, but is a good approximation nonetheless. Determination of the dominant interactions, and order associated with a sample is important for understanding the microscopic interactions within a material. In addition to temperature dependent measurements of a sample it is also useful to perform field dependent measurements, to see how the magnetisation of a sample reacts under changes in field. Application of a field to a paramagnetic or antiferromagnetic sample will increase the magnetisation linearly in small applied magnetic fields and in a sigmoid-like curve in larger applied fields, but no magnetisation will persist after removal of the applied field (see Figure 1.7a). Figure 1.7b shows a typical hysteresis loop for a ferromagnetic sample. If the sample is magnetised to the saturation point, when the magnetic field is reduced to 0, some remnant magnetisation will remain. [31] As the sample is initially magnetised the domain walls of the sample align with the field, until saturation occurs, resulting in the virgin curve. [32] A small hysteresis can sometimes also been observed in antiferromagnetic samples with a ferromagnetic component, as a result of spin canting leading to a weak ferromagnetic state.



|            (a)            |            (b)            |
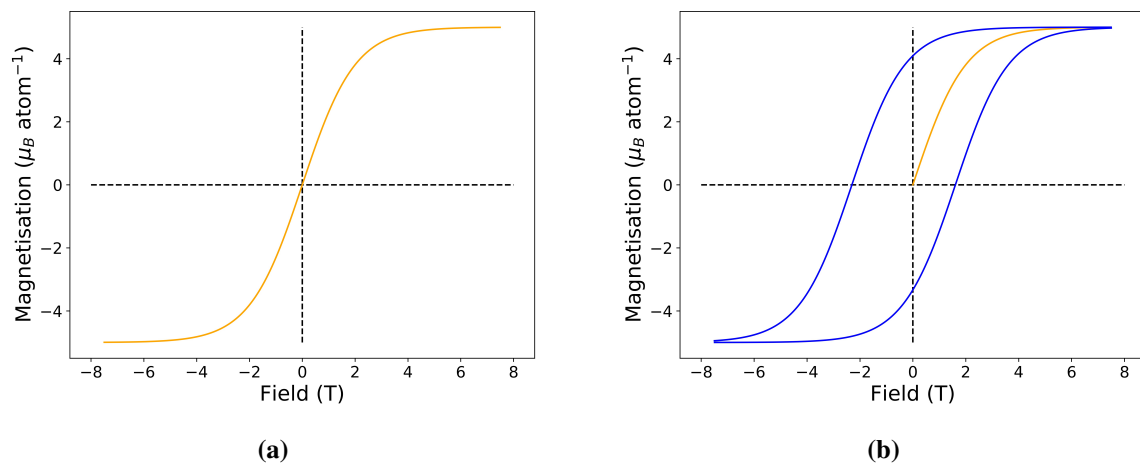
**Figure 1.7** (a) Magnetisation measurement of a paramagnetic sample, antiferromagnets have similar saturation curves in low applied fields, in higher fields stepped magnetisation can occur, as discussed in Section 1.6.4. (b) Magnetisation measurement of a ferromagnetic ordering sample. The virgin curve is shown in orange, and the subsequent field sweeps are shown in blue.

The saturation value of the magnetisation in high fields can yield some additional information about the dimensionality of the magnetic spins. In samples with no magnetic anisotropy, the magnetisation value will approach the moment determined from Curie-Weiss law ($g_J J$), as there are no constraints in which direction the spins can align, and therefore can fully align with field. In powder averaged samples with significant magnetic anisotropy such that the

spins have an easy axis, the saturation values approach $g_j J/2$. [33, 34] In a powder-averaged samples with randomly oriented particles the application of a magnetic field can only be applied along one axis. If the vector of the magnetic field is perpendicular to the easy axis, the spin will not align with the field. If the field is applied near the easy axis the spin will align along the easy axis closest to the applied field vector, but the measured magnetisation will not be the $g_j J$ due to the lack of fully orientation of the spin in that direction. By measuring the saturation value at low temperatures we can determine whether the spins obey Heisenberg or Ising mechanics.

This magnetisation saturation value of a powder-averaged lanthanide uniaxial spin system (Ising), with a angle between the applied field vector and the easy axis vector of $\theta$, can be expressed mathematically as:

$$M_{sat} = \frac{1}{n} \sum_i^n g_J J \cdot sin^2 \theta \qquad (1.10)$$

## 1.6 Magnetic Interactions

To fully understand how magnetic order can occur the microscopic models of magnetism must first be considered. For a spin system constructed of two electrons, the Hamiltonian can be written as the sum of two spin states $S_1$ and $S_2$, the energy of the singlet wavefunction $E_S$ and an antisymmetric triplet wavefunction $E_T$. The Hamiltonian is given by:

$$\hat{H} = \frac{1}{4}(E_S + 3E_T) - (E_S + E_T)S_1 \cdot S_2 \qquad (1.11)$$

The exchange energy which determines if the neighbouring spin state is antisymmetric can be written as:

$$J = \frac{E_S - E_T}{2} \qquad (1.12)$$

therefore the spin-dependent term of the Hamiltonian is:

$$\hat{H}^{spin} = -2J S_1 \cdot S_2 \qquad (1.13)$$

Therefore if J is negative, the neighbouring spin will be antisymmetric (antiparallel) with respect to the nearest neighbour, and symmetric if positive. This applied for a two spin system, but generalised to a many spin system this can be written as:

$$\hat{H} = -\sum_{(i,j)} J_{ij} \vec{S}_i \cdot \vec{S}_j \tag{1.14}$$

which is the simplest model for nearest neighbour magnetic interactions and is also called Heisenberg model.

In this generalised equation $i$ and $j$ are spin sites on a periodic lattice. $\vec{S}$ is a unit vector, representing the magnitude and direction of a magnetic moment, and $J_{ij}$ is the strength of the interaction between neighbouring spins.

### 1.6.1 Dipolar and Direct Exchange

Below some critical temperature, the exchange interactions become significant enough to overcome the thermal energy and allow for ordering of the magnetic moments. The first interaction between magnetic moments that should be considered is the dipolar interaction. If we consider two magnetic dipoles $\mu_1$ and $\mu_2$, separated by a distance of $r$, the exchange energy of this interaction is given by: [31]

$$E = \frac{\mu_0}{4\pi r^3} \left[ \mu_1 \cdot \mu_2 - \frac{3}{r^2} (\mu_1 \cdot r)(\mu_2 \cdot r) \right] \tag{1.15}$$

where $\mu_0$ is the vacuum permeability. Here we can see the energy of the dipolar exchange is inversely proportional to the distance cubed separating the two moments. For two magnetic moments with moment of 1 $\mu_B$ and separated by a distance of 1 Å , this is approximately equal to $10^{-23}J$ or 1 K. This dipolar interaction is therefore extremely weak, and alone cannot explain the higher magnetic ordering temperatures observed in many materials. For two lanthanide ions, this effect is much more significant due to the large magnetic moments and for two $Tb^{3+}$ with a magnetic moment of 9 $\mu_B$ separated by a distance of 5 Å this becomes significant at $\approx$1.2 K.

When exchange happens between two neighbouring atoms, this is known as direct exchange. The exchange interaction can occur through overlap of the orbitals, allowing for direct coupling of two magnetic moments to one another. However, in rare-earth elements, the $4f$ electrons are extremely localised to the core with little probability of the electron density

extending beyond the atomic radii. Therefore, direct exchange is extremely unlikely and cannot explain the observed phenomena at higher temperatures.

## 1.6.2   Superexchange

When magnetic moments on atoms are not close enough to each other, direct exchange is not a significant effect. However, the exchange interactions can occur through another atom, often an oxygen atom and this is referred to as superexchange. Superexchange was first proposed by Kramers [35] and extended by Anderson [36] as a way of explaining the strong interaction observed in MnO, without direct Mn-Mn coupling and a non-magnetic atom separating them. [26]

Goodenough and Kanamori then developed a set of rules for determining the types of interactions dependant on the bond angles. [37–39] For simplicity, if we consider the octahedral coordination environment of a $Ni^{2+}$ ion, a single unpaired electron occupies the $e_g$ orbitals oriented towards an oxygen creating partial or fully covalent bonds with the oxygen $p$ orbitals. The $p$ orbital of the oxygen contains two electrons, antisymmetric to the other. The nickel and oxygen are sufficiently close to create overlap of the orbital and coupling of the electrons between the atom. Superexchange occurs through the intermediate oxygen, thereby coupling the two nickels. A bond between two nickel ions, through an oxygen will have coupling of the spins as shown in Figure 1.8. Here we see antiferromagnetic superexchange of the nickel with bond angles close to $180°$.
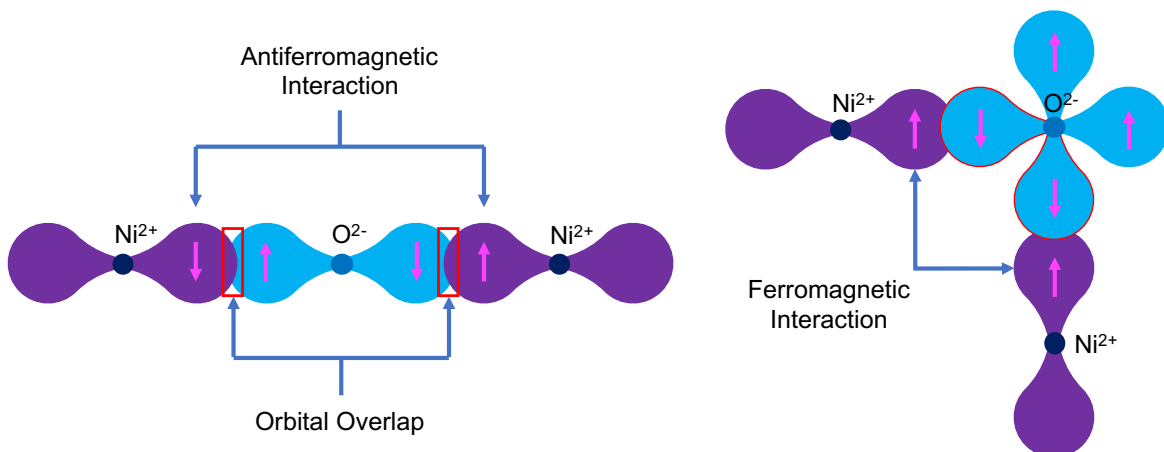


**Figure 1.8** (right) Diagram of the antiferromagnetic superexchange mechanism between two $Ni^{2+}$ ions, through a $180°$ oxygen bond. (left) Diagram of the ferromagnetic superexchange mechanism between two $Ni^{2+}$ ions, through a $90°$ oxygen bond.

If however, the bond angles between the two nickel ions is closer to $90°$, the superexchange is more likely to be ferromagnetic, as shown in Figure 1.8. These Goodenough-Kanamori rules are more guidelines than rules, as they only consider the nearest neighbours, without spin-orbit coupling. In the $Ln^{3+}$ frameworks in this thesis, there is significant spin-orbit coupling, and many interactions within the systems, some of which are competing or rely on coupling through multiple non-magnetic atoms. This somewhat complicates the picture.

### 1.6.3   Heisenberg, XY, and Ising Models

In the simplest model of magnetic interactions, spins are considered to be three dimensional and can be oriented in any direction, this is given by the Heisenberg model as given by equation 1.14. The 3D Heisenberg spins have the dimensionality $D = 3$, and can sit on a lattice with a dimensionality of $d = 1$, 2 or 3. Alternatively, spins can be constrained so they can only point up or down along a single axis, known as the Ising model ($D = 1$), [40] or in a easy plane - the XY model (D = 2).

The Ising model spins are constrained up and down $D = 1$ and so we only need to consider the z component of the coordinate system, such that the Ising model Hamiltonian can be written as:

$$\hat{H} = -\sum_{(i,j)} J_{ij}\vec{S}_i^{\,z} \cdot \vec{S}_j^{\,z} \tag{1.16}$$

The spins can then be placed on crystal lattices with different dimensionalities. The one dimensional Ising model takes spins arranged onto a chain, with the ground state $NJ/2$ for the spin $S_i = \pm 1/2$. Long range 1D magnetic order cannot exist in an isolated system, with the exception of an Ising system exclusively at 0 K due to a spin gap. [41]

### 1.6.4   Theories of Ferro and Antiferromagnetism

**Ferromagnetic Models**

In 1907 Weiss proposed a molecular field to explain the ordered magnetic state. [42] In the Weiss model of ferromagnetism the spins align with the molecular field $F_w$. The molecular field is proportional to the exchange interaction $J$ of the spins, and for a magnetic moment with orbital angular momentum, can be written as:

$$F_w = \frac{2J(g_J - 1)^2}{n g_J^2 \mu_B^2} \tag{1.17}$$

where $J$ is the exchange interaction. This yields the Curie temperature for a ferromagnet as:

$$T_C = \frac{2J_i(g_J - 1)^2}{3k_B} J_q(J_q + 1) \tag{1.18}$$

where $J_i$ is the exchange interaction and $J_q$ is the total angular momentum. Unfortunately these two quantities are often written with the same symbol, and so here they have been differentiated. $g_J$ is the landé factor.

The Landau theory of ferromagnetism takes a slightly different approach which presents a mean-field theory of ferromagnetism. [43] This theory also extends beyond the Weiss model to describe the nature of phase transitions to a ferromagnetic state. This describes the magnetisation ($M$) of the sample, above and below the $T_C$, for materials with a moment $\neq 0$, as given by: [31]

$$M = \pm \left[ \frac{a_0(T_C - T)}{2b} \right]^C \tag{1.19}$$

Where $a_0$ and $b$ are positive constants, and $C$ is the critical exponent, which for the magnetisation is $= 1/2$. This mean-field theory therefore describes a system where all the spins are subject to the same averaged field, and is identical to the Weiss model, but expressed differently. These mean-field theories are the simplest models for ferromagnetism and therefore do not account for complex cases, and ignore small perturbations in the mean field which become important near the phase transition temperatures.

**Antiferromagnetic Model**

When the exchange interaction is negative, the spins will orient antiparallel, with respect to the nearest neighbour leading to an antiferromagnetic magnetically ordered ground state. In a simple model this can be considered two ferromagnetically ordered lattices, that are combined, such that you have two molecular fields, one for the up spins, and another for the down spins. The Weiss model of antiferromagnetism expresses this as:

$$B_- = -|F_w|M_-$$
$$B_+ = -|F_w|M_+$$

(1.20)

For a perfect antiferromagnet where $M_- + M_+ \equiv M$, the Néel temperature becomes:

$$T_N = \frac{g_J \mu_B (J+1)|F_w|M_{sat}}{3k_B} = \frac{n|F_w|\mu_{eff}^2}{2k_B}$$

(1.21)

where $U_{eff}$ is the effective magnetic moment, and $M_{sat}$ is the value at which the materials reaches saturation in high applied fields, and $J$ is the quantum number. For materials where $M_+ \neq M_-$, below $T_N$ the application of sufficiently large magnetic field can result in a staggered magnetisation, such that it requires less energy align one spin lattice with the field, than the other. [44, 45]

So far we have neglected the effect of fluctuations on the mean field, but this has an important effect on the behaviour of magnetism within solids. Divergence from the mean field can be expressed in terms of a correlation length ($\varepsilon$), which physically corresponds to the length of which the correlation extends to. [46] This can also be considered as the distance at which thermal fluctuations become more significant than the strength of the exchange interactions. At high temperatures $T >> T_C$ the correlation length is very small, because fluctuations are so strong. At low temperatures where $T < T_C$, for a fully ordered materials the correlation length should approach infinity. In between where a phase transition is occurring or where we are dealing with disordered materials the correlation length becomes a useful tool for determining the behaviour of magnetic materials.

### 1.6.5 Spin Waves

The excitation of a collection of spins, coupled together through exchange interactions is called a spin-wave. Spin wave theory was first proposed by Bloch and Slater, independently in 1930. [47, 48] The problem with calculating physical properties is the physical nature of spin waves are so complicated some approximation is necessary, [49] therefore the spin-waves are considered to be a perturbation from Landau's mean field. If a local spin is excited into a procession about an axis, this will in turn excite the moments coupled to it. The procession of the spins propagates through the magnetic material, like a wave (Figure 1.9). The spin-wave through a collection of spins can be considered analogous to the vibration of

a lattice. In solids the collection of acoustic vibrations is treated as a quasi-particle, called a phonon, and as such a spin-wave can be considered a magnon, quasi-particle.
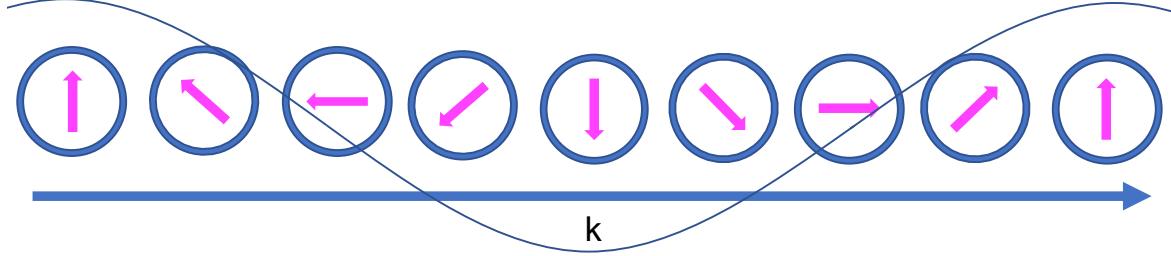


**Figure 1.9** A diagram showing the propagation of a spin wave through a ferromagnet, with vector $k$.

The magnon is a boson propagating through the magnetic order with a frequency, $\hbar\omega$ and momentum $\hbar q$. A simple ferromagnet with moments oriented close to the $z$ axis, Heisenberg interactions, $n$ spins, magnitude $S$ and the exchange interaction $J$, gives the energy of the $n^{th}$ spin as:

$$E = -2J \sum_{n=1}^{N} S_n \cdot S_{n+1} \tag{1.22}$$

Assuming the magnetic moments behave as classical bodies, this gives the effective field acting on the $n^{th}$ spin, due to the exchange interactions as:

$$B_n = -\frac{2J}{g_J \mu_B} \sum_{n=1}^{n} S_n \cdot S_{n+1} \tag{1.23}$$

The linear equation to solving the magnetisation of $S_n$ requires no additional approximations and is given by:

$$S_n = -S\hat{z} + \sigma_n \tag{1.24}$$

where $-S\hat{z}$ is the constant value of $S_n$, and $\sigma_n$ is the vector away from the perfectly aligned moment. This can visually represented as in Figure 1.10a.

The dispersion relation of the spin-wave in 1D spin wave can be given by:

$$\hbar\omega = 4JS(1 - cos k\, a) \tag{1.25}$$
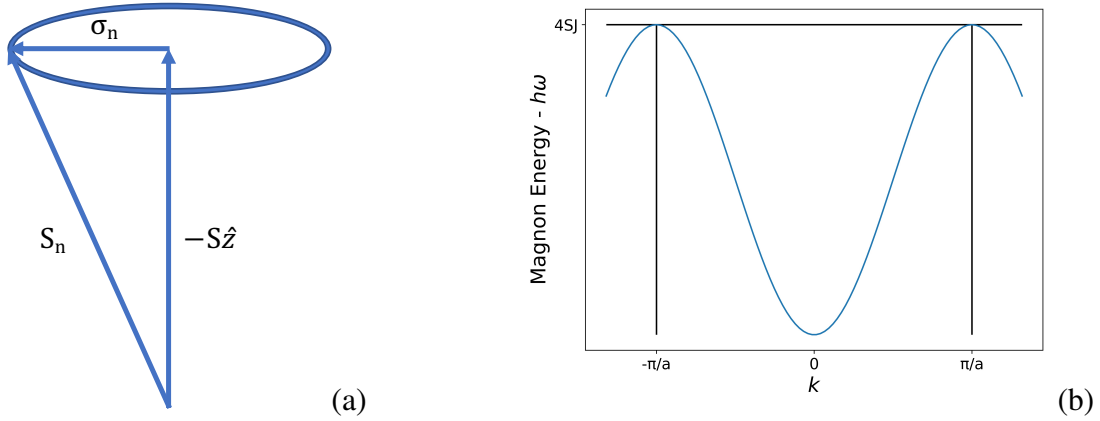
**Figure 1.10** (a) A diagram showing the energy of the $S_n$ (b) The dispersion relation of a 1D ferromagnet

the solution for the spin wave dispersion, shown over the first Brillouin Zone $-\pi/4 - \pi/4$, is shown in 1.10b. For temperatures $T > 0$ the density of modes of magnons is: [50]

$$D(\omega) = \frac{1}{4\pi^2}\left[\frac{\hbar}{2JSa^2}\right]^{3/2}\omega^{1/2} \tag{1.26}$$

where $a$ is a lattice spacing. So we can see that the magnetisation of the sample is: [51]

$$T^{3/2} \propto \frac{M(0) - M(T)}{M(0)} \tag{1.27}$$

which is Bloch's $T^{3/2}$ law. This simply means that the magnetisation of a sample is reduced at temperatures above the ordering temperature, but above zero, by the thermal population of excited states. Hence in inelastic scattering where the excitation are detectable it is possible to recover the full magnetisation value. [52]

## 1.7 The Magnetocaloric Effect

The magnetocaloric effect (MCE) is an entropically driven cooling process that occurs when paramagnets are in a cycled magnetic field. [53] As entropy is the number of available microstates in a system, the magnetic entropy of a system is directly related to the disorder of the spins. Total entropy S of the magnetic material is contributed by three parts, i.e., the magnetic entropy $S_m$, the electronic entropy $S_e$, and the lattice entropy $S_l$. When a magnetic field is applied to the system the spins align with the external magnetic field, to produce a

more ordered state thereby reducing the magnetic entropy of the system. The total entropy of the system stays constant under an adiabatic condition, the lattice contribution $S_l$ increases oppositely to keep total S constant. This results in a positive temperature change, to the material, as the magnetic entropy of the system is lowered. In order to use this effect in the context of magnetic refrigeration this process must be done adiabatically, such that the material heats up without loss of heat to the system ($\Delta T_{ad}$). By removing the heat generated after this step, through an applied heat sink, the materials can be cooled down moving heat from inside the system to the outside. When the magnetic field is removed in the adiabatic demagnetisation step, the materials cools down. [54] This process is summarised in Figure 1.11.
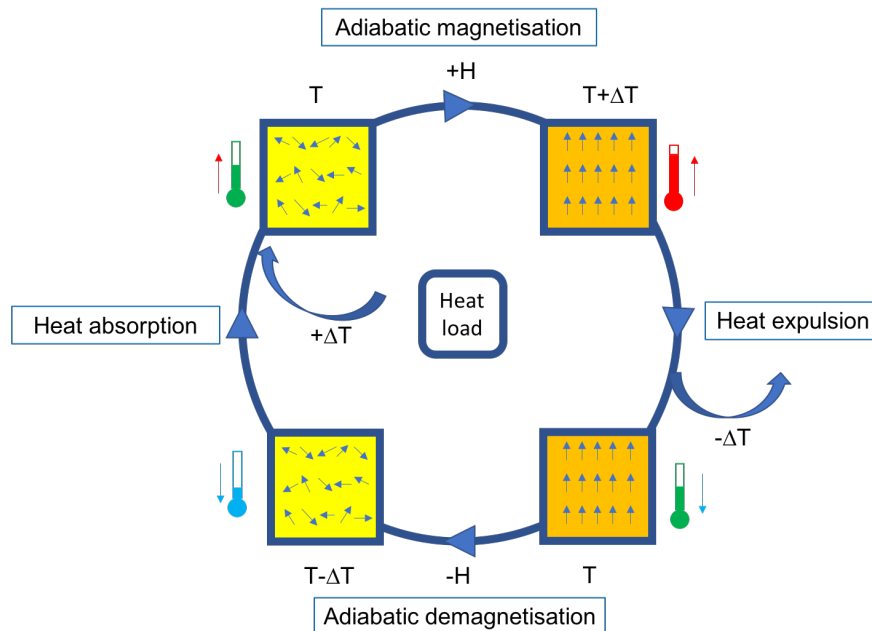


**Figure 1.11** Diagram of the magnetocaloric adiabatic refrigeration cycle.

This process can be iterated to lower the temperature of the material, but for this effect to work optimally the material must remain paramagnetic over the working temperature range. This process was first employed in 1933 on the dilute paramagnetic salt $Gd_2(SO_4)_3 \cdot 8H_2O$ to reach sub kelvin temperatures [55] and now these materials are now often employed in low temperature cooling applications. [56] Dilute salts have been employed because the use of non-magnetic ions reduces the ordering temperature to a few mK, [57] ideal for preventing the entropy loss associated with a phase transition.

Lanthanide ions are most suited to MCE materials, having the largest number of unpaired spins and greatest magnetic moments. The maximum magnetic entropy change ($-\Delta S_m$) is

usually assumed to be $nRln(2S+1)$ for a material. This is neglecting any contribution from the orbital angular momentum, which cannot be readily aligned with a field in a powder sample. [58–61] Table 1.3 summarises the magnetic entropy of some later $Ln^{3+}$ ions based on their magnetic spin.

**Table 1.3** Magnetic entropy for some later lanthanides.

| $Ln^{3+}$ ion | S | $Rln(2S+1)$ (J K$^{-1}$ mol$^{-1}$) |
| --- | --- | --- |
| Gd$^{3+}$ | 3.5 | 17.29 |
| Tb$^{3+}$ | 3 | 16.18 |
| Dy$^{3+}$ | 2.5 | 14.89 |
| Ho$^{3+}$ | 2 | 13.38 |
| Er$^{3+}$ | 1.5 | 11.53 |

When a magnetic field is applied to a paramagnetic material, the entropy is reduced, giving a field induced ferromagnetic state and the magnetisation of the sample is increased. The increase in magnetisation can be easily measured, and using the Maxwell relationship (Equation 1.28) the entropy change can be calculated.

$$\Delta S_m(T) = \int \left[ \frac{\delta M(T,B)}{\delta T} \right]_B dB \tag{1.28}$$

Calculating the entropy change from this method, has its limits because it assumes a field-induced ferromagnetic state. If the application of a magnetic field induces a long range order antiferromagnetic state, such that the magnetisation of the material is reduced, this will produce false negative $-\Delta S$. Gd$^{3+}$ materials have traditionally been favoured as magnetocaloric materials due to their high magnetic spin caused by having exactly half filled $f$-orbitals (S $= \frac{7}{2}$) as they have the largest entropy per single ion. Materials such as Gd$_3$Ga$_5$O$_{12}$ (GGG), are optimised at sub 2 K temperatures for uses, where reaching millikelvin temperatures is priority over energy efficiency, and requiring large fields with superconducting magnets has been deemed acceptable.

The Heisenberg-like spins of Gd, caused by its lack of orbital angular momentum and therefore spin-orbit coupling, can point in any direction and thus applying fields to a powder sample can align the spins fully, producing large changes in entropy from a paramagnetic to an ordered state. In contrast when spins have significant anisotropy such that they are confined to an easy axis, as in the Ising model an applied field, [40] perpendicular to the easy axis, will incur no change in magnetisation. Thus Ising anisotropy prevents full magnetisation with

field in bulk powders, which is detrimental to the magnetocaloric effect. Recently, however, work has shown that materials containing cations with strong Ising anisotropy improves the magnetocaloric effect in powders under the low applied magnetic fields that can be generated using a permanent magnet (< 2 T). [4, 33] This surprising result is an outcome of the greater ease of magnetisation of these materials under low applied fields, but the microscopic cause of this remains unknown. Uncovering how magnetic interactions in such compounds are best optimised to improve magnetocaloric performance requires an understanding of these materials at the microscopic level, which is most readily achieved using neutron scattering rather than indirect bulk property measurements.

The efficiency of MCE cooling can be greatly improved by developing materials that provide large changes of entropy in low fields (below 2 T), allowing them to be used in conjunction with a permanent magnet rather than relying on the use of superconducting magnets. [62] If such optimisation of MCE properties at low applied fields is coupled with an increase in temperature at which the MCE effect peaks to above 4 K, this approach could potentially be used for cooling at liquid helium temperatures. This has a greater range of applications than cooling below 2 K, including for cooling superconducting magnets in devices such as medical resonance imaging (MRI) scanners and NMRs. Such applications typically rely on liquid helium, which is vital to science and medical applications but is becoming an increasingly scarce and expensive resource. [63] While cryogen free cryocoolers are available as alternatives for cooling to the liquid He temperature regimes, their efficiency at such temperatures is particularly low, typically only a couple of percent. [64] It is therefore important to investigate if MCE materials can be optimised to have high performance in low applied magnetic fields between 4 and 20 K. Such materials could then be used for cooling in the liquid helium regime likely in conjunction with, more efficient, higher temperature cryocoolers. [65, 66]

For such optimisation of MCE materials, it is becoming apparent that it is important to not just achieve a high density of magnetic cations but also control the magnetic interactions in these compounds. It is well established that frustrated magnetic interactions can enhance MCE behaviour, including in the benchmark oxide GGG; [67–69] frustrated interactions enable a higher density of magnetic cations to be incorporated in a phase that remains paramagnetic to low temperature than is possible in the alternative "dilute" magnetic salts, which depend on having well separated magnetic centres to remain paramagnetic. [70] As a result, magnetic frustration increases the maximum $-\Delta S_m$ possible per unit volume or weight. It has also been shown that the Ising-like interactions in $Dy_3Ga_5O_{12}$ play a role in it having superior

MCE performance for field changes below 2 T than found in GGG; [71] as mentioned above this concept is supported by similar improvement in the MCE properties of other families of compounds when Gd is substituted with lanthanides with Ising-like interactions. [4, 33, 72] Amongst such Ising-systems $Tb(HCO_2)_3$ is particularly promising as a MCE material for use in low applied fields above 4 K; this has been suggested to be linked to the existence of strong 1D ferromagnetic correlations in this material enabling its magnetic moments to align even more easily with applied magnetic fields. [4, 18]

These results provide a drive for examining MCE materials based on other late lanthanides, including Tb and Dy particularly in structures supportive of frustrated and low dimensional magnetism. An obvious starting point for such studies is families in which the Gd analogue is already known to have promising MCE properties. $GdPO_4$, $GdOHCO_3$ and $GdF_3$ have been shown to have some of the largest peak MCE yet, [62, 69, 73] with $-\Delta S_m$ of $\approx 58$, 69.3 and 67.4 J $K^{-1}$ $mol^{-1}$ at 2 K for a 5-0 T field changes, respectively, compared to a peak entropy change of 32.6 J $K^{-1}$ $mol^{-1}$ for $Gd_3Ga_5O_{12}$. [73, 74] Notably of these high performance families two are dense coordination frameworks, which contain polyatomic anions. Such frameworks tend to adopt highly anisotropic structures with a range of competing magnetic interactions between magnetic cations. [62, 75–77] The $Ln$OHCO$_3$ frameworks appear particularly interesting as they have a conceptually similar structure to the $Ln(HCO_2)_3$, as it can be viewed as having chains packed in a triangular array with previous calculations suggesting the presence of competing antiferromagnetic interchain coupling.

## 1.8 Frustrated and Low Dimensional Magnetism

### 1.8.1 Frustrated Magnetism

Below some temperature the exchange interactions $J$ are sufficient to overcome the thermal fluctuations in the material, and spins can align in a energetically favourable orientation. When the exchange integrals $J_{ij}$ are negative, the spins align anti-parallel to nearest neighbours (antiferromagnetic) (Figure 1.12a); when exchange integrals are positive the spins are parallel (ferromagnetic). On a square lattice, with no next nearest neighbours, either of these ground states can be satisfied.

Magnetic frustration occurs when there are competing magnetic interactions, usually when some of the exchange paths are antiferromagnetic, if only nearest neighbour interactions are considered. The classical example of these systems are Ising antiferromagnetic coupled spins

arranged on a triangular lattice (Figure 1.12b), first studied by Wannier in 1950. [78] In this model system, it is energetically favourable for the spin to be anti-parallel, with respect to its nearest neighbour, but the crystallographic structure of the materials means there are two near neighbours competing for anti-parallel alignment.
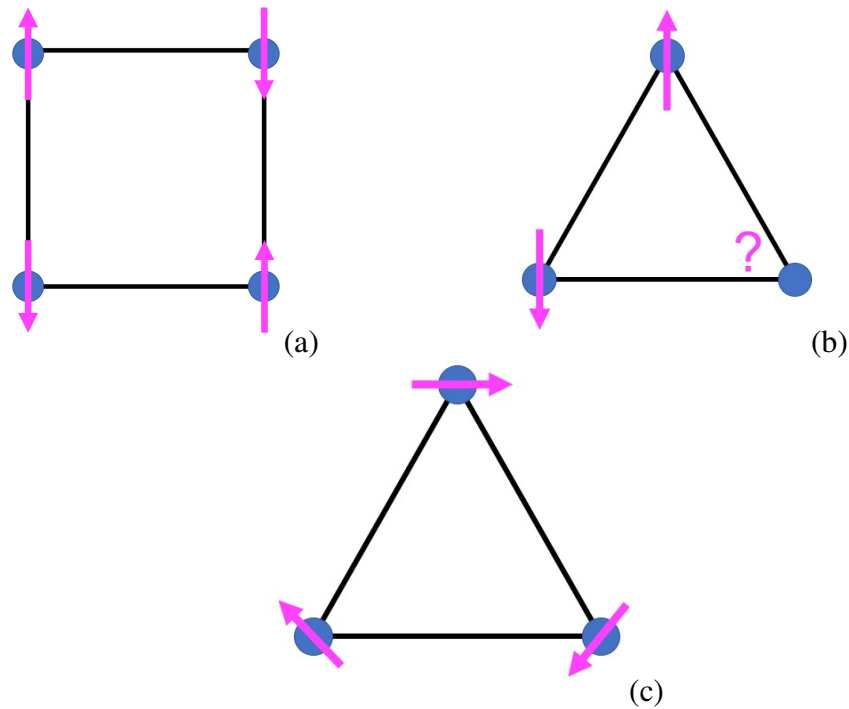


**Figure 1.12** (a) Antiferromagnetically ordered square lattice, (b) a frustrated antiferromagnet on a triangular lattice (c) antiferromagnetically coupled Heisenberg spins on a triangular lattice.

In an Ising system it is not possible to satisfy both simultaneously and so a frustrated ground state emerges with many degenerate energy levels. In a Heisenberg system this frustration can be alleviated though other routes as shown in Figure 1.12c. When frustration arises purely from the topology of the lattice, this is described as geometrically frustrated. Whilst this is a convenient illustrative example, frustration is not limited to two dimensions, or even triangular lattices, for example in three dimensions this corresponds to a pyrochlore motif.

Frustration in materials can lead to exotic states including some of the most studied pyrochlore spin ice materials, $Dy_2Ti_2O_7$ and $Ho_2Ti_2O_7$, consisting of four ferromagnetically coupled lanthanide ions with strong Ising character. [79] Spin ices are named because of their analogy with water ice, with two spins facing the center, and two facing outwards (see Figure 1.13a). This leads to some fascinating properties, such as the existence of magnetic monopole

quasiparticles, [80] that cannot exist in isolation. Spin ice materials are an example of systems which have a highly degenerate ground state and can exhibit magnetically charge ordered states, when one of the spin is flipped. The garnet lattice consists of cations sitting on the vertices of corner sharing triangles, forming a highly frustrated 3D system of interpenetrating rings. Frustration, in the benchmark magnetocaloric GGG, prevents long range order forming, but shows spin-liquid behaviour between 140 mK and 5 K, [67] where despite significant antiferromagnetic interactions the magnetic moments continue to fluctuate. Unlike a paramagnet however, the spins are correlated while remaining dynamic even very close to absolute zero.



(a)                                        (b)
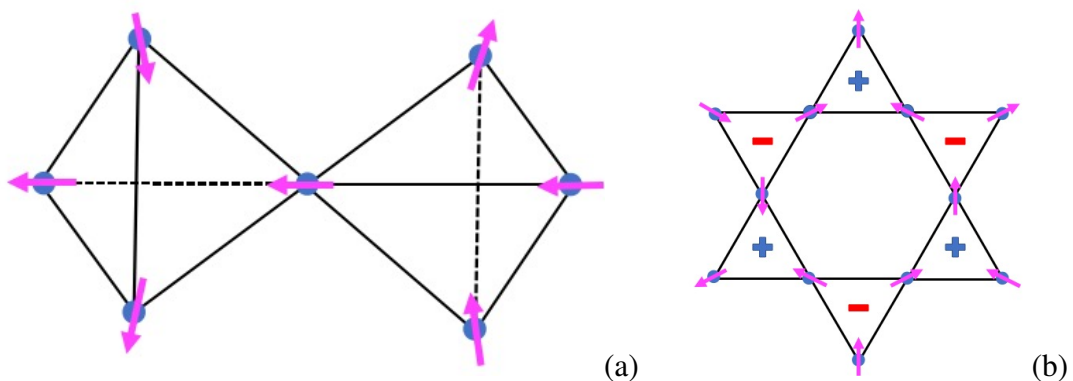
**Figure 1.13** (a) A spin ice tetrahedra with two in, two out spin arrangement (b) a kagome emergent charge ordered state.

By magnetically isolating the layers in crystal lattices from one another, the magnetic order can be reduced to two dimensions, shown in Figure 1.14. The highly studied two dimensional kagome lattice can be described as a pattern of corner sharing triangles and the triangular array is a tessellation of edge sharing triangles with magnetic cations sitting on the vertices. The kagome lattice $Dy_3Mg_2Sb_3O_{14}$ has also shown evidence of emergent charge order (ECO), [81] which displays long range magnetic order, on average, not present on the local scale due to frustration (see Figure 1.13b). This has been described as magnetic fragmentation i.e. the system can be thought of as in two states: a divergence free state (which gives rise to Bragg Scattering) and a divergence full state (which is the origin to the diffuse scattering and the kagome and pyrochlore pinch points). The unequal in/out arrangement of spins on the triangle create magnetic monopoles, which can be considered analogous to electric charges. Like electric charges, the magnetic charges repel and attract opposites, and so are forced to arrange into the lowest possible energy state. [81]
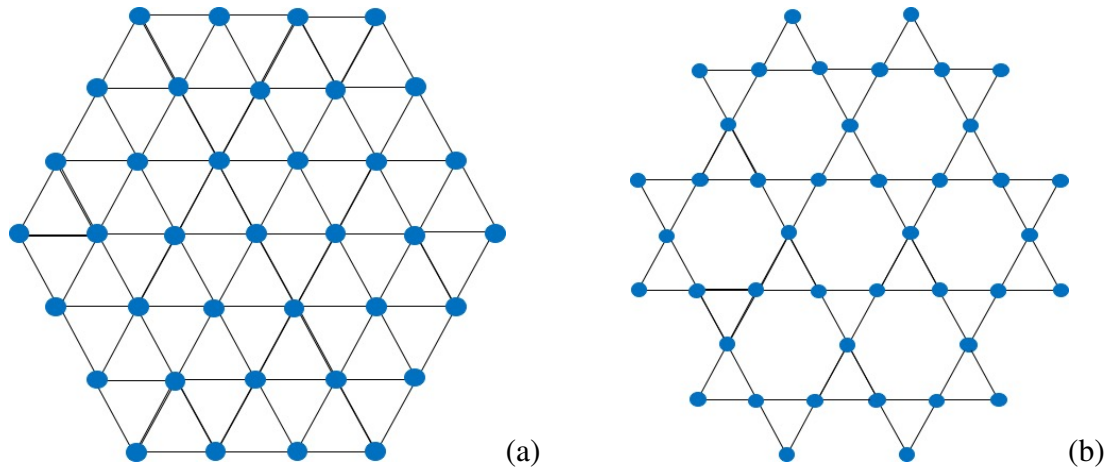
**Figure 1.14** Two 2D geometrically frustrated crystal structures. (a) A triangular array - edge sharing triangles (b) The kagome lattice - corner sharing triangles.

For the two dimensional case, the triangular array is the simplest case which can accommodate frustration, one such example is the yavapaiite mineral with the general structure $AM(SO_4)_2$. Where $M$ is a transition metal, and $A$ is the alkali metal cation which isolates the layers of magnetic ions, so the ground state magnetic order is constrained to two dimensions. Magnetic frustration in $CsFe(SO_4)_2$ and $RbFe(SO_4)_2$, is relieved through rotating the antiferromagnetically coupled spins by $120°$ in the $ab$ plane. [82] This is only possible in this case because the spins are Heisenberg-like and can point in any direction. [83] An Ising system, with a single easy axis, cannot relieve frustration through this method. Long range order is suppressed due to competing interactions, but unlike a paramagnet the spins are strongly correlated with their immediate neighbouring spins. [84]

The Kagomé lattice is well studied, for its high degree of frustration, its potential as a quantum spin-liquid (QSL) state [85] and the variety of minerals whose transition metal ions form such a lattice. QSLs form a novel class of matter where despite strong interactions between neighbouring spins, the system does not form any long range order, due to (zero-point) quantum fluctuations. [86] The first QSL candidate was a structurally perfect $S$ = 1/2 Kagomé antiferromagnet in the mineral Herbertsmithite in 2005. [87, 88] Interest has re-emerged in QSLs since the discovery of Majorana fermions in the QSL $\alpha$-RuCl$_3$ [89] - a type of particle that is it's own anti-particle and does not obey the Dirac equations. First predicted in 1937 [90] but only recently experimentally observed, has opened up new horizons in condensed matter physics. QSL candidates can also be found in the triangular array YbMgGaO$_4$, consisting of highly disordered correlated Ising spins. [91]

## 1.8.2    1D Magnetism

When the exchange interactions between magnetic ions is restricted to one dimension the material behaves as a 1D system. Such systems have attracted great interest for the potential to discover new phases of matter, attracting interest for quantum information transfer [92] and spin quasi-particles. [93]

Examples of low dimensional magnetism do exist, but it's often difficult in mineral and oxide systems to properly isolate magnetic chains from interacting with each other. While this is far from an exhaustive list, [94] some examples of this include the $AFeX_3$ family of compounds (where A = Rb or Cs and X = Cl or Br) consisting of stacked triangular array. These systems behave as Heisenberg quasi-1D spin chains, and in the case of $CsFeCl_3$ does not show any long-range 3D order down to 0.8 K. [95] If chains are poorly isolated as is the case for $RbFeCl_3$, the material will transition to a 3D ordered state. [95]

In the extended perovskite $ABX_3$ family other examples of quasi-1D magnetic compounds include $CsNiF_3$ and $CsCuCl_3$, with the latter being extensively studied. Both have their own associated fascinating ground state physics, but still consist of stronger Heisenberg ferromagnetic correlations in 1D with weaker antiferromagnetic exchange between the ferromagnetic chains. [96, 97] An interesting result in 1D magnetism can be found in the compounds $Sr_3CuIrO_6$ and $Sr_3CuPtO_6$, which are 1D Heisenberg ferromagnetic and antiferromagnetic, respectively. Mixing of the two materials results in a random ferro/antiferromagnetic paramagnetic state, described as a quantum spin chain paramagnet. [98]

More fascinating examples of quasi-1D systems are the Ising 1D systems. $Ca_3Co_2O_6$ has been extensively studied experimentally and theoretically as it undergoes a transition to a quasi-1D magnetic state in zero field and contains unusual magnetic properties. [99, 100] It has 1D ferromagnetic intrachain correlations and weaker interchain antiferromagnetic interactions, and at low temperatures orders into longitudinal amplitude-modulated spin-density wave (SDW) propagating along the $c$-axis. $\alpha$-$CoV_2O_6$, a 1D Ising ferromagnet, [101] undergoes transitions into different phases under variable applied fields. Studies of this material also showed that it was an excellent magnetocaloric, within it's operating temperature, with a steep magnetisation curve as a result of overcoming the antiferromagnetic interchain correlations into a ferromagnetic state. It should be noted that these systems show quasi-1D Ising like behaviour only because they are not truly isolated 1D chains, and exhibit 3D magnetic order.

### 1.8.3   Neutrons for Exotic Magnetism

The discovery of the neutron by James Chadwick in 1932, [102] was significant for the progression of solid state science and worthy of the 1935 Nobel prize in physics. This led to the pioneering work by Shull in 1949 [26, 103] that laid the groundwork for magnetic structure determination, using neutrons. The neutral charge and magnetic moment of neutrons make them an ideal probe for understanding magnetism on a microscopic scale and how this leads to the physical properties. It is therefore the technique of choice among solid state chemists and physicists. Modern neutron sources and detector technology have developed to the point where it is possible to collect high quality diffraction patterns with less than a gram of sample, allowing for the studies of magnetism in materials where synthesising high purity bulk samples is limited. Interactions between the magnetic moment of neutrons and spins, of sufficiently magnetically ordered materials, below it's ordering temperature, cause the appearance of magnetic Bragg peaks observable in diffraction patterns. For highly frustrated or low dimensional materials, with only short-range order, the correlated disorder may materialise as structured diffuse scattering [84].

However, to properly analyse the data and arrive at the correct solution, the quality of data measured must be sufficient to capture the subtle features observed in diffuse scattering to fully understand short-range correlated systems. It is typical for diffuse features to be two to four orders of magnitude weaker than Bragg reflections, [104] but with modern high efficiency detectors, and their low background, it is possible to capture high-quality reciprocal-space data at high flux spallation sources extremely rapidly. [105, 106] Another consideration that must be made is that we need to be able to distinguish between Bragg peaks, produced by truly long range order, and broadened Bragg-like peaks, that may indicate the order is short range or at least has a small domain size. This requires high resolution to distinguish between peaks that are instrument resolution limited, and those that are broad as a result of short range order. Finally, data must be recorded to the shortest possible reciprocal space to capture the diffuse features which appear in this region. With modern advances in understanding of magnetic systems and developed reverse Monte Carlo (RMC) techniques it is now possible to probe the nature of this diffuse from powder neutron diffraction experiments. [107, 108]

With these considerations, the data generated allows the solution of magnetic structures from powder diffraction patterns, and has such been developed extensively for oxide materials. These techniques can also be applied to framework materials that possess magnetic order, but the topology of these materials can lead to a greater variation in the types of magnetism observed. The caveat, however, of frameworks are the lower ordering temperatures, and need

to deuterate any hydrogen containing linkers, which have historically held back the quantity of studies, although these limitations are becoming less restrictive than they once were. The varied structures of frameworks have lead to a catalogue of reported magnetic structures, containing frustration and low dimensional order.

Many of the examples discussed so far, are dense oxides and minerals but the greater flexibility in design of the size, shape and coordination of organic linkers in frameworks allow for more complex magnetic structure and the ability to tailor desired magnetic properties. Forming one or two dimensional magnetic systems in oxides is not trivial, exemplified by the scarce physical realisations of theoretical models in these exotic states of matter. frameworks are a good alternative because they can have longer distances between magnetic centers, and therefore can better isolate the magnetic sheets or chains from each other. However, these low dimensional units can remain strongly coupled through oxygen atoms. It is possible to modify the ligand to achieve desired exchange interactions, making frameworks ideal model systems for the study of new physics. Until recently, the field of magnetic frameworks have been largely overlooked and many studies remain limited to bulk magnetic property measurements. There are fewer detailed studies of the microscopic magnetic phases in frameworks, which typically require neutron based techniques to characterise in detail. [109]

Examples of exotic magnetism in MOFs are present in the literature including chiral, 2D and 1D magnetic structures, in addition to long range magnetically ordered systems.[109] Frustrated magnetism has been experimentally studied in magnetic MOFs in materials such as $Co_3(OH)_2(sq)_2.3H_2O$ and $M(tca)_2$ (tca = tricyanomide), using neutron scattering but these materials undergo phase transitions to 3D long-range ordered structures, at low temperature. $Co_3(OH)_2(sq)_2.3H_2O$ has significant frustration within its $CoO_6$ ribbons, and unusually undergoes a phase transition upon dehydration.[110] In $Mn(tca)$ strong frustration is observed and is relieved by the formation of an incommensurate 3D structure. [111]

## 1.9 Thesis Overview

In this thesis we have explored the magnetocaloric properties, magnetic structure and correlations of some highly efficient magnetocaloric materials. The two main research themes have involved determination of the magnetocaloric effect through magnetisation measurements of other lanthanide frameworks, and determination of the magnetic structure and correlations in the materials which have displayed some of the most promising magnetocaloric results.

The first theme deals with probing the magnetocaloric measurements of some lanthanide frameworks for which the gadolinium framework has previously been found to show an excellent magnetocaloric effect at low temperatures. As discussed, the gadolinium materials do not have any orbital contribution to the magnetic moments and so, whilst unable to be experimentally confirmed with neutron diffraction, are expected to show no magnetic anisotropy. The other lanthanides in the series are expected to show strong anisotropy which may be beneficial to the magnetocaloric effect under modest applied fields. The magnetocaloric measurements of late $Ln$OHCO$_3$ and $Ln$F$_3$ frameworks have been explored, due to the efficient magnetocaloric effects displayed in GdOHCO$_3$ and GdF$_3$. [73, 77]

The second theme explores the magnetic correlations and magnetic structure, which is responsible for the efficient magnetocaloric effect observed. The magnetic structures have been determined with neutron diffraction, and Rietveld refinement in cases were long-ranged ordered magnetic structures evolve. In phases which lack long range order but have significant local magnetic correlations that lead to diffuse scattering, an RMC approach has been employed to uncover the nature of the diffuse scattering in the cooperative paramagnetic phases. Commonly the materials examined in this thesis feature diffuse magnetic scattering at higher temperatures before long-range or quasi-long range ordered states emerge at lower temperatures.

These magnetic phases have been explored in zero field to understand the correlations that are present before the application of a magnetic field, and in applied fields to understand how magnetic phases change under an applied field. Through studying the magnetic phases that emerge in applied magnetic fields we are able to directly observe the mechanism of the magnetocaloric effect. The work, in this aspect of the thesis, focuses on the $Ln$(HCO$_2$)$_3$ and $Ln$OHCO$_3$ frameworks, which have promising magnetocaloric properties for higher temperature applications. Before we describe the work conducted on these materials we will first describe what was known about these compounds prior to the work carried out in this thesis and the aims of our investigation.

As shown in Figure 1.15, the $Ln$(HCO$_2$)$_3$ frameworks have $Ln^{3+}$ ions arranged into chains on a triangular array. As shown in previous studies, [4, 18] Tb(DCO$_2$)$_3$ exhibits a large magnetocaloric effect that supersedes the Gd counterpart in low applied magnetic fields. Tb(DCO$_2$)$_3$ is an excellent example of a dense magnetic MOF with interesting properties at low temperatures and a physical realisation of a stacked triangular array, forming chains of Tb ions (Figure 1.15). The material perfectly combines frustration and 1D magnetic order, [18] making it the ideal model for the triangular array with near equivalent $J$ coupling between Tb

ions, through the formate ligand. The MOF examples discussed so far all have 3D ordered ground states but, for this Ising antiferromagnetic compound, the situation appears to be different.
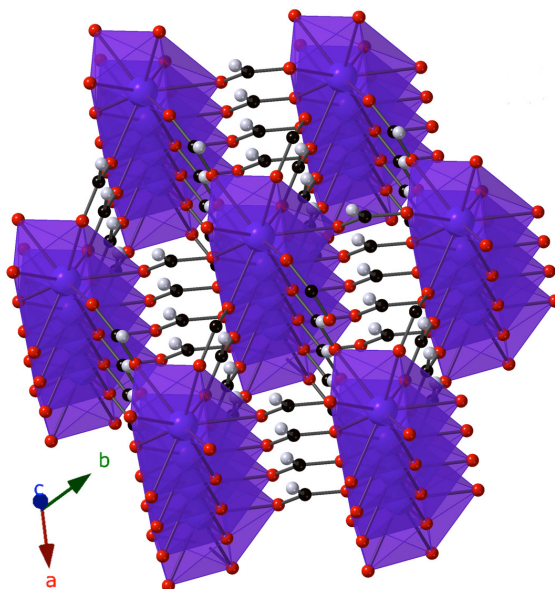


**Figure 1.15** The average crystal structure of $Tb(HCO_2)_3$. Tb ion coordination environments are shown as purple polyhedra, and carbon, oxygen and hydrogen are shown in black, red and white respectively.

Above 1.6 K $Tb(DCO_2)_3$ shows strong magnetic diffuse scattering as a result of short range order emerging from ferromagnetically correlated chains, coupled through frustrated antiferromagnetic interactions on the triangular array. Below 1.6 K it displays long range Ising-like 1D magnetic order along the $c$-axis with spins aligned in the chain direction, but shows no long range order in the $ab$ plane. The lack of long range 3D order appears to be suppressed by the frustrated interactions between chains leading to the emergence of a triangular Ising antiferromagnetic (TIA) state, with a large number of degenerate ground states. [18] In the paramagnetic phase it shows significant magnetic diffuse scattering, due to the frustration caused by antiferromagnetically coupled spins on the triangular motif. The diffuse scattering is consistent with highly disordered 1D ferromagnetic Ising chains, and cooling to ≈1.6 K leads to a stabilised 1D ordered magnetic state, with no long range order.

The 1D ordered state is stabilised by the large predicted difference between interchain and intrachain coupling, [18] combined with the magnetic frustration of the latter. By substituting other lanthanides in the series into isostructural frameworks we aim to explore the

exotic magnetic order over a wide temperature range. The ferromagnetic correlations and antiferromagnetic frustration that persists, in the paramagnetic state, allow for high entropy changes in small applied magnetic fields contributing to a high efficiency as a magnetocaloric. [4] This dominant ferromagnetic intrachain coupling allows the moments to be more easily aligned with the applied field. The additional weaker frustrated antiferromagnetic interchain interactions lead to suppression of magnetic order, in absence of a field, required for paramagnetic magnetocalorics. In these materials we see that $Tb(HCO_2)_3$ and $Ho(HCO_2)_3$ show similar magnetocaloric responses, with respect to field and temperature. [4]. In small applied magnetic fields, it can be seen that the magnetocaloric effects peak at 4 and 2 K for a 1-0 T field change, respectively. The other studied $Ln(HCO_2)_3$ materials, shown typical responses with increasing magnetocaloric effects with lowering temperatures.

Inspired by the recent success of $Tb(HCO_2)_3$ MCE in low fields and at temperatures above 2 K, [4] our study has probed the magnetic interactions and physical properties of this and other members of the $Ln(HCO_2)_3$ series in further detail, including measurements at lower temperatures and under applied magnetic fields. We have focused on the heavier lanthanides due to their high magnetic moments, as required for greater MCE, and large spin-orbit coupling. A key aim was to establish how the TIA phase is modified at lower temperatures, under applied magnetic fields and by replacing Tb with other $Ln$ cations.

The recent discovery of the colossal magnetocaloric effect in the $GdOHCO_3$ framework, [77] and the improved effect in by lanthanide substitution in other isostructural frameworks has lead to the further exploration of the materials in this family. [4, 72, 112] The $P2_12_12_1$ structure has 4 unique oxygen atoms, one for the hydroxide groups and three distinct oxygen atoms in the carbonate anions. The lanthanide can be viewed as being 10-coordinate with chains of $LnO_{10}$ face-sharing polyhedra, with edge-sharing interchain connectivity (Figure 1.16). However, there is some debate over whether the heavier $LnOHCO_3$ crystallise in the $P2_12_12_1$, [113] or the $Pnma$ orthorhombic space group. [114] The initial magnetocaloric study of the $GdOHCO_3$ framework performed density functional theory calculations, finding antiferromagnetic nearest neighbour intrachain coupling. [77]

After initially determining the magnetic entropy change of the $AOHCO_3$ (A = Tb, Dy, Ho and Er) magnetocalorics this study then aimed to establish a clear understanding of how the microscopic interactions of these compounds effect their physical properties. To achieve this we have studied these compounds using neutron diffraction, establishing both the local magnetic correlations in these materials in their paramagnetic phase, in which they exhibit their magnetocaloric properties, and in the case of $HoOHCO_3$ the ordered magnetic states
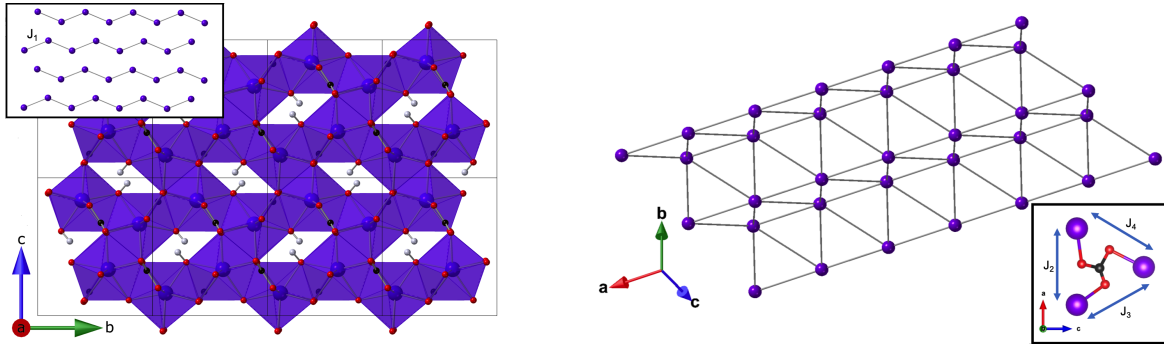
**Figure 1.16** (left) *Ln*OHCO$_3$ crystal structure. *Ln*$^{3+}$ coordination environments are shown as purple polyhedra, and carbon, oxygen and hydrogen are shown in black, red and white respectively, with only *Ln*$^{3+}$ nearest neighbour chains shown in insert, along the [100] direction. (right) *Ln*OHCO$_3$ interactions between *Ln*$^{3+}$ with a distance of 4.0 - 5.0 Å , shown arranged into layers of triangular motifs, along the [010] direction.

they exhibit at low temperatures. Neutron diffraction measurements have also been conducted in the application of the magnetic field to TbOHCO$_3$ in order to explore how it responds during the magnetocaloric cycle.

It has recently been shown that combining this with Ising and 1D ferromagnetic interactions (d = 1, D = 1) likely enhances this further, by making it easier to align the magnetic spins in low applied fields. [4, 18, 31, 72, 101] For an isolated 1D Ising ferromagnet, with a ground state of $-NJ/2$, where $N$ (the number of magnetic ions in the chain) is very large, a defect in the chain has an energy cost of $J/2$, so the energy change is $J$. However, the entropy gain is equal to $k_B \ln N$. Therefore, any defect introduced into the system by magnetic or temperature fluctuations,[31] will induce a response throughout the chain. It's for this reason that Ising ferromagnetic order within chains may be beneficial to the MCE.

Previous research investigated the MCE in the *Ln*(HCO$_2$)$_3$ family of materials, and discovered that Tb(HCO$_2$)$_3$ had the most efficient magnetocaloric behaviour above 4 K and in applied magnetic fields, [4] in a region that would make it suitable for a liquid helium cooling alternative. Neutron diffraction of this material revealed it contains 1D Ising ferromagnetic chains, made possible by frustrated neighbouring chains, arranged into a triangular motif, which has been described as a triangular Ising antiferromagnet (TIA). These results are extremely valuable when you consider that this result confirms what has been theorised about magnetocalorics containing Ising spins being more efficient, and frustration improving entropy changes in field. This work builds on these studies, and we are attempting to characterise the magnetic interactions in similar efficient magnetocalorics, to understand the origin, not only for fundamental understanding, but also to perhaps steer research in a

direction to make these types of magnetocalorics a reality in low temperature refrigeration devices.

Despite the magnetocaloric effect being intimately linked with magnetic order, little research has been done on the mechanism of the MCE.

By probing the magnetic interactions in these materials above and below the ordering temperatures (and in zero and applied magnetic fields) it is possible to understand how magnetic order is related to the MCE, especially in this class of efficient magnetocaloric materials. Additionally, magnetic neutron diffraction on framework materials is relatively uncommon, as greater interatomic separation usually hinders the superexchange, therefore lowering ordering temperatures, making this work novel and valuable for the progression of magnetocaloric research.

# 2

# Experimental Techniques

## 2.1 Introduction

Several experimental techniques have been used to characterise the framework materials studied in this thesis, and this chapter describes these methods along with, where necessary the theoretical background. Diffraction techniques were the primary methods of analysis, with crystal structures and phase purity confirmed with X-ray diffraction. Powder neutron scattering was the primary technique used for analysing the nuclear and magnetic crystal structures in these materials. Analysis methods such as the Rietveld method and reverse Monte Carlo were used to interpret the diffraction observed in these materials, supplemented by representation theory and symmetry analysis. Inelastic neutron scattering was performed to understand the magnetic structure dynamics and interactions. Heat capacity, magnetic susceptibility, thermogravimetric analysis and Fourier transform infrared spectroscopy were conducted for bulk property measurements. Samples were synthesised through hydrothermal and wet chemistry routes.

## 2.2 Synthetic Methods

The methods for synthesis of hydrogenated and deuterated samples used in this thesis are described here. It is necessary to deuterate samples used for neutron scattering experiments to minimise background noise caused by the incoherent scattering of hydrogen. We expect deuteration of the frameworks for neutron studies will have an insignificant effect on the magnetic exchange correlations.

### 2.2.1 Lanthanide Formates (*Ln*(DCO$_2$)$_3$) Frameworks

*Ln*(HCO$_2$)$_3$ and *Ln*(DCO$_2$)$_3$ (where *Ln* = Ce, Pr, Nd, Tb-Er) samples were synthesized by slowly adding 2 g of *Ln*(NO$_3$)$_3$.6H$_2$O (99.9%, Sigma-Aldrich) to a solution of 4.75 mL of formic acid (97.5% Sigma-Aldrich), or d-formic acid (95.0% Sigma-Aldrich), respectively, with 0.25 mL of ethanol added. After several minutes of stirring, NO$_x$ was released and the product precipitated out of solution. The products were collected by vacuum filtration, washed several times with ethanol, and dried in a desiccator.

### 2.2.2 Lanthanide Hydroxycarbonates (*Ln*ODCO$_3$) Frameworks

*Ln*OHCO$_3$ and *Ln*ODCO$_3$ (where *Ln* = Gd, Tb, Dy, Ho, Er) samples were synthesised via a hydrothermal method, by reacting *Ln*(NO$_3$)$_3$.6H$_2$O (99.9 %, Sigma-Aldrich, 1 mmol) and Na$_2$CO$_3$ (99.5 %, Sigma-Aldrich, 1 mmol) in water (10 mL). The hydrothermal synthesis involves heating a solution of reagents to high temperatures and pressures, above 100°C and held for an extended period of time in a pressurised vessel.

The mixture was sealed in a Teflon-lined (23 mL) Parr-Bomb autoclave and heated at 170°C for 72 h, followed by slow cooling to room temperature at a rate of 3°C h$^{-1}$, to improve crystal formation. The samples were isolated by vacuum filtration a washed with water, and dried in a desiccator. 2 g deuterated samples, used for neutron diffraction were produced with D$_2$O (99.9 %) under an N$_2$ atmosphere, in multiple batches.

## 2.3 Scattering Techniques

Scattering techniques have been a staple of solid state science since its inception and occurs when a beam of waves (or particles) interact with matter, causing a change from the incident wave vector ($\boldsymbol{k}_i$) to a final wave vector ($\boldsymbol{k}_f$). The relationship between the incident and final scattering waves are given by **Q**, the momentum transfer, as shown in the Equation 2.1 and Figure 2.1.

$$\boldsymbol{Q} = \frac{2\pi}{d} = \boldsymbol{k}_i - \boldsymbol{k}_f \qquad (2.1)$$

$$Elastic : k_i = k_f$$

$$Inelastic : k_i \neq k_f$$

$$Q = 2ksin\theta = \frac{4\pi sin\theta}{\lambda}$$

$$k_f$$

$$Q$$

$$2\theta$$

$$k_i$$
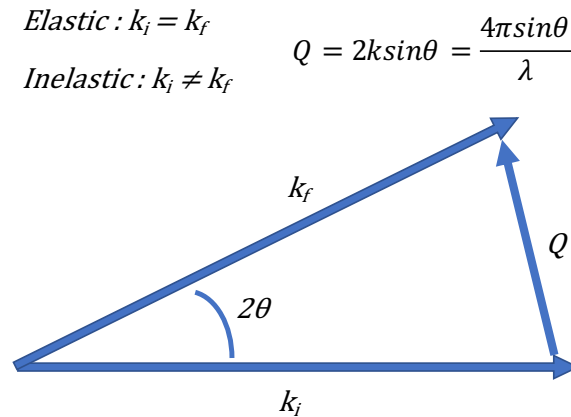
**Figure 2.1** Diagram of the scattering triangle for an elastic collision where the incident energy is equal to the final energy.

## 2.3.1   Diffraction

Diffraction is one of the most powerful structural techniques used in modern science, and has been crucial to many important discoveries since its development across the natural sciences. Diffraction involves the generation of waves/particles which impinge on a sample and elastically scatter (with no loss in energy where the magnitude of the wavevector $k_i = k_f$) off the sample determined by the interatomic distances. The pioneering work by W. Bragg and L.Bragg allowed for structure solution from diffraction of X-rays from crystallographic ordered lattices and yielded the equation for a relationship between scattering angle $\theta$ and the interatomic distances $d$ with a known beam wavelength $\lambda$ given by:

$$n\lambda = 2dsin\theta \tag{2.2}$$

A visual representation of this is depicted in Figure 2.2, showing the real space structure, and the observed diffraction pattern is measured in reciprocal space, containing information about the real space structure.

Diffraction occurs when a collection of individual atoms scatter waves or particles, from the ordered crystallographic lattice, causing constructive or destructive interference. At angles satisfying Bragg's law constructive interference of long range order occurs leading to sharp peaks in the diffraction pattern, referred to as Bragg peaks. The intensity of the elastically scattered waves in diffraction $F(Q)$, from the periodic lattice, can be calculated from the following equation [115]:
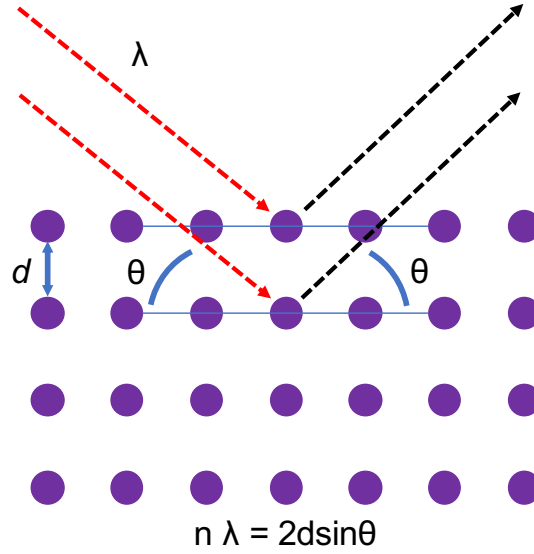
**Figure 2.2** Diagram showing diffraction according to Bragg's Law. Red arrows indicate incoming waves with the wavelength $\lambda$, and the elastically scattered outgoing waves in black. The purple dots indicate atoms in a crystallographically ordered lattice.

$$F(Q) = \sum_{(i,j)} \langle b_i b_j exp(iQ \cdot [r_i - r_j]) \rangle \qquad (2.3)$$

where $b_{ij}$ is the is the scattering length, and $r_i$ and $r_j$ is the atomic positions of the atoms in the crystal structure. For a macroscopic sample, where there are effectively an infinitely large numbers of atoms, the equation simplifies to:

$$F(Q) = \int \rho(r) exp(iQ \cdot r) dr \qquad (2.4)$$

where $\rho$ is the electron density at position $r$. The diffraction pattern made of up reflected intensities (Bragg peaks) in reciprocal space, $Q$ is dependent on the reciprocal lattice parameters and atomic positions. Therefore we can mathematically describe the amplitude, phase and vector of waves diffracted from a crystal lattice with the Miller indices (hkl) of the crystal lattice with the equation [51]:

$$F_{hkl} = \sum_{j=1}^{n} f_j(\theta) exp[2\pi i(hx_j + ky_j + lz_j)] \qquad (2.5)$$

Where $x_j, y_j, z_j$ are the coordinates for the $j^{th}$ atom, and $f_j(\theta)$ is the form factor of the $j^{th}$ atom for X-ray diffraction. In the case of neutron diffraction the form factor is replaced by the neutron scattering length, which will be discussed further below.

Unfortunately, diffraction is insensitive to the global phase of the system, as the intensity of the peaks, proportional to square of the scattering factor $|F(Q)|^2$ is the experimentally measured observation. Therefore, it is not possible to solve the structure by a simple Fourier transform, [116] and therefore assumptions and alternative methods are required to work around this phase problem.

## 2.3.2   X-ray Diffraction

X-rays are high energy electromagnetic waves and commonly used for diffraction techniques. X-ray diffraction is one of the most commonly used techniques in solid state chemistry for structural characterisation and phase identification. [28] Sources of X-rays in a laboratory are made by accelerating a beam of electrons from a tungsten cathode. These electrons strike an anode (usually copper but sometimes molybdenum) which ionises core 1s electrons in the anode. Electrons from higher energy levels relax to fill the empty 1s orbital and energy corresponding the orbital gap is released, which is in the X-ray spectrum. For copper sources electrons from the higher p orbitals drop down, with a $2p_1$->1s, $2p_2$->1s and $3p_1$->1s transitions called the $K_{\alpha 1}$, $K_{\alpha 2}$ and $K_{\beta 1}$ corresponding to 1.5404, 1.5443 and 1.3922 Å , respectively. These transitions are summarised on Figure 2.3.

The $K_\alpha$ transitions are far more common, and therefore more intense, than the $K_\beta$ transition and so are used for diffraction experiments, with the $K_\beta$ filtered out to simplify analysis. X-rays can interact with matter by scattering and absorption. Scattered X-rays interact with the electrons of matter, and so the scattering intensity is proportional to the number of electrons. When no loss of energy occurs in the X-ray scattering this can be used for X-ray diffraction. In this thesis two methods of X-ray crystallography were used for initial structural determination, powder and single crystal diffraction. The advantage of single crystal X-ray diffraction is primarily the large amount of data generated from collecting and being able to distinguish between information in 3D reciprocal space. The amount of data generated through single crystal diffraction makes solutions of structural information possible. However, single crystal diffraction requires synthesis of suitably sized crystals which may not be possible. Powder diffraction allows collection of powder averaged data, suffering from a significant loss of information. The advantages of powder diffraction are the ability to collect structural information from any microcrystalline sample, including long and
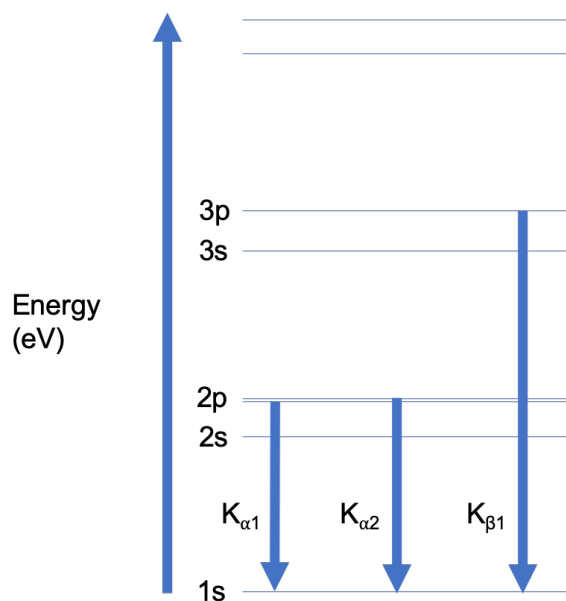
**Figure 2.3** Energy level diagram for a Copper atom showing the electronic transitions.

short range ordered materials, such as glasses and amorphous samples. More importantly, powder diffraction collects additional information about the microstructure of the material, such as strain, defects and particle shape/size. [117] Also, unlike single crystal diffraction, it provide insight into the bulk composition.

Powder X-ray diffraction was used for sample phase purity performed on ground polycrystalline samples on either an Empyrean PANalytical (with Cu $K_{\alpha 1}$ radiation) or a Rigaku MiniFlex 600 (with Cu $K_{\alpha}$ radiation) with the use of a zero-background silicon sample holder. The Empyrean PANalytical is a high resolution monochromatic generated from Cu X-ray tubes, operating at 4.6 kW (40 kV and 40 mA), typically between 10-120 $2\theta$ in increments of $0.05°$ steps. The sample and holder were held in a reflection-transmission spinner, and variable angles measured with a $\theta$-$2\theta$ goniometer, and scattered X-rays detected with X'Celerator detector. The Rigaku Miniflex 600 is a low resolution/intensity bench top diffractometer suitable for phase purity determination, with an operating Cu tube voltage of 40 kV and 15 mA, typically operating between 10-70° in increments of 0.1°. The samples were loaded into the 6 position sample change, with data collected with a $\theta$-$2\theta$ goniometer using a D/teX Ultra.

Single-crystal diffraction data was recorded for TbOHCO$_3$ on a Rigaku Supernova with Mo $K_{\alpha}$ radiation ($\lambda = 0.7107$ Å) generated from a microfocus source, operating at 0.8 kV

and 50 mA, with multi-layer focusing optics. The sample was held in a MiTeGen micro-loop and cooled to 169 K using an Oxford Cryosystem and diffraction data measured with a Atlas CCD detector. The data obtained was indexed, integrated and reduced using the CrysAlisPro software suite version 1.171.38.4131, with empirical absorption corrections performed using the same packages. The structure was solved using the Patterson method in SHELXS-2008 [118] and refinements subsequently carried out using a least-squares method with SHELXL-2015 [119] using the Olex2 graphical user interface. [120] Only the atomic displacement parameters for the lanthanide were refined anisotropically, with lighter elements refined isotropically as the quality of the fit is insensitive to these values. The hydrogen atom positions were determined from the Fourier difference and refined with a restraint so that it remains 0.96 Å from the oxygen to which it is attached, typical for an O-H bond, [121] and its displacement parameters constrained to be 1.5 times the oxygen that it is attached to.

### 2.3.3 Neutron Diffraction

Neutrons can be generated, in sufficient quantities, for use in scattering experiments through two main methods. The discovery of the neutron by James Chadwick in 1932, [102] for which he was awarded the 1935 Nobel prize in physics, was significant for the progression of solid state science. The neutral charge and magnetic moment of neutrons make them a highly penetrating technique, sensitive to the magnetic moment of an atom. This makes neutrons an ideal probe for understanding microscopic magnetism in bulk materials, and therefore is the technique of choice among solid state chemists and condensed matter physicists. The wavelength of neutron is given by:

$$\lambda = \frac{h}{m_n v_n} \qquad (2.6)$$

where $m_n$ is the mass of the neutron = $1.674929 x 10^{-27}$ kg and $v_n$ is the velocity of the neutrons.

Bulk property magnetic susceptibility and heat capacity measurements are a useful tool for a macroscopic understanding of these materials and muon and Mössbauer spectroscopy enable inferences to be drawn regarding magnetic coupling via the effect this has on the internal magnetic field but neutron diffraction and spectroscopy remain the most powerful experimental tools currently available for unravelling the magnetic structure. Modern neutron sources and detector technology have developed to the point where it is possible to collect

high quality diffraction patterns with less than a gram of sample, allowing for the studies of magnetism in materials where synthesising high purity bulk samples is limited.

Neutrons are commonly generated at particle-accelerator spallation sources and nuclear reactors, which typically provide pulsed and continuous supplies of neutrons, respectively. Neutron diffraction instruments at these facilities therefore usually have distinct characteristics based on time-of-flight and constant wavelength approaches. Both of these types of instrument are used in this project and are thus described below. [122]

**Time-of-Flight Powder Neutron Diffraction**

Time-of-flight (TOF) neutron diffraction starts by generating pulses of neutrons. This is achieved by accelerating pulses of hydrogen nuclei, in a synchrotron, and bombarding a heavy metal (tungsten at ISIS), under constant cooling to dissipate the heat from the collision. [123] The generation of neutrons in this method (Figure 2.4) creates a Maxwell-Boltzmann distribution of neutron wavelengths, with a high energy peak distribution, therefore the neutrons need to be slowed down (cooled).
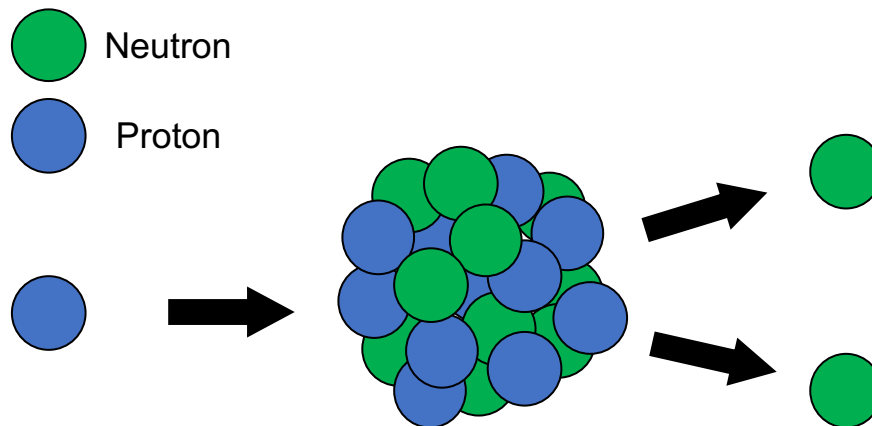


**Figure 2.4** Diagram of the production of neutrons from proton spallation on a heavy nuclei.

To cool the hot neutrons from the heavy metal target it is necessary to use a moderator made of a material that has a small absorption cross section (so it does not absorb and remove flux) and a high scattering cross section (so it interacts strongly with the neutron). For these reasons materials with a high content of hydrogen or deuterium are often used. Within the ISIS facility a number of different moderators are used to produce different distributions of energies including water, methane and hydrogen. For the TOF WISH instrument, which is on Target Station 2, a solid methane moderator is used to provide ultra cold, long wavelength neutrons, required to reach low $Q$. After interacting with the moderator there is still a

large spread of neutron wavelengths and so to improve the resolution of the instruments a chopper is used to narrow the distribution. The chopper is typically a rotating disc of a highly absorbing material (such as gadolinium) with a flight path cut through the middle. This creates a narrow window of time where neutrons can pass through the centre, as the disc rotates the flight path is blocked by gadolinium and is strongly absorbed, stopping large intensities of flux. The rotating chopper creates narrow pulses of neutrons with a smaller distribution of wavelengths.

The resulting beam of neutrons still contains a distribution of wavelengths and not a single wavelength so measuring the angle of the diffracted neutrons is not sufficient to analyse the structure. The relationship between neutron wavelength and velocity presented in Equation 2.6, however, enables neutrons of different energies to be separated based on the time they arrive at the detector allowing a wide range of diffraction $Q$-space to be measured from a detector angle at a fixed angle. The relationship between $Q$ and neutron time-of-flight is given by:

$$Q = \frac{4\pi m_n L sin\theta}{ht} \tag{2.7}$$

where $m_n$ is the mass of the neutron, $L$ is the flight path length (in meters), $2\theta$ is the angle of the detector in degrees and $t$ is the time-of-flight, where the relationship between the time-of-flight and the neutron wavelength is given by:

$$t = \frac{m_n L \lambda}{h} \tag{2.8}$$

where $h$ is Plank's constant.

**WISH time-of-flight Diffractometer**

The majority of neutron diffraction experiments in this thesis were conducted on the high-resolution time-of-flight (TOF) WISH diffractometer (Figure 2.5) at the ISIS neutron source, Rutherford Appleton Laboratory. [124] WISH is a long-wavelength diffractometer primarily designed for collecting high quality powder diffraction data at long $d$-spacing (or low $Q$) with minimal instrumental background. This makes WISH optimised to analyse materials with magnetic structures and/or large unit cell systems, with options for enabling single-crystal experiments. In particular the magnetic diffuse scattering that provides key insights into the local magnetic structures probed during this study are typically two to four orders of

magnitude weaker than Bragg reflections, [84] and so the low instrumental background is essential to carry out the analysis presented in this work.
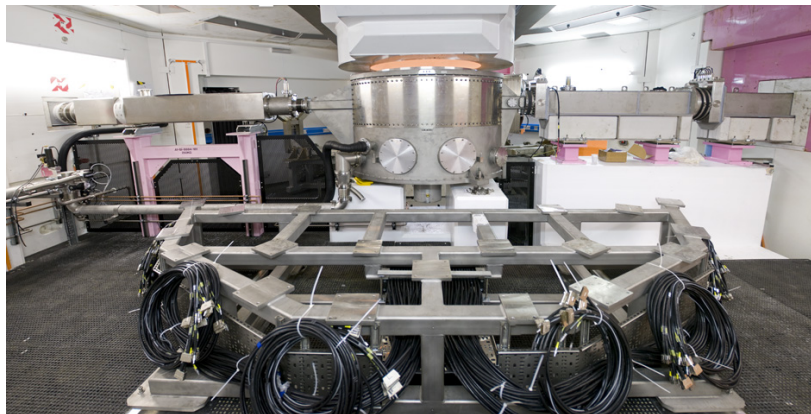


**Figure 2.5** Photograph of the inside of the WISH instrument. (Image reproduced from the WISH, ISIS website [125])

In order to achieve the low Q space and resolution WISH employs a long flight path of 42.2 metres, cold neutrons with an effective wavelength of 8 Å and wide angle detector with the long $d$-space bank situated at $27°$, the detector array is shown in Figure 2.6 The wide area detectors has given it the name WISH - **W**ide-angle **I**n **S**ingle **H**istogram.

$Ln$ODCO$_3$ and $Ln$(DCO$_2$)$_3$ sample measurements that were carried out between 1.6 K to 100 K, were loaded into 8 mm vanadium cans and cooled using the standard Oxford Instruments WISH cryostat. Low temperature measurements of Tb(DCO$_2$)$_3$, Ho(DCO$_2$)$_3$ and HoODCO$_3$ were carried out between 0.28 K to 1.95 K, with the sample loaded in an 8 mm copper can and cooled using a $^3$He Heliox sorption refrigerator.

Strong absorption was noted in dysprosium frameworks, as to be expected from the large absorption cross section of Dy and absorption corrections were applied to the raw data before fitting. Packing densities were calculated as a basis for absorption corrections, however the parameters were optimised such that the backgrounds approached linearity across the different detector banks. The absorption was negligible in other frameworks and so absorption corrections were not applied but included in the Rietveld refinements.

For applied field measurements of Tb(DCO$_2$)$_3$ and TbODCO$_3$ powders were loaded into 8 mm vanadium cans and wetted with d$_6$-isopropyl alcohol, sealed with indium wire and flash frozen in the standard WISH Oxford Instruments cryostat. The d$_6$-isopropyl alcohol was included to minimise the effect of preferred orientation on the diffraction patterns in the application of the magnetic field, and indeed prevented any significant orientation of the
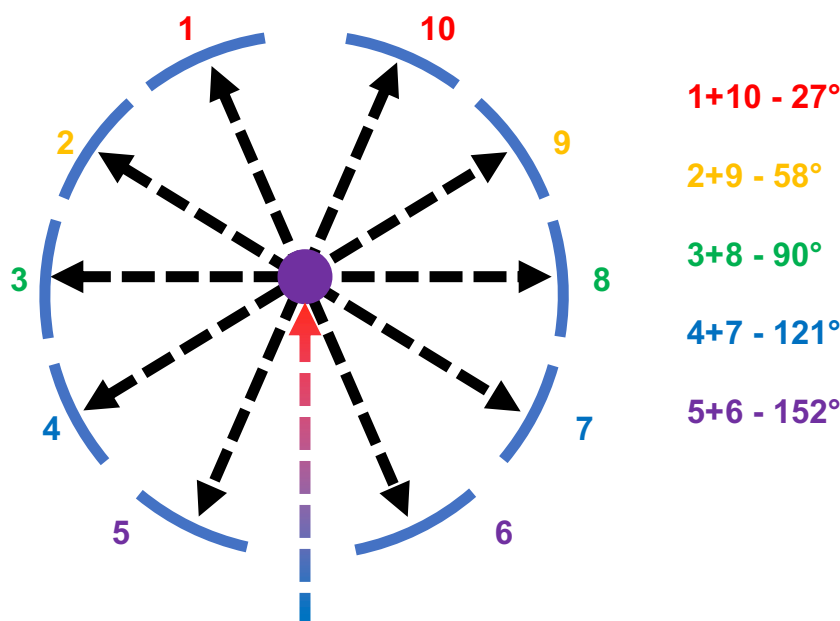
**Figure 2.6** Diagram of the detector array of the WISH instrument. Incoming beam spectra shown as a red/blue gradient arrow. Outcoming beams shown as black arrows. Sample shown in purple. Adjacent banks are equivalent and colour coded, to increase statistics the banks are merged. Detector banks are located at fixed angles around the sample, and record different ranges of $d$-space.

powder sample with the applied magnetic field. The sample was flash frozen in order to prevent the $d_6$-isopropyl alcohol crystallisation and resulted in the formation of an amorphous solid, as indicated by the diffuse scattering centred around 4.2 Å. Magnetic fields between 0 and 3 T were generated using the 10 T GEM superconducting magnet, which the sample and cryostat were placed within. The presence of the cryomagnet produced aluminium reflections, which were fitted with a Le Bail model to negate the effects of the highly textured surface, and un-indexable peaks in the highest resolution bank. Diffraction patterns were recorded on the high resolution time-of-flight WISH diffractometer at the Rutherford Appleton Laboratory at Harwell.

**Constant Wavelength Neutron Diffraction**

Constant wavelength neutron diffractometers are typically associated with nuclear reactor based sources, where neutrons are generated by fission. [122] In this process incident neutrons bombard heavy Uranium-235 isotopes, splitting the isotope and, thereby producing $\gamma$-rays, two smaller nuclei and, crucially, more neutrons (See Figure 2.7). The thermal neutrons produced go on to split other nuclei in a chain reaction, and so the process must be cooled and moderated, with water, to prevent a meltdown.
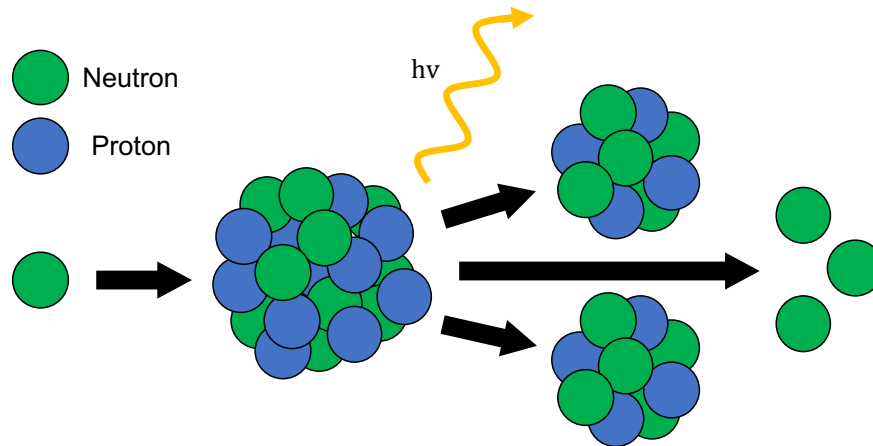
**Figure 2.7** Diagram of the production of neutrons from nuclear fission by bombarding a heavy nuclei with neutrons, creating a chain reaction.

For these neutrons to be made useful for neutron scattering they must be cooled further with a secondary moderator, which as for spallation sources controls the spectrum of neutrons available. For constant wavelength neutron diffraction, the spectrum of high energy neutrons is slowed such that the energy is reduced to a single wavelength by a moderator made of materials such as pyrolytic graphite or germanium. [122] In constant wavelength neutron sources, diffraction occurs with a single neutron wavelength, and therefore the angle of diffraction is measured in order to collect a diffraction pattern, typically but not always by moving the detector. The relationship between $Q$ and the angle of diffraction $\theta$ is given by:

$$Q = 4\pi \frac{sin\theta}{\lambda} \tag{2.9}$$

where $\lambda$ is the wavelength of the incoming neutron beam. The relative merit of constant wavelength and time-of-flight neutron scattering is very dependent on the characteristics of the precise instrument used. [122] For example one typical advantage of constant wavelength instruments is the ability to collect high quality data to lower $Q$ than is typical on a TOF instrument but WISH is clearly an exception to this rule. Another advantage of constant wavelength instruments is the smaller amount of data processing and calibration required to achieve high quality patterns. Generally, however, for an instrument with comparable resolution with regards to instrumental peak width TOF instruments are able to collect data with better signal to noise due to the greater intensities of spallation neutron sources.

**Wombat Constant Wavelength Diffractometer**

The Wombat instrument [126] at the OPAL reactor is a high flux, medium-resolution powder diffractometer and does not get its name from an acronym but named after the Australian marsupial. Wombat employs the powder diffraction scanning method proposed by Hewat, [127] providing suitable resolution for diffraction experiments. Due to its high flux and large detector that can collect data over a continuous range of $160°$ it is optimised for time-resolved studies or for probing small volumes of materials, at the expense of only having moderate resolution. It has recently been upgraded to implement polarised neutrons and a dilution fridge. [128]

Data were collected on $Ho(DCO_2)_3$ and $Er(DCO_2)_3$ in a dilution fridge inside a cryocooler, using 2.41 and 4.61 Å neutrons, from 50 mK and 20 K. The initial intention was to use the dilution fridge in conjunction with the $^3$He neutron polariser, but due to technical issues this failed prior to the measurements. The outcome of this is that the weak magnetic peaks observed were not easily resolved, and the presence of the polarisation instrumentation leads to areas in the diffraction pattern of missing information, requiring data collection of two wavelengths to obtain a full diffraction pattern.

## 2.3.4 X-ray vs Neutron Diffraction

For structure determination X-ray diffraction is usually the method of choice, however it is not without its issues. The advantages and disadvantages of neutron and X-ray diffraction compared to each other are discussed below [117, 122]:

**Interaction with matter** Neutrons interact with matter through the strong force, only interacting with the nuclear force of atom over a length scale of $\approx 1$ fm. To a neutron the nuclei are effective point sources, from which the angle independence of neutron scattering arises (see Figure 2.8a). In contrast X-rays interact with a diffuse cloud of electrons, meaning there is an atomic form factor that drops off with increasing $Q$. The ability to achieve high quality measurement at low $d$-spacing makes neutrons the ideal probe for pair distribution function studies.

Neutrons interact weakly with matter and so they penetrate the sample deeply and probe the entire sample, including penetrating through a wide range of sample environments. X-rays are strongly diffracted by the surface molecules and therefore are predominantly a surface probe, but because they strongly interact with matter small sample sizes are required, and collect times can be fractions of a second. The weak interactions of

neutrons lead to an individual pattern taking between 30 minutes and a day to collect an individual measurement even using multi gram samples.

**Zero charge** Neutrons have no charge allowing high penetration of the neutron deep into the materials, due to the lack of coulomb repulsion. This allows the whole material to be probed not just the surface and sample environments readily designed to work under a wide range of temperatures and other in-situ environments.

**Useful Energy Scale** Commonly used thermal neutron have energies comparable to excitation energies in condensed matter. Therefore, as discussed in Section 4.2.3, using inelastic neutron spectroscopy one can extract information about the dynamics of the system by measuring the change in energy of a neutron beam after interacting with the system.

**s = 1/2 Magnetic Moment** X-rays strongly interact with electron clouds, but extremely weakly to magnetic moments because of their lack of magnetic moment. Neutrons have magnetic moment with spin $s = 1/2$ and, as a result, can interact magnetically with unpaired electrons in the system and provide information about the magnetic structure. This enables the position, direction, and magnitude of magnetic moments to be determined.

**Production** X-ray are easily produced, and can be made in house. Neutrons require synchrotrons, linear accelerators or nuclear reactors to generate neutrons and in small quantities. X-rays produced by synchrotrons are orders of magnitude more bright than the sun, [129] and produce enough flux to make collections time short.

**Sample Discrimination** The atomic form factor of X-rays scales linearly with increasingly number of electrons meaning heavy element scattering far more strongly than light atoms. (see Figure 2.8b) In contrast to X-ray diffraction the neutrons scattering length varies wildly between atoms and different isotopes. This makes it possible to easily differentiate between oxygen and nitrogen, for example, making structural determination of unknown atoms possible, which in X-ray diffraction would not be possible.

Whilst X-rays are useful for many problems, this thesis is mostly concerned with magnetic structure and properties, hence neutron diffraction has been the primary method for analysis. Neutron diffraction is still the most widely use method for magnetic correlations and structure determination, despite new methods in non-resonant X-ray scattering which provide some advantages over magnetic neutron scattering. [130] X-ray advantages include decoupling
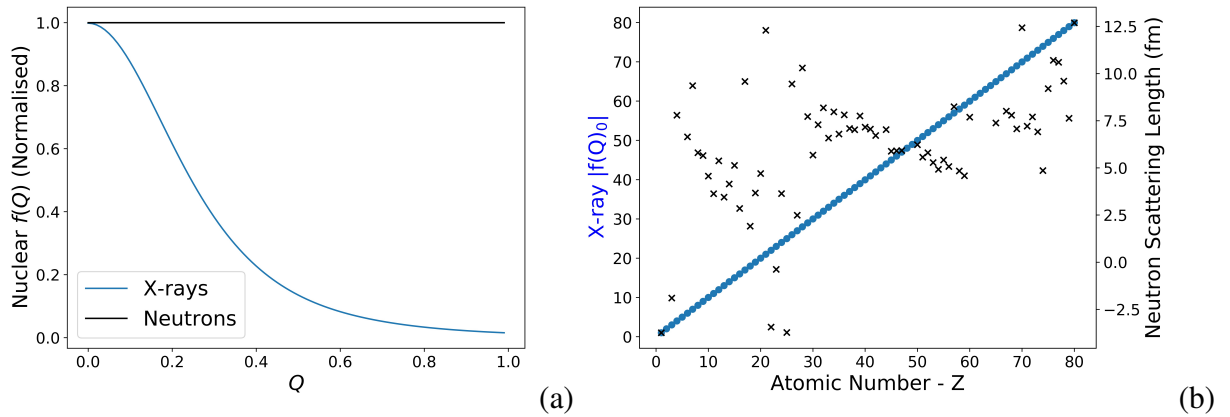
**Figure 2.8** (a) Comparison between the nuclear scattering power of X-rays vs Neutrons for a single hydrogen atom. (b) Comparison between the scattering power of X-rays vs Neutrons. Measured by the X-ray form factor at $Q = 0$ and the neutron scattering length, for each atomic number.

the spin and orbital contribution to the magnetic moment [131] and, as a surface technique, probing magnetic thin films. However they are not able to determine the length of the vector and do not provide good resolution in Gamma point of the Brillouin zone, and so neutron scattering will always be necessary for magnetic structure determination. There is also the practical consideration for softer materials such as those in this thesis, which would likely decompose under the high energy and intensity X-rays.

### 2.3.5 Magnetic Neutron Scattering

The neutron has an $s = \frac{1}{2}$ and a moment $= -1.913 \, \mu_N$, where $\mu_N = \frac{e\hbar}{2m_p} = 5.051 \times 10^{-27} JT^{-1}$, which makes neutrons a probe sensitive to the magnetic moment of atoms, as they scatter from the unpaired electrons of paramagnetic ions. [132] Between 1937 - 1941 Halpern and Johnson *et al.* [133–136] gave the first full descriptions of magnetic neutron scattering from paramagnetic and magnetically ordered materials. When a sample forms long range magnetic order, this causes magnetic Bragg reflections to occur in the diffraction pattern while in purely paramagnetic samples this scattering just contributes to the incoherent background at low $Q$. Magnetic Bragg reflections can be used to determine the magnetic structure of a material in a similar fashion to how Bragg peaks from scattering from atomic nuclei can be used to determine the crystal structure of a material. The diffraction angle of these reflections can then be used to determine the interatomic space of the magnetic spins and the intensity of magnetic Bragg peaks are proportional to the square of the magnetic moment of the sample, enabling the size and direction of the magnetic moment to be determined. [31] This was first achieved experimentally by the pioneering work of Shull, [103] in the 1950's which

determined the antiferromagnetic structure of later first row transition metal oxides such as MnO and laid the groundwork for magnetic diffraction studies of materials.

In contrast to the neutron scattering length, which measures the strength of the scattering from a particular atomic nucleus, and is independent of $Q$, magnetic neutron scattering has a magnetic form factor with a logarithmic decay like $Q$ dependence. [137] This leads to the magnetic scattering intensity approaching 0 with increasing $Q$, as shown by the magnetic form factors of some late lanthanides in Figure 2.9.
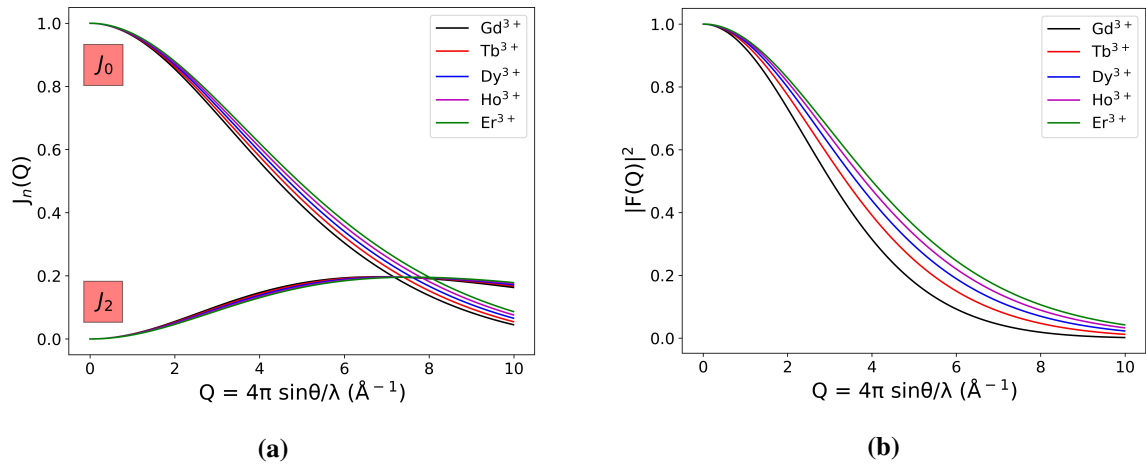


**Figure 2.9** (a) Plot of the calculated neutron magnetic form factors, from the analytical approximation, for select $Ln^{3+}$ ions. (b) Plot of the calculated scattering amplitude, from the analytical approximation, for select $Ln^{3+}$ ions.

The form factor of a moment with only spin-only contribution is given by $\langle j_0 \rangle$ only, but for lanthanide ions with a strong spin-orbit coupling the $\langle j_2 \rangle$ is necessary which are given by:

$$\langle j_0 \rangle = Ae^{-as^2} + Be^{-bs^2} + Ce^{-cs^2} + D \tag{2.10}$$

and

$$\langle j_2 \rangle = s^2(A'e^{-a's^2} + B'e^{-b's^2} + C'e^{-c's^2} + D') \tag{2.11}$$

where:

$$s = \frac{k}{4\pi} = \frac{sin\theta}{\lambda} \tag{2.12}$$

and the form factor is given by:

$$F(k) = \langle j_0 \rangle + C_2 \langle j_2 \rangle \tag{2.13}$$

where $C_2$ is the ratio of the orbital magnetic moment to the total contribution of the magnetic form factor. The empirical values for Aa, Bb, Cc and Dd in these equations can be found in the International Crystallographic Tables C [138] or on the Institut Laue–Langevin website. [139] The $Q$ dependence of magnetic neutron scatterings means that in order to achieve the maximum amount of information possible for magnetic structure determination it is important to probe low $Q$ areas of reciprocal space with wide angle area detectors using cold neutrons, taking advantage of their long wavelengths.

Another consideration that must be made is that the neutron only interact with moments perpendicular to the scattering vector, this be described by the scattering length of the magnetic ion [140]:

$$F_m^2 = b^2 + 2bpq \cdot v + p^2 q^2 \tag{2.14}$$

where $b$ is the nuclear scattering amplitude, $p$ is the magnetic scattering amplitude, $v$ is the unit vector direction of the scattered neutron, $q$ is given by:

$$q = \varepsilon(\varepsilon \cdot \kappa) - \kappa \tag{2.15}$$

where $\varepsilon$ is the unit vector along the direction of the neutron beam and $\kappa$ is the unit vector parallel to the magnetic moment, and $p$ is described by:

$$p = \frac{e^2 \gamma}{2m_e c^2} g_J J f \tag{2.16}$$

where $g_J J$ is the magnetisation perpendicular to the direction of the momentum transfer for atom with an orbital contribution, $e$ is the electron charge, $m_e$ is the electron mass, $c$ is the speed of light $\gamma$ is the neutron magnetic moment in units of nuclear magneton, $J$ is the spin-orbit coupling term and $f$ is the magnetic form factor.

We can therefore see for moments parallel to the direction of the neutron beam, this equation reduces to 0. For single crystal magnetic neutron scattering this is extremely important to

consider when making measurements, however in powder averaged samples (used in this thesis) this means that the intensity of the Bragg peaks will never quite be equal to $g_J J$.

## 2.4 Structural Analysis Techniques

### 2.4.1 The Rietveld Method

The Rietveld method [141] is a whole pattern least squares fitting method for fitting experimental data to refine average nuclear and magnetic structures from powder diffraction data. The method requires a starting model close to that of the true model for which the powder diffraction pattern can be calculated and compared to the experimental data. Rietveld refinements involve optimising a range of parameters determined by the sample, instrument and/or both to best fit the data, including a phase scale, lattice parameters, atomic positions and displacement parameters, zero offset, background parameters and peak shape parameters. Before discussing the mathematical models used for some of these terms we will first discuss how the quality of the fit is calculated. Two of these factors, $R_p$ and $R_{wp}$ are the profile factor and weighted profile factor, $y_{obs}$ is the intensity of the experimental reflection, $y_{calc}$ is the intensity of the calculated reflection and $w_i$ is a weighting factor.

$$R_p = \frac{\Sigma[y_{obs} - y_{calc}]}{\Sigma[y_{obs}]} \tag{2.17}$$

$$R_{wp} = \sqrt{\frac{\Sigma w_i [y_{obs} - y_{calc}]^2}{\Sigma w_i [y_{obs}]^2}} \tag{2.18}$$

The value for which $R_{wp}$ should approach for a perfect fit is:

$$R_{exp} = \sqrt{\frac{N - P}{\Sigma w_i [y_{obs}]^2}} \tag{2.19}$$

where $N$ is the number of reflections and $P$ is the number of used parameters. During the refinement the sum of the squared differences $\chi^2$ is minimised during the refinement, where $\chi^2 = 1$ corresponds to a perfect fit.

$$\chi^2 = \Sigma w_i [y_{obs} - y_{calc}]^2 \tag{2.20}$$

It is preferable to use the fewest number of parameters to fit a pattern. This is preferable to prevent the possibility of over-fitting data, for example fitting the data with non-physical variables, providing better statistics but producing models not justified by the quality of the data available.

We now turn to a description of the parameters determined by the experimental measurement rather than the crystal structure itself. Background parameters are approximated either with a mathematical function, such as a Chebyshev polynomial [142] or with an interpolation of user given points. The reflections list and $d$-spacing must be calculated, the peak shape fit and then compared against the experimental data. The other parameters are dependent on whether the measurement is done on a constant wavelength or TOF instrument so we will discuss these in turn.

**Constant Wavelength**    The parameters for a constant wavelength instrument, necessary for a refinement, consist of a zero offset to account for any error in the sample or detector position, and a known wavelength. Taking into account Bragg's law the equation peak position in terms of $d$-space then becomes:

$$d = \frac{n\lambda}{2sin(\theta + zero)} \tag{2.21}$$

In constant wavelength data, most commonly a pseudo-Voight function is used to fit the peak shape of the reflections, consisting of a convolution of Gaussian and Lorentzian components (see Figure 2.10).
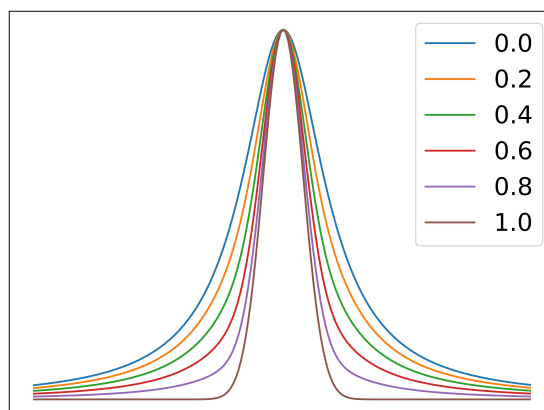


**Figure 2.10** Plots comparing Gaussian, Lorentzian and Pseudo-Voight Peaks. 0 is fully Lorentzian, and 1 is fully Gaussian. Mixing the two produces a pseudo-Voight.

The angle dependence of the FWHM is defined by two terms. The Gaussian FWHM, defined by the Caglioti formula [143], and the Lorentzian components are given by:

$$FWHM_{G-CW} = \sqrt{U tan^2\theta + V tan\theta + W}$$

$$FWHM_{L-CW} = X tan\theta + \frac{Y}{cos\theta}$$

(2.22)

where $U, V, W$ and $X, Y$ are refineable parameters, which are modified to minimise the difference between the observed and calculated peaks, and $\theta$ is the angular dependence. Considerations must also be made for peak asymmetry causing tailing on peaks, and can be fit with appropriate functions, which is more prevalent at low scattering angles.

**Time-of-flight**    TOF instruments are more complicated than constant wavelength with a quadratic TOF dependence on $d$-space given by:

$$TOF = Zero + DTT1d + DTT2d^2$$

(2.23)

DTT1 relates the theoretical time-of-flight position of the reflections to $d$-space, is calculated from the length of flight path ($L$), the detector angle ($\theta$), Planck's constant ($h$) and the mass of a neutron ($m_n$).

$$DTT1 = \frac{2m_n l sin\theta}{h}$$

(2.24)

Zero accounts for the difference in timing signal between the time at which data is acquired versus when the time it should arrive, caused by the response time in detector electronics and processing, and usually expressed in terms of $\mu S$. DTT2 is an empirically derived addition to the $d$-space relationship to account for small differences in absorption for shorter versus longer wavelengths, and therefore shifts in peaks.

The TOF peak shape is also more complicated, containing asymmetric peaks shapes as a result of the pulsed neutron source. The peak-shape can be described by an Ikeda-Carpenter function [144] which is a convolution of a pseudo-Voight with back-to-back exponentials to account for the neutron wavelength distribution. The Gaussian and Lorentzian components of the TOF peak shape $d$-space dependence follows the equations:

$$FWHM_{G-TOF} = \sqrt{\sigma_0 + \sigma_1 d^2 + \sigma_2 d^4}$$

$$FWHM_{L-TOF} = \gamma_0 + \gamma_1 d + \gamma_2 d^2$$

(2.25)

In some cases, including where noted in this thesis for some magnetic Bragg reflections, [hkl] dependent anisotropic peak broadening has been fitted with spherical harmonics expansion of the domain shape. [145] For more information regarding the mathematical explanation of the Rietveld method see the FULLPROF manual. [146]

In this thesis average structure patterns have been primarily fitted with several Rietveld refinement programs. LHPM-Rietica [147] has been used to fit constant wavelength laboratory X-ray data and FULLPROF [146] has been used to fit most TOF and CW neutron data, with occasional use of EXPGUI + GSAS. [148, 149] Additionally, places where JANA2006 [150] has been used to fit TOF data have been noted in the text.

For TOF data a linear interpolation of points were used to fit the background and using a profile function built from a convolution of back-to-back exponentials with a pseudo-Voight TOF function to fit the peak shapes. The full width half-maximums of the finite correlation length magnetic peaks were fitted with a anisotropic broadening model. [145] Where observed peaks caused by the sample environment, such as the copper sample can and the aluminium magnet, these were fitted with a Le Bail method.

## 2.4.2 Diffuse Scattering and Reverse Monte Carlo

Diffuse scattering arises from short-range interactions in a material, structural diffuse scattering can arise from a range of phenomena including short-range ordered defects such as oxygen vacancies or mixed cations. [151] In magnetic materials, short-range order can occur due to 1 or 2D magnetic order or magnetic frustration from competing interactions, either of which prevent the spins from achieving long range order. In contrast with the sharp Bragg peaks associated with long range magnetic order when order is short-range (in real space) this corresponds to a large area of reciprocal space, hence diffuse scattering covers a large $Q$-space. Diffuse features from correlated disorder may occur with or without the presence of Bragg peaks, although in some cases it can be difficult to determine whether moderately sharp features are true Bragg peaks associated with three dimensional magnetic order or an intermediate form of magnetic order. [18, 84, 152, 153]

It is important to note that in order to properly analyse the data and develop a reasonable model of the local magnetic ordering in a material the quality of data measured must be sufficient to capture the subtle features observed in magnetic diffuse scattering. As a result of short range order, it is typical for diffuse features to be two to four orders of magnitude weaker than Bragg reflections, [104] but with modern high efficiency detectors, and their low background, it is possible to capture high-quality reciprocal-space data at high flux spallation sources extremely rapidly. [105, 106] High resolution data remains important, however, to enable any indication of broadening of Bragg-like features that might indicate features worthy of deeper analysis. Finally, data must be recorded to the shortest possible reciprocal space to capture these features, which appear in this region, especially in materials with large structures.

Modern advances in understanding of magnetic systems and recently developed reverse Monte Carlo (RMC) techniques enable the diffuse scattering to be interpreted from powder neutron diffraction experiments as well as long established from single crystal diffraction approaches, which typically are based on Monte Carlo models. [107, 108] These new methods enable a wider range of compounds with local magnetic correlations to be probed, including the types of materials examined in this thesis for which single crystals are not available. Indeed these techniques are ideally suited to frameworks, which often possess low dimensional or frustrated magnetic order due to the versatile structures they adopt but rarely grow the several mm$^3$ size single crystals needed for single crystal neutron diffraction.

RMC methods involve fitting observed diffuse scattering data using a large supercell of spins with fixed magnetic moments and no enforced symmetry. As computer power has increased Monte Carlo based big box methods such as Monte Carlo and RMC [154, 155] have become ideal for their flexibility and applications to a variety of problems and data types. [156] The reverse Monte Carlo method has been used throughout this thesis, and it follows the same algorithmic procedure as Monte Carlo methods. While Monte Carlo methods aim to minimise the energy of the system reverse Monte Carlo methods minimise the error of the calculated fit, to the experimental diffraction pattern. The general RMC method, for magnetic systems, is summarised in Figure 2.11, starting from an initial disordered supercell of spins which is to approach a suitable model that best fits the data. Spins can be give some orientation rules, e.g. a Heisenberg model where the spins are free to orient in any direction or an Ising model, where the spins are given a fixed easy axis, and may point either up or down along this axis. In this thesis initial RMC refinements were performed

with unconstrained Heisenberg spins, and upon further investigation fixed to an Ising model, consistent with the large spin-orbit coupling in these systems.
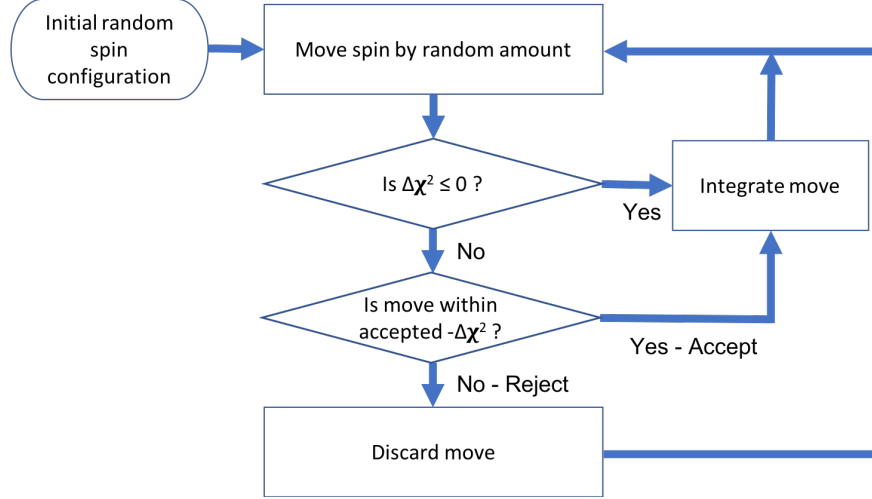


**Figure 2.11** A flow diagram describing the reverse Monte Carlo algorithm.

For analysing the magnetic diffuse scattering, with unpolarised neutrons, as used in the studies in this thesis, it is necessary to isolate the total magnetic contribution from the neutron-scattering data and normalise the intensity of the data. Data subtraction is done by taking measurements at a temperature well above that at which magnetic diffuse scattering emerges. To normalise the data we start by assuming that the observed nuclear Bragg peak intensity ($I_{obs}$) is proportional to the absolute nuclear intensity ($I_{abs}$) of the material in units of barn sr$^{-1}$ atom$^{-1}$:

$$I_{obs} = s \times I_{abs} \tag{2.26}$$

In order to find the proportionality constant (s) that converts the observed intensity into the absolute a refinement of the nuclear intensity is required at temperatures above the magnetic order, so that we can determined the scale factor (Scale) obtained from a Rietveld refinement. This parameter is multiplied by the calculated intensity of the Bragg peaks, during refinement, such that:

$$I_{obs} = Scale \times I_{calc} \tag{2.27}$$

therefore:

$$s = Scale \times \frac{I_{calc}}{I_{abs}} \tag{2.28}$$

In order to determine the proportionality constant, s, we require expression for both $I_{calc}$ and $I_{abs}$. The profile intensity calculated in FULLPROF is expressed as :

$$I_{calc} = \sum_G m_G |F_G|^2 L_G^x R^x(x - x_G) \tag{2.29}$$

where $G$ is a set of equivalent Bragg reflections, having the multiplicity $m_G$ and the Lorentz factor and $x$ is the scattering angle $2\theta$ (in constant wavelength data) and time $t$ in $\mu_S$ (for time-of-flight) data, and $R^x(x - x_G)$ is the resolution function. This assumes that the data has already been corrected for absorption and the occupation factor is the site multiplicity divided by the general multiplicity of the site. However absorption can be taken into account, during the calculation of the scale factor. The structure factor as calculated in FULLPROF is:

$$F_G = \sum_{j=1}^{N} b_j T_j exp(iG \cdot r_j) \tag{2.30}$$

where $r_j$ and $b_j$ are the position of the j$^{th}$ atom, and its nuclear scattering length (in units of $10^{-12}$ cm). $T_j$ is it's Debye-Waller factor, used to describe the thermal motion of the atom, and the sum is taken over all atoms in the unit cell. This thesis has dealt with RMC on temperature subtracted data of both TOF and CW data, but data normalisation is calculated differently for each experimental method. Here temperature subtracted data is defined has $T_{sub} = T_{low} - T_{high}$, where $T_{low}$ is the diffraction pattern data of interest containing magnetic diffuse scattering, and $T_{high} \gg T_N$ and is a diffraction pattern containing little or no magnetic information.

The equation for $I_{abs}$ can be expressed in terms of scattering angle or time-of-flight, using the $Q$-dependence of the Bragg scattering intensity: [157]

$$I_{abs}(Q) = \frac{2\pi^2}{NV} \sum_G \frac{m_G |F_G|^2}{G^2} R^Q(Q - G) \tag{2.31}$$

where $N$ is the number of magnetic atoms in the unit cell, $V$ is the volume of the unit cell ($\text{Å}^3$).

For TOF data we know the $Q$ dependence from equation 2.7, and so substituting this into the above equations yields the formula for $I_{abs}$ as:

$$I_{abs}(TOF) = \frac{m_n l}{2\pi h N V} \sum_G m_G |F_G|^2 L_t R_t (t - t_G) \tag{2.32}$$

where the Lorentz factor in time-of-flight is given by $L_G = d^4 sin\theta$, and $d$ is the $d$-spacing of the Bragg reflection. This gives the proportionality constant for time-of-flight as:

$$s_{TOF} = Scale \times \frac{4\pi N V sin\theta}{DTT1} \tag{2.33}$$

DTT1 is the instrument parameter, dependant on the flightpath (l) and the angle of the detector ($\theta$), and has the units of $\mu S^{-1}$. DTT1 is given by equation 2.24

For constant wavelength neutron the relationship between Q and scattering angle is given by equation 2.9, and substituted into equation 2.31 gives us:

$$I_{abs}(CW) = \frac{45\lambda^2}{2\pi^2 N V} \sum_G m_G |F_G|^2 L_G^{2\theta} R^{2\theta}(2\theta - 2\theta_G) \tag{2.34}$$

where the Lorentz factor for constant wavelength neutrons is $L_G^{2\theta} = \frac{1}{2sin^2\theta_G cos\theta_G}$, giving the proportionality constant for constant wavelength data as:

$$s_{CW} = Scale \times \frac{2\pi^2 N V}{45\lambda^3} \tag{2.35}$$

Therefore in order to obtain the absolute intensity of the temperature subtracted data, we divide the experimentally observed profile by the proportionality constant for TOF and CW data, respectively.

In the work in this thesis data collected at a high temperature $T_{high}$ were subtracted from the low-temperature data of interest, where $T_{high}$ = 20-30 K. TOF data banks were merged over a $Q$ range of 0.2 to 3.75-4 Å$^{-1}$ to improve statistics, areas with Bragg peak contamination excised and data re-binned to improve the signal to noise in the data without losing any

resolution with regards to the shape of the magnetic diffuse scattering. As previously discussed in Section 2.3.5 the magnetic form factor decays as a function of increasing $Q$, and magnetic diffuse scattering features are much weaker than Bragg reflections. Above 4 Å, the signal to noise ratio becomes so significant, that no information can be reliably resolved, therefore $\approx$4 Å is a suitable cut off for magnetic diffuse scattering to reduce computation time and minimise fitting to artefacts in the data.

The data were placed on an absolute intensity scale (barn $sr^{-1}$ $Ln^{-1}$ by normalisation to the calculated nuclear Bragg profile at $T_{high}$. Diffuse neutron patterns were fitted with the RMC program - SPINVERT. [108] For the $Ln(DCO_2)_3$ frameworks a supercell of 52 x 54 x 55 Å$^3$ or 5 x 5 x 13 unit cells was used. For the $Ln(DCO_2)_3$ frameworks a supercell of 49 x 49 x 51 Å$^3$ or 10 x 7 x 6 unit cells was used. A supercell of $\approx$50 Å$^3$ was chosen as this provided a good balance of resolution and speed of computations. Each RMC refinement provides a 'snapshot' into the disorder of a system, and so we must compile many refinements to build an accurate description of the system, and thereby decrease the statistical error. However we cannot distinguish between dynamic or static structural disorder which is one limitation to this method. These possibilities can only be distinguished between using spectroscopic methods.

## 2.5 Magnetic Symmetry Analysis

Symmetry is vital to many disciplines of technology and science, making complex problems more tractable by breaking down the problem into its most fundamental parts. The selection rules of spectroscopy are symmetry defined and without symmetry analysis, the discipline of, crystallography would not have become the success that it is today. In order to determine magnetic structures of materials, magnetic symmetry becomes a useful tool to narrow down the possible solutions and discover what is symmetry allowed.

### 2.5.1 Magnetic Symmetry Groups

Magnetic symmetry follows the same rules as structural space group symmetry, however for magnetic symmetry, the time-inversion or spin-flip operation, which reverse the direction all all magnetic moments is also important. If we consider a magnetic moment to be a rotating electric charge, as seen in Figure 2.12 then a normal mirror acting on a will cause the moment to invert. That is to say the magnetic moment (an axial vector) is invariant under rotation but when a reflection operation is applied an additional time-reversal symmetry must be applied.

Crystallographic symmetry when applied to nuclear structures does not need to consider this for the spherical atom and when a time-reverse operator is applied or not makes no difference, but to axial vector this is not so.
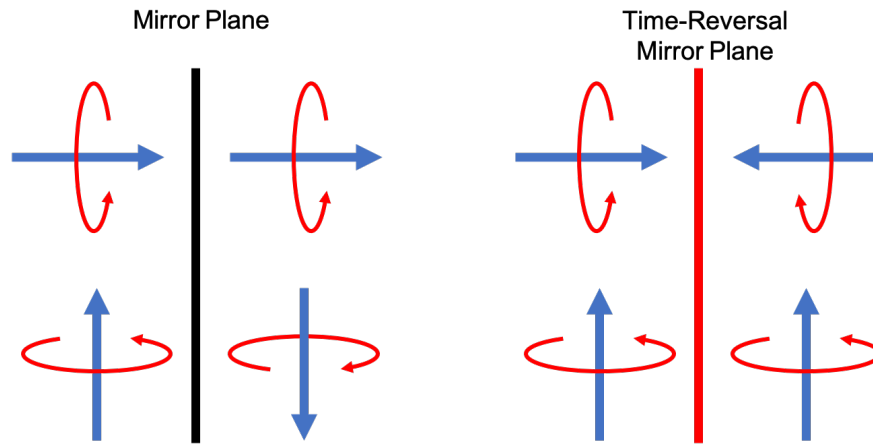


**Figure 2.12** Diagram showing time-reversal or spin-flip operators applied to a magnetic moment.

The first mathematical description of magnetic symmetry came from Heesch [158] and Shubnikov [159] which extended the 32 crystallography point groups by means of an anti-symmetry operation. Describing the groups in terms of colours and yielding the 122 magnetic point groups. This was then further extended to the space groups giving 1651 commensurate magnetic space groups. The use of magnetic crystallography is a powerful technique, and is the definitive way to describe a set of symmetries within magnetic crystallography. However it becomes exponentially more complicated when dealing with more complicated magnetic structures as seen in geometrically frustrated systems. The superspace formalism has been used to describe modulated systems in 1, 2 and 3D and yielding 11764 superspace groups. [160] The method of symmetry analysis developed by Stokes and Campbell [161] breaks down the magnetic symmetry groups into symmetry modes, valid for a magnetic space group and using that as a method for determination of the magnetic structure. The community has developed tools for analysing modulated and incommensurate magnetic structures, using superspace symmetry groups, but when dealing with incommensurate magnetic structures it is much more elegant to use representation theory.

## 2.5.2   Representation Theory

Representation theory is the extension of group theory from point groups to include space groups, and has been used to deal with commensurate and incommensurate magnetic struc-

tures with great success. In Landau theory of phase transitions, any magnetic ordering occurring in a continuous transition necessarily transforms under the symmetry operations of the paramagnetic phase according to a single irreducible representation of the the symmetry group of this phase. This is the basis of representation theory with regards to magnetic structure and can be attributed to Bertaut in 1968. [162, 163]

This approach starts by considering the unit cell, and states that the propagation of a magnetic structure through a solid can be described using plane waves (Bloch wave), and then relates it back to the unit cell ($G_0$) through a phase relation. The moment of atom j ($\vec{V_j}$) with respect to the moment of atom i ($\vec{V_i}$) is described by the equation for a plane wave, and for a simple case is described simply by:

$$\vec{V_j} = \vec{V_i}cos(-2\pi\vec{k}\cdot\vec{t}) \tag{2.36}$$

where $\vec{t}$ is the translation between the moment of the $i^{th}$ and $j^{th}$ atom, $\vec{k}$ is the frequency of the wave in terms of unit cells. The **k**-vector $\vec{k}$ is the reciprocal of the number of unit cells needed to describe the magnetic supercell ie. a supercell 4x that of the nuclear unit cell has the vector 0.25.

A symmetry operation of a space group ($G_0$) which only involves a translation of the unit cell, and leaves $\vec{k}$ unchanged are known as the little group $G_k$. However, there can be operations which can be equivalent but involve a rotational aspect, meaning there can be equivalent **k**-vector depending on the setting. The goal of representation theory is finding the irreducible representation of the magnetic supercell, that describes the magnetic structure. [164] The irreducible representations are made of up basis vectors, equivalent to the vibrational modes of spectroscopy. Representation theory only tells you what is symmetry allowed, not the energies, and therefore it does not determine the ground state magnetic structure. Only experimental techniques and comparison with data can determine the magnetic structure. The success of representation analysis lies in its generality describing magnetic, structural and other orders of crystallography within a single theory and be extended to complex systems with ease.

### 2.5.3   Magnetic Structure Determination

Magnetic structure model refinements were was carried out in FULLPROF. [146] Magnetic propagation vectors were determined with the **k**-search functionality in WINPLOTR, [165]

taking into consideration the breaking of symmetry for centred cells, and looking at the symmetry points of the Brillouin zone using ISODISTORT [161]. For determination of magnetic crystallography groups a combination of ISODISTORT [161] and the Bilbao Crystallographic Server [166] were used. For symmetry analysis using representation theory, a combination of SARAh [167] and BASIREPS (within the FULLPROF suite) were used to determine the irreducible representations and basis vectors. Where multiple magnetic phases were required to fit the diffraction patterns, the phase scales were fixed to be equal, and the magnetic moments were refined, as it is not possible to refine the phase scale and magnetic moment on each of the phases. Therefore we have assumed that the magnetic moment vector is proportional to the magnetic phase fraction.

## 2.6 Inelastic Neutron Scattering

Inelastic neutron scattering is a scattering technique used for measuring the dynamics of samples. [122, 168] When probing the magnetic order, both long range and local, it can be used to measure the dynamics of the motion of spins, so called spin-waves. These spin waves can also be considered boson quasi-particles known as magnons, that propagate through magnetic order, in an analogous way to phonons propagating through a lattice. [31] The inelastic scattering method involves determining the changes in energy by measuring the incident and scattered energies in order to determine the wave vector (see Figure 2.13). The conservation of energy allows changes in energy be calculated from the relationship shown below.
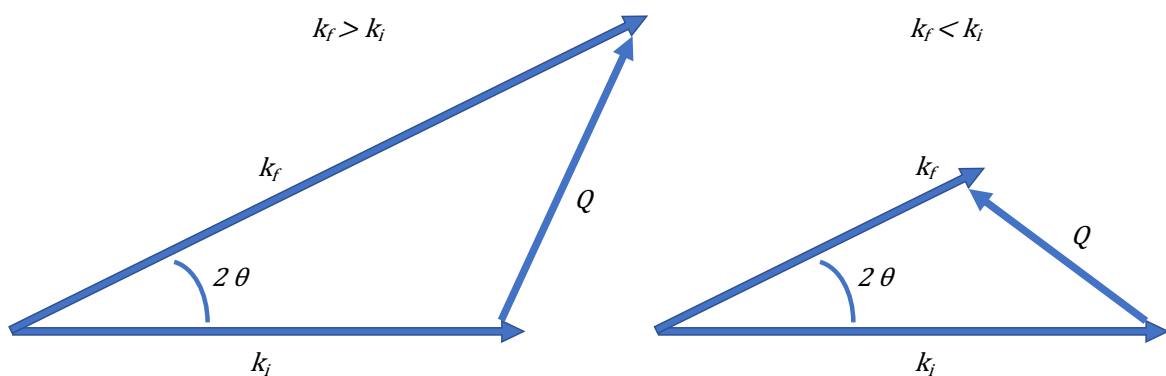


**Figure 2.13** Diagram of the inelastic scattering triangles.

Momentum and energy transfer allow for fitting of inelastic neutron spectra to reveal information about the dynamics of atoms and magnetic spins. TOF spectrometers come in two

varieties, direct and indirect geometries. Direct geometry spectrometers define the incident energy with choppers and the final energy is determined by the time-of-flight between the sample and the detectors. Indirect (inverted) geometry spectrometers expose the sample to a white incident beam, and the incident energy is determined at the sample position by the measurement of the time-of-flight, and the final energy is measured by a monocrystal.

## 2.6.1 LET

The inelastic neutron scattering study in this thesis used the Low Energy Transfer (LET) spectrometer. This is a direct geometry cold-neutron multi- chopper spectrometer on TS-2 at the ISIS neutron source. This combines large area detectors, advanced neutron beam transport and state-of-the-art computational tools to maximise the efficiency of delivering neutrons to the sample and to their subsequent detection and analysis, by using large area detectors (see Figure 2.14). [169] Such instrumentation has the ability to cover a highly diverse range of science from bio-molecular materials through to quantum matter.



**Figure 2.14** Photograph of the inside of LET, showing the large area detectors.

In this study an incident energy $E_i$ = 15 meV, in High resolution mode with a chopper frequency of 240 Hz was used. $Tb(DCO_2)_3$ was loaded into a copper annular can, consisting of a 18 mm inner can and 22 mm outer can. Measurements were carried out between 50 mK to 120 K, with the samples cooled using a dilution refrigerator, inside an Orange cryostat. The data were reduced using the MSlice package within the Mantidplot software suite. [170] Calculations of the spin wave dispersion were performed using a semiclassical method using the SpinW software, [171] using linear spin wave theory.

## 2.7    Physical Property Measurements

The theory of magnetism and the measurement quantities such as magnetic susceptibility and magnetisation have previously been introduced. Here the experimental methods for measuring these quantities is described.

### 2.7.1    Magnetic Susceptibility

The Quantum Design magnetic property measurement system (MPMS) is able to detect magnetic susceptibilities to a high degree of precision, able to resolve changes in magnetic fields as small as $10^{-15}$, over a wide temperature range and applied magnetic fields by using superconducting components. The principal components of this DC measurement system comprise of [172]:

**Temperature Control System**  Control of the sample temperature, requiring heat flow to the sample, and control of liquid helium coolant.

**Magnetic Control System**  A large superconducting coil, made of a niobium germanium alloy ($Nb_3Ge$) and a $T_C$ of 23 K, submerged in liquid helium to remain cool. An applied current is proportional to the magnetic field generated.

**Superconducting SQUID Amplifier System**  The Superconducting Quantum Interference Device (SQUID) is the magnetic measurement detector of the MPMS, built from two Josephson junctions, which will be discussed in further detail.

**Sample Handling System**  The system that controls the position of the sample, and is able to move the sample through the detector without mechanical vibrations.

**Computer System**  A computer with software to automate the functions of the MPMS.

The Josephson junction was theoretically proposed in 1962 [173] and experimentally observed in two years later [174], yielding Josephson the Nobel prize for his discovery. The Josephson junction consists of two superconducting wires electrically separated by a small insulating material junction, over which quantum tunnelling of electron Cooper pairs occurs. If a constant biasing current ($I_B$) is applied to either sides of the ring, and is greater than the critical current for the junction, a voltage is produced.

A SQUID consists itself of two Josephson junctions in a ring, as shown included in the MPMS diagram in Figure 2.15. The electrical current density through a Josephson junction depends on the phase difference $\Delta\Phi$ of the two superconducting wave functions. The time derivative of

$\Delta\Phi$ is proportional to this bias current. The SQUID is connected to superconducting detector coils and when a magnetic sample is passed through a voltage is induced, due to Faraday's law, which causes a change in $\Delta\Phi$ and therefore in voltage. Electronic measurement systems are extremely sensitive to changes in voltage and therefore the SQUID can achieve high resolution in changes of magnetic flux. During measurement the sample is aligned in the centre of the detector coils, and at each data point is moved through the coils to measure the magnetic susceptibility.
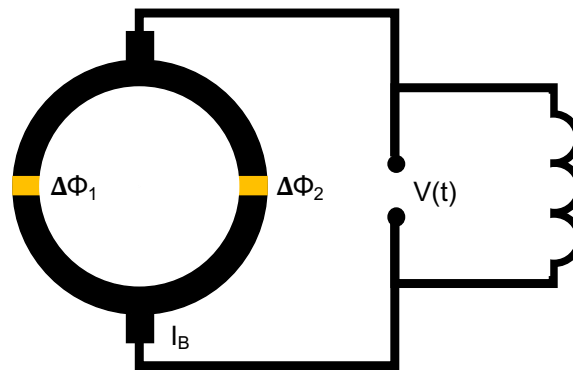


**Figure 2.15** Diagram of the detector coils of the MPMS connected to the SQUID, by superconducting wires. The yellow sections of the ring indicates the Jospehson junctions, with a biasing current across.

In this thesis two measurements have been conducted with the MPMS SQUID magnetometer, measurements of magnetic susceptibility ($\chi$) measured in Zero-Field Cooled (ZFC) and Field-Cooled (FC) conditions, and magnetisation (MvH) curves. ZFC measurement are initially cooled in zero-applied field, a field is applied and then measurements are taken on warming. Field-Cooled measurements involve measuring a sample cooled in the same magnetic field the measurement is performed in and can be done on warming or cooling. Deviations from the ZFC and FC measurements provide information about the type of magnetic order occurring. Magnetisation measurements were conducted at constant temperature with the sample measured over a variety of field strengths. A single magnetisation curve provides information about the dimensionality of the spin (Ising v.s. Heisenberg), and sweeping the field from $-H$ to $+H$ suggests whether it is ferromagnetically ordered. A series of magnetisation measurements at variable temperatures can be used to calculate magnetocaloric values, as will be discussed.

Magnetic susceptibility measurements were typically performed on a Quantum Design magnetic properties measurement system (MPMS), equipped with a $^4$He cryostat. Samples were measured between 2-300 K with susceptibility measurements performed in an applied field of 1000 Oe . Samples were placed in gelatin capsules enclosed inside a pierced straw

with a uniform diamagnetic background. Magnetic properties measured below 2 K were performed on MPMS with a $^3$He insert in a 100 Oe DC field, with samples held in a diamagnetic film and placed into a Quantum Instruments MPMS sample holder.

### 2.7.2 Magnetocaloric Measurements

The magnetocaloric effect can be measured directly, through heat capacity and temperature measurements [175] or indirectly through magnetisation measurements. [176] Throughout this thesis the magnetocaloric effect has been measured indirectly through magnetisation measurements. Despite indirect measurements, for GdOHCO$_3$ [77], Gd(HCO$_2$)$_3$ [62] and other similar materials [177] excellent agreement between direct and indirect measurements has been observed, and so we have confidence in the accuracy of these measurements.

The magnetocaloric effect was determined from calculating the magnetic entropy $-\Delta S_m$, by taking magnetisation curves at regular temperature intervals, using the Maxwell relation in Figure 2.37.

$$\Delta S_m(T) = \int \left[ \frac{\delta M(T,B)}{\delta T} \right]_B dB \qquad (2.37)$$

Magnetisation measurements were taken between 0 and 5 T, at variable temperatures. The entropy was calculated for each temperature point, and change in entropy calculated by subtracting the entropy at zero field from those in applied field. Measurements were put into appropriate units for comparison.

### 2.7.3 Heat Capacity

Heat capacity is a useful physical property measurement to understand the entropy of a material at variable temperature and in zero and applied fields. This can give important physical information because it can show the entropy changes associated with phase transition to a high degree of precision. The heat capacity of a sample is defined as the energy required to raise the temperature of the sample by an amount, this can be described by:

$$C_p = \left( \frac{dQ}{dT} \right)_P \qquad (2.38)$$

For a constant pressure, the second law of thermodynamics states:

$$dQ = TdS \tag{2.39}$$

Therefore, at constant pressure, the heat capacity is directly related to the entropy of the system given by:

$$S = \int_0^{T_{max}} \left( \frac{C_T}{T} \right) dT \tag{2.40}$$

Where $T_{max}$ is the maximum temperature heat capacity has been measured. The total heat capacity of a system is made of a several parts described by:

$$C_{total} = C_{lattice} + C_{mag} + C_{nuclear} + C_{Schottky} \tag{2.41}$$

Where $C_{total}$ is the total energy of the material, comprised of $C_{lattice}$ - the lattice heat capacity, $C_{mag}$ - the magnetic heat capacity, [178] $C_{nuclear}$ - the hyperfine contribution and $C_{Schottky}$ the heat capacity resultant of the Schottky term. Phonons in the material are responsible for the lattice contribution of the heat capacity and are proportional to temperature. This can be modelled with the Debye equation: [178]

$$C_{lattice} = \frac{9nRT^3}{\theta_D^3} \int_0^{\theta/T} \frac{x^4 e^x}{(e^x - 1)^2} dx \tag{2.42}$$

Where $\theta_D$ is the Debye temperature, $N$ is the number of atoms in the unit cell, $R$ is the universal gas constant, $T$ is the temperature and $x$ is the range needed to integrate over to provide the heat capacity.

The Debye temperature describes the temperature when all atoms are vibrating with the same frequency, below which quantum effects may be observed. This is given by: [179]

$$\theta_D = \frac{h v_m}{k_B} \tag{2.43}$$

where $h$ is Planck's constant, $k_B$ is the Boltzmann constant and $v_m$ is the Debye frequency.

For experimental data it is often difficult to de-convolute the contributions from all of the heat capacity contributions, and other anomalous effects, and so we have reported the heat capacity

after subtraction of the sample holder, the silver powder (used for better heat transfer) and the lattice contributions. This is sufficient as the important conclusion we can draw from heat capacity is the ordered temperature and how it effects changes in entropy rather than the entropy results themselves.

Heat capacity measurements in zero and applied field were performed on a Quantum Design PPMS DynaCool with 14 T superconducting magnet and $^3$He insert, between 400 mK and 14 K. Insulating materials such as the frameworks in this thesis, typically have poor thermal conductivity therefore samples were ground into a powder, mixed with an equal amount of powdered silver, to improve heat transfer, and pressed into a pellet. Empty sample holder measurements were taken to allow for subtraction after measurement of the sample. To isolate the magnetic contribution to the heat capacity, the blank sample holder, lattice (calculated from the Einstein-Debye equations), and the silver contributions (taken from literature data [180]) were subtracted.

## 2.8 Characterisation Techniques

### 2.8.1 TGA/DSC

Thermogravimetric analysis (TGA) with Differential Scanning Calorimetry (DSC) is a method for testing the thermal stabilities, mass loss and heat absorption of materials at room temperature and above. The mechanism of heat absorption follows the same equations for lattice vibration energies as described in Section2.7.3, but at much higher temperatures, and therefore quantum effects and magnetic entropy are not significant. Heating of the sample is performed on a high precision mass balance, and a loss of mass is assumed to be due to loss of material in the sample, either due to de-solvation or breakdown of the lattice.

The thermal stabilities of selected $Ln$OHCO$_3$ samples of about 5 mg were characterized with a Netzsch STA 409 PC TGA-DSC between 20-800°C, heating at a rate of 10°C min$^{-1}$ with data analysed using Netzsch Proteus. Data were recorded under an atmosphere of air, Background measurements were initially conducted on an empty ceramic crucible, and subtracted from measurements to isolate the sample contribution.

### 2.8.2 Infrared Spectrometry

Infrared spectroscopy is a means of probing the covalent bonds in a materials by exposing it to a broad spectrum of incident infrared waves, and detecting the absorption or transmission

at a detector. Different wavelengths of infrared light will be absorbed by different types of covalent bonds, and vibrational modes corresponding to a quantized energy level of that mode. The bending and/or stretching modes of different chemical bonds typically occur in the absorption bands (above 1500 cm$^{-1}$) and so it is trivial to qualitatively analyse bonds in materials. [19]

The absorption infrared absorption spectra of $Ln$OHCO$_3$ samples was recorded with a Shimadzu IRaffinity-1 Fourier transform infrared spectrometer in the range 500-4000 cm$^{-1}$, and analysed with LabSolutions IR. Infrared spectra measurement were initially conducted on a blank background for subtraction for the sample data. Measurements were used as confirmation of the synthesised samples, and to confirm deuteration of samples used for neutron scattering experiments.

# 3

# Structural and Magnetic Properties of the $Ln$OHCO$_3$ and $Ln$F$_3$

## 3.1  Introduction

The need for dense magnetocaloric phases with high magnetic moments has driven an interest in MCE materials based on late lanthanide frameworks (where lanthanide ($Ln$) = Gd-Er) because of the high magnetic entropy change they support. A new wave of non-oxide magnetocalorics have recently been reported to have particularly high magnetocaloric effects, including Gd(HCO$_2$)$_3$, GdOHCO$_3$ and GdF$_3$, which have superior performance to the benchmark Gd$_3$Ga$_5$O$_{12}$ phase as shown in Figure 3.1. [4, 5, 62, 69, 73, 74, 77, 177] Several of these phases contain polyatomic anions which adopt highly anisotropic structures to incorporate their non-spherical cations while hosting a range of competing magnetic interactions between them. [62, 75–77] Exploring dense framework materials containing smaller polyatomic ligands and a range of different lanthanides are potentially of great interest for MCE applications.

Recent work has shown the substitution of Gd for other lanthanide ions (in particular Tb), with Ising-like spins has led to larger magnetocaloric responses above 2 K in low applied fields, [4, 5, 72, 181] at the expense of some decrease of performance for larger field changes. This has inspired the search for other magnetocaloric materials by substituting gadolinium for other lathanides, in gadolinium containing materials which have already been shown to perform well. The benefits of such an approach has already been highlighted by studies of the $Ln$(HCO$_2$)$_3$ phases, which show that Tb(HCO$_2$)$_3$ outperforms Gd(HCO$_2$)$_3$ above 4 K

and for the field change possible using a permanent magnetic (< 2 T). [4] Therefore we have
chosen to investigate the magnetocaloric effect of some high performance magnetocaloric
materials, highlighted by earlier studies of the gadolinium analogues.
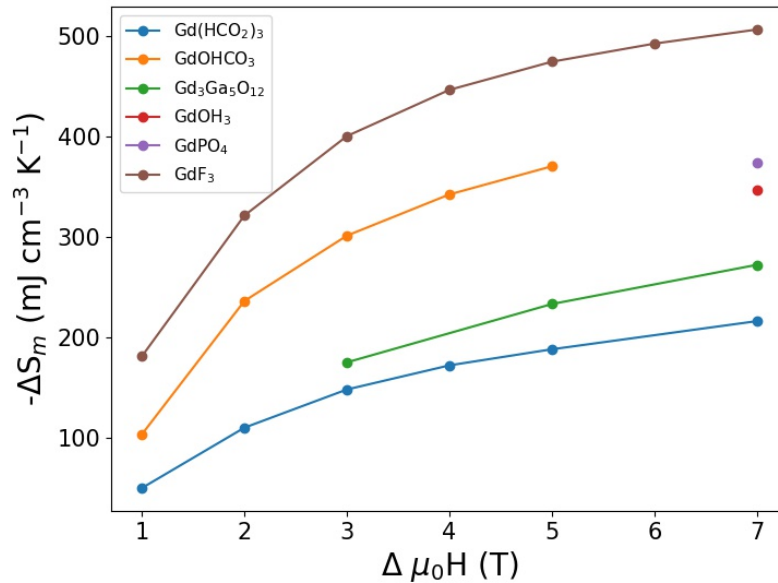


**Figure 3.1** A comparison of the magnetocaloric effect for various materials, in variable fields. Data
reproduced from literature values. [4, 5, 62, 69, 73, 74, 77, 177]

## 3.2   *Ln*OHCO$_3$ Frameworks

### 3.2.1   X-ray Diffraction of the *Ln*OHCO$_3$ Phases

In order to ensure phase purity of the *Ln*OHCO$_3$ samples Le Bail fits were performed on
X-rays patterns (see Figure A.1), providing excellent fits to the data. This confirms the
phase purity and yields the room temperature lattice parameters and fitting statistics shown
in Table 3.1. Lattice parameters determined from these fits have been used for the volumetric
magnetocaloric effect calculations in Section 3.2.2. There is some debate about whether the
*Ln*OHCO$_3$ crystallise in the *Pnma* or $P2_12_12_1$ space group. [73, 77, 113, 114] We initially
chose the $P2_12_12_1$ space group as this gave a slight improvement to the fitting statistics over
*Pnma*, and is the most commonly reported space group for these *Ln*OHCO$_3$. The refinements
indicated the expected reduction in the unit cells across the series, as a result of the lanthanide
ion radii contraction. [182]

**Table 3.1** Summary of the *Ln*OHCO$_3$ refinements in the $P2_12_12_1$ space group, from powder X-ray diffraction

| *Ln* | *a* (Å) | *b* (Å) | *c* (Å) | R$_p$ (%) | R$_{wp}$ (%) |
|------|---------|---------|---------|-----------|--------------|
| Gd | 7.07339(8) | 4.87444(6) | 8.44347(11) | 2.05 | 3.02 |
| Tb | 7.01195(11) | 4.85322(8) | 8.44689 (15) | 3.27 | 4.25 |
| Dy | 6.97710(20) | 4.83203(14) | 8.44309(24) | 4.88 | 6.05 |
| Ho | 6.95637(6) | 4.81218(4) | 8.45494(7) | 3.13 | 4.12 |
| Er | 6.92541(5) | 4.79026(4) | 8.46914(7) | 2.71 | 3.51 |

## 3.2.2 Magnetic Properties of *Ln*OHCO$_3$

Field cooled (FC) and zero-field cooled (ZFC) magnetic susceptibility data of the *Ln*OHCO$_3$ frameworks (*Ln* = Gd$^{3+}$, Tb$^{3+}$, Dy$^{3+}$, Ho$^{3+}$ and Er$^{3+}$) were measured in a 1000 Oe field from 2 K to 300 K and did not show any indication of long range magnetic order. This data was found to obey the Curie-Weiss law over the full temperature range, with the exception of DyOHCO$_3$ where significant deviations were found to occur above 200 K that likely result from crystal field effects (see Figure A.2c). Effective magnetic moments were found to be broadly consistent with the values expected for these trivalent lanthanides according to the Russell–Saunders coupling scheme [25] (see Table 3.2) calculated from mean field Curie-Weiss behaviour - see Figure A.2 for associated fits.

**Table 3.2** Summary of Curie-Weiss temperatures and magnetic moments for lanthanides in *Ln*OHCO$_3$, calculated from the Curie-Weiss fits to the data.

| *Ln* | $\theta_{CW}$ (K) | Curie Constant (emu mol$^{-1}$ Oe$^{-1}$) | Magnetic Moment ($\mu_B$) |
|------|-------------------|-------------------------------------------|----------------------------|
| Gd | −1.013(4) | 6.6863(20) | 7.3123(11) |
| Tb | −2.82(7) | 10.20(5) | 9.029(20) |
| Dy | −2.79(4) | 14.40(6) | 10.732(21) |
| Ho | −3.149(11) | 13.371(16) | 10.340(6) |
| Er | −2.47(9) | 9.65(6) | 8.784(28) |

Curie-Weiss temperatures were determined and suggest moderate antiferromagnetic interactions in all materials. Aside from Gd, however, the depopulation of Stark levels at lower temperatures in lanthanides with significant orbital angular momentum means that these Curie-Weiss temperatures must be considered tentatively. [183]

Isothermal magnetisation measurements on the *Ln*OHCO$_3$ frameworks measured at 2 K (see Figure 3.2) reveals that both TbOHCO$_3$ and DyOHCO$_3$ are easily magnetized under modest applied fields, with both close to saturation under applied fields of 10 kOe. In contrast, the other frameworks, including GdOHCO$_3$ continue to magnetize with applied magnetic field up to 50 kOe. The greater ease of magnetisation in TbOHCO$_3$ and DyOHCO$_3$ of the frameworks in low applied fields is the source of their high MCE performance in fields below 20 kOe, as discussed below. The saturation value of the magnetisation can provide some insight into whether a magnetic material is a Ising or Heisenberg system, in which cases limits of $g_J J/2$ and $g_J J$ are expected. [33, 34, 184, 185] The magnetic saturation of Gd approaches 7 $\mu_B$, consistent with a Heisenberg cation, while those of Ho and Er approach values expected in a purely Ising case. Those for DyOHCO$_3$ and TbOHCO$_3$ are close to the limit expected for the magnetic cations in an Ising case but are above this suggesting other contributions to the magnetic observed saturation magnetisation.
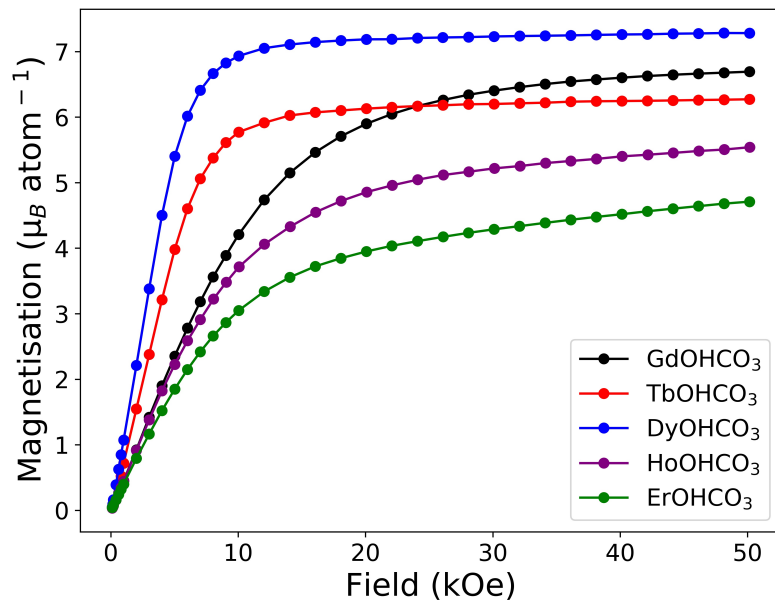


**Figure 3.2** Isothermal magnetisation measurements on the *Ln*OHCO$_3$ frameworks measured at 2 K.

Magnetic entropy change, $\Delta S_m$, was calculated from the Maxwell relation between 2 and 10 K, and for field changes between 0 and 1-5 T (see Figures A.3 for magnetisation plots). While this is an indirect way of measuring the magnetocaloric effect, recent work on Gd(HCO$_2$)$_3$ and GdOHCO$_3$, have shown that for similar frameworks excellent agreement is usually obtained between this approach and the direct determination of $\Delta S_m$ from heat capacity

measurements. [4, 62] The $\Delta S_m^{max}$ values determined from this approach are presented in Table 3.3.

**Table 3.3** Summary of the peak MCE ($\Delta S_m^{max}$) at peak temperatures (T$_{max}$) of the studied *Ln*OHCO$_3$ at different field changes. Mass refers to changes in entropy per mass in units of J Kg$^{-1}$ K$^{-1}$ and volume refers to change in entropy per volume in units of mJ cm$^{-3}$ K$^{-1}$.

| *Ln* | T$_{max}$ (K) | $\Delta\mu_0$H = 1-0 T | | $\Delta\mu_0$H = 2-0 T | | $\Delta\mu_0$H = 5-0 T | |
| | | Mass | Volume | Mass | Volume | Mass | Volume |
|---|---|---|---|---|---|---|---|
| Gd | 2 | 19.32 | 103.37 | 44.17 | 236.31 | 69.33 | 370.42 |
| Tb | 4 | 17.64 | 95.97 | 30.99 | 168.62 | 33.72 | 183.40 |
| Dy | 4 | 20.76 | 115.87 | 33.34 | 186.15 | 34.46 | 192.42 |
| Ho | 4 | 10.84 | 61.53 | 19.85 | 112.67 | 24.38 | 138.36 |
| Er | 2 | 15.04 | 86.43 | 28.11 | 161.51 | 31.98 | 183.73 |

As expected from other lanthanide magnetocaloric materials, the previously reported GdOHCO$_3$ is observed to have the greatest $-\Delta S_m^{max}$ at 2 K, particularly in multiple Tesla magnetic fields (see Figures 3.3 and 3.4). For moderate field changes of less than 2 T, TbOHCO$_3$ and DyOHCO$_3$ are found to perform exceptionally well between temperatures of 4 and 10 K with $-\Delta S_m^{max}$ at 4 K (Figure 3.3b). TbOHCO$_3$ and DyOHCO$_3$ have a higher $-\Delta S_m$ than GdOHCO$_3$ at all temperatures between 4 and 10 K for a 2-0 T field change and exhibit a trend that suggests this will continue at higher temperatures. Of these two compounds DyOHCO$_3$ has the highest $-\Delta S_m^{max}$, at 4 K, of 33.34 J Kg$^{-1}$ K$^{-1}$ with TbOHCO$_3$ having a $\Delta S_m^{max}$ of 30.99 J Kg$^{-1}$ K$^{-1}$ *c.f.* GdOHCO$_3$ that has a $-\Delta S_m$ of 29.54 J Kg$^{-1}$ K$^{-1}$ for the equivalent temperature and field change. The difference in the performance of TbOHCO$_3$ and DyOHCO$_3$ is even greater for $\Delta\mu_0$H = 1-0 T where they are observed to have $-\Delta S_m^{max}$ of 17.64 J Kg$^{-1}$ K$^{-1}$ and 20.76 J Kg$^{-1}$ K$^{-1}$ at 4 K respectively, *c.f.* GdOHCO$_3$, which we find to have an equivalent $-\Delta S_m$ of 11.67 J Kg$^{-1}$ K$^{-1}$. In $\Delta\mu_0$H = 1-0 T DyOHCO$_3$ outperforms all other *Ln*OHCO$_3$ at all temperatures above 3 K, and the $-\Delta S_m^{max}$ for DyOHCO$_3$ is almost twice the $-\Delta S_m$ of GdOHCO$_3$ at the same temperature.

These results are particularly impressive when compared to the benchmark material GGG or Dy$_3$Ga$_5$O$_{12}$ (DGG). For $\Delta\mu_0$H = 2-0 T GGG has a $-\Delta S_m^{max}$ = 17.7 J Kg$^{-1}$ K$^{-1}$ or 145 mJ cm$^{-3}$ K$^{-1}$ at 1.2 K [77] and DGG has a $-\Delta S_m^{max}$ = 11.64 J Kg$^{-1}$ K$^{-1}$ or 95 mJ cm$^{-3}$ K$^{-1}$ at 1.2 K, although the performance of DGG is modestly better for a 1-0 T field change and at higher temperatures compared to GGG. [71, 112] DyOHCO$_3$ however, has a $-\Delta S_m^{max}$ = 33.34 J Kg$^{-1}$ K$^{-1}$ or 186.15 mJ cm$^{-3}$ K$^{-1}$ at 4 K and retains a greater $-\Delta S_m$ per weight than GGG's $-\Delta S_m^{max}$ up to 8 K. TbOHCO$_3$ also maintains a $-\Delta S_m$ that is higher than
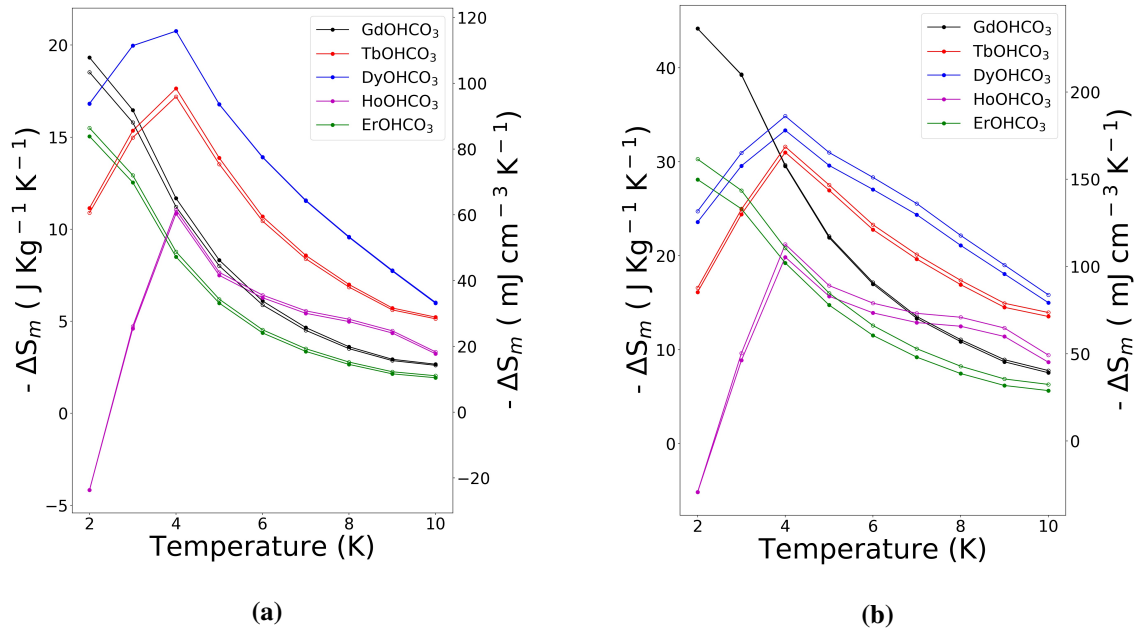
**Figure 3.3** The magnetocaloric effect of the late *Ln*OHCO$_3$ frameworks for field changes of (a) 0-1 T, (b) 0-2 T. The filled and hollow symbols mark mass and volumetric units, respectively.
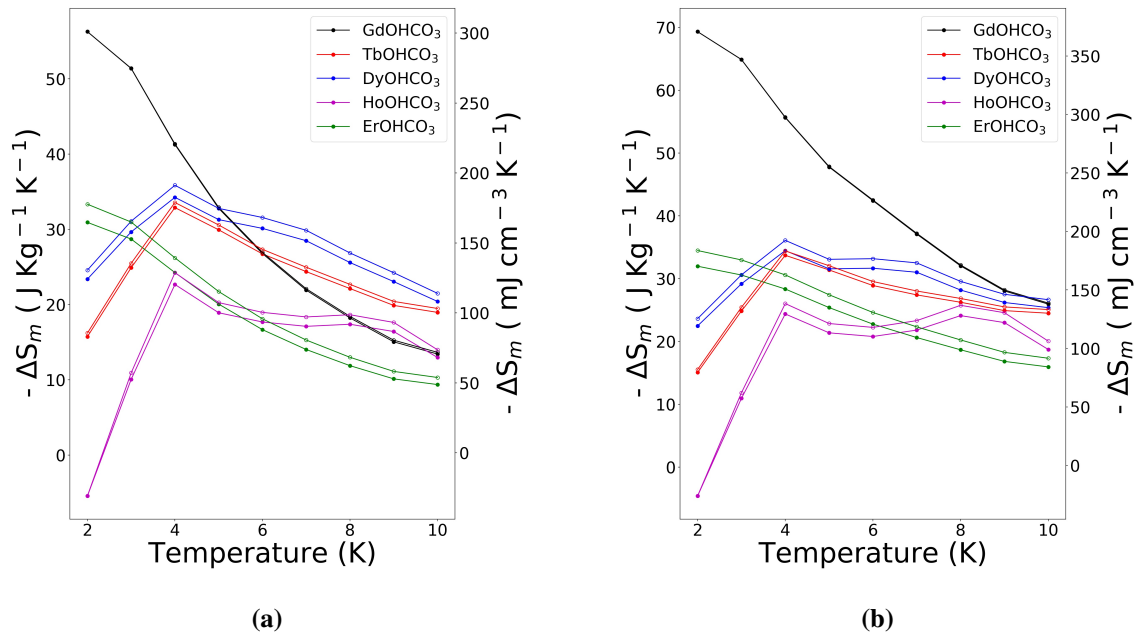


**Figure 3.4** The magnetocaloric effect of the late *Ln*OHCO$_3$ frameworks for field changes of (a) 0-3 T and (b) 0-5 T. The filled and hollow symbols mark mass and volumetric units, respectively.

GGG's $\Delta S_m{}^{max}$ for $\Delta\mu_0 H$= 2-0 T between 3-6 K. The MCE performance of HoOHCO$_3$ and ErOHCO$_3$ are less remarkable. The later continues to decrease on cooling to 2 K but with much poorer performance for a given temperature and applied field change compared to GdOHCO$_3$. HoOHCO$_3$, in contrast has its $-\Delta S_m{}^{max}$ at 4 K but this is much lower than observed for DyOHCO$_3$ and TbOHCO$_3$. Thus its $-\Delta S_m$ only exceeds that of GdOHCO$_3$ for $\Delta\mu_0 H$ = 1-0 T and 2-0 T, respectively, above 6 K and 7 K and this is then only by small amounts. Perhaps more notably $-\Delta S_m$ becomes negative at 2 K, which from the Maxwell relation can be interpreted as indicating that is becoming negative at low temperatures, consistent with the material being close to a transition to an antiferromagnetic state.

The results obtained here vary from those obtained from the previous study of the $Ln$(HCO$_2$)$_3$ family in two key respects. [4] Firstly, in the formates, Tb(HCO$_2$)$_3$ showed the greatest MCE performance [4] between 4-10 K, for applied field changes of less than 2 T. The magnetocaloric measurements of TbOHCO$_3$ indicate the MCE behaviour is qualitatively similar to Tb(HCO$_2$)$_3$ above 4 K in low applied fields, but with greater performance. Unlike the $Ln$(HCO$_2$)$_3$ family, the best performer of the $Ln$OHCO$_3$ family is DyOHCO$_3$. This is distinct from the behaviour of Dy(HCO$_2$)$_3$, which continues to increase at low temperatures in a similar fashion but with much lower performance than Gd(HCO$_2$)$_3$. Secondly the value of $-\Delta S_m{}^{max}$ for TbOHCO$_3$ and DyOHCO$_3$ is much closer to that of GdOHCO$_3$ (see Table 3.3) than is the case for Tb(HCO$_2$)$_3$ compared to Gd(HCO$_2$)$_3$ ( *c.f.* 8.08 J Kg$^{-1}$ K$^{-1}$ and 10.64 J Kg$^{-1}$ K$^{-1}$ for 1-0 and 2-0 T field changes in Tb(HCO$_2$)$_3$ to 13.23 J Kg$^{-1}$ K$^{-1}$ and 25.37 J Kg$^{-1}$ K$^{-1}$ for 1-0 and 2-0 T field changes in Gd(HCO$_2$)$_3$) . [4] This is related to much larger MCE effects above 4 K in TbOHCO$_3$ and DyOHCO$_3$ compared to Tb(HCO$_2$)$_3$, offering performance comparable to that found in GGG, below 2 K, at higher temperatures for the first time.

### 3.2.3 Tb$_x$Gd$_{1-x}$OHCO$_3$ and Dy$_x$Gd$_{1-x}$OHCO$_3$ Solid Solutions

The higher T$_{max}$ of TbOHCO$_3$ and DyOHCO$_3$ encouraged further solid solution studies of Tb$_x$Gd$_{1-x}$OHCO$_3$ and Dy$_x$Gd$_{1-x}$OHCO$_3$ in order optimise the higher temperature and peak performance, simultaneously. Previous studies of *Ln* substituted magnetocalorics have found to improve magnetocaloric performance, particularly in Tb$_x$Gd$_{1-x}$(HCO$_2$)$_3$. [4, 186] In the Tb$_x$Gd$_{1-x}$(HCO$_2$)$_3$ series doping with up to 40 % Tb improved the MCE effect observed above 4 K without significantly decreasing the performance at lower temperatures. [4]

Doping Tb$^{3+}$ and Dy$^{3+}$ with GdOHCO$_3$, to produce Tb$_x$Gd$_{1-x}$OHCO$_3$ and Dy$_x$Gd$_{1-x}$OHCO$_3$ frameworks, was successful with stoichiometric control over doping confirmed from the unit cell volume change consistent with Vegard's law (Figure A.4). The trend in unit cell volume obtained from fits to powder X-ray diffraction patterns suggest stoichiometries of x = 0.18, 0.37, 0.63, 0.81 for Tb and x = 0.22, 0.40, 0.60, 0.77 for Dy have been achieved, close to the nominal stoichiometries.

The magnetic properties of doped GdOHCO$_3$ with Tb$^{3+}$ and Dy$^{3+}$ were therefore explored with steps of x=0.2 across the Tb$_x$Gd$_{1-x}$OHCO$_3$ and Dy$_x$Gd$_{1-x}$OHCO$_3$ series. The performance of these doped compounds were found to vary from a physical mix of the end member compounds, suggesting that magnetic coupling between magnetic cations plays a key role in their MCE (see Figure 3.5. In particular there is a sharp change between GdOHCO$_3$-like MCE performance and DyOHCO$_3$ and TbOHCO$_3$ performance between 40 and 60 % Dy doping and 60 and 80 % Tb doping, respectively. Unfortunately, even a small doping of any of the three end members leads to a significant reduction in $-\Delta S_m^{max}$ without any compensating increase in performance at other temperature ranges. Potentially improving the magnetocaloric performance of this family could be explored further using other doping strategies, such as other lanthanide cations or lower doping percentages, but this is beyond the immediate focus of this work.
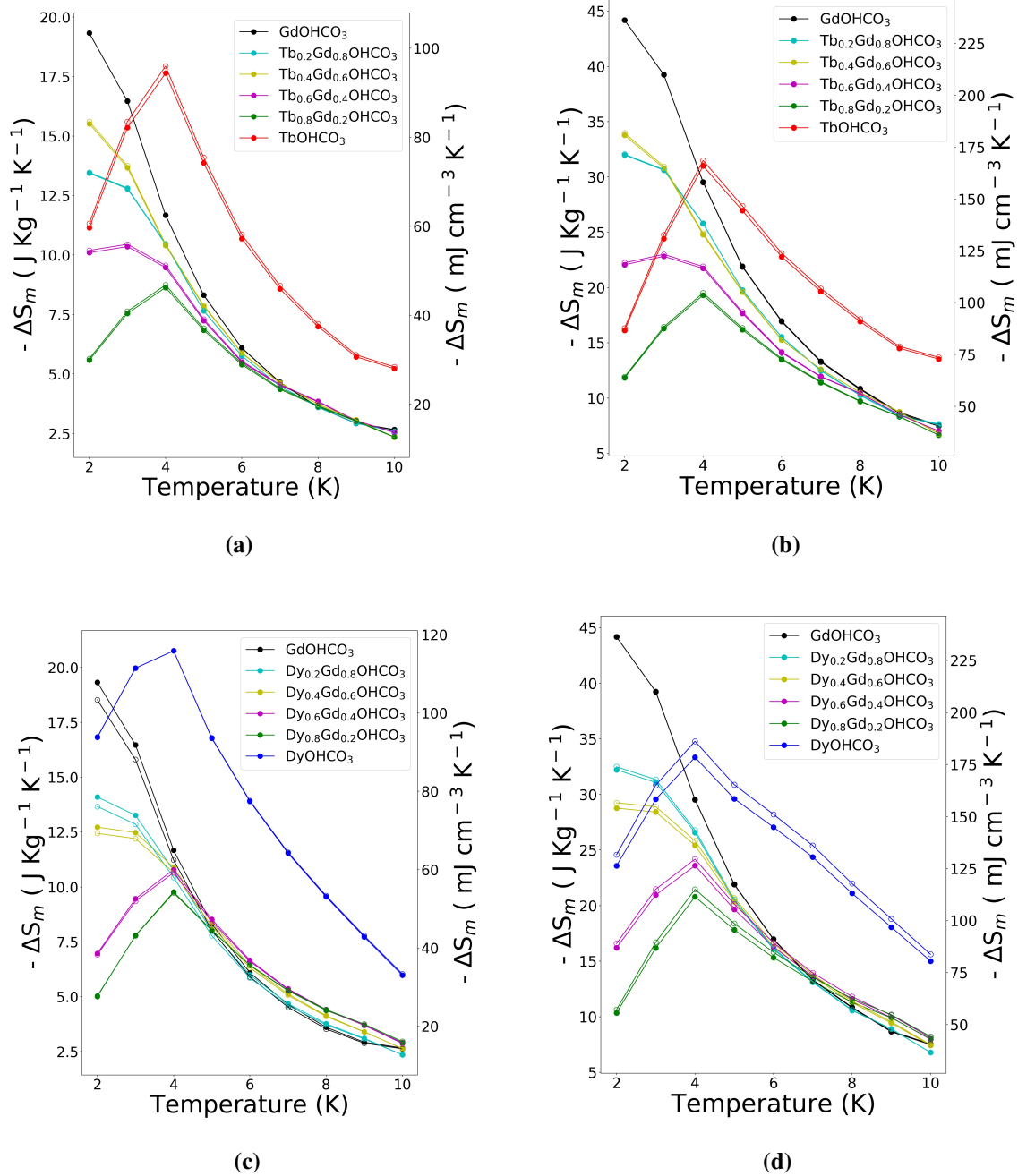
**Figure 3.5** The magnetocaloric effect of *Ln*OHCO$_3$ solid solutions for *Ln* = Tb/Gd for field changes of (a) 0-1 T, (b) 0-2 T and *Ln* = Dy/Gd for field changes of (c) 0-1 T and (d) 0-2 T. The filled and hollow symbols mark mass and volumetric units, respectively.

### 3.2.4 Magnetostructural Relationships

There are a number of structural differences between the *Ln*(HCO$_2$)$_3$ and *Ln*OHCO$_3$ frameworks that could lead to the observed differences in their magnetocaloric properties. Firstly, while the *Ln* cations in the *Ln*(HCO$_2$)$_3$ are in a highly symmetric 9 coordinate tricapped trigonal prism environment with 3*m* site symmetry; those in the *Ln*OHCO$_3$ structure have 1 site symmetry, which can be either viewed as a 10-coordinate environment or a highly distorted *Ln*O$_8$ square antiprism coordination environment, as shown in Figures 1.16 and 1.15. This difference may influence the magnetic anisotropy [187] and affect the relative ease with which the orbital angular momentum may partially align with the applied magnetic field, effecting the MCE observed. As discussed above the magnetisation of DyOHCO$_3$ is essentially saturated at 20 kOe at approximately 7 $\mu_B$ atom$^{-1}$, while the magnetisation of Dy(HCO$_2$)$_3$ increases relatively rapidly to about 5 $\mu_B$ atom$^{-1}$ by 20 kOe before increasing more slowly to just above 6 $\mu_B$ mole$^{-1}$ at 50 kOe, where it is far from saturation. [4] The magnetisation value observed for Dy(HCO$_2$)$_3$ at low applied fields is close to the expected contribution to the moment expected from a purely Ising ion (g$_J$J/2 = 5 $\mu_B$ atom$^{-1}$ for $f^9$ Dy$^{3+}$) while that observed for DyOHCO$_3$, as discussed above, is significantly higher than this but well short of that expected from a Heisenberg ion (g$_J$J = 10 $\mu_B$ atom$^{-1}$). This additional magnetisation in DyOHCO$_3$ at such low applied fields is unusual since Dy typically exhibits Ising anisotropy and is likely to further enhance its MCE properties. This could be interpreted as indicating the alignment of some fraction of the orbital angular momentum with the applied field although this typically requires a very strong field. [23]

Since Dy, which is a Kramer ion, responds very differently between the two series alternating between exhibiting MCE properties qualitatively similar to Gd(HCO$_2$)$_3$, which also contains a Kramers ion, and TbOHCO$_3$, which contains a non-Kramers ion, suggests Kramer ion effects do not primarily determine which systems have MCE maximised below or above 4 K. That Tb and Ho containing members of both *Ln*OHCO$_3$ and *Ln*(HCO$_2$)$_3$ have MCE optimised for use above 4 K may suggest non-Kramers ions more commonly have MCE of this type, although it is notable that, for example, A$_3$Ga$_5$O$_{12}$ (A = Tb or Ho) do not [112] so the relevance of this is far from clear.

Another factor that likely effects the magnetic properties of these two families of materials is the different ways in which the cations in their structures are connected, which will play a key role in their magnetic coupling. The structure of *Ln*(HCO$_2$)$_3$ can be readily simplified into face-sharing chains packed into a frustrated triangular lattice and it has been argued that the combination of ferromagnetic chains and magnetic frustration plays a key role in

the magnetocaloric properties of this family. [4, 18] In particular, the high magnetocaloric performance of Tb(HCO$_2$)$_3$ above 4 K in low applied magnetic fields has been attributed to the presence of ferromagnetic coupling within chains with complete magnetic order suppressed by the frustrated coupling between chains. [4, 18] Direct analysis of the magnetic interactions in the *Ln*OHCO$_3$ frameworks is, however, required to confirm to what extent their dominant magnetic interactions resemble the interactions in *Ln*OHCO$_3$ and whether additional interactions, such as through J$_4$ which couples neighbouring chains diagonally, modify this. Efforts to achieve this are described in detail in Chapters 5 and 6.

## 3.3 *Ln*F$_3$

The impressive magnetocaloric effect observed in GdF$_3$, as shown in Figure 3.1, and the success of improving the MCE efficiency through substitution of the Gd for other late lathanides (Tb-Er), inspired investigation of the MCE in the *Ln*F$_3$ materials. The simplicity and commercial availability, makes these materials ideal for industry.

### 3.3.1 *Ln*F$_3$ Crystal Structure

*Ln*F$_3$ (*Ln* = Gd, Tb, Dy, Ho and Er) were purchased from Fisher Scientific (Alfa-Aesar 99.99%) and were measured without any additional purification. With the exception of HoF$_3$ which was purchased as a 'crystalline lump', the samples were sold as fine powders. The samples were tested for quality and phase purity through powder X-ray diffraction of ground samples, using a Rigaku MiniFlex with Cu K$\alpha$ radiation and a zero-background silicon sample holder, between 10 and 70° at 300 K.

The *Ln*F$_3$ materials are isostructural, crystallising in the orthorhombic *Pnma* space group. Indexing of the diffraction patterns agrees that the reflections of these materials are from the *Pnma* space group. [73, 188] Le Bail refinements were performed on the diffraction patterns as seen in Figure A.5. These highlighted that GdF$_3$, TbF$_3$ and HoF$_3$ were phase pure, however DyF$_3$ and ErF$_3$ contained significant non-hydrated *Ln*(NO$_3$)$_3$ impurities, and DyF$_3$ also contained another unknown phase - shown by the un-indexed peak at $\approx$1.75 Å$^{-1}$. Only HoF$_3$ was highly crystalline, and the diffraction patterns of the other materials suffered from small particle sizes indicated by the broadening of the reflection, which were fit using an anisotropic peak broadening model. Limited attempts were made to purify and improve crystallinity the samples for several reasons. Firstly, recrystallisation of *Ln*F$_3$ is not possible without the use of concentrated HF, which was considered too risky considering the small

level of impurities involved. Secondly, the aim of this sub-study was to investigate the bulk magnetic properties and magnetocaloric effect between 2-10 K, of commercially available materials that could readily be deployed in a device.

## 3.3.2  Magnetic Properties of the *Ln*F$_3$

Field cooled (FC) and zero-field cooled (ZFC) magnetic susceptibility data of the *Ln*F$_3$ frameworks (*Ln* = Gd$^{3+}$, Tb$^{3+}$, Dy$^{3+}$, Ho$^{3+}$ and Er$^{3+}$) were measured in a 1000 Oe field from 2 K to 300 K. The magnetic susceptibility data for all *Ln*F$_3$ were found to obey Curie-Weiss law over between 100 - 300 K (see Figure A.6). Effective magnetic moments were found to be broadly consistent with the values expected for these trivalent lanthanides according to the Russell–Saunders coupling scheme [25] (see Table 3.4) calculated from mean field Curie-Weiss behaviour above 50 K, and extrapolated to lower temperatures. The Curie-Weiss temperatures of *Ln*F$_3$ = Tb-Er indicates predominantly antiferromagnetic interactions within these materials, although as for the *Ln*OHCO$_3$ phases this must be interpreted carefully due to a likely contribution from crystal field effects of the *Ln* cations at low temperatures. These results of the DyF$_3$ and ErF$_3$ materials must be considered tentatively, due to the presence of nitrate impurities.

**Table 3.4** Summary of Curie-Weiss temperatures and magnetic moments for lanthanides in *Ln*F$_3$.

| *Ln* | $\theta_{CW}$ (K) | Curie Constant (emu mol$^{-1}$ Oe$^{-1}$) | Magnetic Moment ($\mu_B$) |
|------|-------------------|-------------------------------------------|---------------------------|
| Gd | 0.1293(16) | 7.3132(18) | 7.6474(9) |
| Tb | 0.898(24) | 9.84(5) | 8.870(22) |
| Dy | −1.440(31) | 11.62(6) | 9.639(25) |
| Ho | −1.05(6) | 14.43(16) | 10.74(6) |
| Er | −3.97(8) | 9.78(8) | 8.845(34) |

GdF$_3$, DyF$_3$ and ErF$_3$ did not show any indication of deviation from purely paramagnetic behaviour down to 2 K. In contrast TbF$_3$ and HoF$_3$ showed some behaviour in their low temperature magnetic properties that suggest some deviation from pure paramagnetism. In HoF$_3$ there is a small divergence in magnetic susceptibility measurements between zero field-cooled and field-cooled measurements, below 100 K, which may reflect limited weak ferromagnetic order or be an instrumental artefact (see Figure 3.6a). While the latter is more likely, if the former this indicates the presence of some correlations to such high temperatures, despite no long range order forming indicates there are some strong interactions in HoF$_3$. In contrast TbF$_3$ was found to deviate from Curie-Weiss law below 2.9 K with $\chi_M T$ also

increasingly rapidly at low temperature, with a maximum observed at 2.9 K (see Figure 3.6b). A weak divergence of ZFC and FC magnetic susceptibility is also observed at this temperature so this likely reflects the onset of long range antiferromagnetic order.



(a)                                                                          (b)
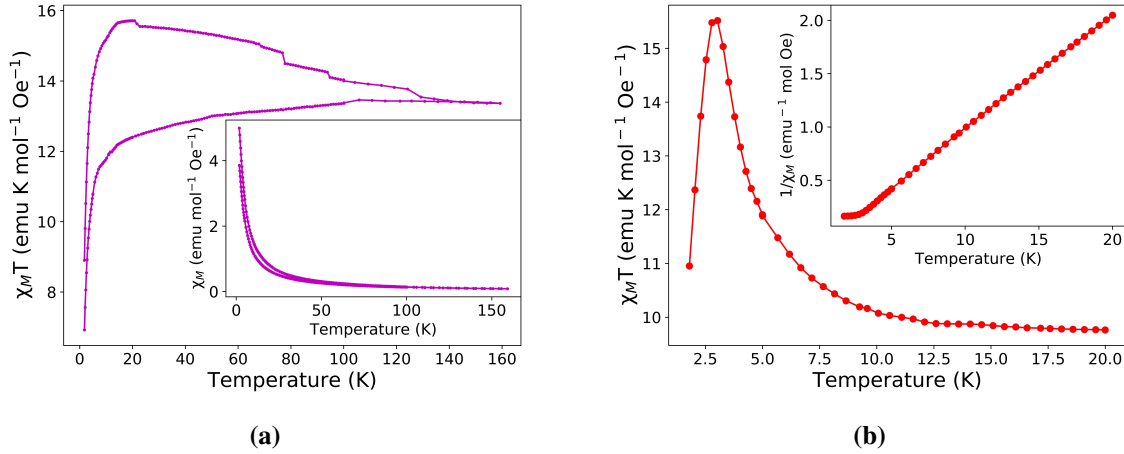
**Figure 3.6** $\chi_M T$ data for (a) HoF$_3$, with magnetic susceptibility shown in the insert and (b) $\chi_M T$ data for TbF$_3$, with inverse magnetic susceptibility shown in the insert.

Isothermal magnetisation measurements on the *Ln*F$_3$ frameworks measured at 2 K (see Figure 3.7) reveal that only GdF$_3$ which has magnetisation consistent with a Heisenberg spin, that which approaches 7 $\mu_B$ under high applied magnetic fields.

In contrast TbF$_3$, DyF$_3$ and ErF$_3$ all show saturations values close to that of g$_J$J/2 expected for purely Ising anisotropy, [33, 34, 184, 185] and materials with large spin-orbit coupling. Finally, HoF$_3$ shows a saturation value close, but noticeable exceeding, the limit expected for the magnetic cations in an Ising case suggesting other contributions to the magnetic observed saturation value. This is analogous to the effect we have reported in DyOHCO$_3$, where the saturation value indicates Ising like anisotropy but greater, which showed the largest magnetocaloric effect out of the *Ln*OHCO$_3$. The magnetisation of GdF$_3$, TbF$_3$ and HoF$_3$ show a steep rise in magnetisation with all nearing plateau below 2 T.

### 3.3.3   Magnetocaloric effect of the *Ln*F$_3$

Magnetic entropy changes, $\Delta S_m$, were calculated using the Maxwell relation between 2 and 10 K, and for field changes between 0 and 1-5 T (see Figures 3.8 and 3.9 for magnetocaloric effect plots). As expected from other lanthanide magnetocaloric materials, the previously reported GdF$_3$ is observed to have the greatest $-\Delta S_m^{max}$ at 2 K, particularly in multiple tesla magnetic fields. For moderate field changes of less than 2 T TbF$_3$ and HoF$_3$ are found
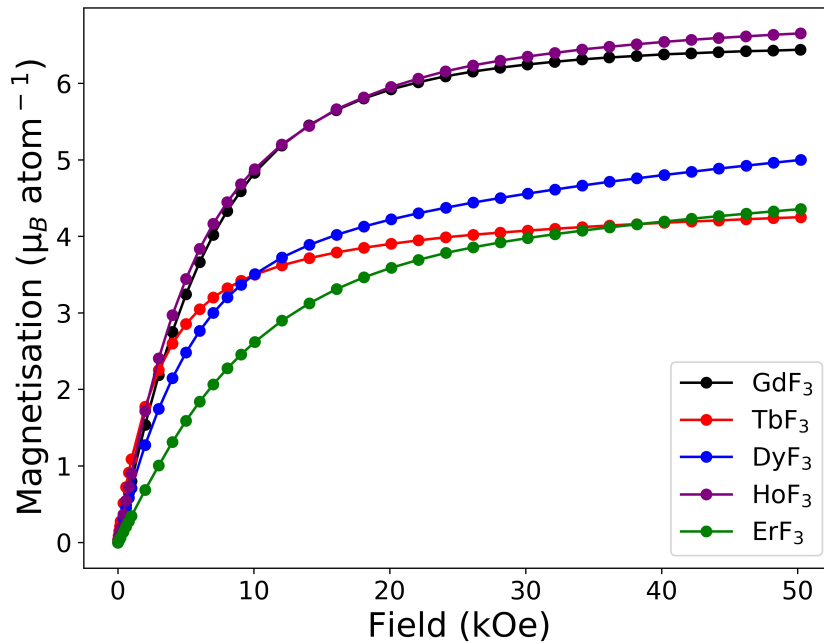
**Figure 3.7** Isothermal magnetisation measurements on the *Ln*F$_3$ frameworks measured at 2 K.

to perform well with $-\Delta S_m^{max}$ at 4 K , with HoF$_3$ outperforming GdF$_3$ above 5 K with a very gradual decrease that suggests this differential will increase significantly at higher temperatures.

The almost linear response of the magnetocaloric effect with respect to temperature in these initial studies inspired further investigation into the magnetocaloric effect of HoF$_3$ to higher temperatures. As shown in Figures 3.10 these enable the magnetocaloric entropy change for HoF$_3$ to be calculated up to 25 K.
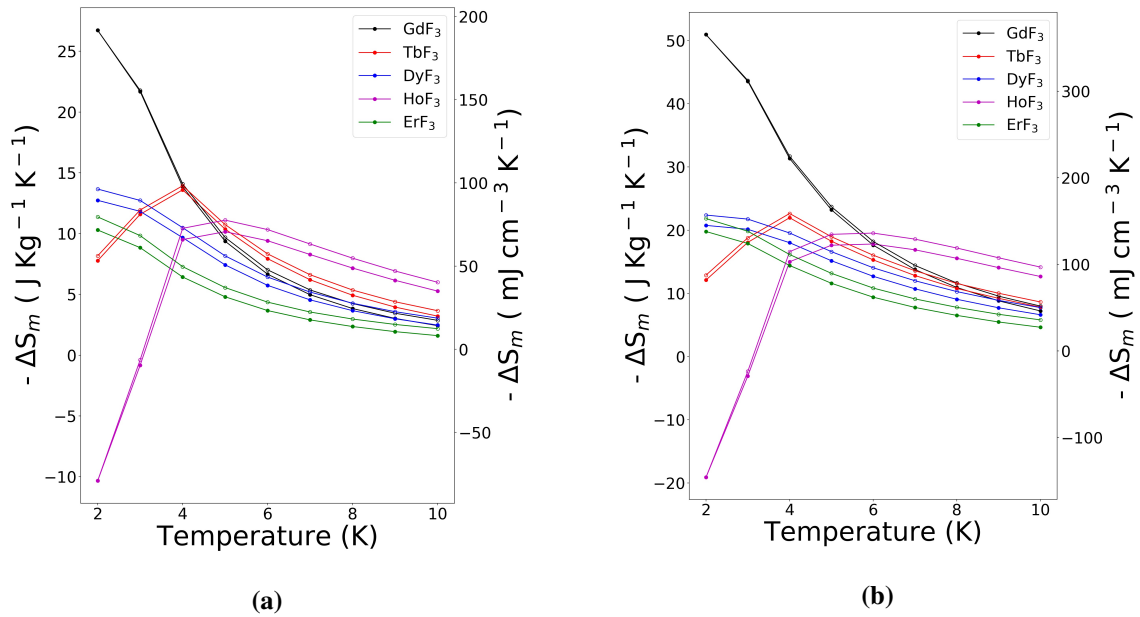
**Figure 3.8** The magnetocaloric effect of the late *Ln*F₃ frameworks for field changes of (a) 0-1 T, (b) 0-2 T. The filled and hollow symbols mark mass and volumetric units, respectively.
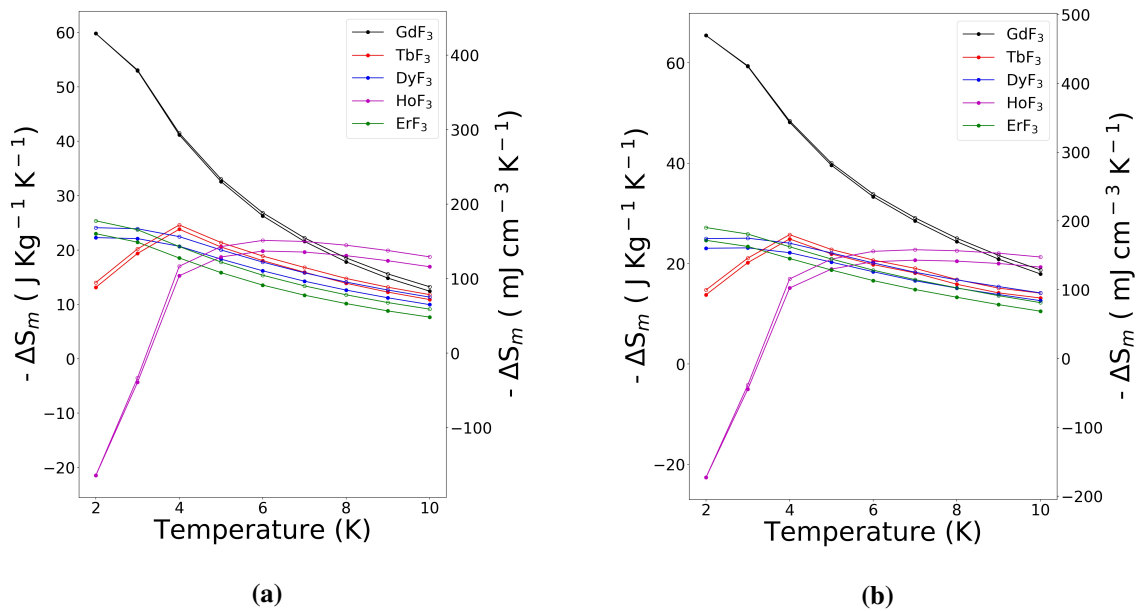


**Figure 3.9** The magnetocaloric effect of the late *Ln*F₃ frameworks for field changes of (a) 0-3 T, (b) 0-5 T. The filled and hollow symbols mark mass and volumetric units, respectively.
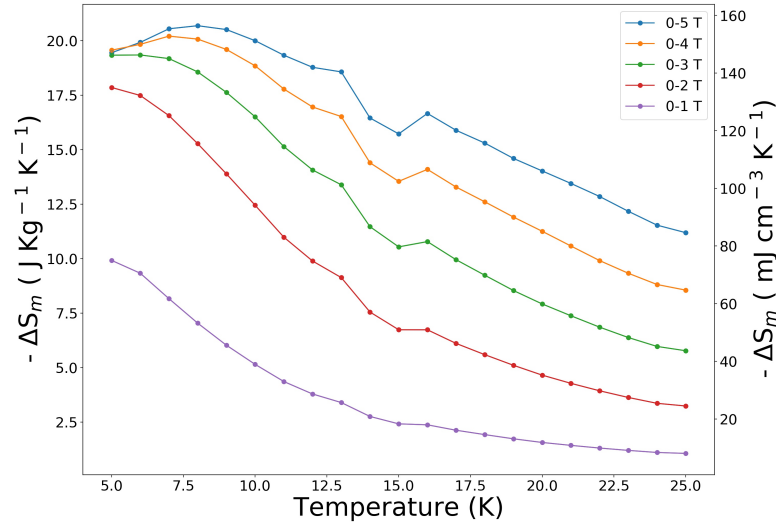
**Figure 3.10** The magnetocaloric effect of HoF$_3$ between 5-25 K for field changes of 0-(1-5) T.

A summary of the peak MCE temperatures of all the $Ln$F$_3$ is given in Table 3.5, showing the temperatures at which the MCE peaks in both mass and volumetric units, with regards to the performance above 4 K. In comparison to the $Ln$OHCO$_3$ in mass units, the $Ln$OHCO$_3$ phases outperform the $Ln$F$_3$ phases, important in applications where low mass is crucial but low volume is less necessary, when comparing HoF$_3$ to DyOHCO$_3$, the compounds with the best high temperature performance in each family. Due to the high density of the $Ln$F$_3$ materials HoF$_3$ outperforms DyOHCO$_3$, when comparing volumetric units, above 8 K. [5, 77] However, DyOHCO$_3$ has a peak performance greater than that of HoF$_3$ (186 and 136 mJ cm$^{-3}$ K$^{-1}$ at 2-0 T field change), and when compared in mass units DyOHCO$_3$ outperforms HoF$_3$ up to the highest measured temperature.

Perhaps more notably $-\Delta S_m$ becomes negative in HoF$_3$ at 2 and 3 K, which from the Maxwell relation can be interpreted as indicating a decrease in magnetisation with decreasing temperature, consistent with the material being close to a transition to an antiferromagnetic state. A secondary interesting feature of HoF$_3$, in contrast to other materials discussed in this thesis, is the field change dependence of the peak temperature of the magnetocaloric effect. It appears that with larger changes in magnetic field the temperature at which the magnetocaloric effect peaks increases significantly. Large changes in entropy are observed in both HoF$_3$ and DyOHCO$_3$ above 4 K, and these materials also display magnetisation saturations larger than for purely Ising spins. The effect contributing to this may be from

**Table 3.5** Summary of the peak MCE ($\Delta S_m^{max}$) at peak temperatures (T$_{max}$ (K)) of the studied *Ln*F$_3$ at different field changes. Mass refers to changes in entropy per mass in units of J Kg$^{-1}$ K$^{-1}$ and volume refers to change in entropy per volume in units of mJ cm$^{-3}$ K$^{-1}$.

| | $\Delta\mu_0$H= 1-0 T | | | $\Delta\mu_0$H = 2-0 T | | | $\Delta\mu_0$H = 5-0 T | | |
|---|---|---|---|---|---|---|---|---|---|
| *Ln* | T$_{max}$ | Mass | Volume | T$_{max}$ | Mass | Volume | T$_{max}$ | Mass | Volume |
| Gd | 2 | 26.72 | 191.69 | 2 | 50.94 | 365.45 | 2 | 69.13 | 495.95 |
| Tb | 4 | 13.59 | 98.27 | 4 | 21.96 | 158.75 | 4 | 25.65 | 185.40 |
| Dy | 2 | 12.73 | 96.30 | 2 | 20.75 | 156.94 | 3 | 23.75 | 179.64 |
| Ho | 5 | 10.15 | 77.62 | 6 | 17.80 | 136.12 | 8 | 21.22 | 162.25 |
| Er | 2 | 10.29 | 79.55 | 2 | 19.78 | 152.89 | 2 | 25.51 | 197.19 |

a orbital contribution but also anisotropy that does not quite behave fully Ising. This is still unclear and inelastic neutron spectroscopy data would provide suitable understanding. An anomalous reduction in the magnetocaloric effect is observed in HoF$_3$, in higher fields changes at 14 and 15 K, which is not due to any experimental errors or temperature excursions. This may indicate the onset of some partial ordering of the magnetic moments in higher applied magnetic fields that is only present over a narrow temperature/field range.

HoF$_3$ has interesting properties compared to GGG and DGG. For $\Delta\mu_0$H = 2-0 T GGG has a $\Delta S_m^{max}$ = 17.7 J Kg$^{-1}$ K$^{-1}$ or 145 mJ cm$^{-3}$ K$^{-1}$ at 1.2 K [77] and DGG has a $-\Delta S_m^{max}$ = 11.64 J Kg$^{-1}$ K$^{-1}$ or 95 mJ cm$^{-3}$ K$^{-1}$ at 1.2 K [71, 112] HoF$_3$ provides an entropy change of 17.80 J Kg$^{-1}$ K$^{-1}$ or 136.12 mJ cm$^{-3}$ K$^{-1}$ at 5 K for the same field change and even at 12 and 16 K has entropy changes greater than 10 J Kg$^{-1}$ K$^{-1}$ or 50 mJ cm$^{-3}$ K$^{-1}$, respectively. This gives commercially available HoF$_3$ a potential use for magnetic refrigeration over a wide temperature. The large magnetocaloric effect in these materials is partly due to the high density of the *Ln*F$_3$ (7.6441(20) g cm$^{-3}$ for HoF$_3$ at 300 K), and the large magnetic entropy of the *Ln* ions coupled with rapidly increasing magnetisation at low applied magnetic fields.

The performance of the Ising *Ln*OHCO$_3$ phases is generally superior to the Ising *Ln*F$_3$ phases so our studies attempting to relate the magnetic interactions to their magnetocaloric properties will generally focus on the former. We will attempt to draw some conclusions here about why TbF$_3$ and HoF$_3$ may exhibit MCE values that peak at higher temperatures, from knowledge drawn from existing studies. Figure 3.11 shows the nuclear structure of the *Ln*F$_3$ and the face-sharing chains of *Ln*$^{3+}$ cations that extend along the *a*-axis.
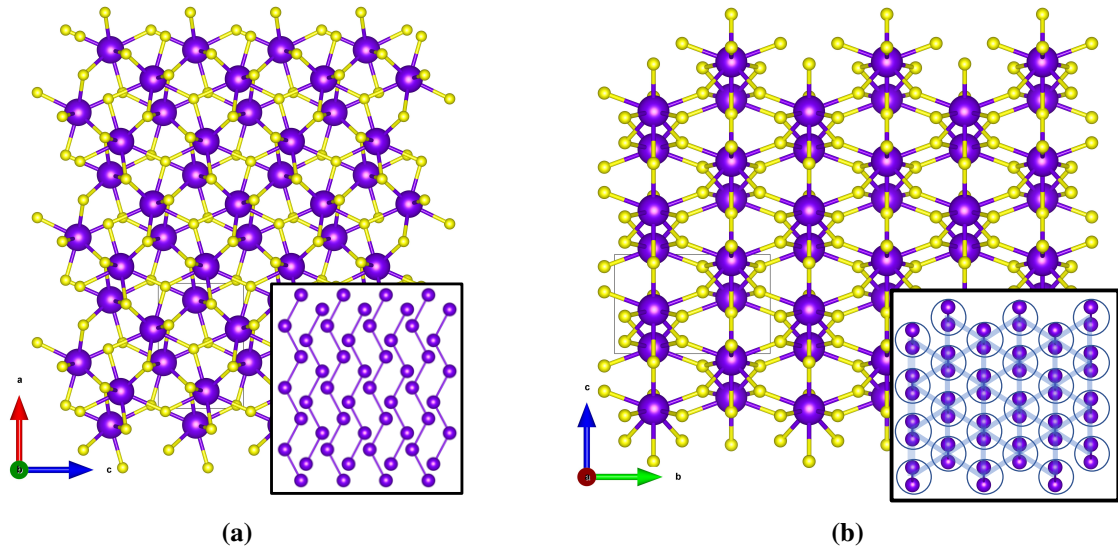
**Figure 3.11** Structure of the *Ln*F$_3$, with the *Ln*$^{3+}$ cations shown in purple, and fluoride anions shown in yellow. The unit cell is shown in black. (a) The structure shown along the *b*-axis, with the nearest neighbour interactions in the insert, displaying the buckled chains present in the structure. (b) Structure shown along the *a*-axis, looking down the buckled chains. The triangular motifs are shown in the insert, consisting of next-nearest neighbour interactions. The chains are circled for clarity.

Early neutron studies of HoF$_3$ determined a canted antiferromagnetic structure at $T_N = 0.53$ K, with moments oriented along the buckled chains, towards the nearest neighbour. [189, 190] Allowing for this spin canting coupling within the face-sharing chains is ferromagnetic and, by comparison to the magnetocaloric properties of Tb(HCO$_2$)$_3$ it is possible, that these may also contribute to the magnetocaloric properties of HoF$_3$ if they persist locally to high temperatures.

Studies of TbF$_3$ have determined the presence of an incommensurate antiferromagnetic structure below $T_N = 3.97$ K possibly induced from magnetic frustration, formed of Ising spins in ferromagnetic chains. [191, 192] The discrepancy between our $T_N$ from magnetic susceptibility measurements and $T_N$ from this may be related to the poorer degree of crystallinity of the commercially available sample used for our study. Moments in TbF$_3$ are primarily oriented along the *a*-axis with similar spin vectors as the HoF$_3$ structure. [188–191]

TbF$_3$ and HoF$_3$ show similar magnetic structures at low temperatures, and have the largest magnetocaloric effect in low applied fields, which suggests the relative strength of the magnetic interactions within these materials may play a role in their magnetocaloric performance. From these early studies, the magnetic moment of HoF$_3$ was determined to be 5.7(2) $\mu_B$ at 70 mK for Ho$^{3+}$, far below the expected 10 $\mu_B$ for a fully ordered moment. This is indicating

there is still significant disorder within this system at 70 mK well below the $T_N = 0.53$ K.
The disorder in $HoF_3$ and the incommensurate phase in $TbF_3$ can be ascribed to competing
interactions, if we assume that all neighbouring interactions are antiferromagnetic within the
triangles (Figure 3.11b), which would be consistent with the antiferromagnetic ground state.
It is therefore possible that the combination of ferromagnetic chains and magnetic frustration
may be linked their MCE properties. In contrast $ErF_3$ has been reported to develop long
range magnetic order at $T_N = 1.05(3)$ K, but differs to that seen in $TbF_3$ and $HoF_3$. [193]
The magnetic moments in $ErF_3$ are oriented primarily along the $c$-axis, with a magnitude of
6.7 $\mu_B$ closer to that of a fully ordered $Er^{3+}$ ion. This indicates that the simple presence of
magnetic order below the paramagnetic magnetocaloric operating temperatures is not suffi-
cient to improve the magnetocaloric performance, but that the magnetostructural-property
relationship plays an important role. These early studies do not show full diffraction patterns,
which is unfortunate as it prevents examining these for any indication of magnetic diffuse
scattering although by the same token this may not have been clearly visible on the diffrac-
tometers available 30 years ago. [84] With the increase of $Q$ range and resolution of modern
instruments, it would be wise to revisit the magnetic structure determination of $HoF_3$ and
$TbF_3$, below these transition temperatures and near in search of short range order.

From the survey of the literature above we can speculate that the efficient magnetocaloric
effect of $TbF_3$ and $HoF_3$ may be due to the presence of ferromagnetic Ising chains observed in
these materials. Therefore, large changes in entropy are induced by small changes in magnetic
field as the chains are readily aligned in them. At temperatures where the magnetocaloric
effect has been measured, it is possible that these ferromagnetic interactions are still present,
and beneficial to the magnetocaloric effect, as observed in other materials. [4, 17, 18,
194]

## 3.4   Conclusions

The magnetic properties of the $Ln$OHCO$_3$ frameworks have been characterized with a focus
on the magnetocaloric properties of the later lanthanides between Tb and Er. We find that
$TbOHCO_3$ and $DyOHCO_3$ are exceptional MCE materials above 4 K, both surpassing the
peak MCE of the benchmark magnetic cooler $Gd_3Ga_5O_{12}$ (GGG) observed at much lower
temperature in the lower applied fields accessible using permanent magnets; [74] $DyOHCO_3$
is particularly promising having the highest performance in the 4-10 K temperature range.
Doping of $Gd^{3+}$ into $TbOHCO_3$ or $DyOHCO_3$ has also been explored and while good

stoichiometric control has been achieved this does not result in improved MCE, in contrast with the $Ln$(HCO$_2$)$_3$ frameworks. [4] These results highlight that the MCE is not only determined by the magnetic ion, but that structural and ligand field effects can contribute greatly to this behaviour.

Magnetic properties of the $Ln$F$_3$ are equally interesting yielding large changes in volumetric entropy at temperatures above 2 K. Amongst these materials HoF$_3$ exhibits the best magnetocaloric entropy change above 4 K under modest applied magnetic fields. While generally inferior to the $Ln$OHCO$_3$ phases this compare well to the benchmark $Ln_3$Ga$_5$O$_{12}$ series, particularly with regards to the retention of performance above 10 K. Examining how the magnetocaloric performance of these materials relate to the magnetic interactions within them requires the analysis of these materials using modern neutron scattering. The subsequent chapters in this thesis will focus on precisely this sort of analysis, starting with the $Ln$(HCO$_2$)$_3$ phases that had already been reported to have enhanced magnetocaloric properties above 4 K for low applied field changes and then moving onto the $Ln$OHCO$_3$ phases, which have the best physical properties reported in this work. Equivalent studies for the $Ln$F$_3$ phases would also be desirable, particularly in the case of HoF$_3$ but this has not been prioritised in this work due to the superiority properties of the $Ln$OHCO$_3$ phases.

# 4

# Magnetic Structure and Correlations of the *Ln*(DCO$_2$)$_3$ Frameworks

## 4.1   Introduction

Several frameworks were recently reported to have magnetocaloric effects comparable or superior to that of the benchmark magnetocaloric material Gd$_3$Ga$_5$O$_{12}$ below 10 K. [62] It is key to explore the performance of magnetocalorics in this temperature range to optimise their potential for use as solid state refrigeration devices that can replace the expensive and non-renewable liquid helium refrigeration. [60] In light of the promising magnetocaloric properties of Gd(HCO$_2$)$_3$, [62] the other isostructural heavy lanthanide formate frameworks were investigated. This revealed the superior magnetocaloric entropy change of Tb(HCO$_2$)$_3$ and Ho(HCO$_2$)$_3$ frameworks in low applied magnetic fields above 4 K compared to Gd(HCO$_2$)$_3$, unusual for materials with lower total theoretical magnetic entropy. [4] It was found that short range order was present in the temperatures at which Tb(HCO$_2$)$_3$ performed most efficiently, consisting of 1D ferromagnetic correlations within its face-sharing chains, as shown in Figure 1.15. At ≈1.6 K Tb(HCO$_2$)$_3$ was found to form quasi-long range order, consisting of 1D ferromagnetic correlations within its face-sharing chains. [4, 18] Inspired by the connection between promising magnetocaloric properties and interesting magnetic correlations in Tb(HCO$_2$)$_3$ this and other *Ln*(HCO$_2$)$_3$ have been furthered investigated for the presence of any short and long-range magnetic order in and if present, determine the link between it and the magnetocaloric effect. This includes the first neutron scattering studies of these materials below 1 K.

## 4.2 Tb(HCO$_2$)$_3$

### 4.2.1 Physical Property Measurements

It has previously been reported that the *Ln*(HCO$_2$)$_3$ frameworks do not show any indication of long range order down to 2 K, and follow Curie-Weiss behaviour, with Weiss temperatures of $-0.6$ K, $-0.9$ K, $-6.1$ K, $-10.3$ K and $-16.0$ K, for *Ln* = Gd–Er. [4] Since neutron diffraction measurements indicated the emergence of magnetic order in Tb(HCO$_2$)$_3$ at 1.6 K we have probed the physical properties down to 0.4 K to identify the effect this order has on it's physical properties. Zero-field cooled (ZFC) magnetic susceptibility data for Tb(HCO$_2$)$_3$ shows indications of magnetic transitions at $\approx$1.6 K and $\approx$0.5 K, (see Figure 4.1). Heat capacity measurements shown in Figures 4.1b and A.7 show a have a large peak in 1.68 K for zero applied field, this is suppressed in applied fields consistent with the onset of a magnetic transition. Despite the small change in susceptibility, associated with the TIA transition, the signal in heat capacity is much more significant. Both of these features are consistent with the emergence of the TIA, as a transition to a long range 1D order would result in a large entropy change, while the strong short range antiferromagnetic coupling of the chains would prevent any great change in magnetic susceptibility. It is also possible that the signal at 1.6 K is an experimental artefact from the MPMS switching between high and low temperature modes. A clearer transition can be seen at $\approx$0.5 K indicating more complete, possibly long-range antiferromagnetic order. [4, 18] A second large change in the heat capacity is observed below 600 mK, this may be the onset of long-range order but could also be the onset of a hyperfine Schottky anomaly.



(a)



(b)
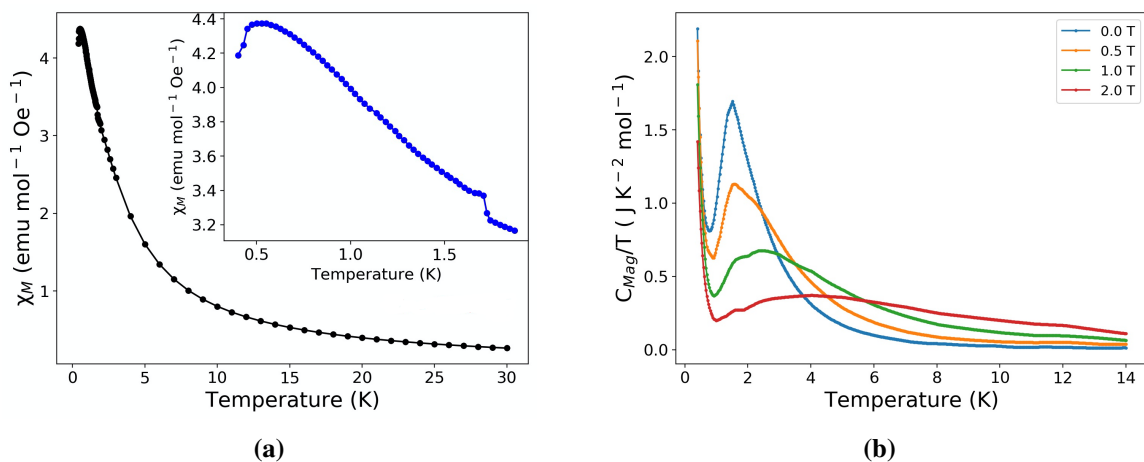
**Figure 4.1** Magnetic measurements of Tb(HCO$_2$)$_3$. (a) Magnetic susceptibility in 100 Oe field below 30 K, close up below 1.6 K in insert, (b) C$_{mag}$/T in variable fields between 400 mK and 14 K.

The broad feature in the heat capacity is sometimes ascribed to the Schottky anomaly, [195] however this would indicate an onset of this phenomenon at temperatures far too high for either nuclear or electronic Schottky, and responds too strongly to an applied magnetic field. It is therefore likely this feature is caused by the short range magnetic order we see developing in the neutron diffraction data, as indicated by magnetic diffuse scattering. [4, 18] However, 1D magnetism can give rise to the emergence of solitons, as seen in CsNiF$_3$. [196, 197] The broad feature of this heat capacity feature may arise due to the presence of these solitons, [198] which can be calculated with a sine-Gordon model, [199] but testing this hypothesis is beyond the scope of this study.

Magnetisation data were measured at variable temperatures below and above the ordering temperatures detemined from susceptibility and heat capacity data. Magnetisation curves measured at 0.5 K, 1.5 K and 2 K are virtually identical and approach saturation around 1 T (see Figure 4.2), the value observed is up to >95 % of the $g_J J/2$ value expected for Ising anisotropic spins, as seen in the previous RMC studies. [4, 18] This highlights the ease of magnetisation in low applied field, in agreement with the magnetocaloric abilities of this compound in low applied magnetic field. A further gradual linear increase with applied fields above 3 T observed is consistent with the onset of Van Vleck paramagnetism, [183] due to field induced electronic transitions. [200, 201] The similarities of the magnetisation curves above and below the transition temperatures suggests that if antiferromagnetic order does emerge at low temperature it is unlikely to be a conventional long range magnetic state.
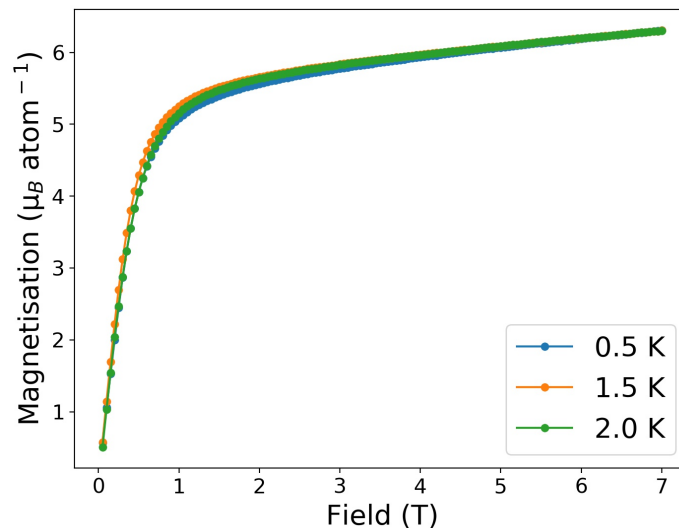


**Figure 4.2** Magnetisation measurements of Tb(HCO$_2$)$_3$ between 0-7 T, at variable temperatures.

## 4.2.2 Emergent Charge Order (ECO)

Consistent with the previous studies by Saines *et al.*, [4, 18, 202] upon cooling below 1.6 K the neutron diffraction measurements performed on Tb(DCO$_2$)$_3$ show the appearance of extra reflections ascribable to the development of long range magnetic ordering albeit these features are much broader than the instrumental resolution. This can be appreciated from the broad peak observed around 9 Å (Figure 4.3b). If treated as conventional crystallographic magnetic order, as previously established, [4, 202] the extra reflections can be indexed with a propagation vector $\mathbf{k}_1 = [0,0,1]$ belonging to the LD line $(00\gamma)$ of the first Brillouin zone (BZ). The quantitative Rietveld refinement agrees with the $P3m'1$ magnetic space group corresponding to the mLD2LE2 irreducible representation with order parameter $(\xi_1,\xi_2)$ as previously reported. [4] The group subgroup relationship, as shown in Figure 4.4, is in agreement with Landau theory, demonstrating this magnetic structure can be formed of a single irreducible representation.



(a)  (b)  (c)
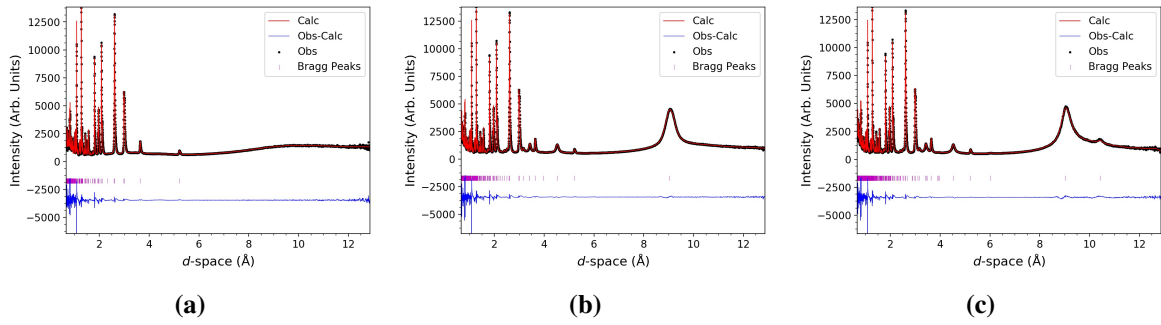
**Figure 4.3** Rietveld fits to neutron diffraction patterns of Tb(DCO$_2$)$_3$ at variable temperatures from bank 2 and 9 of WISH along with the fitting statistics (a) 1.7 K, $R_p$ = 6.45 %, $R_{wp}$ = 5.27 % (b) 1.2 K, $R_p$ = 6.51 %, $R_{wp}$ = 5.44 % (c) 0.28 K, $R_p$ = 6.58 %, $R_{wp}$ = 5.41%.

It is worth underlining that the observed propagation vector does not correspond to a special point of the BZ and the $\gamma$ value can, in principle, be incommensurate. The broad nature of the diffraction peaks does not allow us to determine with absolute certainty that the propagation vector is locked to the commensurate [0,0,1] value. Nevertheless the comparison with similar systems in the literature and the good refinement of the diffraction data with the commensurate value let us to conclude that the real propagation vector is likely to be $\gamma$=1, as previously reported. [4] The spin ordering can be described two different global phases. One of these resembles a partially disordered antiferromagnet (PDA) in which each of the triangles has one chain ordered up, one down, and the third remaining disordered $(\pi/4)$. The other up-down-down model contains one TbO$_9$ chain ordered up, and two down with the latter having half the magnetic moment of the former $(\pi/6)$. [4, 202] The two
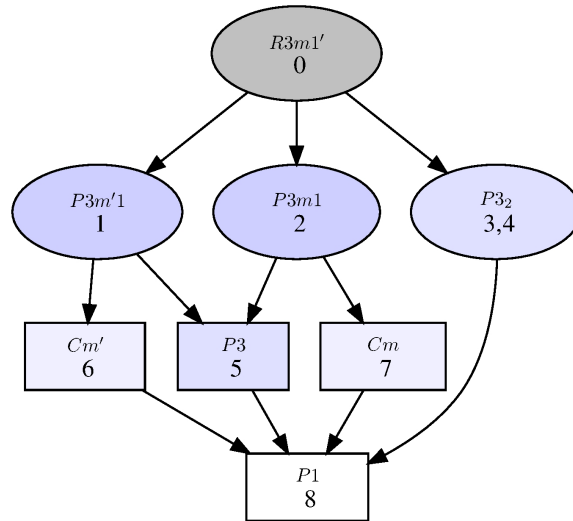
**Figure 4.4** Group subgroup relationship of *Ln*(DCO$_2$)$_3$ for the **k**-vector = [0,0,1]. Generated using the Bilbao Crystallographic Server.

descriptions for the magnetic structure cannot be distinguished between, as they only vary in the phase ($\pi/4$ and $\pi/6$), which diffraction is not sensitive to. It should be emphasized that, as reported previously [4, 18] both of these possibilities are conventional crystallographic approximations of the TIA, which only has long range 1D order in the chains, and which is able to not only explain the Bragg-like reflections in this material but also the underlying magnetic diffuse scattering.

Patterns collected below 1.2 K revealed the presence of additional broad reflections at high *d*-spacing, the most significant Bragg-like peak can be seen at $\approx$10.5 Å (see Figure 4.3c). The broad nature of these features, comparable to those associated with the TIA phase and the retention of the diffuse scattering suggest these are also associated with a state that lacks conventional crystallographic order. We have, however, treated them with conventional crystallographic approaches, as in the absence of clearly established prediction of the scattering as established for the TIA, [78, 152, 153] we cannot completely exclude that the peak broadening is not a result of small magnetic domains. The peak width was fit with an anisotropic peak broadening model, and the broadening is an indication of a finite correlation length. When the diffuse Bragg-like peak (7.85-9.37 Å or 0.80 to 0.67 Å$^{-1}$) with a Warren-like peak shape function, [203, 204] the correlation length, considered to be associated with correlations in the *ab* plane, was found to be $\approx$52 Å (see Figure 4.5 for quality of fit).
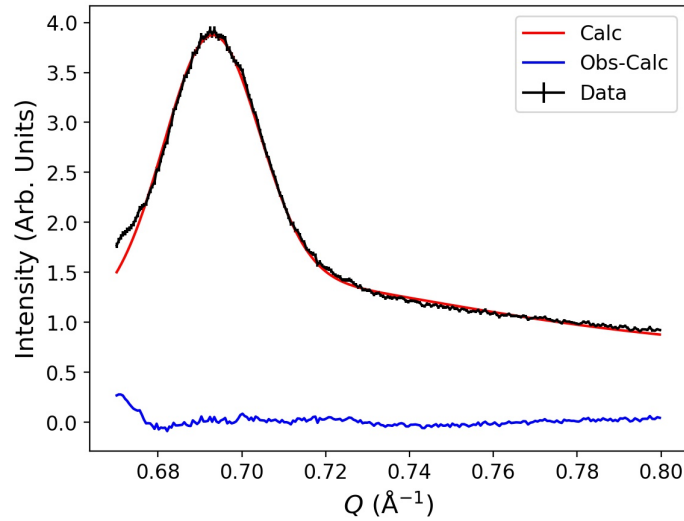
**Figure 4.5** Warren fit to the diffuse Bragg-like peak of the TIA phase of Tb(DCO$_2$)$_3$ with the experimental data shown in black, the fit shown in red, and the difference shown in blue.

We observed no reduction in the width of the magnetic peaks upon cooling below 1.6 K indicating the magnetic correlation length remains unchanged. These extra reflections can be indexed to a supercell violating the parent rhombohedral symmetry and doubled along the *b*-axis with a $\mathbf{k}_2$-vector = [0,0.5,1] corresponding to F point of the BZ and associated with the mF2 mode. These new reflections here have been interpreted as an additional component of the magnetic structure, but the possibility of magnetic phase separation in the material cannot be completely excluded. The lack of intensity on the satellites of the *00l* reflections indicate that the moment remains along the *c*-axis only, in agreement with the Ising character of the Tb spins.

Using ISODISTORT [161] we have found that the low temperature magnetic phase can be described in the *Pm'* space group in which there are six independent Tb sites with moments dependant on the global phase, with the lattice parameters *a* = 3.96860(13) Å, *b* = 10.42077(15) Å, *c* = 18.0493(3) Å as shown in Figure 4.6. Since the structure factors are insensitive to the choice of the global phase, it is not possible to distinguish between the two structures from the neutron diffraction alone. In agreement with Landau theory the combination of the two $\mathbf{k}$-vectors acting on this material allows for a continuous transition to the *Pm'* space group with a single irreducible representation, as shown in the graph of subgroups - Figure 4.7.

**(a)** **(b)**
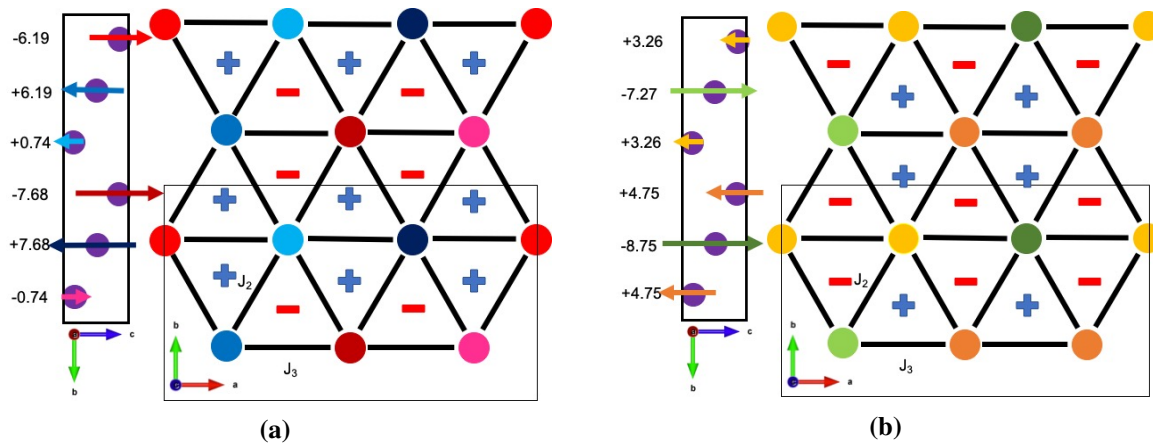
**Figure 4.6** Tb(DCO$_2$)$_3$ two possible magnetic average structure solutions at 0.28 K. Unit cell shown as black box with magnetic moments in *Pm'* space group. The spin charges are shown as minus and plus signs. $J_2$ and $J_3$ are shown next to the corresponding interaction and $J_1$ not shown, goes into the plane. On the right of each figure is shown the projection of the structure in the *ab* plane and on the left of each figure the *bc* plane. Magnetic moments colour coded, but not to scale. (a) Global phase = $\pi/4$ (b) Global phase = $\pi/6$.
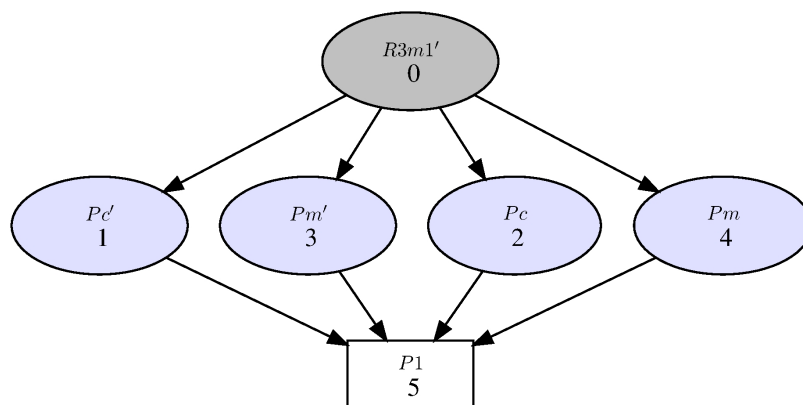


**Figure 4.7** Group subgroup relationship of *Ln*(DCO$_2$)$_3$ for the **k**$_1$-vector = [0,0.5,1] and **k**$_2$ = [0,0,1]. Generated using the Bilbao Crystallographic Server.

As can be seen in Figure 4.6 the solution with global phase $\pi/4$ results in a modification of the PDA structure in which the $\mathbf{k}_2$ propagation modulates the moment in the chains resulting in pairs of large moment Tb chains ($\pm7.68(3)$ $\mu_B$ and $\pm6.19(3)$ $\mu_B$) antiferromagnetically coupled to each other and separated from other pairs by a chain with a small moment ($\pm0.74(3)$ $\mu_B$). For the high temperature magnetic structure this phase choice gives a partially disordered antiferromagnet solution closest to the TIA model proposed, [18] and therefore is our preferred model. The $\pi/6$ solution, is a slight modification of the up $\frac{1}{2}$down $\frac{1}{2}$down structure on a triangular lattice in which the moments are modulated along the $b$-axis of the parent structure. [202] This phase choice gives the most symmetric solution with the less spread of the Tb moment size with refined lengths of 4.75(3), 7.27(3), 8.75(4) and 3.26(3) $\mu_B$.

Both solutions find the moments on each triangle sum to be $\pm0.75$ $\mu_B$, which arrange into an emergent antiferromagnetic-like state, absent from nearest neighbour interactions alone. This is analogous to the emergent charge order observed in the kagome ECO states, [81, 205] which has two observed experimental signatures; non-zero entropy and the presence of magnetic diffuse scattering and Bragg-like peaks in the neutron diffraction measurements. [206] Such exotic magnetic states are elusive and have so far only been reported in oxide materials. Based on observing similar features this may be the first example of such a state present in a MOF. The emergence of antiferromagnetic order, associated with $\mathbf{k}_2$, is consistent with the observation of antiferromagnetic-like transitions in the physical property data. The magnetic scattering associated with the emergent order does suggest that the 1D order of the TIA phase is retained in this lower temperature phase and together with the magnetisation behaviour suggests that this is not a conventional antiferromagnetic state.

The evolution of the magnetic moments, with respect to temperature, associated with the two $\mathbf{k}$-vectors is shown in Figure 4.8. Whilst the high temperature transition is consistent with the physical property measurements we attribute the low temperature transition discrepancy to temperature equilibration issues, in particular that the physical property measurements were measured on cooling and neutron diffraction patterns on warming. The phase transition is also clearly seen as a sharp peak in the unit cell volume at $\approx$1.6 K, as shown in Figure 4.9, indicative of an expansion in the unit cell volume, and of the lattice parameters at this temperature. Interestingly, we do not see any other significant changes in the unit cell volume at 1.2 K, upon transition to the ECO phase.
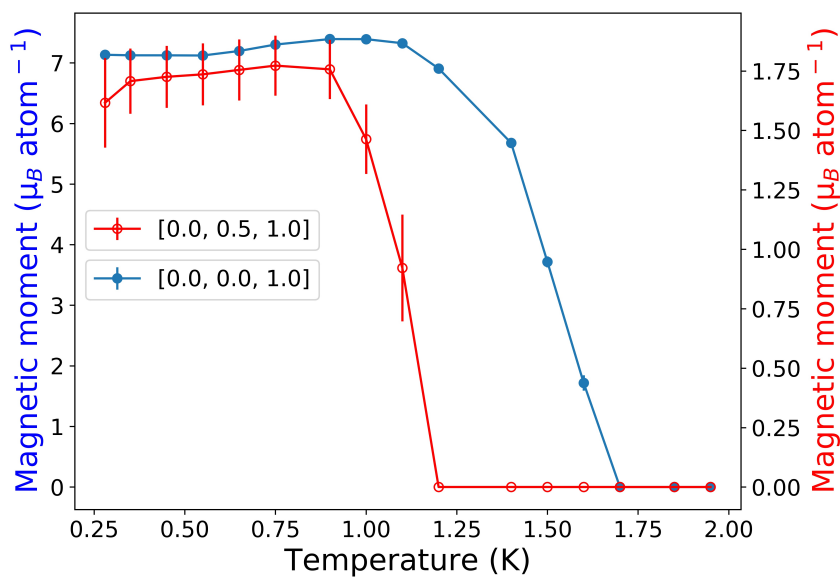
**Figure 4.8** Evolution of the ordered magnetic moments associated with $\mathbf{k}_1$ and $\mathbf{k}_2$, in Tb(DCO$_2$)$_3$, with respect to temperature.
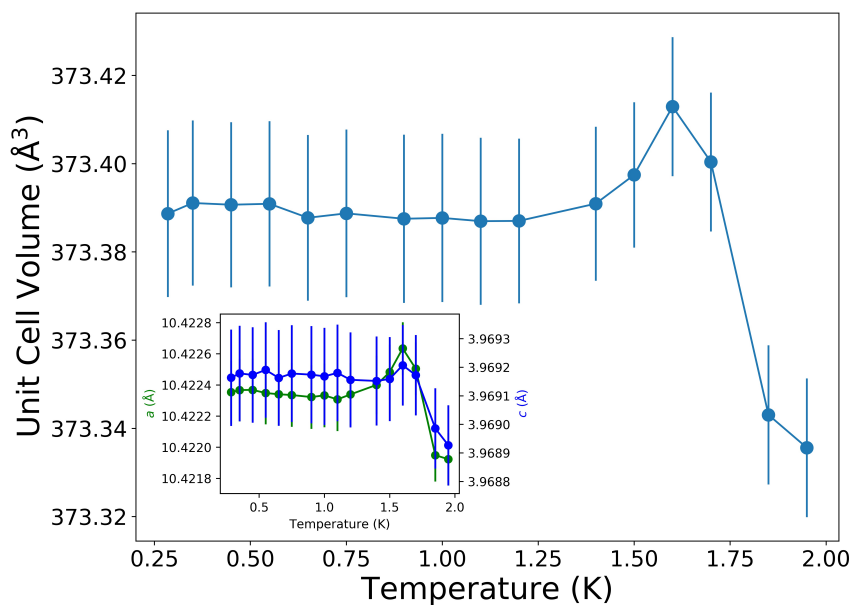


**Figure 4.9** Change in the unit cell of Tb(DCO$_2$)$_3$, and the lattice parameter length in the insert, with respect to temperature between 0.28 and 1.95 K.

A summary of atomic information of Tb(DCO$_2$)$_3$ at 0.28 K, from the Rietveld refinements is summarised in Table 4.1. Using the bond valence method for calculating oxidation states, [121] the atomic positions below yielded a bond valence of 2.87(3) for Tb, close to that expected for a Tb$^{3+}$ ion. This bond valence must be considered tentatively, as the empirical bond valence sum values are calculated for room temperature structures. [207] The refined occupancy of the 98 % indicates the deuteration of Tb(DCO$_2$)$_3$ was overall successful, resulting in only a 2 % hydrogen impurity on the deuterium sites.

**Table 4.1** Tb(DCO$_2$)$_3$ atomic Summary, with atomic positions given as fractional coordinates and occupations given as fractional occupancies, refined in the *R*3*m* space group.

| Atom | x | y | z | $U_{iso}$ x 100 (Å$^2$) | Occupancy |
|------|---------|---------|------------|-------------------------|-----------|
| Tb | 0.33333 | 0.66667 | 0.000 | 0.014(8) | 1.000 |
| C | 0.5131(2) | 0.4869(2) | 0.23103(9) | 0.11259(10) | 1.000 |
| D | 0.4971(3) | 0.5029(3) | 0.48473(9) | 0.30589(18) | 0.980(14) |
| O1 | 0.4667(3) | 0.5333(3) | −0.01430(9) | 0.2259(13) | 1.000 |
| O2 | 0.5840(3) | 0.4160(3) | 0.17390(9) | 0.24539(8) | 1.000 |

## 4.2.3    Inelastic Neutron Scattering

Following from the neutron diffraction studies of Tb(DCO$_2$)$_3$ the magnetic excitations and interactions of this material were probed directly using inelastic neutron scattering using the LET spectrometer. Initial inspection of the inelastic neutron scattering at 50 mK revealed information-rich spectra, with excitations that varied as a function of both *Q* and energy (see Figure 4.10). The strong *Q* dependence of the 6.5 meV signal indicates the excitation is that of propagating magnetic excitations. [208] There is a clear gap in intensity between the elastic line, and the first excited state at ≈5.8 meV, this spin-gap is a clear indication of a magnetic system with Ising anisotropy. SpinW was employed to calculate the powder inelastic scattering function of the long range ordered structure as a function of *Q* and energy, by calculating the spectra in full reciprocal space and then powder averaging. This is one shortcoming of SpinW and linear spin wave theory in that it cannot calculate the scattering function of short range ordered component of this system, [171] which is expected to contribute a significant scattering component. Initial simulations of the magnetic excitation near 6.5 meV using SpinW (see Figure 4.10a), using the *Pm'* space group and initial energies provided by earlier Monte Carlo studies, [18] provided promising results. Despite long computation times, a grid search was used to further refine the energies of Hamiltonian.
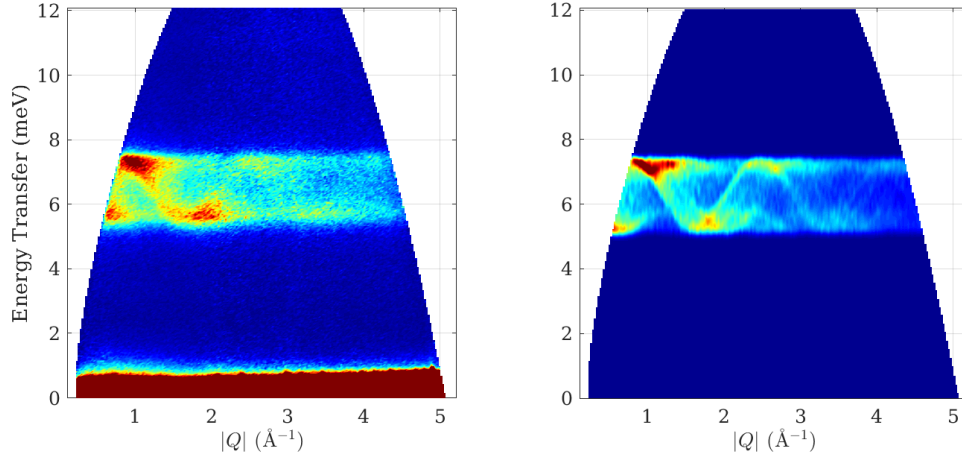
**Figure 4.10** Inelastic neutron scattering of Tb(DCO$_2$)$_3$ on LET (left) The experimental scattering spectra at 200 mK and (right) The calculated spin-wave excitation using SpinW.

Simulations of the magnetic excitation near 6.5 meV using SpinW (see Figure 4.10b) gave an excellent match to this feature with the values for $J$ interaction energies shown in Table 4.2, and indicating the spins in Tb(DCO$_2$)$_3$ behave with Ising mechanics. [171] In this interpretation $J_1$ corresponds to the intrachain coupling, $J_2$ and $J_3$ are the interchain coupling and the anisotropy is the Ising-like anisotropy along the $c$-axis (see Figure 4.11). In reality these correlations correspond to slightly different distances (6.17/6.59 Å) but changing these values made little to no improvement on the quality to the fits.

**Table 4.2** Exchange interactions between Tb ions in Tb(DCO$_2$)$_3$

|  | Energy | |
| --- | --- | --- |
|  | meV | Kelvin |
| $J_1$ | 0.162 | 1.88 |
| $J_2/J_3$ | -0.005 | 0.058 |
| Anisotropy | 0.90 | 10.44 |

The direction determination of the $J$ interaction strengths and the Ising anisotropy are all qualitatively consistent with the previous Monte Carlo and reverse Monte Carlo work. [18] The temperature of the intrachain $J_1$ coupling is consistent with the ordering temperatures we have observed for the TIA transition and both this and the strength of $J_2/J_3$ are very close to the values determined in the previous work. [18] The Ising-like anisotropy determined
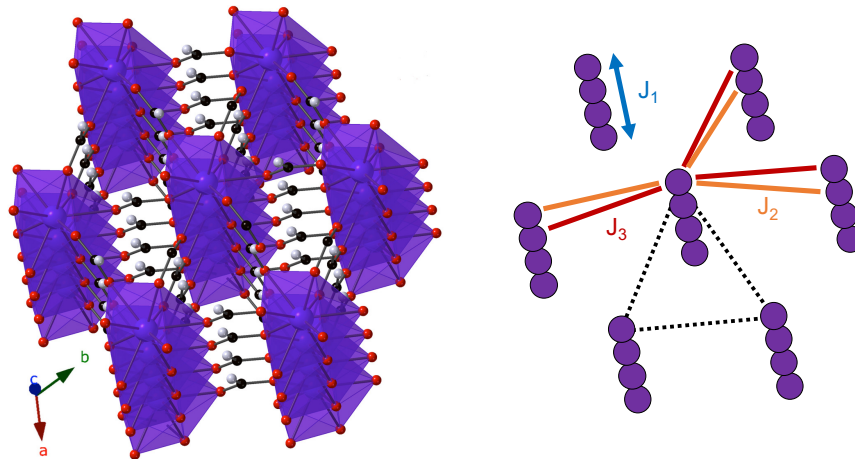
**Figure 4.11** The left image shows the nuclear model of Tb(DCO$_2$)$_3$ with Tb shown in purple, carbon shown in black, oxygen shown in red and hydrogen shown in grey. The right image shows are cartoon of just the Tb atoms and the $J$ interactions between them. $J_1$ is the intrachain coupling shown in blue. $J_2$ is the next-nearest neighbour interchain interaction shown in orange, and $J_3$ is the next-next-nearest neighbour interchain interaction shown in red. The black triangle is highlighting the triangular motif.

here is much weaker than the estimate of the previous studies, emphasizing the importance of directly determining magnetic interactions using inelastic scattering.

Interestingly the spin wave excitation persists at temperatures well above the transition temperature at $\approx$1.6 K. Cuts along energy at constant $Q$ show the spin wave is present in the ECO and TIA phase. The spin-wave remains qualitatively the same in both ordered states, persisting far above $T_N$ but decaying in intensity above 10 K to a diffuse spin-wave. The intensity of the spin wave increases above the ECO transition, which we attribute to an increase in the fluctuations present in the TIA phase, as shown in Figure 4.12. The strong $Q$ dependence of this high energy excitation is consistent with this being the remnant of the magnetic excitation rather than a crystal field transition. At high temperatures the diffuse nature of this excitation means the scattering is dominated by short-range ordering, similarly to that seen in the spin-liquid Mn$_2$(OD)$_2$(C$_4$O$_4$). [209] This may suggest that a similar spin liquid exists in Tb(DCO$_2$)$_3$ well above its ordering temperature. This is consistent with the continued presence of magnetic diffuse scattering to near 20 K. [18, 194]

The emergence of this spin-wave well above its transition temperature would mean that it cannot be a simple magnon mode of the ordered phase – as it would no longer be present so far above $T_N$. This excitation could be evidence of a singlet triplet excitation as predicted in a valence bond solid, [210] as observed in Mn$_2$(OD)$_2$(C$_4$O$_4$). [209, 211] Below 1.6 K at which point the intrachain interactions become sufficient to provide long-range order in 1D, but still

disordered between the chains, the excitation doesn't change in feature (see Figure 4.12a). On further cooling below the ECO transition temperature this excitation remains unchanged. Regardless of the true nature of the spin-wave the presence of the magnetic excitations survives well above the magnetic ordering temperature of $T_N$ = 1.6 K, persisting above 90 K, (see Figure 4.12b) unambiguously indicating the quasi-1D nature of the magnetic interactions in Tb(DCO$_2$)$_3$. [212]



**(a)**   **(b)**
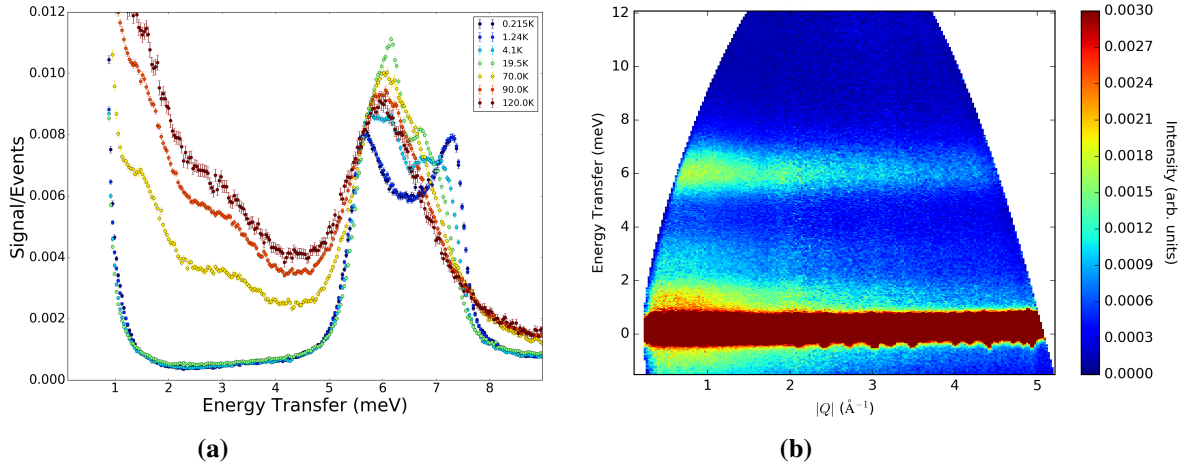
**Figure 4.12** (a) The temperature dependence of the spin-wave excitation. Cut over E = 0.1-9.0 meV and integrated over $Q$ = 0-5 Å. (b) The short ranged spin-wave excitations remaining at 90 K.

Ideally we would model the data with a function for describing a powder averaged $S = \frac{6}{2}$ spin chain, with nearest neighbour interactions on a triangle. However, to the best of our knowledge this type of system is not well understood and no function has been derived. The results obtained would suggest that this $S = \frac{6}{2}$ is showing non-classical behaviour, which is untypical for materials with such high spin - but not unobserved. [208, 209]

We attribute this quantum-like behaviour to two observations. Firstly, the one-dimensionality of the chains caused by the geometric frustration between them. Secondly, an effective spin $\frac{1}{2}$ state, consistent with Ising anisotropy that has been observed in $Ln_3$Ga$_5$O$_{12}$, $Ln_3$Al$_5$O$_{12}$ for $Ln$ = Tb, Dy and Ho, [185, 213–215] and Tb$_2$Ti$_2$O$_7$. [216] In order to investigate this possibility further inelastic neutron measurements should be performed to higher energies, in order to probe the crystal field ground state.

The strong anisotropy of the system prevents tilting of the moments out of the plane, that would lift the degeneracy, which forces this exotic magnetic state. In light of this peculiar magnetic feature it should be investigated further to determine the true nature of this excitation.

## 4.3   Ho(HCO$_2$)$_3$

### 4.3.1   Short Range Magnetic Order

Neutron diffraction measurements of A(DCO$_2$)$_3$ frameworks (A = Ce-Nd and Dy-Er) at 1.5 K indicated that of the neutron accessible $Ln$(DCO$_2$)$_3$ phases studied, excluding Tb(DCO$_2$)$_3$, only Ho(DCO$_2$)$_3$ exhibits structured magnetic scattering above 1.6 K. Ho(DCO$_2$)$_3$ begins to exhibit diffuse scattering below 10 K, whilst remaining paramagnetic to 1.6 K, see Figure 4.13 for the normalised and temperature subtracted neutron patterns.
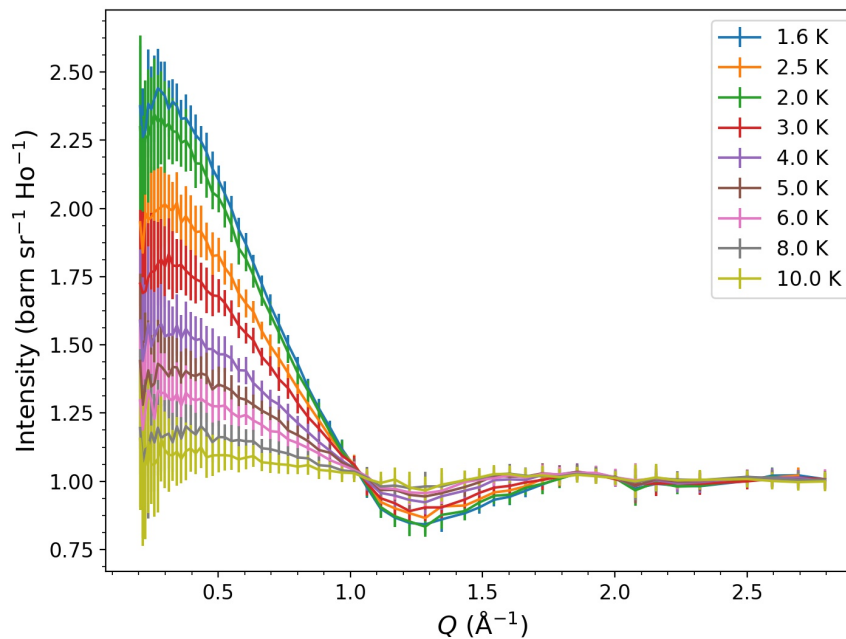


**Figure 4.13** Evolution of the diffuse scattering, in Ho(DCO$_2$)$_3$, with respect to temperature.

Diffuse scattering in Ho(DCO$_2$)$_3$ emerges at temperatures below 10 K, and increases with decreasing temperature. This, in addition to its $Q$ dependence, indicated that the diffuse scattering was magnetic in origin. Using a magnetic supercell of 50 Å along all the unit cell directions and 1000 RMC moves, the magnetic diffuse scattering was fit well with SPINVERT. The stereographic projections, showing the average of the refined spin orientations indicate that the spins are preferentially aligned along the $c$-axis (see Figure 4.14). This is consistent with the large spin-orbit coupling and the Ising-like magnetic anisotropy of Ho$^{3+}$, and similar to that seen in Tb(DCO$_2$)$_3$. [4, 217]
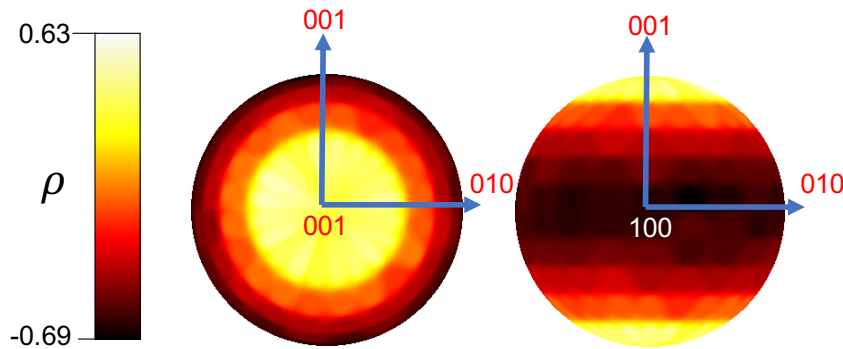
**Figure 4.14** Stereographic projections of the spin orientations averaged over 100 RMC Heisenberg-like fits to diffuse neutron scattering data from Ho(DCO$_2$)$_3$ at 1.6 K. The relative spin density, $\rho(\theta,\phi)$, is defined as $\rho(\theta,\phi) = \ln\left[\frac{\rho(\theta,\phi)}{Nd(\cos\theta)d\phi}\right]$

Attempts were therefore made to fit the diffuse scattering data with a model consisting of Ising spins, using the same parameters as the unconstrained Heisenberg refinements. These were constrained with uniaxial easy axes along the $c$-axis, such that the spins can be oriented up or down, in agreement with the stereographic projections. These Ising refinements also yielded a reasonable fit (Figure 4.15a), though of somewhat lower quality than the Heisenberg-like refinement (Figure 4.15b, $\chi^2$ = 2.53 and 8.29), expected as the Ising refinement is more highly constrained compared to Heisenberg fits.
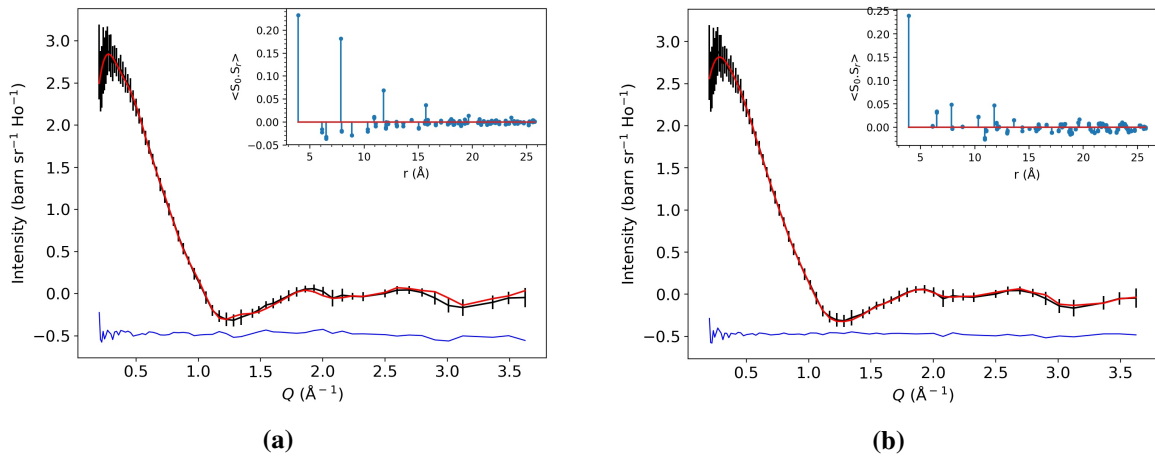


**Figure 4.15** RMC fit to magnetic diffuse with an (a) Ising model and (b) Heisenberg model. Data points in black, fit in red and the difference in blue. The correlations of each fit is shown in the insert.

This result suggests that the spins have a strong, although probably not purely, Ising character which is often observed for Ho$^{3+}$ as seen, for example, in the spin-ice materials Ho$_2$Ti$_2$O$_7$ and Ho$_2$Sn$_2$O$_7$. [218] We would therefore expect to see a gap in the inelastic neutron

spectra of Ho(DCO$_2$)$_3$ similar to that noted in Tb(DCO$_2$)$_3$. Spin correlations $\langle S_0 \cdot S_r \rangle$, averaged over 100 RMC refinements, for Ho(DCO$_2$)$_3$ show that dominant spin correlations in this material are ferromagnetic along the chain direction, with weaker antiferromagnetic interchain interactions (see Figure 4.16 insert).
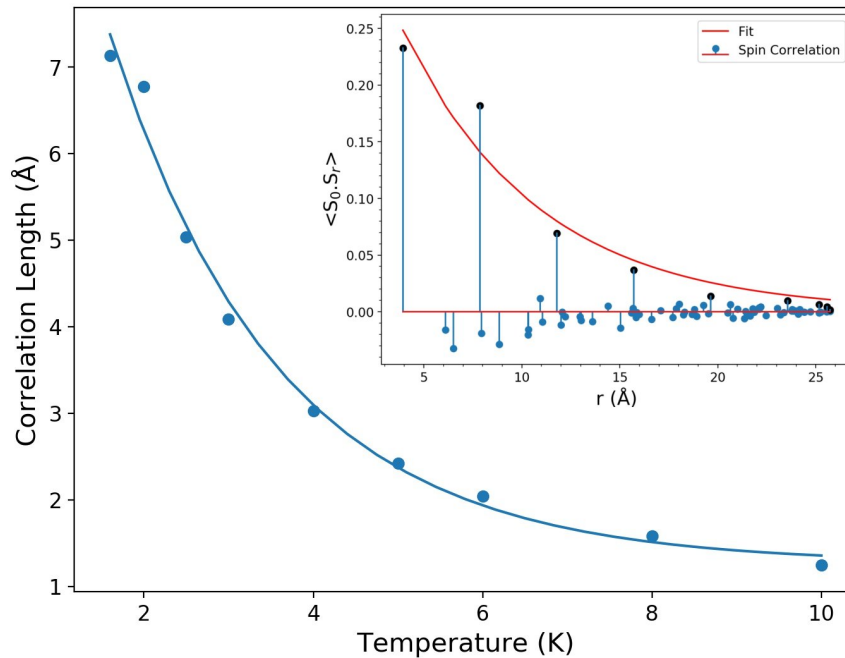


**Figure 4.16** Correlation lengths, from Ising model fits, at various temperature with spin correlations and fit of Ho(DCO$_2$)$_3$ at 1.6 K in insert with chain correlations highlighted in black.

We have extracted correlation lengths with the function $\langle S_0 \cdot S_r \rangle = A exp(-r/\varepsilon)$, where A is the Ising-like anisotropy, r is the correlation distance, and $\varepsilon$ is the correlation length (see Figure 4.16 for the evolution in ferromagnetic correlation length with temperature). As the temperature was raised and the correlations became significantly weaker, the best fit to data was found with unphysical A values, for this reason A was fixed to the value - 0.72 - determined for the lowest temperature fit. For correlation fits see Figure A.8.

At 1.6 K, the ferromagnetic chain correlation length is 7.3(6) Å with weaker antiferromagnetic inter-chain correlations of $-0.018(2)$ and $-0.034(2)$ observed for Ho$^{3+}$ cations separated by 6.10 and 6.57 Å within the triangles, respectively. This indicates that the correlations in Ho(DCO$_2$)$_3$ are weaker than Tb(DCO$_2$)$_3$ for a given temperature (0.14 vs 0.33 for the strongest correlation at 3 K). [4, 18] This observation indicates that the formation of this order is not simply due to direct or dipolar exchange, which would be expected to be stronger for Ho(DCO$_2$)$_3$ and the shorter bond lengths. It is possible the stronger interactions of

Tb(DCO$_2$)$_3$ are caused by the crystal field, but additional crystal field studies would be required for both systems to confirm this hypothesis. In the *Ln*(DCO$_2$)$_3$ series Tb(DCO$_2$)$_3$ and Ho(HCO$_2$)$_3$ were both noted to have their magnetocaloric properties optimised for use above 4 K, these are also the only two compounds to show structured diffuse scattering above 1.6 K. Ho(HCO$_2$)$_3$ may be a worse magnetocaloric than Tb(HCO$_2$)$_3$ due to its weaker ferromagnetic correlations, needing greater changes in magnetic fields to align spins with the field. The decrease in correlation lengths in Ho(DCO$_2$)$_3$ follows the same exponential law seen in the Tb(DCO$_2$)$_3$ framework and the relative strength of the ferromagnetic intrachain and antiferromagnetic interchain correlations in the two compounds is the same. Therefore it is necessary to probe to sufficiently low temperatures, to probe if the Ho(DCO$_2$)$_3$ framework will feature similar exotic magnetic states to that of Tb(DCO$_2$)$_3$.

### 4.3.2 Physical Property Measurements

With the emergence of short range order in the Ho(DCO$_2$)$_3$, probing the physical property measurements to lower temperature was the next sensible step to determine whether magnetic order occurs at low temperatures. Zero-field cooled magnetic susceptibility data for Ho(DCO$_2$)$_3$ shows features at $\approx$1.5 K and $\approx$0.5 K (see Figure 4.17a). The small change in susceptibility at 1.5 K can be interpreted similarly to the feature in Tb(DCO$_2$)$_3$ at a similar temperature, as either an experimental artefact from the MPMS switching between high and low temperature modes or an indication of a TIA-like phase. A significant feature in the heat capacity of Ho(DCO$_2$)$_3$ is observed at $\approx$1.2 K, similarly to the feature caused in Tb(DCO$_2$)$_3$ by the emergence of the TIA-phase (see Figure 4.17b).

The feature in the magnetic susceptibility of Ho(DCO$_2$)$_3$ at 1.5 K is thus more likely an artefact of the measurement, implying that this may also be true for Tb(DCO$_2$)$_3$, unless the temperature discrepancy is caused by temperature equilibration issues. A clearer transition can be seen at $\approx$0.5 K indicating more complete, possibly long-range antiferromagnetic order, particularly given its tendency to be suppressed under an applied magnetic field. [4, 18] A second large change in the heat capacity is observed below 600 mK, this may also be associated with the onset of long-range order but could also be caused by a hyperfine Schottky anomaly. [195] As with Tb(DCO$_2$)$_3$ the broad feature of this heat capacity feature may arise due to the presence of solitons, [198] or the formation of magnetic structure with a finite length correlation length.
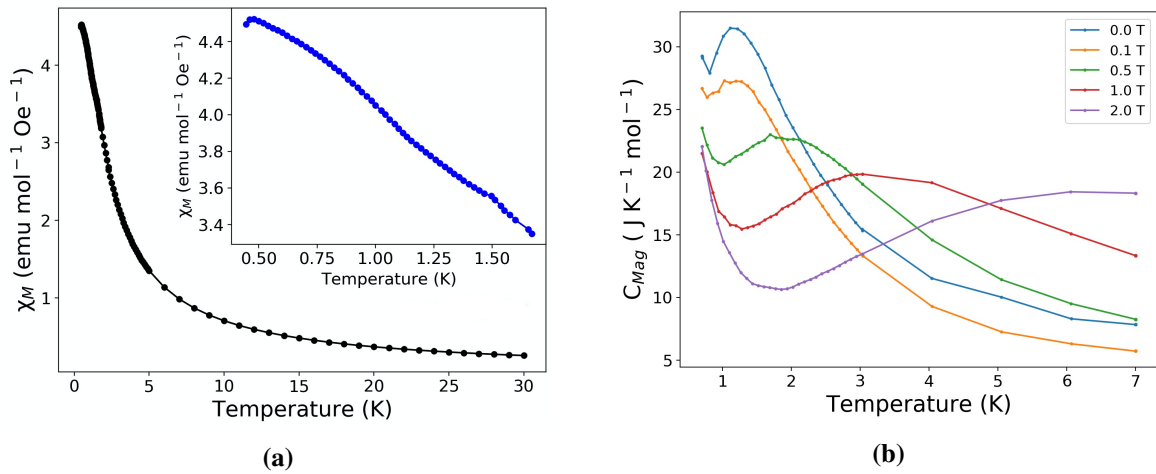
**Figure 4.17** Magnetic measurements of Ho(HCO$_2$)$_3$. (a) Magnetic susceptibility in 100 Oe field below 30 K, close up below 1.6 K in insert, (b) C$_{mag}$ in variable fields between 400 mK and 14 K.

Magnetisation data of Ho(HCO$_2$)$_3$ (see Figure 4.18) has been performed above and below the phase transitions and follows a typical curve up to ≈3 T, saturating near $G_J J/2$ as expected for Ising spins, in agreement with the RMC refinements of the short range order.
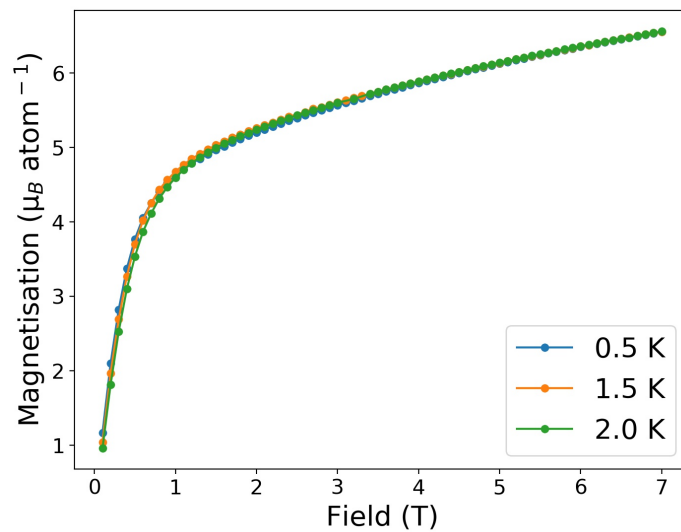


**Figure 4.18** Magnetisation measurements of Ho(HCO$_2$)$_3$ between 0-7 T, at variable temperatures.

The magnetisation is seen to reach the M$_{sat}$ value less rapidly than the Tb(HCO$_2$)$_3$, which is consistent with the less efficient magnetocaloric effect in low applied field as seen in previous studies. [4] The slower magnetisation can be attributed to weaker coupling between spins which would explain the lower ordering temperatures observed in Ho(HCO$_2$)$_3$.

### 4.3.3 Emergent Charge Order

Crash cooling Ho(DCO$_2$)$_3$ in the $^3$He to base temperature = 0.25 K revealed the presence of magnetic diffuse Bragg-like peaks in the neutron diffraction pattern, shown in Figure 4.19a. Indexing of these peaks reveals that the peaks arise from a similar ECO magnetic state, as seen in Tb(DCO$_2$)$_3$. However, measurements taken on warming indicated the FWHM of these magnetic peaks decreasing with varying temperature, indicating the magnetic domains in these materials were growing. These magnetic reflections are lost above 0.7 K, indicating the disappearance of this ordered magnetic phase. It is noticeable that this temperature varies significantly from the temperature of the transition indicated by the heat capacity measurements, which suggests a phase transition of 1.2 K.
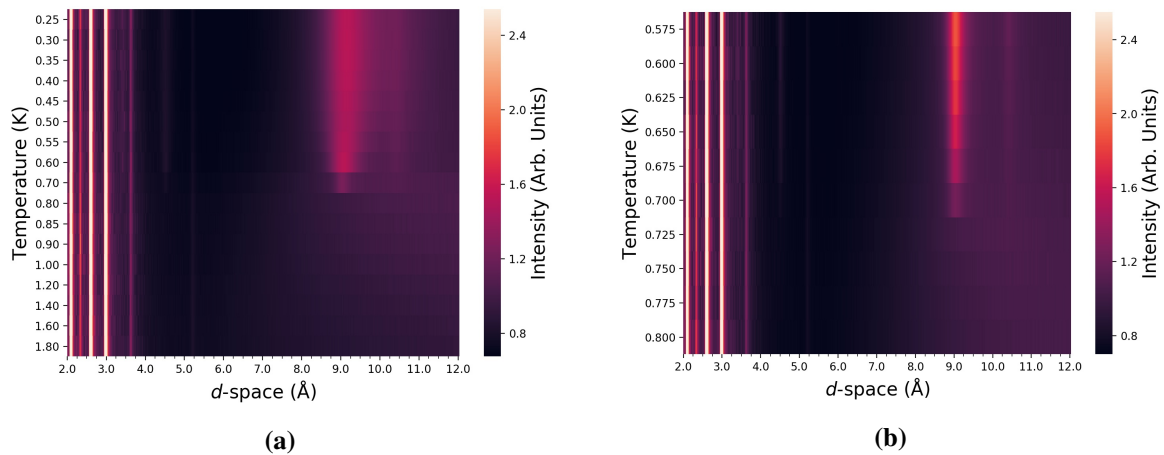


**Figure 4.19** Contour plots of Ho(DCO$_2$)$_3$ on (a) warming and (b) cooling. Measurements taken on warming were crashed cooled to 0.25 K, and then slowly warmed. The extremely broad magnetic peaks are a consequence of small magnetic domains. Measurements taken on cooling were cooled from 3 K slowly. The peaks are much sharper but still significantly broader than instrumental resolution, indicating the broad peaks are likely inherent to the system, due to a finite magnetic correlation length.

To determine if the emergence of the ordered magnetic state in Ho(DCO$_2$)$_3$ is a sluggish process and to what extent the broadening for the peaks is purely a result of crash cooling leading to small magnetic domains the sample was cooled again from 3 K to below $T_N$ = 0.7 K, with measurement taken on cooling. These measurements reveal peaks with a FWHM much sharper than measurements taken on warming, but still much broader than instrumental resolution, at 0.7 K, the same temperature these are observed at on warming. This indicates that the broadness of these peaks are likely intrinsic to the magnetic phase having a finite correlation length and not purely a results of the finite magnetic domains caused by crash cooling.

Unlike the magnetic ECO state seen in Tb(DCO$_2$)$_3$, which is proceeded by a stabilised intermediate magnetic phase that is best thought of as a TIA state, in Ho(DCO$_2$)$_3$ the ECO state emerges immediately from the correlated paramagnetic phase. This is indicated by the magnetic reflections associated with both **k**-vectors appear simultaneously at 0.7 K, giving rise to the magnetic ECO state. It was previously noted, in Tb(DCO$_2$)$_3$, that due to the appearance of the two **k**-vectors at different temperatures we could not rule out the possibility of magnetic phase separation. In Ho(DCO$_2$)$_3$ the likelihood of two magnetic phases appearing simultaneous is unlikely, therefore we assert that the magnetic emergent charge ordered state, determined from refinement of the magnetic phase, is an accurate representation of the average magnetic phase of this system.

As seen in Tb(DCO$_2$)$_3$ the ordered magnetic phase of Ho(DCO$_2$)$_3$ adopts the space group $Pm'$, and the lattice parameters $a = 3.94050(13)$ Å, $b = 10.3582(3)$ Å, $c = 17.9409(3)$ Å at 0.575 K. The fits to this temperature measured on cooling is shown in Figure 4.20.



(a)



(b)
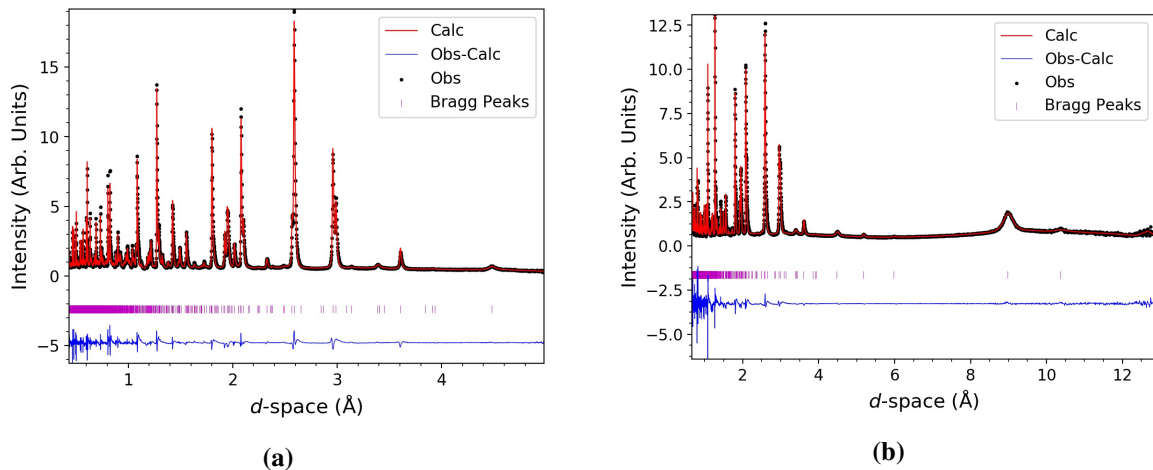
**Figure 4.20** Rietveld fits to neutron diffraction patterns of Ho(DCO$_2$)$_3$ at 0.575 K from WISH along with the fitting statistics (a) bank 5/6, R$_p$ = 6.96 %, R$_{wp}$ = 7.08 % (b) bank 2/9, R$_p$ = 8.36 %, R$_{wp}$ = 4.87 %

A summary of crystal structure of Ho(DCO$_2$)$_3$ at 0.575 K, from the Rietveld refinements is summarised in Table 4.3. Using the bond valence method for calculating oxidation states, [121] the atomic positions below yielded a bond valence of 3.04(2) for Ho, close to that expected for a Ho$^{3+}$ ion. The deuterium occupancy was refined to yield a value of 98 % indicating that deuteration of Ho(DCO$_2$)$_3$ was successful, containing only 2 % hydrogenated formates.

**Table 4.3** Ho(DCO$_2$)$_3$ atomic Summary, with atomic positions given as fractional coordinates and occupations given as fractional occupancies.

| Atom | x | y | z | $U_{iso}$ x 100 (Å$^2$) | Occupancy |
|------|------|------|------|------|------|
| Ho | 0.33333 | 0.66667 | 0.000 | 0.000 | 1.000 |
| C | 0.5109(2) | 0.4891(2) | 0.22690(11) | 0.12789(10) | 1.000 |
| D | 0.4970(3) | 0.5030(3) | 0.49144(8) | 0.22983(14) | 0.978(7) |
| O1 | 0.4655(3) | 0.5345(3) | −0.01582 (10) | 0.28733(12) | 1.000 |
| O2 | 0.58424(19) | 0.41575(19) | 0.17818(6) | 0.28832(22) | 1.000 |

Figure 4.21 depicts the evolution of its magnetic moment with temperature. Examining the conventional crystallographic interpretation of the ordered magnetic state in Ho(DCO$_2$)$_3$ we need to consider the two distinct global phases that are possible for a conventional crystallographic interpretation of these features.
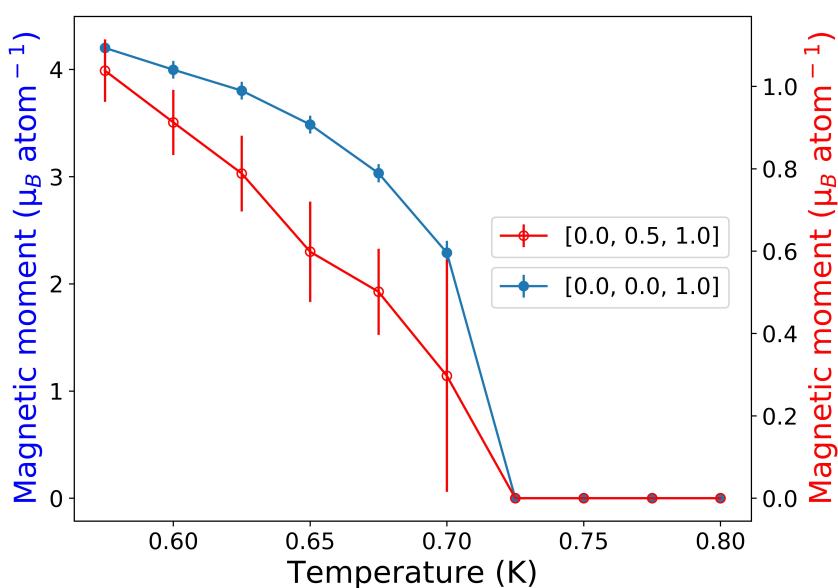


**Figure 4.21** Evolution of the ordered magnetic moments associated with $\mathbf{k}_1$ and $\mathbf{k}_2$, in Ho(DCO$_2$)$_3$, with respect to temperature.

At 0.575 K the solution with global phase $\pi/4$ results in a modification of the PDA structure in which the $\mathbf{k}_2$ propagation modulates the moment in the chains resulting in pairs of large moment Ho chains ($\pm4.01(5)$ $\mu_B$ and $\pm3.09(3)$ $\mu_B$) antiferromagnetically coupled to each other separated by a chain with a smaller moment ($\pm0.93(4)$ $\mu_B$), as shown in Figure 4.22.
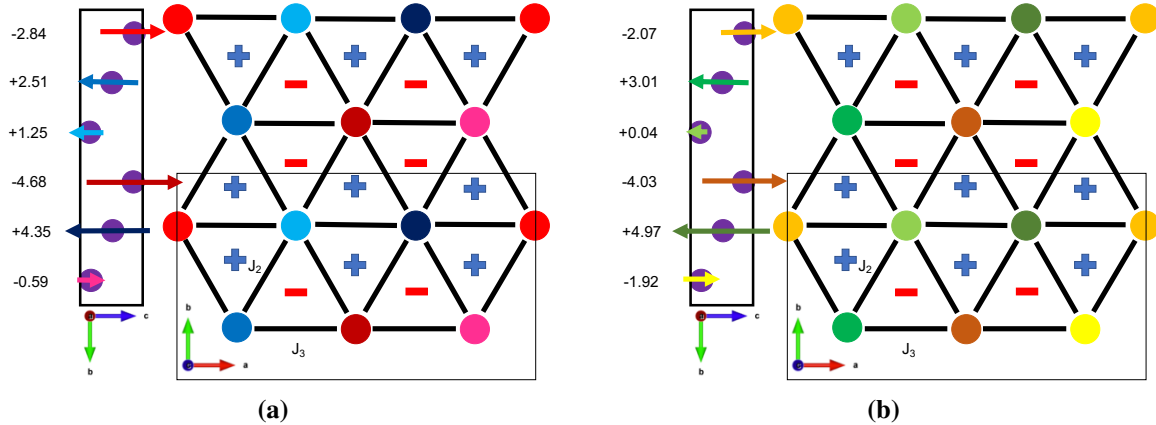
**Figure 4.22** Ho(DCO$_2$)$_3$ magnetic average structure solutions at 0.575 K. Unit cell shown as black box with magnetic moments in *Pm'* space group. The spin charges are shown as minus and plus signs. $J_2$ and $J_3$ are shown next to the corresponding interaction and $J_1$ not shown, goes into the plane. On the right of each figure is shown the projection of the structure in the *ab* plane and on the left of each figure the *bc* plane. Magnetic moments colour coded, but not to scale. (a) Global phase = $\pi/4$, (a) Global phase = $\pi/6$.

At 0.575 K the solution with the global phase $\pi/4$ results in a modification of the ECO structure seen in Tb(DCO$_2$)$_3$, with six independent magnetic moments and the lengths $+4.35$, $+2.51$, $+1.25$ and $-4.68$, $-2.84$, $-0.59$ $\mu_B$, with spin vectors are oriented along the *c*-axis, with no intensity in the *ab*-plane. The sum of these spin vectors on each of the triangles sums to produce $\pm 0.92$ $\mu_B$, yielding the same ECO seen in Tb(DCO$_2$)$_3$ with different intensities of spin charges. The solution with the global phase $\pi/6$ produces the same spin orientation but with the magnetic vectors of $+4.97$, $+3.01$, $+0.04$ and $-4.03$, $-2.07$, $-1.92$ $\mu_B$, and spin charges of $\pm 0.98$ $\mu_B$. The magnetic structure of Ho(DCO$_2$)$_3$ differs from that of Tb(DCO$_2$)$_3$, in that the different global phases of the system produce slightly different spin charges within the ECO. It cannot be ruled out that this discrepancy is due to the error of the measurements, and not inherent to the system. However, it may be possible to differentiate between the two phases through some technique sensitive to this. The phase transition indicated by the appearance of new Bragg-like peaks, did not produce any significant change in the lattice parameters of Ho(DCO$_2$)$_3$, in either cooling or warming measurements. This suggests that such this deviation is associated with the emergence of a TIA phase in Tb(DCO$_2$)$_3$, which is absent in Ho(DCO$_2$)$_3$.

The existence of this emergent phase in Ho(DCO$_2$)$_3$, as well as in Tb(DCO$_2$)$_3$, and the persistence of some order into the paramagnetic phases is likely contributing to the magnetocaloric behaviour of these materials. In the previous magnetocaloric studies of the *Ln*(DCO$_2$)$_3$ [4], Ho(DCO$_2$)$_3$ and Tb(DCO$_2$)$_3$ both show the same magnetocaloric behaviour with respect to

field and temperature. In a 1-0 T field change it can be seen that the magnetocaloric effect of Ho(DCO$_2$)$_3$ peaks at 2 K, compared to 4 K for Tb(DCO$_2$)$_3$. This is likely a direct result of the weaker interaction in Ho(DCO$_2$)$_3$ and hence the lower ordering temperature. This is further supported by the emergence of the diffuse scattering in the paramagnetic phase becoming significant at 10 K in Ho(DCO$_2$)$_3$, compared with $\approx$20 K in Tb(DCO$_2$)$_3$. The existence of predominantly 1D ferromagnetic correlations in the paramagnetic phases, is beneficial the magnetocaloric effect and is observed in the diffuse and magnetcaloric measurements of these materials.

## 4.4 Er(HCO$_2$)$_3$

### 4.4.1 Crystal Structure

Er(DCO$_2$)$_3$ was measured on WISH to 1.5 K in search of any evidence of long or short range magnetic order at 1.6 and 20 K. No evidence of magnetic Bragg peaks were observed in Er(DCO$_2$)$_3$ at 1.5 K, indicating a lack of magnetic structure, and remained in the *R3m* space group over its entire temperature range (see Figure 4.23 for quality of fit at 1.5 K).



(a)                                                    (b)
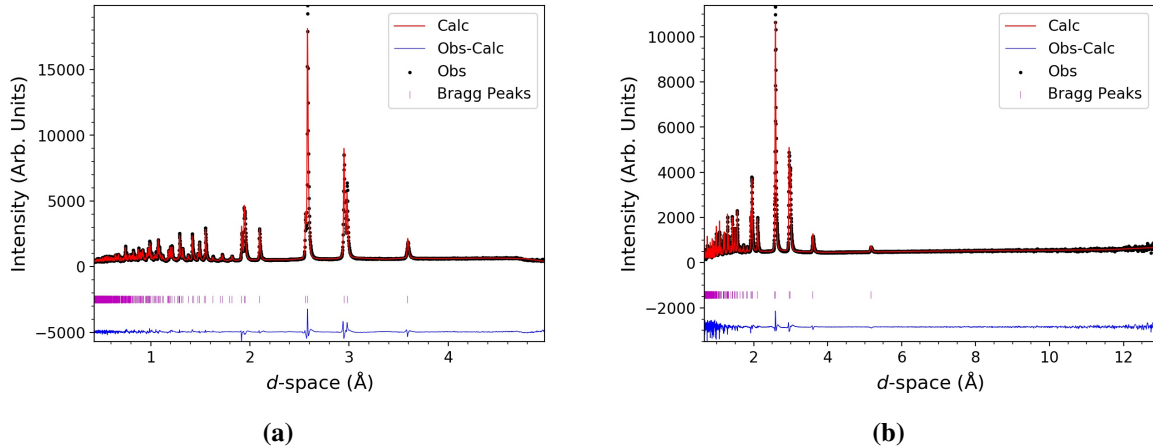
**Figure 4.23** Rietveld fits to neutron diffraction patterns of Er(DCO$_2$)$_3$ at 0.575 K from WISH along with the fitting statistics (a) bank 5/6, R$_p$ = 5.50 %, R$_{wp}$ = 7.08 % (b) bank 2/9, R$_p$ = 6.31 %, R$_{wp}$ = 4.21 %

A small discrepancy was noted between the low and high temperature neutron diffraction patterns of Er(DCO$_2$)$_3$ between 1.6 and 20 K. Temperature subtraction of the data sets (see Figure A.9) shows very small intensities and large standard deviations of the data points. Fitting to this diffuse scattering, using and RMC approach, yielded unphysical poor fits, suggesting this is more likely an artefact of the instrument. The high resolution and

low background of the WISH diffractometer combined with the lack of significant diffuse scattering, as seen in Tb(DCO$_2$)$_3$ and Ho(DCO$_2$)$_3$, [18, 194], suggests that there is no short range order in Er(DCO$_2$)$_3$, above 1.5 K.

## 4.4.2 Magnetic Properties

Physical property measurements performed on Er(DCO$_2$)$_3$ show no indication of long-range magnetic order forming down to 0.4 K. The fit to the magnetic susceptibility data yielded an effective magnetic moment of 8.97 $\mu_B$, a Curie constant of 10.06 and a $\theta_{CW}$ temperature of $-14.21$ K. The large Weiss temperature with respect to the lack of transition temperature may indicate that this material is quite frustrated but care should be taken in this interpretation given the quenching of the orbital angular moment in isolated lanthanide centres at low temperatures can cause a similar effect. Heat capacity data also show no significant features in the data, only increasing with lowering temperature, which can be ascribed to the nuclear heat capacity effects or the Schottky anomaly. [195]
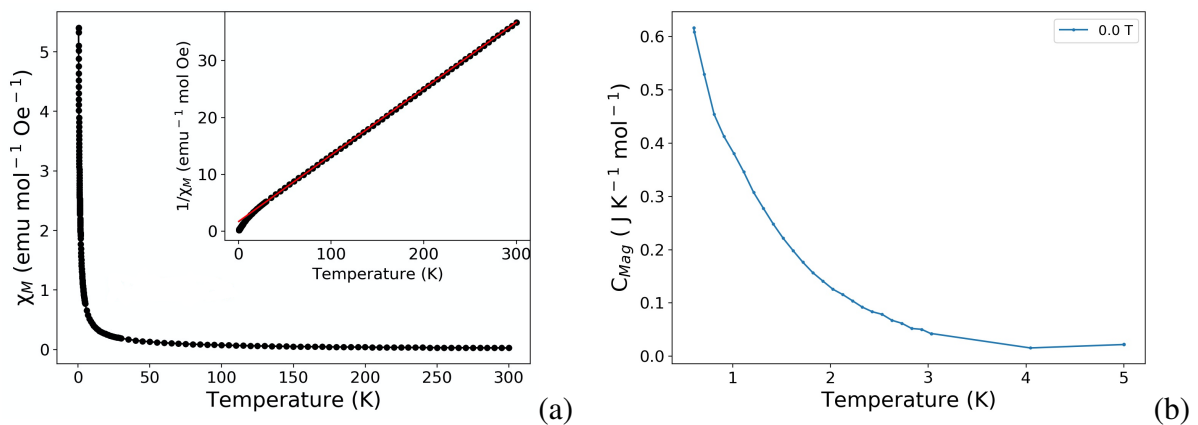


**Figure 4.24** (a) Magnetic susceptibility of Er(DCO$_2$)$_3$ in a 100 Oe field, between 0.4 - 300 K, with the Curie-Weiss fit in the insert. (b) Heat capacity measurements in zero applied field, of Er(DCO$_2$)$_3$ between 0.5 - 5 K, indicating a lack of phase transitions.

Magnetisation measurements, shown in Figure 4.25, indicate the spins are not Heisenberg shown by a $M_{sat}$ of less than $g_jJ$. The $M_{sat}$ is close to $g_jJ/2$ suggesting that the spins, in Er(DCO$_2$)$_3$, are likely Ising. In high fields ($>3$ T) the magnetisation data becomes linear-field dependent, consistent with the onset of Van Vleck paramagnetism, [183] related to the field induced electronic transitions. [200, 201]
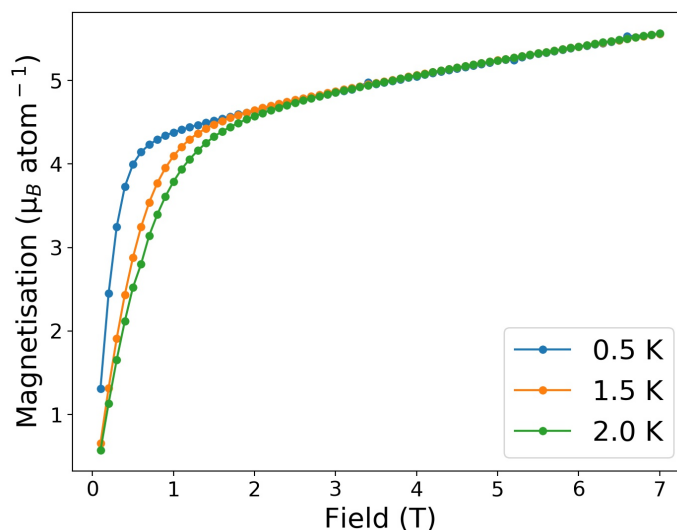
**Figure 4.25** Magnetisation measurements of Er(HCO$_2$)$_3$ between 0-7 T, at variable temperatures.

### 4.4.3 Antiferromagnetic Order

Upon cooling to 50 mK the neutron diffraction measurement performed on Er(DCO$_2$)$_3$ show the appearance of extra weak reflections ascribable to the development of long-range magnetic ordering. These extra reflections can be indexed to a supercell, doubled along the *a* and *b* axes, with the propagation vector $\mathbf{k}_1 = [0, -0.5, 0.5]$, corresponding to the L-point of the Brillouin zone. Given the moderate resolution of the Wombat diffractometer used for these measurements no conclusions can be drawn regarding the size of the magnetic domains in this materials.

Due to the modest quality of the data it was decided to refine the magnetic structure against temperature subtracted data to best enabled the weak magnetic reflections observed to be isolated. This involved subtracting the data collected at 6 K from that obtained at 50 mK. This process first required a refinement of the nuclear structure at 50 mK, which produced the atomic position as summarised by Table 4.4 and the fits displayed in Figure 4.26a.

The quality of the data was compromised by the presence of many sample environment reflections, including the copper can and aluminium from the dilution fridge. This resulted in obscured Er(DCO$_2$)$_3$ reflections, meaning the refinement of the data was unstable with all parameters turned on. For this reason the isotropic displacement was fixed, and assumed to be near zero at 50 mK. The calculation of bond valence sums resulted in a value of 2.98(1) for Er, close to that expected for a Er$^{3+}$ ion.

**Table 4.4** Summary of nuclear component of Er(DCO$_2$)$_3$ refined in the *R*3*m* space group, with atomic positions given as fractional coordinates. The quality of the data was not high quality enough to refine the fractional occupancies or isotropic displacement parameters. The fractional occupancies were fixed to 1, and all isotropic displacement parameters were fixed to 0.01 x 100 Å$^2$.

| Atom | x | y | z |
|------|-----------|-----------|----------|
| Er | 0.33333 | 0.66667 | 0.000 |
| C | 0.5154(8) | 0.4846(8) | 0.254(6) |
| D | 0.4982(10) | 0.5018(10) | 0.504(6) |
| O1 | 0.4672(6) | 0.5328(6) | 0.008(5) |
| O2 | 0.5871(8) | 0.4128(8) | 0.159(5) |



(a)                                                                          (b)
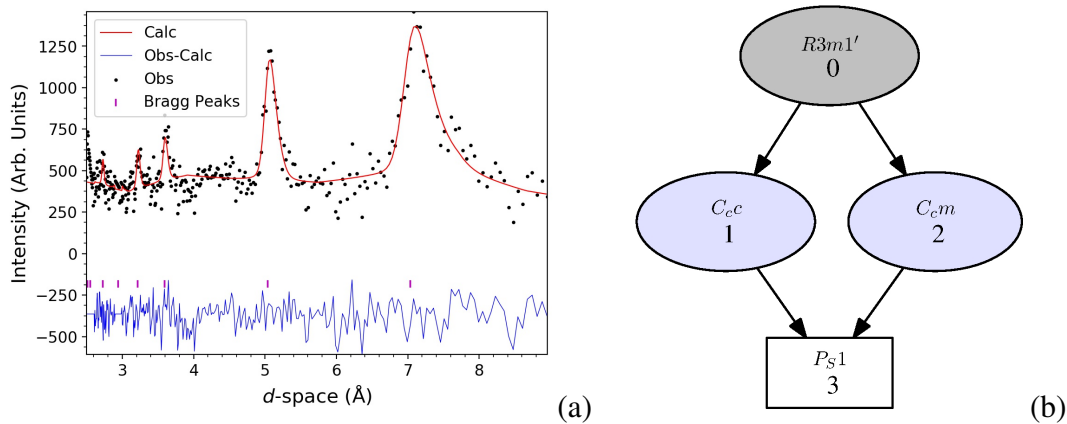
**Figure 4.26** (a) Temperature subtracted magnetic only neutron diffraction pattern fit of Er(DCO$_2$)$_3$ at 50 mK, using a 2.41 Å wavelength. The fit to the data yielded the fitting statistics, for the magnetic phase, of R$_p$ = 13.5 %, and R$_{wp}$ = 15.8 %, which whilst high, is to be expected for data of this quality. (b) Group subgroup relationship for the [0,-0.5,0.5] in Er(DCO$_2$)$_3$, made using the Bilbao crystallographic server.

Once refinement of the nuclear structure was completed a fit to the magnetic reflections was performed (see Figure 4.26a). The best fits for the reflections observed is obtained with an antiferromagnetic structure in space group $C_cc$ (see Figure 4.27 for a depiction of this phase). The group subgroup relationship is also seen in Figure 4.26b, and we see that the phase transition for Er(DCO$_2$)$_3$, is comprised of a single irreducible representation, in agreement with Landau theory. [31, 43] In this structure there is only one independent Er site with an ordered magnetic moment of 0.75(4) $\mu_B$ at base temperature. The magnetic moment intensity lies in the *a*-axis and canted into the *b*-axis, oriented along the [0.720,−0.217,0.00] vector, as shown in Figure 4.27, and the lattice parameters *a* = 10.293(1), *b* = 20.554(2) and *c* = 7.8279(5). Unlike Tb(DCO$_2$)$_3$ and Ho(DCO$_2$)$_3$, which we have shown to be ferromagnetic along the *c*-axis and chain direction, Er(DCO$_2$)$_3$ is antiferromagnetic within the chains.

Indeed such interactions between the chains is directly implied for the **k**-vector [0,-0.5,0.5] in Er(DCO$_2$)$_3$.
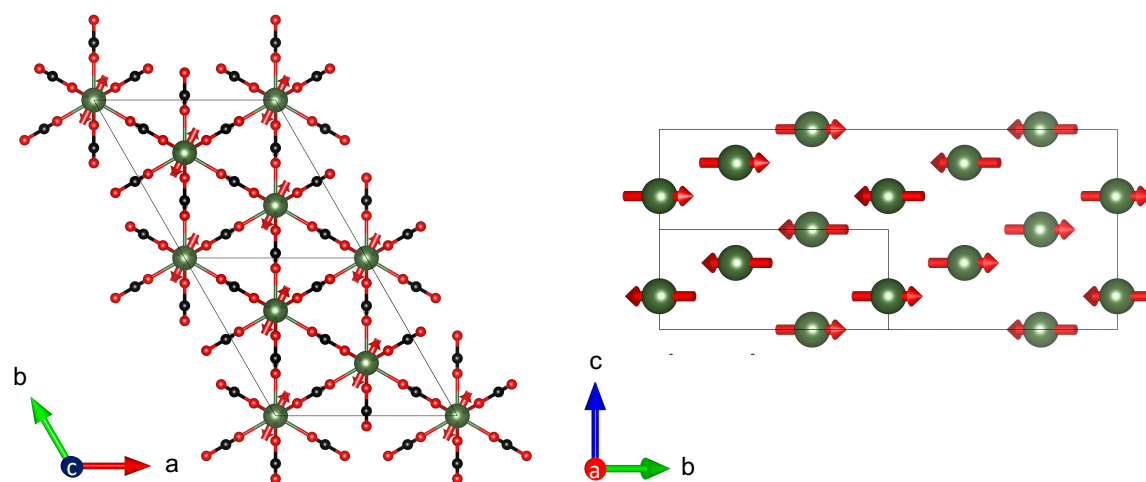


**Figure 4.27** Antiferromagnetic structure of Er(DCO$_2$)$_3$ at 50 mK, as determined from Rietveld refinement of WOMBAT neutron data. (left) Viewed along the *c*-axis and showing the antiferromagnetic interactions within the chains, and (right) viewing along the *a*-axis, showing only the erbium atoms for clarity. Erbium shown in green, oxygen shown in red, hydrogen shown in grey and carbon shown in black. Unit cell shown in black.

Heating the sample to 100 mK, the weak magnetic reflections seen in Figure 4.26a did not persist, indicating the $T_N$ is between 50 and 100 mK. To avoid additional scattering from the sample environment a thermal conductor was not used inside the sample can, instead relying on the presence of a condensed He from the atmosphere under which the sample was loaded. It is possible, therefore, that the sample can may not be precisely at this temperature due to poor thermal conduction between the refrigerator setup and the sample. There was no evidence of magnetic diffuse scattering in temperature subtracted data from temperatures above 100 mK, although the modest quality of the data does not exclude the possibility of weak diffuse scattering being observed, in higher quality measurements. In either case the weak antiferromagnetic ordering in Er(DCO$_2$)$_3$ may explain why this material performs more poorly, as a magnetocaloric compared to Tb(DCO$_2$)$_3$ and Ho(DCO$_2$)$_3$. The antiferromagnetic interactions between spins likely requires greater magnetic fields to align the spins with the applied magnetic field to overcome these interactions. Why Er(DCO$_2$)$_3$ is antiferromagnetic within the chains, in contrast to Tb(DCO$_2$)$_3$ and Ho(DCO$_2$)$_3$, despite being isostructural is open for discussion, but could be due to the crystalline electric field of these systems. Notably Er$^{3+}$ has a non-degenerate Kramers ground state compared to Kramers Tb$^{3+}$ and Ho$^{3+}$. [35]

# 4.5   Other *Ln*(HCO$_2$)$_3$ Phases

As indicated in Section 4.3, Ce(HCO$_2$)$_3$, Pr(HCO$_2$)$_3$, Nd(HCO$_2$)$_3$ and Dy(HCO$_2$)$_3$ showed no clear sign of magnetic diffuse scattering down to 1.5 K and, furthermore, lower temperature physical property measurements of these materials failed to reveal any interesting features. This will be discussed briefly below.

## 4.5.1   Magnetostructural Properties

Magnetic susceptibility measurements were obtained for Nd(HCO$_2$)$_3$ and Dy(HCO$_2$)$_3$ down to 0.4 K, with no indication of magnetic order found. Curie-Weiss fits, above 100 K, to this magnetic susceptibility data have been performed as shown in Figure 4.28.
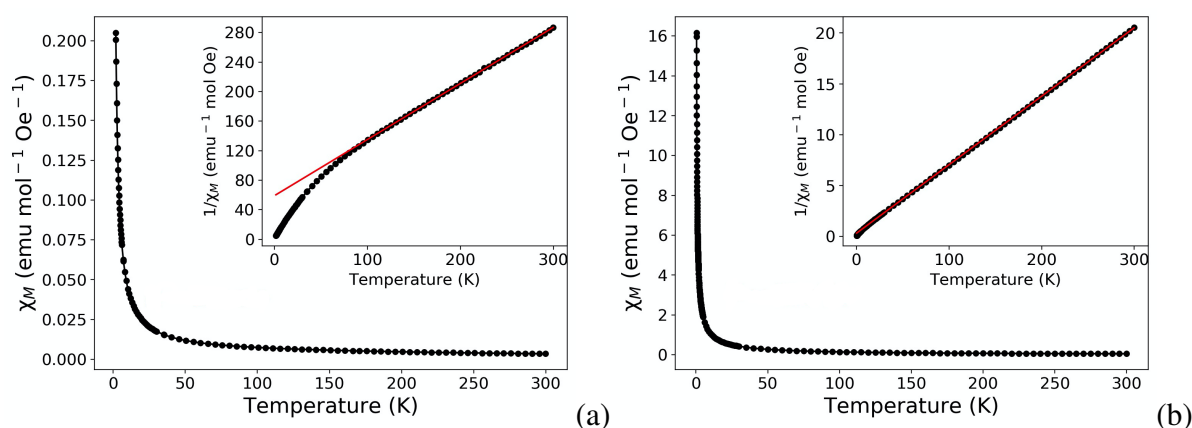


**Figure 4.28** (a) Magnetic Susceptibilities of (a) Nd(HCO$_2$)$_3$ and (b) Dy(HCO$_2$)$_3$ in a 100 Oe field, between 0.4 - 300 K, with the Curie-Weiss fit in the insert.

Dy(HCO$_2$)$_3$ follows Curie-Weiss behaviour to low temperatures while Nd(HCO$_2$)$_3$ deviates from this near 80 K, suggesting quenching of orbital angular moment happens at higher temperatures in the latter. The Curie-Weiss temperatures and effective magnetic moments obtained from these fits are shown in Table 4.5, and are close to the values expected of 3.62 and 10.65 $\mu_B$. [25] The fits to the data yield a effective magnetic moments, Curie constants and $\theta_{CW}$ summarised in Table 4.5 for Nd(HCO$_2$)$_3$ and Dy(HCO$_2$)$_3$.

**Table 4.5** A summary of the magnetic properties of Nd(HCO$_2$)$_3$ and Dy(HCO$_2$)$_3$.

| Framework | $\theta_{CW}$ (K) | Curie Constant (emu mol$^{-1}$ Oe$^{-1}$) | Magnetic Moment ($\mu_B$) |
|---|---|---|---|
| Nd(HCO$_2$)$_3$ | $-77.49$ | 1.31 | 3.24 |
| Dy(HCO$_2$)$_3$ | $-4.14$ | 14.84 | 10.89 |

Isothermal magnetisation of $Nd(HCO_2)_3$ and $Dy(HCO_2)_3$, shown in Figure 4.29 suggest spins with single ion anisotropy, as indicated by $M_{sat}$ significantly less than that the expected $g_J J$. The $M_{sat}$ value in moderately applied field indicate the spins are most likely Ising. In high fields ($> 5$ T) the magnetisation becomes linear-field dependent, indicating the onset of Van Vleck paramagnetism, [183] related to the field induced electronic transitions. [200, 201]
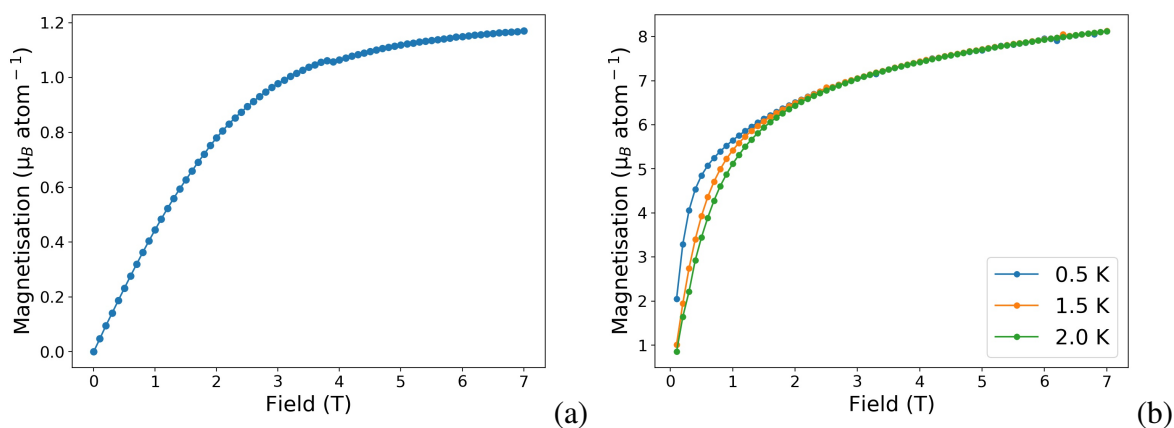


**Figure 4.29** Magnetisation measurements between 0-7 T for (a) $Nd(HCO_2)_3$ at 2 K and (b) $Dy(HCO_2)_3$ at variable temperatures.

The heat capacity data on $Dy(HCO_2)_3$, collected between 450 mK and 3 K, also lacks any significant features, other than an increasing in heat capacity with lowering temperature, which can be ascribed to the nuclear heat capacity effects or the Schottky anomaly. [195]
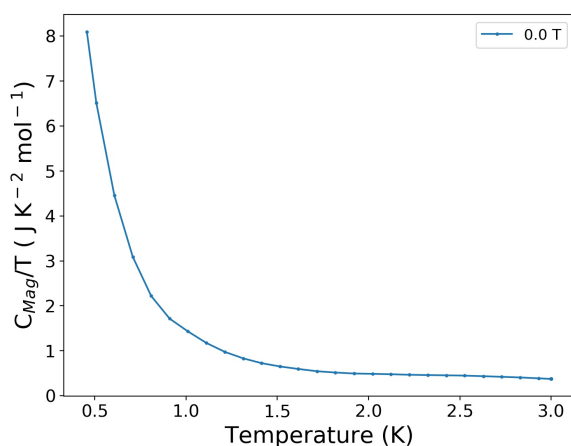


**Figure 4.30** Heat capacity measurements in zero applied field, of $Dy(DCO_2)_3$ between 0.5 - 3 K, showing the magnetic heat capacity and indicating no phase transitions.

## 4.5.2 Neutron Diffraction

Samples of Ce(DCO$_2$)$_3$, Pr(DCO$_2$)$_3$, Nd(DCO$_2$)$_3$ and Dy(DCO$_2$)$_3$ were measured on the WISH diffractometer to 1.5 K in search of any evidence for magnetic diffuse scattering. We note that A(DCO$_2$)$_3$ samples (where A = Pm, Sm, Eu and Gd) were not tested due to the high absorption cross sections, or in the case of Pm, its radioactivity. No evidence for magnetic diffuse scattering was found in these four compounds, indicating a lack of significant magnetic interactions in these materials. This may suggest why, in the hydrogenated analogues, Dy(HCO$_2$)$_3$ lacks the higher magnetocaloric performance found Tb(HCO$_2$)$_3$ and Ho(HCO$_2$)$_3$ at higher temperatures and in applied magnetic fields as previously reported by Saines *et al.*. [4] This emphasizes that while Ising spins may help to optimise magnetocaloric properties under low applied fields it is not sufficient unless accompanied by optimised magnetic interactions between cations. The magnetocaloric properties of Dy(HCO$_2$)$_3$ continues to increase gradually down to 2 K, the lowest temperature measured where the entropy change exhibited is higher than Er(HCO$_2$)$_3$, which is likely due to the smaller magnetic moment of erbium compared to dysprosium. Further characterisation of Dy(DCO$_2$)$_3$ should be performed at temperatures lower than 0.5 K in search of order to confirm the nature of the weak magnetic interaction within this material. If the chain interactions are determined by the ground state of the lanthanide ion, from the observation of the weak antiferromagnetism seen in Er(DCO$_2$)$_3$ and the Kramers ground state of dysprosium we would expect an antiferromagnetic structure at lower temperatures in Dy(DCO$_2$)$_3$.

The neutron diffraction patterns obtained from Ce(DCO$_2$)$_3$, Pr(DCO$_2$)$_3$, Nd(DCO$_2$)$_3$ and Dy(DCO$_2$)$_3$ were fitted to obtained their low temperature crystal structures, which were found to be well fitted in *R*3*m* symmetry. This is particularly significant in the case of Pr(HCO$_2$)$_3$, because a previous Raman study concluded there was a second order phase transition at ≈140 K to *R*3 symmetry. [219] In contrast we find that an excellent fit to the data is achieved with the *R*3*m* model in all the *Ln*(DCO$_2$)$_3$, at all temperatures with no significant improvement found when symmetry is lowered to *R*3. Fits to the 1.5 K diffraction pattern can be seen in Figure 4.31 and crystallographic details seen in Table 4.6 and A.1.
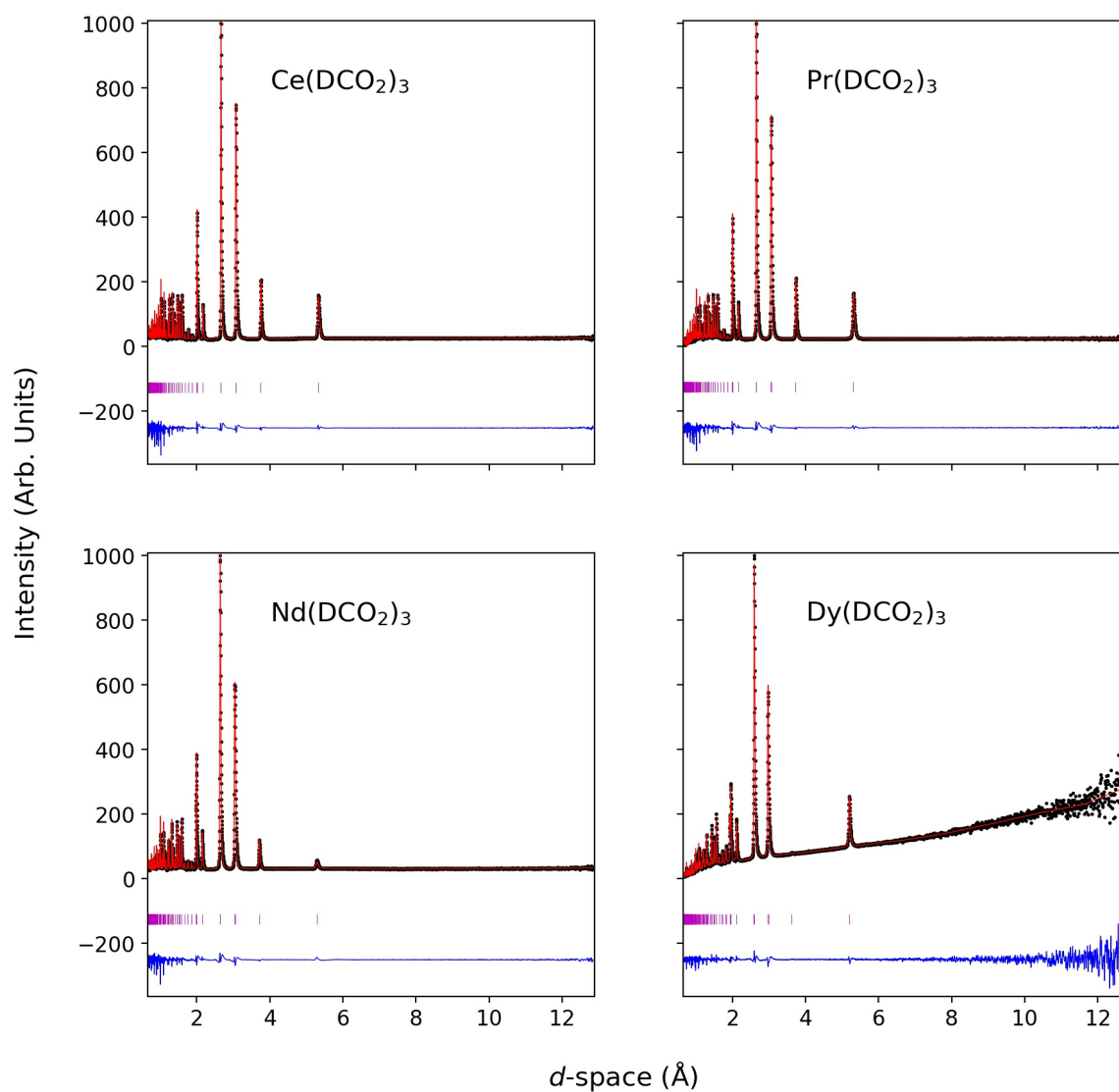
**Figure 4.31** Rietveld fits of *Ln*(DCO$_2$)$_3$ from bank 2/9 of WISH, at 1.5 K, with a *R3m* model of the *Ln*(DCO$_2$)$_3$. Experimental data shown in black, fit shown in red, Bragg reflections shown in magenta and the difference curve shown in blue.

**Table 4.6** A table summarising the structural properties of the non-magnetically ordering *Ln*(DCO$_2$)$_3$ frameworks at 1.5 K.

| Framework | a (Å) | c (Å) | R$_p$ (%) | R$_{wp}$ (%) | Space Group |
|---|---|---|---|---|---|
| Ce(DCO$_2$)$_3$ | 10.65644(32) | 4.11018(16) | 7.05 | 5.73 | *R3m* |
| Pr(DCO$_2$)$_3$ | 10.61446(36) | 4.08233(18) | 7.30 | 5.91 | *R3m* |
| Nd(DCO$_2$)$_3$ | 10.57028(42) | 4.05726(19) | 5.88 | 5.16 | *R3m* |
| Dy(DCO$_2$)$_3$ | 10.39072(38) | 3.95551(16) | 4.22 | 3.45 | *R3m* |

# 4.6 Conclusions

This chapter has explored the physical properties, the magnetic structure and correlations of the $Ln(DCO_2)_3$, in the short and long range ordered magnetic phases and related this to the magnetocaloric effect. Materials with the highest magnetocaloric effects in low applied fields, namely $Tb(HCO_2)_3$ and $Ho(HCO_2)_3$ are the materials which contain magnetic diffuse scattering, for the deuterated analogues. RMC analysis of the diffuse scattering reveals it corresponds to short range 1D ferromagnetic correlations along the chains of $Ln^{3+}$ Ising-like spins aligned along the $c$-axis. The correlations length of these 1D ferromagnetic chains grows with decreasing temperature before transitioning to a quasi-long range ordered TIA state at 1.6 K and an ECO state at 1.2 K for $Tb(DCO_2)_3$ and an ECO state at 0.7 K in $Ho(DCO_2)_3$. While the TIA state has previously been studied the new ECO states are reported for the first time as a result of the work in this thesis.

These ECO states are determined to be consistent with materials with a complex average structure within which can be reduced to an elegant emergent feature. The Bragg-like peaks, which in this work we have analysed in a conventional crystallographic fashion have significant diffuse scattering present, indicating the correlations are finite. Thus, as seen in the previous work on the TIA phase, the models we report for these materials may simply be an approximation of the magnetic structure of these phases that neglects the correlated disorder that gives rise to the diffuse scattering. Careful analysis of the Ho analogue have determined the broad nature of the Bragg-like reflections are most likely intrinsic to the system and not a result of finite magnetic domains. In contrast with these compounds the $Ln(DCO_2)_3$ phases, which show poorer magnetocaloric performance above 4 K and in low applied magnetic fields display no magnetic diffuse scattering at 1.5 K, indicating the absence of significant magnetic correlations in these materials. Analysis of neutron diffraction patterns of $Er(DCO_2)_3$ indicates the emergence of a phase with antiferromagnetic intrachain coupling near 50 mK, but the temperature at which this emerges emphasizes the weak nature of the magnetic interactions in this material.

The understanding of $Tb(DCO_2)_3$ and $Ho(DCO_2)_3$ is far from complete. Further analysis is required to understand the peculiarities of the features in the inelastic neutron scattering spectra of $Tb(DCO_2)_3$, and to investigate that of $Ho(DCO_2)_3$. The analysis performed on the ECO of these materials only characterises the average structure, but further Monte-Carlo analysis can be performed to fit the diffuse features underneath the Bragg-like peaks, and therefore provide insights into its true nature.

The combination of frustration and 1D ferromagnetic Ising chains in these materials appears to be directly responsible for the highly efficient magnetocaloric effect in these materials, inducing a strong change in magnetisation under a moderate applied magnetic field. The accompanying magnetic frustration prevents long range order from forming in the paramagnetic operating temperatures but are easily overcome by a moderate applied magnetic field, allowing for high changes in entropy. The combination of these factors leads to some highly efficient magnetocaloric materials, produces the exotic magnetic ground states observed and highlights the practical uses for these fundamentally interesting magnetic systems.

# 5

# Structural and Magnetic Order of the $Ln$ODCO$_3$ Frameworks

## 5.1   Introduction

As shown in Chapter 3, several $Ln$OHCO$_3$ ($Ln$ = Tb, Dy and Ho) frameworks provide optimised $-\Delta S_m$ above 4 K and for applied magnetic field changes of less than 2 T, at the expense of decreasing performance below this temperature. [5] These orthorhombic frameworks are isostructural with a lattice structure that combines the elements required for 1D and frustrated magnetism, with nearest neighbour chains along the $b$-axis and a triangular-like lattice in $ac$ plane. While three $Ln$OHCO$_3$ members of this family have magnetocaloric performance optimised for these conditions, the performance of the Tb and Dy materials is particularly notable.

These compounds feature higher $-\Delta S_m$ for lower applied fields than the maximum of the canonical magnetocaloric material Gd$_3$Ga$_5$O$_{12}$, which peaks at a much lower temperature of 1.2 K. [5] In contrast, ErOHCO$_3$, which also appears to feature Ising-like spins based on its magnetisation, does not feature such optimised magnetocaloric performance but instead this increases gradually at all temperatures down to 2 K. Therefore, while Ising-like interactions may play a role in optimising the performance of such materials it is not sufficient on its own. This is perhaps unsurprising given magnetic frustration, in which all magnetic interactions in a material are unable to be optimised simultaneously, is well known to play a key role in the properties of magnetocaloric oxides, including Gd$_3$Ga$_5$O$_{12}$ itself. [67, 220, 221]

Chapter 4 presented the neutron scattering studies of $Tb(HCO_2)_3$ and $Ho(HCO_2)_3$ and indicated that their magnetocaloric properties, also optimised for use above 4 K in less than 2 T applied fields, are linked to the presence of 1D ferromagnetic chains packed in a frustrated antiferromagnetic triangular array. [4, 18, 194] A subsequent study finds ferromagnetic chains improve magnetocaloric performance, over a similar temperature range, in oxide materials also. [17]

The higher magnetocaloric entropy changes of $DyOHCO_3$ and $TbOHCO_3$ compared to the $Ln(HCO_2)_3$ emphasises the case for using neutron diffraction to understand the way in which the atomic-level magnetic interactions in these materials influence the macroscopic properties of the $LnOHCO_3$ phases. The $LnOHCO_3$ frameworks structure is more complex than that of the $Ln(HCO_2)_3$ phases and can be viewed as either consisting of face-sharing chains of $LnO_{10}$ polyhedra or corner sharing zig-zag chains of $LnO_8$ polyhedra. Density-Functional Theory calculations by Chen *et al.*, [222] on $GdOHCO_3$ suggested the presence of dominant antiferromagnetic coupling within the face-sharing chains ($J_1$ in Chapter 1), with frustrated antiferromagnetic coupling between them ($J_2$ and $J_3$). This is consistent with the shortest superexchange pathway being through the hydroxide oxygen atom along the $b$-axis, such that coupling between face-sharing chains of $LnO_{10}$ polyhedra may dominate even if the other two superexchange pathways along such chains are longer than others in this material (see Figure 1.16 for structure). While dipole-dipole magnetic coupling can also be significant quantifying these interactions for a particular structure requires further analysis, which was omitted by the previous study of Chen *et al.* [222].

In this chapter to establish a clear understanding of how the microscopic interactions of $LnOHCO_3$ effect their magnetocaloric entropy change we have studied these compounds using neutron diffraction. We have established both the local magnetic correlations in these materials in their short ranged ordered phase, in which they exhibit their magnetocaloric properties, and in the case of $HoOHCO_3$ the long range ordered magnetic states they exhibit at low temperatures. Those compounds with magnetocaloric properties optimised for use above 4 K in low applied magnetic fields all exhibit clear magnetic diffuse scattering. The diffuse scattering arises from a lattice featuring competing antiferromagnetic couplings in the $ac$ plane, and ferromagnetic Ising chains along the $b$-axis. The ferromagnetic chains are arranged into non-collinear chains with a preference for spin orientations close to the $b$-axis, but canted into the $ac$ plane. The long range incommensurate and commensurate magnetic structures of $HoOHCO_3$ exhibited below 1.2 K and 0.8 K, respectively, also feature ferromagnetic chains that are coupled together antiferromagnetically. This highlights that

ferromagnetic units coupled antiferromagnetically to each other in a frustrated lattice can be lead to optimised magnetocaloric performance under more moderate conditions. This is in sharp contrast to GdOHCO₃, which is optimised for application at lower temperatures, that features antiferromagnetic coupling within the chains.

## 5.2   *Ln*OHCO₃ Crystal Structure and Thermal Stabilities

*Ln*OHCO₃ are known to form as different polymorphs in at least 2 different space groups: $P\bar{6}$, most commonly adopted at higher synthetic pressures, and orthorhombic space group(s) *Pnma* or $P2_12_12_1$, which typically form at lower synthetic pressure. [76] The $P\bar{6}$ polymorph is distinctly different from the other two reported structures, having a much larger unit cell with layers of edge and face sharing polyhedra separated by $CO_3^{2-}$, through corner sharing polyhedra. The $P\bar{6}$ can also be considered consisting of layers of triangular arrays. In our study it is found to only be adopted by the larger lanthanides, Pr and Nd. SmOHCO₃ made at 170°C is a mixed phase of hexagonal and orthorhombic structures but lowering the hydrothermal temperature to 150°C forms a pure orthorhombic phase. The heavier lanthanides Gd-Er were only found to adopt orthorhombic structures so, since they are more likely to have the significantly magnetocaloric properties of interest to this study, the rest of this section will focus on distinguishing which of the two possible orthorhombic structures they adopt.

The *Pnma* and $P2_12_12_1$ structures are very similar and indeed we could not distinguish between these using powder X-ray diffraction results presented in chapter 3. The $P2_12_12_1$ structure has 4 unique oxygen atoms, one for the hydroxide groups and three distinct oxygen atoms in the carbonate anions (see Figure 1.16) while the *Pnma* structure has 3 unique oxygen atoms, with two oxygen atoms in each carbonate anion being related by symmetry. The only other significant difference between the two structures is that the identity of the *a* and the *b* axis are reversed in their conventional settings. In both, the lanthanide can be viewed as being 10 coordinate with chains of $Ln$O₁₀ face-sharing polyhedra, with edge-sharing inter-chain connectivity. Alternatively, if the longest two bonds in the $Ln$O₁₀ polyhedra are neglected, which are 0.1-0.2 Å longer than other *Ln*-O bonds in this structure, it can be simplified as consisting of highly distorted $Ln$O₈ square antiprisms; these can in turn be viewed as being packed into edge-sharing $Ln$O₈ chains connected by oxygen atoms from the carbonate ligands with corner-sharing interchain connectivity via the hydroxide groups. Either of these simplifications of this complex structure feature magnetic chains, shown to be linked with

low-field high performance magnetocalorics, with previous calculations indicating intrachain coupling is dominant. [18, 77]

Through slow cooling of the hydrothermal parr bomb, (see Section 2.2 for synthetic details) we have been able to synthesize single crystals of TbOHCO$_3$ and the single crystal structures determined from these have $P2_12_12_1$ orthorhombic symmetry, with systematic absences required for the *Pnma* structure clearly violated.

Only the atomic displacement parameters for Tb were refined anisotropically, with lighter elements refined isotropically as the quality of the fit is insensitive to these values. The hydrogen atom positions were determined from the Fourier difference and refined with a restraint that it remains 0.96 Å from the oxygen, typical for an O-H bond, [121] to which it is attached and its displacement parameters constrained to be 1.5 times the oxygen that it is attached to (See Table 5.1 for crystallographic details). Despite equivalent synthesis methods for all the *Ln*OHCO$_3$ and attempted synthetic optimisation, single crystals were not available from the other members of this series.

**Table 5.1** Crystallographic data for the structure of TbOHCO$_3$ determined by single crystal X-ray diffraction.

| Parameter | Statistic |
|---|---|
| Formula | TbCHO$_4$ |
| Formula Weight | 235.94 |
| T (K) | 169(2) |
| Crystal System | Orthorhombic |
| Space Group | $P2_12_12_1$ |
| a (Å) | 4.8551(2) |
| b (Å) | 7.0178(3) |
| c (Å) | 8.4394(4) |
| V (Å$^3$) | 287.55(2) |
| Z | 4 |
| $\rho_{cal}$ (g $cm^{-3}$) | 5.450 |
| $\mu$ ($cm^{-1}$) | 24.402 |
| Refl. meas./unique | 2063/710 |
| Parameters refined | 33 |
| $R_1$, $wR_2^a$ (all) | 0.0400, 0.0776 |
| $R_1$, $wR_2^a$ (obs) | 0.0341, 0.0725 |
| Goodness of Fit | 1.062 |

Powder X-ray diffraction patterns of the two possible orthorhombic polymorphs cannot distinguish between the two symmetries because the weak reflections indicating violation

of *Pnma* symmetry are weaker than the background of the instruments used in this study even for longer measurements. The greater sensitivity of neutron diffraction to the positions of light atoms, such as the oxygen atoms that are the primary difference between these two structures, enables this to clearly distinguish between these two possibilities.

Neutron diffraction patterns we have measured on *Ln*ODCO$_3$ (*Ln* = Tb-Er) samples on the WISH neutron diffractometer clearly all show reflections that violate the systematic absences expected for the *Pnma* space group confirming that all samples adopt the $P2_12_12_1$ space group. This is most clearly highlighted by a weak reflection observed at a *d*-spacing of about 3.18 Å (the [102] reflection in $P2_12_12_1$) in all diffraction patterns of these compounds, which is allowed by $P2_12_12_1$ symmetry but not in *Pnma* where this is the [012] reflection (see Figure 5.1).
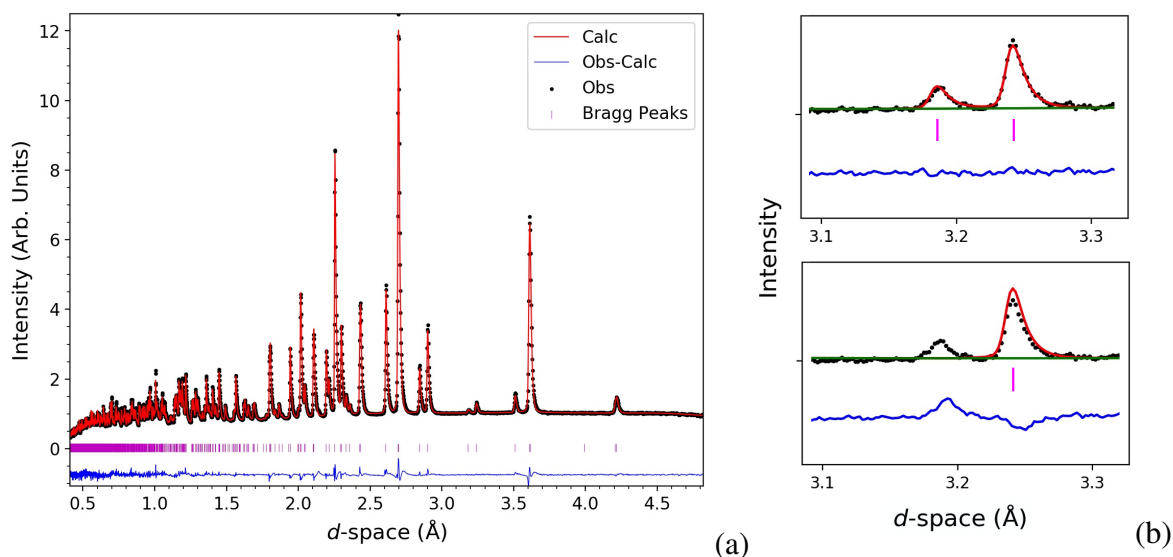


**Figure 5.1** (a) Neutron diffraction patterns of TbODCO$_3$ at 100 K from banks 5/6 of the WISH diffractometer. (b) close up of the [102] reflection at 3.18 Å, and correct fitting using $P2_12_12_1$ space group – R$_p$, R$_{wp}$ and $\chi^2$ of fit = 1.73%, 2.52% and 16.09 respectively, and close up of Rietveld fit in *Pnma* showing systematically absent [012] reflection in *Pnma* - R$_p$, R$_{wp}$ and $\chi^2$ of fit = 2.24%, 4.26% and 45.98 respectively. Black points, red line, blue line and purple markers indicate the data, calculated intensity, difference plot and position of the Bragg markers, respectively.

These structures remain in the $P2_12_12_1$ space group for all temperatures recorded between 1.5-100 K for all four compounds studied. Additional diffraction patterns of TbOHCO$_3$ and ErOHCO$_3$ obtained at 300 K indicate these materials retain $P2_12_12_1$ symmetry up to ambient conditions (Figure 5.2 and 5.3). Given Tb and Er are the largest and smallest lanthanides, respectively, hosted in the series of compounds studied by neutron diffraction, we suggest that none of these compounds have any structural phase transitions between 1.5-300 K retaining

$P2_12_12_1$ throughout this temperature range. This precludes the possibility of observations of a *Pnma* polymorph due to structural phase transition up to ambient temperature in these four compounds. Unfortunately, due to its high neutron absorption cross section it is not possible to use neutron diffraction to directly study the Gd member of this series, although it is likely it adopts the same structure as found for Tb-Er, at least under the synthetic conditions used in this study. Bond distances determined by Rietveld refinements of neutron diffraction data can be seen in the Table A.2, and bond valence sums [207] were determined to be consistent with trivalent oxidation states for Tb, Dy, Ho and Er in *Ln*ODCO$_3$; values of 3.12(3), 3.14(9), 3.10(4) and 3.16(5) respectively, were obtained. These values must be considered tentatively, because they have been calculated for materials measured at temperatures well below room temperature, and the empirical bond valence method values have been calculated for structures at room temperature.
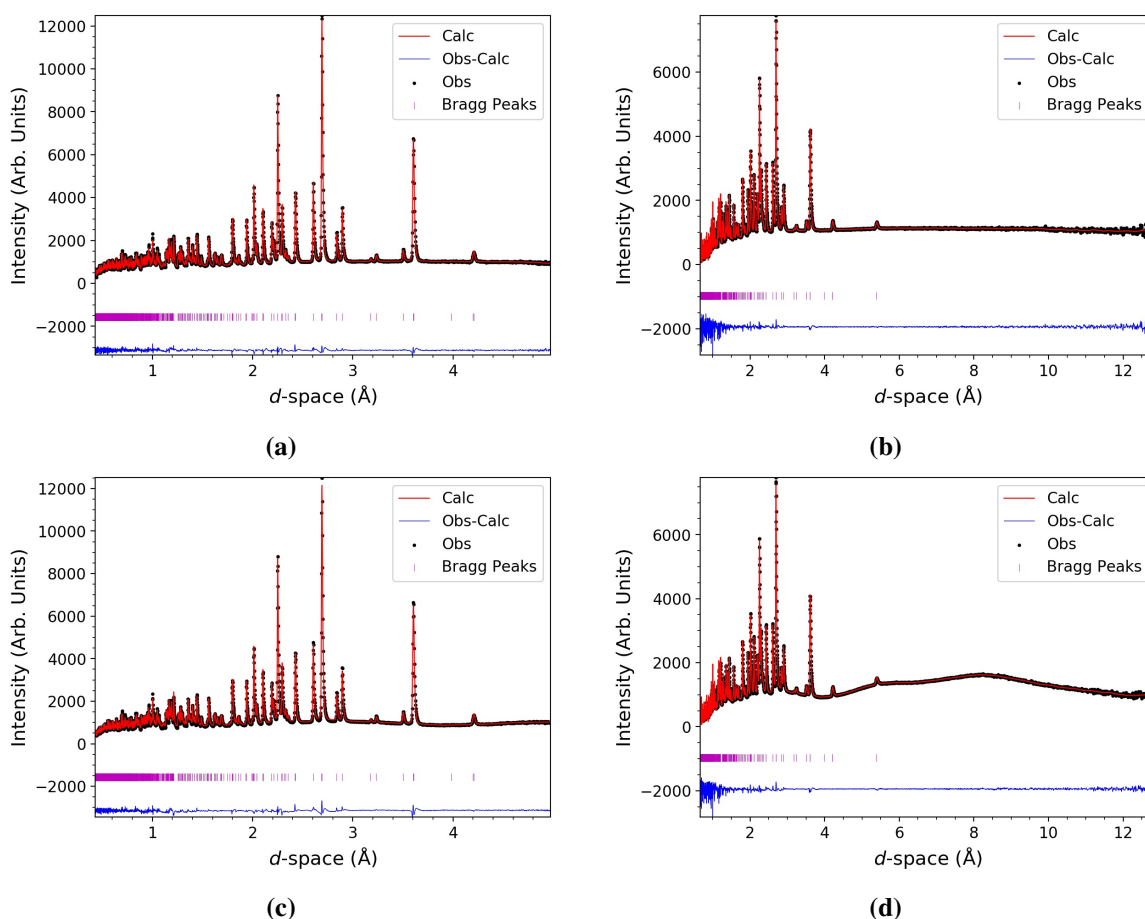


**Figure 5.2** Rietveld refinements of neutron diffraction data of TbODCO$_3$ (a) 300 K - Bank 5/6, (b) 300 K - Bank 2/9, (c) 1.5 K - Bank 5/6, (d) 300 K - Bank 2 using the $P2_12_12_1$ space group
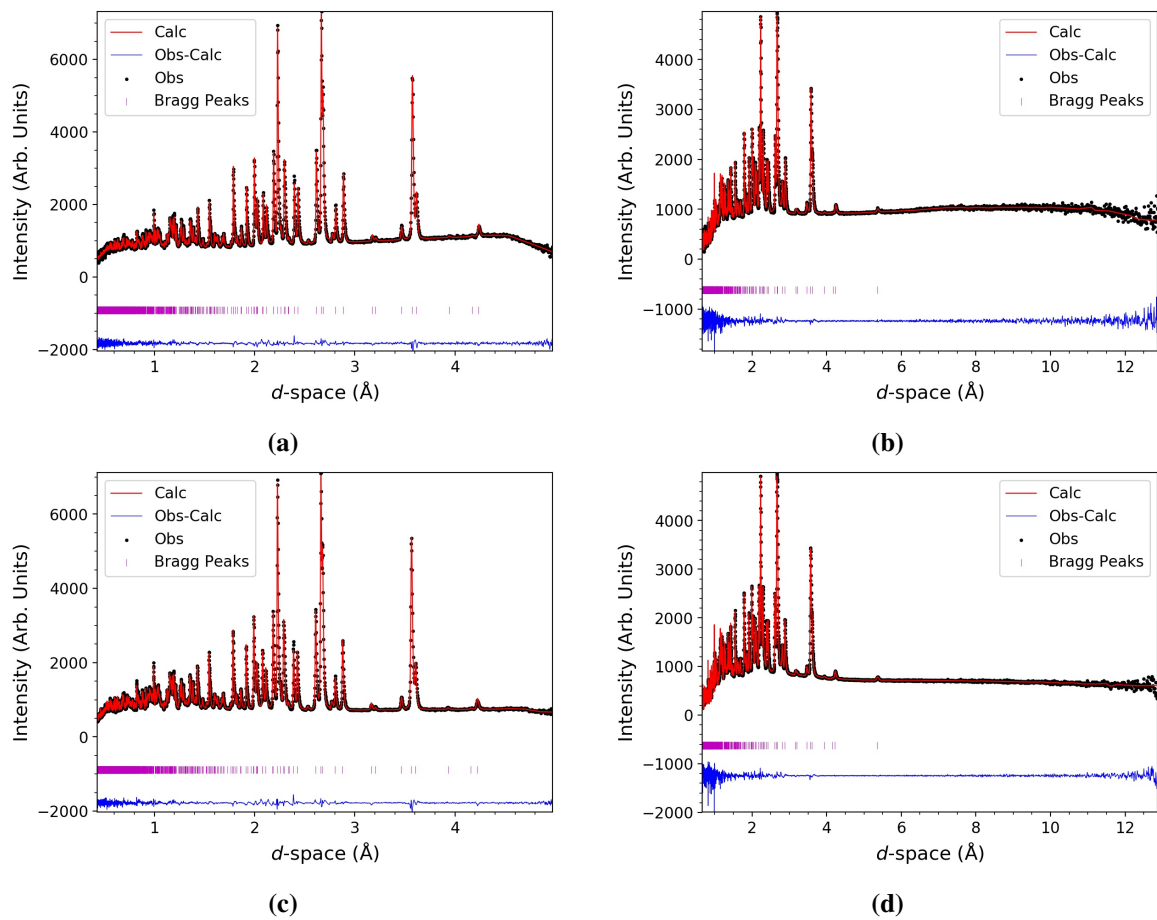
**Figure 5.3** Rietveld refinements of neutron diffraction data of ErODCO$_3$ (a) 300 K - Bank 5/6, (b) 300 K - Bank 2/9, (c) 1.5 K - Bank 5/6, (d) 1.5 K - Bank 2/9 using the $P2_12_12_1$ space group

Neutron diffraction measurements of the *Ln*ODCO$_3$ (where *Ln* = Tb, Dy, Ho and Er) frameworks showed typical reduction in the lattice parameters on cooling as shown in Figure 5.4.
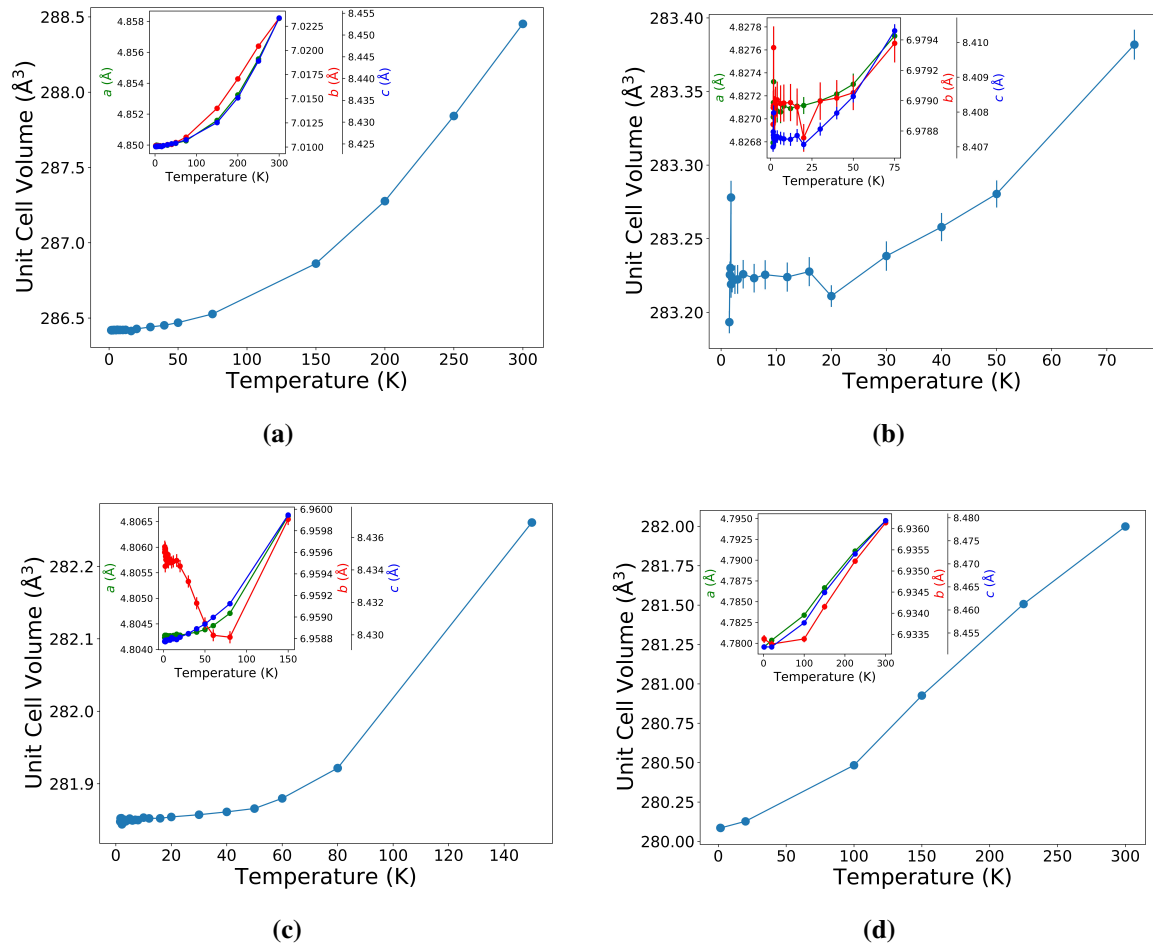
**Figure 5.4** The change in unit cell volume and lattice parameters, in the insert, with respect to temperature for (a) TbODCO$_3$, (b) DyODCO$_3$, (c) HoODCO$_3$ and (d) ErODCO$_3$. Errors are shown on the unit cell value, but smaller than the markers.

In DyODCO$_3$ the deviations from thermal expansion of the lattice parameters can be ascribed to noisy data, caused by the high absorption cross section of Dy. HoODCO$_3$ shows an anomalous decrease of the *b* length between 20-80 K, however there is no change in diffraction patterns to suggest a phase transition. This anomalous negative thermal expansion may indicate some, yet unknown, feature that neutron diffraction data is not sensitive to. Refinements down to the base temperature of T$_{base}$ = 1.5 K, revealed typical reduction in the unit cell volume upon cooling. Refined models of the nuclear structures at 1.5 K of TbODCO$_3$, DyODCO$_3$ and HoODCO$_3$ yield $J_1$ distances of 3.799(3), 3.778(5) and 3.762(5) Å, $J_2$ distances of 4.851(9), 4.843(9) and 4.802(12) Å; $J_3$ distances of 5.077(5), 5.048(6) and 5.101(7) Å; and $J_4$ distances of 5.162(5), 5.183(6) and 5.115(7) Å, respectively. These interactions are summarised in Figure 5.5.
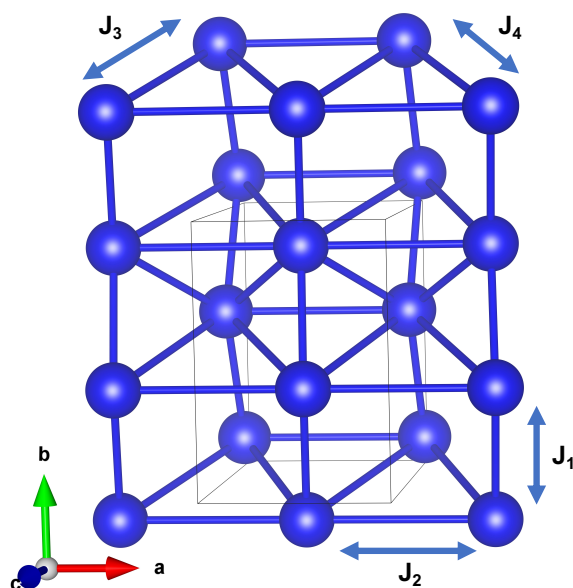
**Figure 5.5** A diagram showing the J magnetic exchange interactions in the *Ln*ODCO$_3$, shown off the *c*-axis, only the magnetic cations, shown in purple, have been shown for clarity.

## 5.3 Physical Property Measurements

TGA studies of *Ln*OHCO$_3$ have shown the frameworks to be stable until around 450°C whereby they endothermically undergo oxidation of the carbonate ligand to produce *Ln*$_2$O$_3$ (Figure A.10). Fourier transform infrared spectrometer in the range 500-4000 cm$^{-1}$, revealed IR absorptions for what we have assigned as O-H at 3400 cm$^{-1}$, C-O at 1400 cm$^{-1}$, *Ln*-OH at 823 cm$^{-1}$, and *Ln*-OC at 705 cm$^{-1}$ (See Figure A.11).

In Section 3.2.2 it was reported that the *Ln*OHCO$_3$ frameworks do not show any indication of long range order down to 2 K, and follow Curie-Weiss behaviour, with Weiss temperatures of $-5.04$ K, $-0.84$ K, $-3.83$ K and $-7.47$ K, for Tb, Dy, Ho and Er. [5] Our magnetic susceptibility measurements below 2 K of TbOHCO$_3$ and HoOHCO$_3$ show features indicative of the formation of long range order at $\approx$1.2 K and $\approx$0.8 K, respectively (see Figure 5.6). The observed divergence of the zero field-cooled (ZFC) and field-cooled (FC) susceptibility suggest a weak ferromagnetic nature to this order, which we ascribe to a small degree of spin canting of the long-range ordered antiferromagnetic structure since, as discussed below, there is no indication of a net ferromagnetic moment in the ordered magnetic structure of HoOHCO$_3$ determined by neutron diffraction.
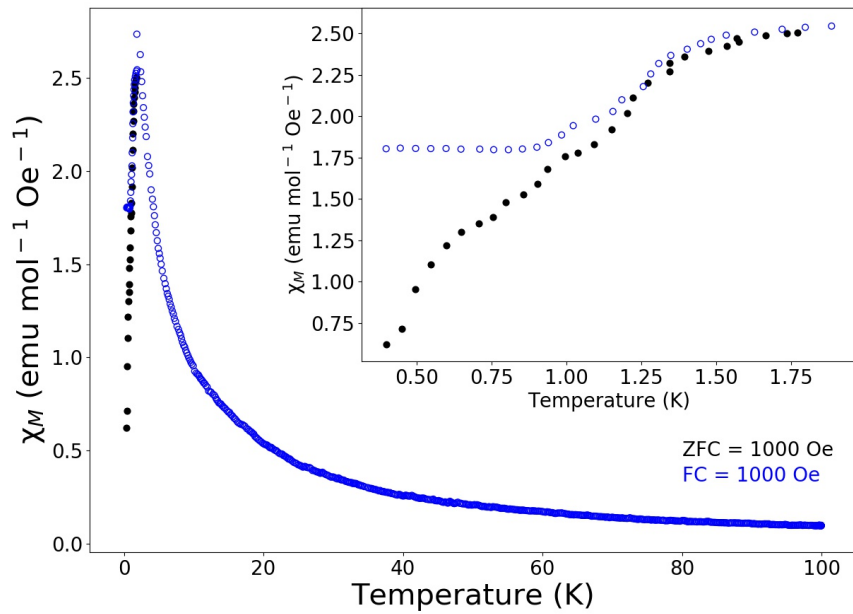
(a)
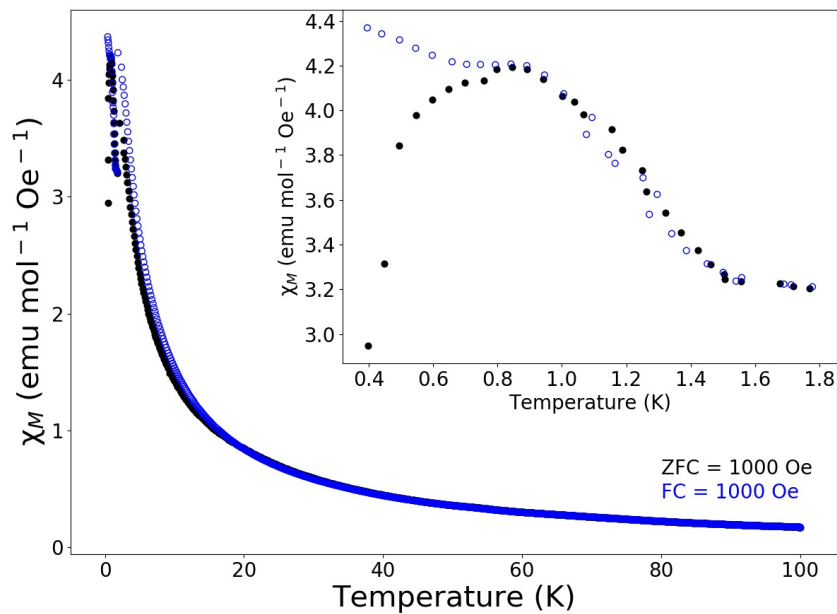


(b)

**Figure 5.6** Magnetic susceptibility of (a) TbOHCO$_3$ and (b) HoOHCO$_3$ in a 1000 Oe field, below 100 K, with a close up of temperatures below 1.8 K in the insert.

## 5.4   *Ln*ODCO$_3$ Short Range Order

Neutron diffraction measurements in zero-field of the *Ln*OHCO$_3$ frameworks indicated that, of the samples measured, TbOHCO$_3$, DyODCO$_3$ and HoODCO$_3$ showed significant magnetic diffuse scattering below 20 K, indicative of short range order. This is an important result, as these materials show magnetocaloric properties maximised for use above 4 K for low applied magnetic field changes. Only ErODCO$_3$, whose magnetocaloric properties gradually increases on cooling down to 2 K and, resembles GdOHCO$_3$ but with overall poorer performance, did not show any sign of magnetic diffuse scattering, indicative of the lack of significant magnetic correlations. It was noted that the strength of magnetic diffuse scattering observed at 1.5 K decreased significantly from TbOHCO$_3$ to HoODCO$_3$ to DyODCO$_3$, indicating a decrease in the strength of the magnetic correlations giving rise to this, but does not correlate with bond distances. The observed diffuse magnetic scattering of TbOHCO$_3$, DyODCO$_3$ and HoODCO$_3$ were well fitted by the RMC method, with stereographic projections of refined Heisenberg-like moments, which have unconstrained spin orientations, showing the spin preferentially aligned close to the *b*-axis, as shown in Figure 5.7.
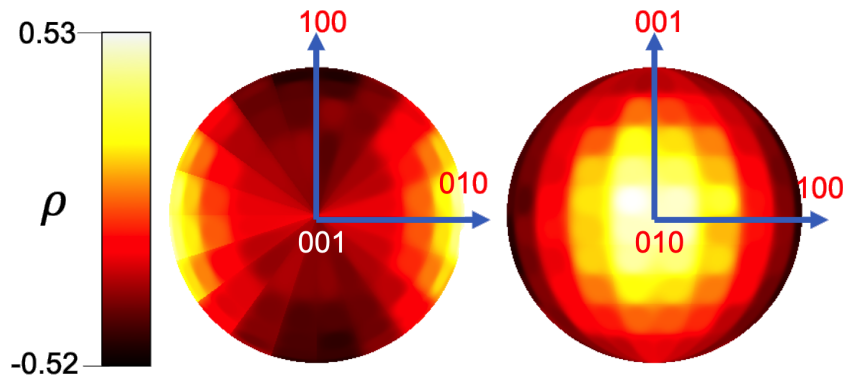


**Figure 5.7** Stereographic projections of the spin orientations averaged over 100 RMC Heisenberg-like fits to diffuse neutron scattering data from TbODCO$_3$ at 1.6 K. The relative spin density is defined as $\rho(\theta,\phi) = \frac{\rho(\theta,\phi)}{Nd(cos\theta)d\phi}$. Bright spots indicate areas of high spin density.

Attempts were therefore made to fit the diffuse scattering data with Ising spins constrained to point only along the *b*-axis. These refinements produced poor fits to the data and so Ising moments directions were manually modified and repeatedly tested until an optimal fit was achieved for TbODCO$_3$ at 1.5 K, because this data provided the best signal to noise ratio. The best fit was found to occur using a model in which the orientations of the Ising spins were allowed to orient towards four independent easy axes, primarily along the *b*-axis but

canted into the *ac* plane. This four-site Ising model indicates the easy axes are oriented in the direction of the nearest chain neighbour with the unit vectors of these moments corresponding to [$\pm$0.33, 1, $\pm$0.66]. These spin orientation produced excellent fits to the data for TbODCO$_3$ at all temperatures (Figure 5.8), although of slightly lower quality than the Heisenberg refinement ($\chi^2 \approx$130 and $\approx$150 at 1.5 K for typical Heisenberg and Ising models respectively); the marginal improvement of the Heisenberg model is inevitable due to its higher degrees of freedom.
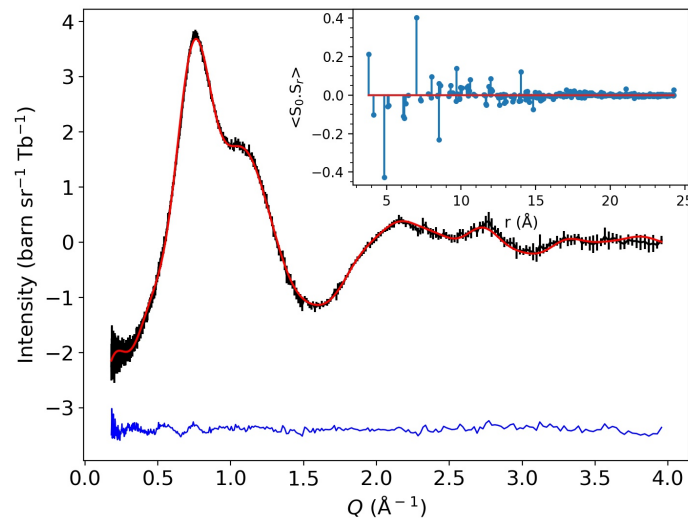


**(a)**
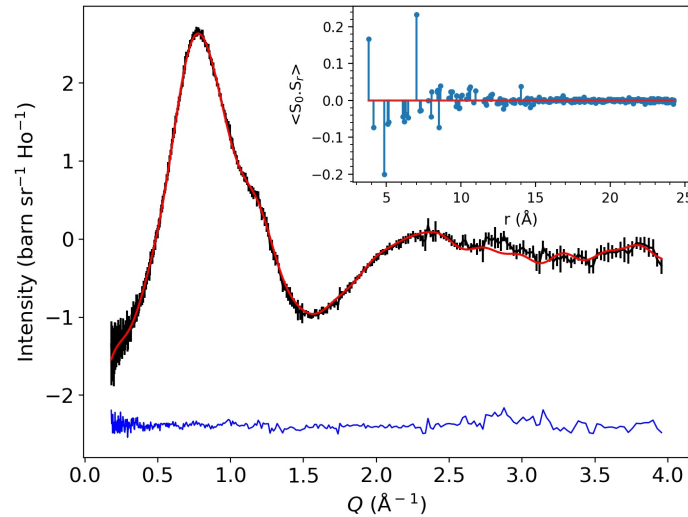


**(b)**

**Figure 5.8** Reverse Monte Carlo fits to magnetic diffuse of (a) TbODCO$_3$ and (b) HoODCO$_3$ at 1.5 K, data points in black, fit in red and the difference in blue, using an Ising model at 1.5 K. Spin correlations as produced from SPINVERT are shown in the insert.

Since the HoODCO$_3$ data are qualitatively similar and Heisenberg refinements yield similar spin orientations the same Ising model was also used to fit the HoODCO$_3$ data, producing equally good fits ($\chi^2 \approx 120$ and $\approx 170$ at 1.5 K). Fitting the same model to the DyODCO$_3$ data, however, did not produce suitable fits and despite refinement of the spin orientation for the DyODCO$_3$ no quality fits were obtained for an Ising model ($\chi^2 = \approx 112$ for Heisenberg compared to $\approx 450$ for Ising at 1.5 K (Figure 5.9).



**(a)**                                                                  **(b)**
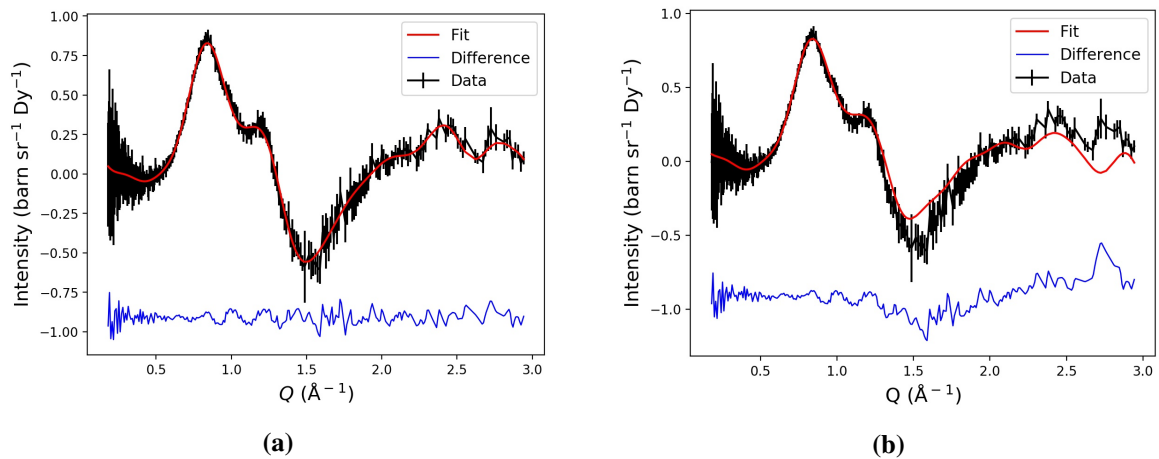
**Figure 5.9** Reverse Monte Carlo fits to magnetic diffuse of DyODCO$_3$ at 1.5 K, using a Heisenberg model (a) and an Ising model (b) data points in black, fit in red and the difference in blue, using an Ising model at 1.5 K.

We expect that the significantly poorer fit for DyODCO$_3$ using Ising-like spins is a result of the combination of the failure to fully correct the high level of absorption caused by the presence of Dy and the large degree of incoherent scattering caused by this element, combined with the weaker diffuse scattering observed. The strong similarity of the diffuse scattering features of the three samples, and previous inference of Ising-like dimensionality based on magnetisation of these materials (see Section 3.2.2), leads us to suggest all three compounds have Ising-like spins. The resulting short range magnetic structure can be seen in Figure 5.10. It would be possible to investigate this hypothesis, using isotopically enriched samples of $^{160}$Dy or $^{163}$Dy that have smaller absorption cross sections. [223] However, respective $^{160}$Dy and $^{163}$Dy natural abundances of 2.34 and 24.9 %, made this option prohibitively expensive for these studies.
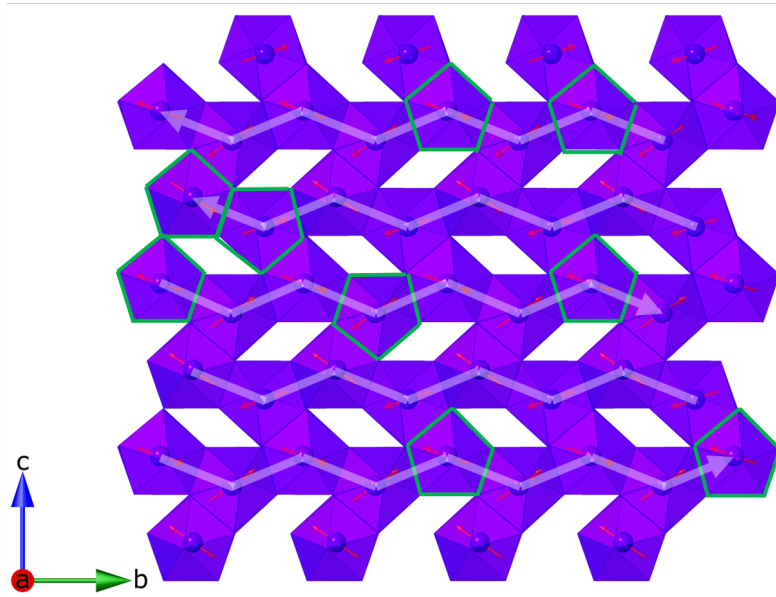
**Figure 5.10** Spin orientations in the short range ordered phase of *Ln*ODCO$_3$, along the [100] direction. *Ln*$^{3+}$ coordination environment shown as purple polyhedra, magnetic vectors shown as red arrows, and nearest neighbour chains highlighted with translucent white arrows. The spins disordered from the average ferromagnetic chain direction are highlighted in green.

Spin correlations $\langle S_0 \cdot S_r \rangle$, averaged over 100 RMC refinements show that the dominant spin correlations in all these materials are qualitatively very similar, in both Heisenberg and Ising refinement models. Significant ferromagnetic correlations are clearly noted along the chain direction out to distances of about 15 Å at low temperatures with significant nearest neighbour antiferromagnetic correlations between chains packed into a distorted triangular array (see Figure 5.11 inserts). The strongest ferromagnetic correlations at 3.79 and 7.01 Å correspond to the first and second nearest neighbours in the chain, coupled through oxygen and O-C-O bridges from the hydroxy and carbonate groups. The strongest antiferromagnetic correlation at 4.85 and 8.52 Å corresponds to the neighbouring atom within the triangles along the *a*-axis and the analogous interaction with a cation that is the next-nearest neighbour along a chain from one of these atoms in the triangle. The former are coupled by a O-C-O bridge of the carbonate group (see Figures 1.16 and 5.5).

We have extracted intrachain correlation lengths with the function:

$$\langle S_0 \cdot S_r \rangle = A e^{-r/\varepsilon} \tag{5.1}$$

where A is the Ising-like anisotropy, r is the correlation distance and $\varepsilon$ is the correlation length, from the Ising fits to the data. Due to the non-linear alignment of spins along the
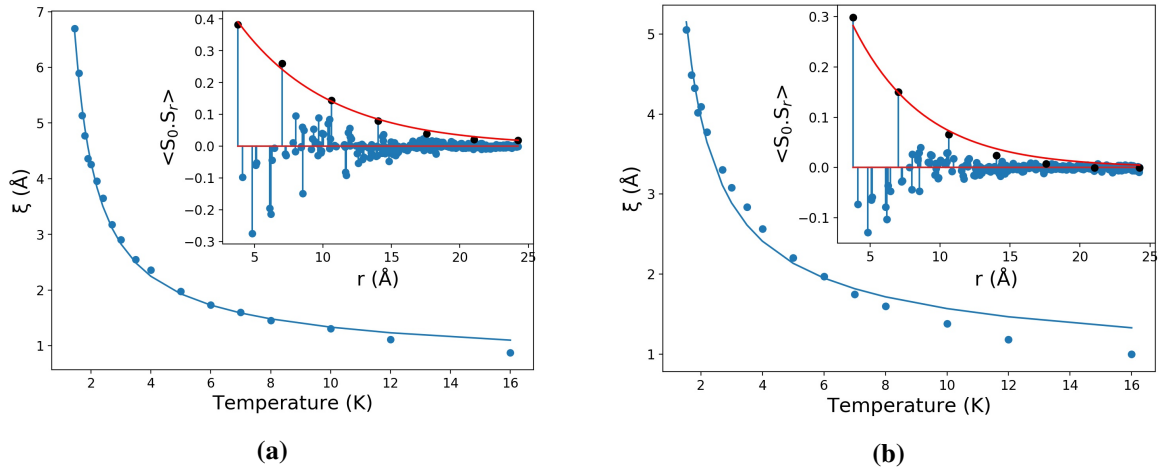
**Figure 5.11** Chain correlation lengths with respect to temperature for (a) TbODCO$_3$ and (b) HoODCO$_3$. The solid blue line shows the fit. Spin correlations in the *b*-axis only at 1.5 K shown in the insert. The black points indicate the correlations within the chains.

buckled chain direction, it is necessary to only consider the correlations of the components of the magnetic moment along the *b*-axis when extracting the ferromagnetic correlation length. This is required because otherwise the non-collinear nature of the spins lead to next nearest neighbour in the chain, whose spins are collinear, having higher correlations than the nearest neighbour. Considering only the component of the magnetic moment along the *b*-axis allows us to decouple the Ising-like interactions in these materials, which would be expected to arise from the strong single-ion of lanthanides, from the magnetic interactions between neighbouring lanthanide cations. This yields a correlation length of 6.69(11), 1.49(4) and 5.06(2) Å for TbODCO$_3$, DyODCO$_3$ and HoODCO$_3$, respectively, at 1.5 K, consistent with the overall weaker interactions in DyOHCO$_3$ and the weaker diffuse scattering observed. The values of A determined for TbODCO$_3$, DyODCO$_3$ and HoODCO$_3$ are 0.689(9), 0.514(5), and 0.596(13) at 1.5 K close to the value of 1 that would be expected for the ideal Ising system, suggesting some deviation from a purely Ising model.

As the temperature was raised and the correlations became significantly weaker, the best fit to data was found with unphysical A values; for this reason A was fixed to the values determined for the lowest temperature fit for all temperatures. Temperature evolution of the ferromagnetic intrachain correlation length $\varepsilon$ follows the expression for an independent ferromagnetic Ising chain [100, 224], as shown in Figures 5.11 and A.12:

$$\varepsilon = \frac{c}{2ln[coth\frac{J_1J}{T}]} \tag{5.2}$$

In this expression $J_1$ is nearest neighbour exchange interaction from the Ising Hamiltonian. At higher temperatures the correlation length evolution diverges from the fit indicating the limitation of the approach, but this only occurs above 12 K and 8 K for TbODCO$_3$ and HoODCO$_3$, respectively, at which point magnetic correlations are very short. The fit to the correlation length yields values for $J_1$J of TbODCO$_3$, DyODCO$_3$ and HoODCO$_3$ of 1.11, 0.1, 0.76 K – consistent with the strength of the magnetic interactions following the trend TbODCO$_3$ > HoODCO$_3$ » DyODCO$_3$. The values for TbODCO$_3$ and HoODCO$_3$ are very close to the ordering temperatures shown in magnetic susceptibility measurements, reflecting their Ising chain behaviour.

We expect the short-range magnetic correlations in these materials are key to the highly efficient magnetocaloric effect of these materials above 4 K under modest applied magnetic fields. As previously suggested for Tb(HCO$_2$)$_3$ and Ho(HCO$_2$)$_3$ the ferromagnetic Ising chains allow for high entropy changes in small applied magnetic fields as ferromagnetic units are more readily aligned with the applied magnetic field. [4, 194] The competing weaker antiferromagnetic interactions help to suppress long-range order, required for paramagnetic magnetocalorics, but are weak enough to require only small fields to be overcome to lead to a ferromagnetic field-induced state. This dominant ferromagnetic intrachain coupling allows the moments to be more easily aligned with the applied field. In the magnetocaloric studies of these materials, [5] the materials that show this structured diffuse scattering, and this exotic magnetic order are the materials that have optimised performance in low applied magnetic fields above 4 K.

The precise extent to which these three systems resemble ideal Ising system may be somewhat different, which likely effects how these materials respond to applied magnetic fields. Given the powder averaging this data suffers from, it is possible there may be other solutions that provide suitable fits to the diffuse scattering data, or there are some deviations in the precise spin orientations that have been overlooked. However, the data are consistent with a four site Ising model, and long range order discussed for HoODCO$_3$ in Section 5.5.2, so this is likely an optimal model. The Ising-like nature of the spins of these materials would be ideally confirmed by measuring the inelastic neutron spectra of these materials, where a spin gap is expected to be present. Such measurements would also more clearly identify the strength of the Ising-like interactions. This may be an important as the magnetisation measurements of TbODCO$_3$ and DyODCO$_3$ indicate magnetisation is somewhat higher than that expected for Ising powder averaged samples, but far lower than a Heisenberg magnetisation curve, suggesting that these compounds are mostly but not entirely Ising. This combined with

the large magnetic moments in these systems allows for large changes in magnetisation in applied fields, greater than that of a purely Ising material, and beneficial to the magnetocaloric effect in this sample. This, along with the greater overall magnetic moment of DyOHCO$_3$ may explain why it exhibits a greater magnetic entropy change despite its weaker magnetic interactions.

## 5.5 Magnetic Order in HoODCO$_3$

### 5.5.1 Incommensurate Magnetic Order

To probe the nature of the magnetic transitions observed via low temperature magnetic susceptibility measurements of these compounds we continued these studies on HoODCO$_3$, below 1.6 K. Upon cooling the sample further, the magnetic diffuse scattering shifts and sharpens into Bragg peaks ascribable to the development of long range order (Figure 5.12)
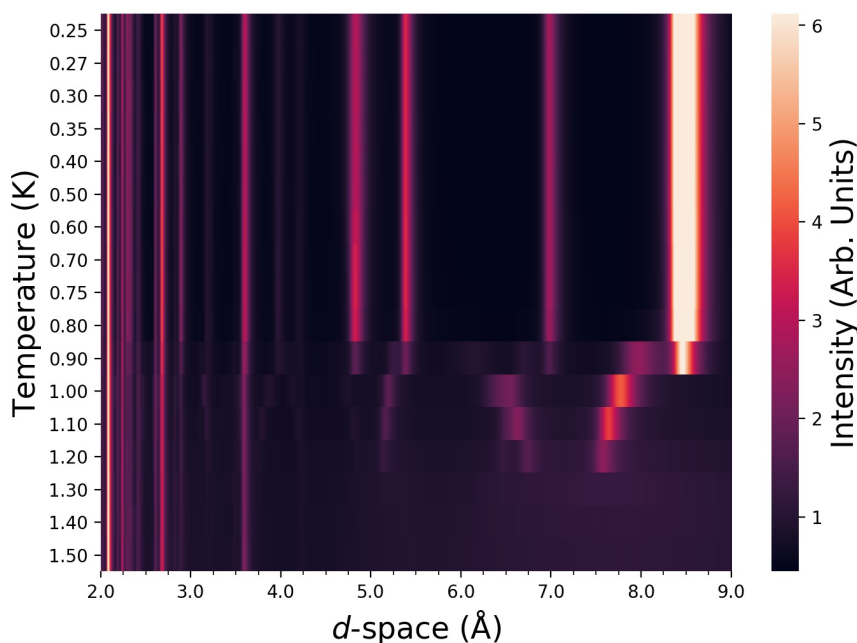


**Figure 5.12** Contour plot of HoODCO$_3$ with respect to temperature, between 0.25 and 1.5 K, showing the movement of the magnetic peaks with temperature and thus a changing propagation vector.

The broadening of these Bragg peaks is an indication of the finite correlation length in this material, varying from $\approx 419$ to $\approx 1520$Å, between 1.2 and 0.9 K. These broad Bragg features sharpen with decreasing temperature, and indicate a growing correlation length. Between 1.2

and 0.9 K, these magnetic reflections can be indexed with a **k**-vector – [$\alpha$,0,0], summarised in Table 5.2, corresponding to the $\Sigma$ symmetry line of the first Brillouin zone (BZ).

**Table 5.2** Summary of **k**-vectors and moments of the incommensurate phase of HoODCO$_3$.

| Temperature (K) | $\alpha$ | Moment ($\mu_B$) |
|---|---|---|
| 1.0 | 0.24811(12) | 7.68 (04) |
| 1.1 | 0.27259(8) | 6.54(04) |
| 1.2 | 0.28421(13) | 4.20 (05) |

Rietveld refinements of the data with these **k**-vectors produced an excellent fit to the data. The broadening of the peaks associated with finite correlations length, was modelled with an anisotropic broadening model and accounted for the peak broadening sufficiently well to model the peak intensities. This magnetic phase can be described by a longitudinal amplitude modulated spin-density wave propagating along the *a*-axis, summarised in Figure 5.13 for the magnetic structure at 1.1 K.
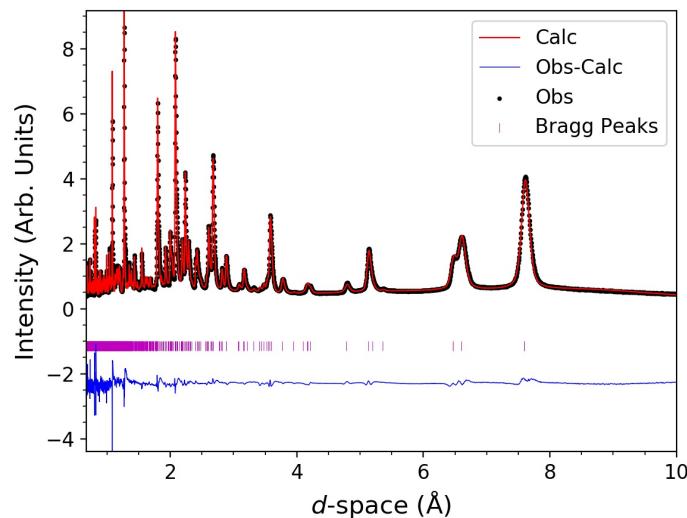


**Figure 5.13** Rietveld fits to neutron diffraction pattern of HoODCO$_3$ at 1.1 K, from bank 2/9 of WISH, along with the fitting statistics R$_p$ = 6.72 % and R$_{wp}$ = 4.20 %.

The moments are oriented primarily along the *b*-axis, canted into the *ac* plane (Figure 5.14), with the unit vector [$\pm$0.28, 1.06, $\pm$0.66] consistent with the RMC refinements. In insulating materials, such as *Ln*ODCO$_3$, the total magnetic moment on each is expected to remain constant so the modulated moment reflects an average structure interpretation of a structure in which some of the magnetic moment remains disordered. The observation of such a state, therefore, is support for magnetic frustration between adjacent chains caused

by Ising-like spins on a distorted triangular array. In particular the magnetic modulation is observed along the same axis in which there are ferromagnetic coupling between chains in the incommensurate structure despite the antiferromagnetic correlations observed in the short range ordered phase, reflecting the comprise needed to achieve long-range magnetic order.



(a)                                                (b)
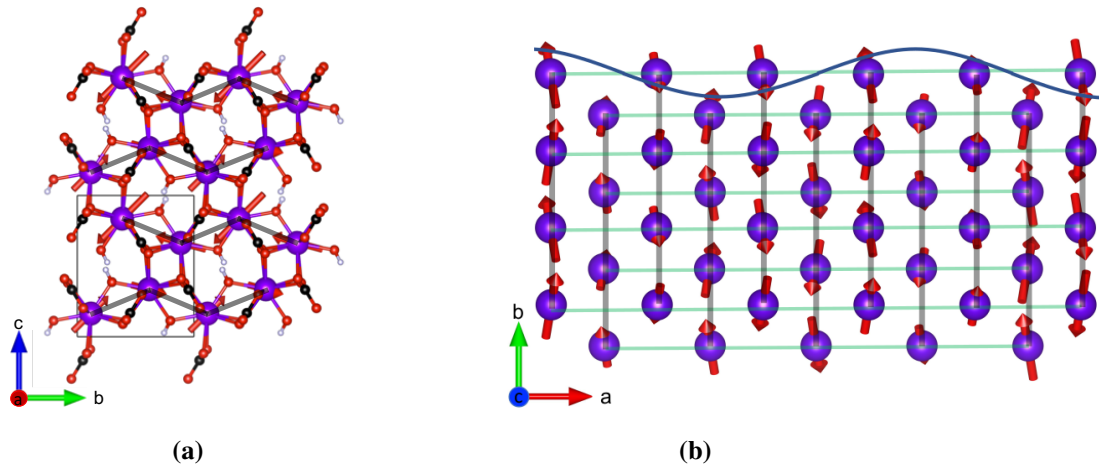
**Figure 5.14** Magnetic structure of the incommensurate magnetic phase of HoODCO$_3$ at 1.1 K, (a) along the [100] direction, and (b) the [001] direction. Moments are aligned primarily along the *b*-axis, and canted into the *ac*-plane. The amplitude modulated spin-wave propagates along the incommensurate *a*-axis. Only magnetic atoms are included for clarity. Black lines indicate the ferromagnetic chains, the green lines indicate magnetic moments with the same fractional coordinates in translated unit cells. Sine wave indicates the propagation of the amplitude modulated magnetic moments.

### 5.5.2   Commensurate Magnetic Order

Cooling further, at 0.9 K there is some magnetic phase separation, with the model producing the best fit to our data consisting of two magnetic phases, an incommensurate and a $\mathbf{k} = 0$ phase. At 0.8 K and below only the commensurate magnetic order exists. Using the Bilbao Server [166] and Rietveld refinement we have determined the data agrees with the $P2_12_12_1$ magnetic space group, with the lattice parameters $a = 4.80206(15)$ Å, $b = 6.95563(20)$ Å, $c = 8.42543(27)$ Å at 0.25 K (see Figure 5.15 for quality of the fit). A summary of the refined atomic positions is given in Table 5.3 and bond distances in Table A.3. Since the $\mathbf{k}$-vector is a special point of the Brillouin zone, the phase of the system is fixed to a solution that produces symmetry equivalent magnetic moments, with a single independent magnetic site, and a moment of 7.63(7) $\mu_B$ at 0.25 K.
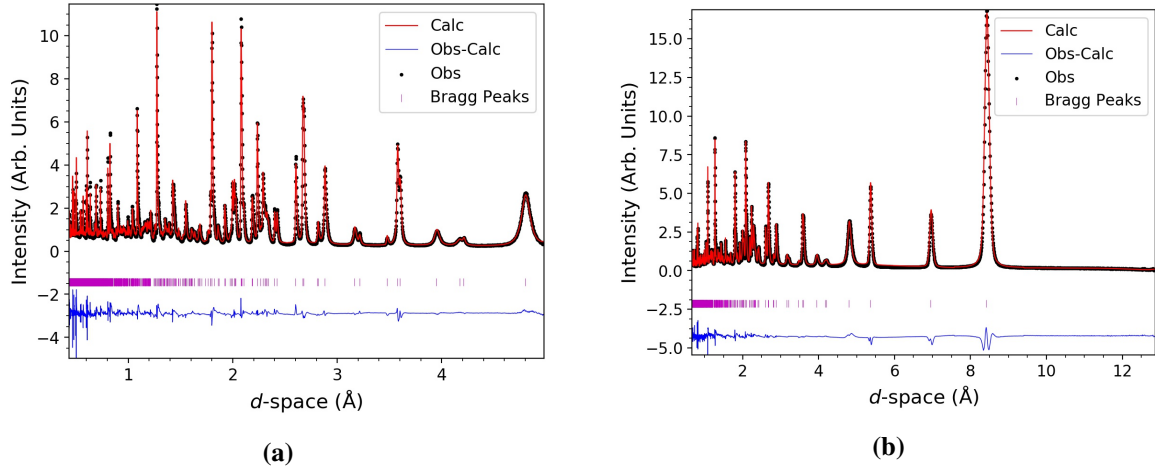
**Figure 5.15** Rietveld fits to neutron diffraction patterns of HoODCO$_3$ at 0.25 K, in the **k**=0 phase, from the 90° bank (a) and the high resolution 153° (b) of WISH along with the fitting statistics R$_p$ = 7.06 %, R$_{wp}$ = 6.00 % and R$_p$ = 7.84 %, R$_{wp}$ = 4.74 %. Fit in red and the difference in blue.

**Table 5.3** HoODCO$_3$ at 0.25 K atomic Summary, with atomic positions given as fractional coordinates and occupations given as fractional occupancies, determined from Rietveld refinement.

| Atom | x | y | z | $U_{iso}$ x 100 (Å$^2$) | Occupancy |
|------|------|------|------|------|------|
| Ho | 0.00000 | 0.1155(5) | 0.1649(4) | 1.29(13) | 1.000 |
| C | 0.515(2) | 0.4494(7) | 0.1646(6) | 0.20(13) | 1.000 |
| D | −0.1158(13) | −0.2618(13) | 0.0378(8) | 2.8(3) | 0.97(2) |
| O1 | −0.273(2) | 0.4270(16) | 0.1251(10) | 2.1(2) | 1.000 |
| O2 | 0.539(2) | 0.0575(9) | 0.2014(6) | 0.22(14) | 1.000 |
| O3 | 0.024(2) | −0.1982(8) | 0.1155(8) | 0.50(14) | 1.000 |
| O4 | 0.272(2) | 0.3914(12) | 0.0906(10) | 0.24(20) | 1.000 |

The $P2_12_12_1$ magnetic space group does not allow any ferromagnetic component, while magnetic susceptibility suggests a ferromagnetic component in applied fields indicating this symmetry is likely lowered further. The weak ferromagnetic order that leads to this, however, is evidently too subtle to be observed in the neutron diffraction patterns. Figure 5.16 shows the moments oriented in the direction of the nearest neighbour along the face-sharing polyhedra, in the direction of the chain. Magnetic coupling along the chains remains ferromagnetic, with spins canted into the *ab* plane caused by the strong Ising-like single ion anisotropy, with antiferromagnetic coupling of chains along the *c*-axis but ferromagnetic correlation of spins along the *a*-axis.
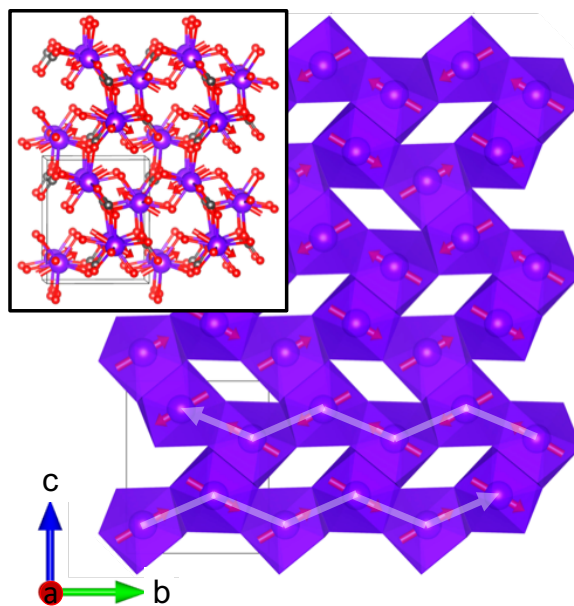


**Figure 5.16** Magnetic structure of the **k**=0 ordered magnetic phase of HoODCO$_3$ at 0.25 K, along [100] direction. Showing ferromagnetic interchain coupling along the *b*-axis, and antiferromagnetic interchain coupling. Ho coordination environment shown as purple polyhedra, and magnetic vector orientations shown as red arrows. Nearest neighbour interchain correlations have been highlighted with translucent white arrows in the direction of the ferromagnetic chain vector. The insert shows the ball and stick model off the [100] direction, carbon and oxygen are shown in black and red respectively. Deuterium has been omitted for clarity. Nuclear unit cells are shown as black boxes.

In the commensurate magnetic structure the spins remain oriented in the same direction as in the incommensurate phase, but are now fully ordered. In this ordered phase the magnetic Bragg peaks are sharper than in the incommensurate phase but still much broader than instrumental resolution, and we observed no reduction in the width of the magnetic peaks upon further cooling, indicating the magnetic domain size remains unchanged. Therefore, even in this commensurate long range ordered state the magnetic domains remain relatively

small, with an average correlation length is $\approx$1580 Å. The correlation length along the
$a$-axis is even shorter, as indicated by the most significant broadening of the [100] reflection.
Extracting the correlation length from the anisotropic broadening, reveals a correlation length
of $\approx$438 Å along this direction. We attribute this anisotropic peak broadening to underlying
frustration since in this commensurately ordered phase the moment along the $a$-axis are
aligned ferromagnetically with respect to each other while in the short range ordered phases
we observe significant antiferromagnetic correlations in this direction. The ordered magnetic
moment observed at 0.25 K is still significantly lower than the 10 $\mu_B$ expected from a
fully ordered Ho$^{3+}$ moment, observed through neutron diffraction (see Figure 5.17a for the
magnetic moment evolution); indicative of the retention of significant disorder within the
system. The phase transition to the incommensurate phase is also indicated by the modest
magnetorestriction of the unit cell (Figure 5.17b).
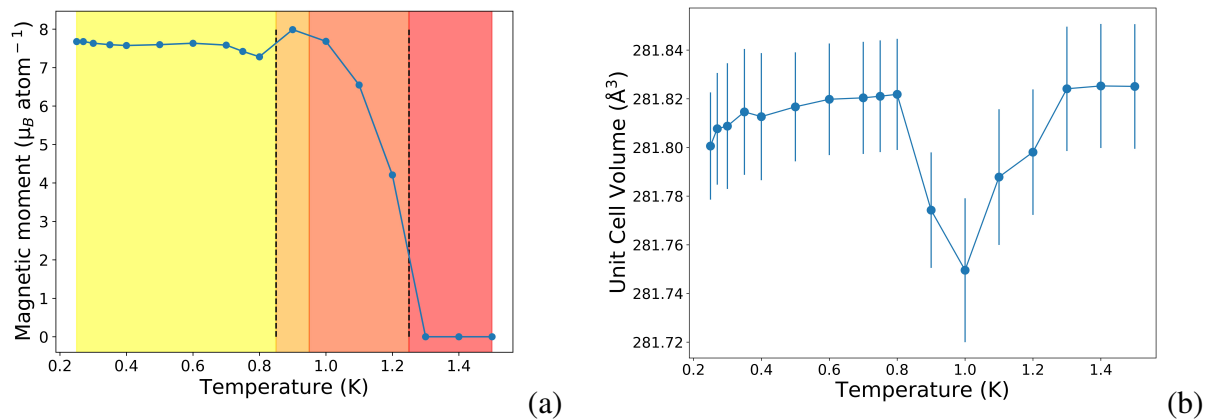


**Figure 5.17** (a) Plot of the evolution of the magnetic moments of HoODCO$_3$ with respect to temperature. The short range ordered, incommensurate and **k**=0 phase regions are shaded in red, orange and yellow, respectively. The temperature point with phase coexistence is shaded in light orange. (b) Plot of the change of the unit cell volume of HoODCO$_3$ with respect to temperature. HoODCO$_3$ undergoes modest unit cell magnetorestriction when in the incommensurate phase.

It should be noted that the model of the magnetic interactions of the short range ordered
phase is consistent with the order seen in the commensurate and incommensurate phases
of HoODCO$_3$. The 1D ferromagnetic correlations remain present in the ordered phases,
while the Ising-like character is reflected by the non-collinear ordered magnetic structures.
Clear evidence of magnetic frustration presented by both the nature of the incommensurately
modulated phase and the reduced magnetic domain size and ordered moment. Given the
similar short range order and susceptibility data we expect that TbODCO$_3$, will also un-
dergo a transition to a similar longer range ordered state, which could be confirmed using
neutron diffraction. Further exploration of the magnetic frustrations within these frame-

works with inelastic neutron scattering would enable the magnetic interactions to be probed directly.

## 5.6    Conclusions

This chapter reports the low temperature crystal structure, physical properties, magnetic susceptibility and magnetic order of $Ln$ODCO$_3$ frameworks. We have synthesized and structurally characterized a family of these materials using a combination of powder and single crystal diffraction, focusing on the heavier lanthanides due to their high magnetic moments as required for greater MCE. Finding that under moderate hydrothermal conditions these form $P\bar{6}$ hexagonal crystal structures for Pr, Nd and Sm and $P2_12_12_1$ orthorhombic structures for the later lanthanides, which has previously been debated. [76, 77, 113, 114]

We show that that the promising magnetocaloric phases for higher temperature applications develop significant magnetic correlations below 20 K. In the short range ordered phase these systems show features consistent with a ferromagnetic Ising chains with frustrated antiferromagnetic interchain packing and non-collinear magnetic moments. At 1.2 K, HoODCO$_3$ undergoes a transition to an incommensurate magnetic state, with the **k**-vector [$\alpha$,0,0], characterised by a spin-density wave in the same direction. Upon further cooling HoODCO$_3$ transitions to a **k**=0 commensurate magnetic state with similar spin orientation and magnetic order to the incommensurate ordered state, with a finite correlation length of $\approx$438 Å along the $a$-axis, which may arise from the magnetic frustration in this material. We attribute these correlations to the efficient magnetocaloric effect observed in these materials. We propose that frustration and ferromagnetic chains present in these materials, which persist in the short range ordered phase, are responsible for the excellent magnetocaloric properties in these materials and are a recipe for enhanced refrigeration materials. Direct observation of the magnetocaloric effect in these materials, through neutron diffraction in applied fields should provide great detail about the mechanism of the magnetocaloric effect; this will be discussed for TbODCO$_3$ alongside of Tb(DCO$_2$)$_3$ in the next, and final, chapter in this thesis.

# 6

# Observation of the Magnetocaloric Effect Through Neutron Diffraction

## 6.1 Introduction

Magneto-structural coupling plays an important role in the magnetic behaviour of materials. In order to tune the physical properties and field behaviour of these materials, we must first understand what is occurring at the microscopic level. We have shown in previous chapters the highly efficient and promising magnetocaloric effects in the $Ln$ODCO$_3$ and $Ln$(DCO$_2$)$_3$ frameworks, and the link between the interactions in the short and long range ordered phases. However, in order to fully appreciate the subtleties of the mechanism of the magnetocaloric effect in these materials, it is important to understand the magnetic phases that develop in the presence of a magnetic field. Therefore, we have investigated the magnetic structure of some of the highest efficiency magnetocaloric materials (TbODCO$_3$ and Tb(DCO$_2$)$_3$) in applied field, using neutron diffraction.

### 6.1.1 Applied Field Experimental Methods

Tb(DCO$_2$)$_3$ and TbODCO$_3$ powders were loaded into 8 mm vanadium cans and wetted with d$_6$-isopropyl alcohol, sealed with indium wire and flash frozen using the 10 T GEM cryomagnet. The d$_6$-isopropyl alcohol was included to minimise the effect of preferred orientation on the diffraction patterns in the application of the magnetic field, and was successful in this preventing any significant orientation. The sample was flash frozen in order to prevent the d$_6$-isopropyl alcohol crystallisation and resulted in the formation of an

amorphous solid, as indicated by the diffuse scattering centred around 4.2 Å. The presence of the cryomagnet produced aluminium reflections, which were fitted with a Le Bail model to negate the effects of the highly textured surface, and un-indexable peaks in the highest resolution bank which were excluded from refinements. Diffraction patterns were recorded on the high resolution time-of-flight WISH diffractometer at the Rutherford Appleton Laboratory at Harwell with fields up to 3 T applied.

## 6.2 Neutron Diffraction of Tb(DCO$_2$)$_3$ in Applied Fields

### 6.2.1 Field Sweep

Tb(DCO$_2$)$_3$ was cooled from room temperature to base, and no significant change in the intensity of the Bragg-like reflections was observed. This suggests that the TIA phase [4, 18, 194] has not formed in the absence of a notionally zero applied field at 1.5 K, despite having been observed to form below 1.6 K in other measurements in this thesis. This could be a result of a discrepancy in the measured temperatures of different cryostats, poorer temperature equilibration due to the d$_6$-IPA glass not properly conducting heat or a result of trapped magnetic flux present within the magnet affecting the formation of the TIA state at very low applied fields. It was also not possible to accurately measure the diffuse scattering previously found in Tb(DCO$_2$)$_3$ at low temperature in this study precisely due to the higher background of these measurements, including scattering from the frozen d$_6$-IPA.

At 1.5 K, the magnetic field was swept from 0-3 T in variable steps. With an applied field of $\mu_0 H = 0.1$ T, the appearance of new peaks was noted that were found to be consistent with the formation of the previously reported TIA phase. [4, 18, 194] When treated as conventional Bragg-reflections these peaks can be indexed with the $\mathbf{k}_1$-vector = [0,0,1], belonging to the $P3m'1$ magnetic space group, discussed in Section 4.2.2, with moments aligned along the $c$-axis. We note that in doing so we are again treating the observed features as a conventional PDA phase, this is unavoidable for the data obtained in this chapter since the diffuse scattering that is key evidence for the unconventional magnetic order of the TIA phase is partially obscured by the higher backgrounds involved in these measurements. Since it has previously been established, however, that the TIA phase is the most likely explanation of these Bragg-like features we will continue to refer to this as the TIA phase. The most intense peak associated with the TIA phase can be seen at 9.1 Å as shown in Figure 6.1.
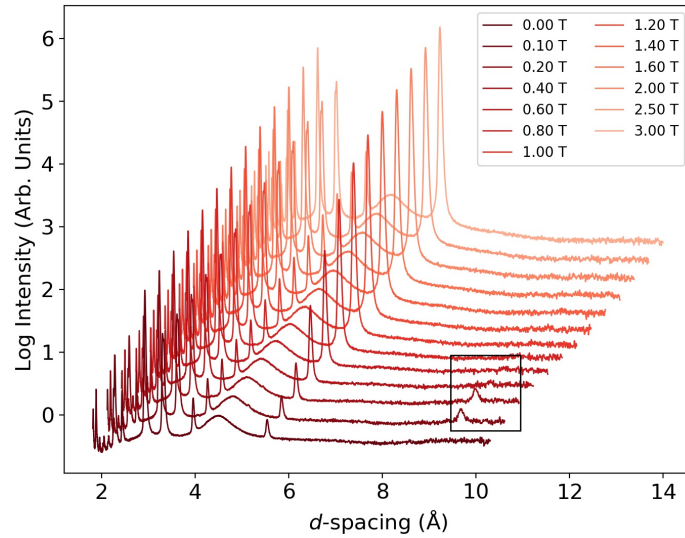
**Figure 6.1** Waterfall plot of data from bank 2/9 of WISH, plotted on a log scale, for Tb(DCO$_2$)$_3$ with respect to field, at 1.5 K. The strong peaks at ≈5.2 Å indicates the ferromagnetic phase, and the weak peaks highlighted with a box at ≈9.1 Å indicate the TIA phase.

The interesting feature of the Bragg peaks observed in this applied field data, as compared to the previous zero-field studies, is the much smaller FWHM of the peaks associated with the TIA phase, although they are still broader than the instrumental resolution of WISH. We previously assigned the peak broadening of this phase to the inherent disorder of this state, which lacks conventional 3D crystallographic order. The smaller FWHM of this phase in applied field corresponds to a much larger correlation length, likely within the chains of the TIA state.

Increasing the field to 0.2 T, the intensities of the peak associated with the TIA phase increased in intensity and additional intensity was observed on existing reflections, which can be indexed to a $\mathbf{k}_2$-vector = 0 (see Figures 6.2 and A.13 for quality of selected fits).

The intensity of the magnetic reflections associated with the $\mathbf{k}_2 = 0$ phase can be described by a simple ferromagnetic structure, with all moments aligned along the $c$-axis. The alignment of the moments along the $c$-axis, is in agreement with the anisotropic easy axis and Ising character of the spins, determined in Section 4.2.3. At 0.2 T the maximum intensity of the reflections associated with the TIA phase is observed, with a refined magnetic moment of 0.86(7) $\mu_B$ obtained. Between 0.2 - 0.6 T there is phase coexistence of the TIA and the ferromagnetic phase, with the TIA phase dropping in intensity at fields above 0.2 T and the ferromagnetic phase growing in intensity. Here we have treated the observed magnetic scattering as phase coexistence, however we cannot rule out that this scattering arises from a
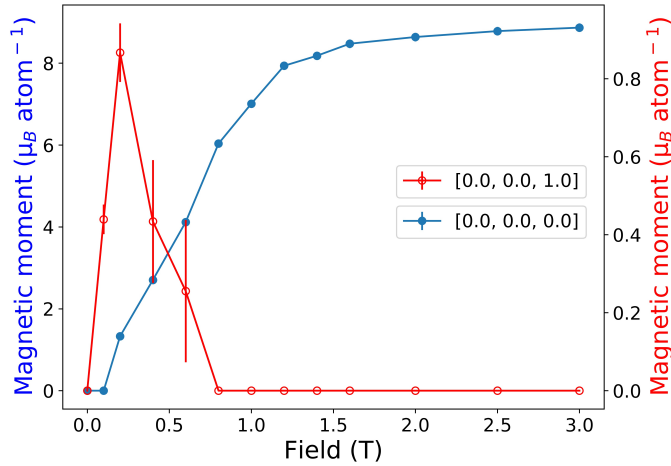
**Figure 6.2** Evolution of the ordered magnetic moments associated with $\mathbf{k}_1$ and $\mathbf{k}_2$, in Tb(DCO$_2$)$_3$, with respect to field.

single, more intricate, magnetic phase. At 0.8 T only the ferromagnetic phase exists scattering from this phase increases in intensity up to 3 T, although it is near saturation (8.63(11) $\mu_B$) at $\approx$2 T, as shown in Figure 6.2. The saturation value at 3 T = 8.86(10) $\mu_B$ is close to the 9 $\mu_B$ value expected for Tb$^{3+}$.

The formation of the TIA phase in small magnetic fields, before the emergence of the ferromagnetic phase indicates that the application of the applied magnetic field supports ferromagnetic ordering of the magnetic chains before high applied magnetic fields overcome the weaker antiferromagnetic coupling between the chains. To explain this in zero field the short range 1D ferromagnetic correlations that persist, [18, 194] enable the spins within the chains to be readily aligned in magnetic field, forming the TIA. The TIA still has significant disorder, and therefore still large amounts of residual entropy. Once the magnetic field is such that the antiferromagnetic interchain correlations are overcome (beginning above 0.2 T), the disorder is removed and transitions into a ferromagnet (see Figure 6.3). The alignment of the ferromagnetic chains in the TIA phase to simple ferromagnetic structure leads to large changes in entropy for small applied magnetic fields, which has been suggested in previous studies. [4, 17] In this study we have confirmed and directly observed the evolution of the TIA phase under a magnetic field and its conversion into a ferromagnetic phase under moderate applied fields. This is analogous to the behaviour we would expect at and above 4 K, where the magnetocaloric effect of Tb(HCO$_2$)$_3$ (4 - 10 K) peaks. In this regime the dominant ferromagnetic correlations allow the TIA to emerge as magnetic field is applied

and long range order of the magnetic chains occurs before the spins in all chains are aligned with the magnetic field to yield a ferromagnetic state.
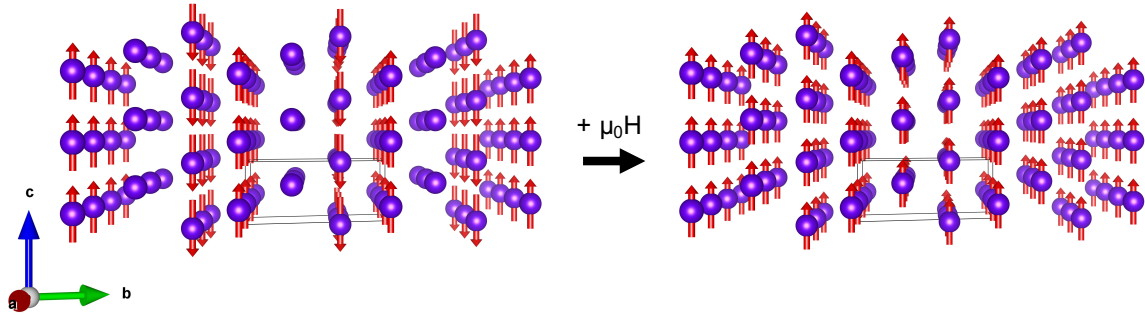


**Figure 6.3** Diagram showing the phase transition from the PDA approximation to the TIA phase to a ferromagnetic phase in applied magnetic field. The Tb$^{3+}$ atoms are shown in purple, all other atoms have not been included for clarity and magnetic vectors are shown as red arrows. The unit cell is shown as a black box. Left shows the PDA phase, and the right shows the ferromagnetic phase along the [100] axis.

## 6.2.2   Variable Temperature Measurements in a 0.1 T Magnetic Field

In order to confirm whether the TIA phase persists into the peak magnetocaloric temperatures, we have explored the features associated with this phase under a fixed applied field at variable temperatures. Between the field sweep and the variable temperature measurements the applied field was removed. A 0.1 T magnetic field was then applied to the sample and it was found that a similar intensity of the magnetic reflections associated with the TIA were observed as when the sample had first been exposed to a 0.1 T magnetic field. This was observed to coexist with the ferromagnetic phase, with refined magnetic moments of 3.32(5) $\mu_B$ for the TIA phase and 5.59(6) $\mu_B$ for the ferromagnetic phase.

Measurements were then taken at variable temperatures, with a 0.1 T applied field, between 1.5 and 40 K. The diffraction patterns are shown in Figure 6.4. Raising the temperature resulted in continuous reductions of the magnetic moments, before a rapid decrease in their intensities above 3 and 4 K for the TIA and ferromagnetic phases.

All intensity in the reflections is lost upon reaching critical temperatures of $\approx$8 and $\leq$40 K, for the TIA phase and between 20 and 40 K for the ferromagnetic phase, respectively (Figure 6.5a). We note that the critical temperature for the TIA phase observed here is higher than that observed in zero applied fields, about 1.6 K, confirming it is stabilised by application of
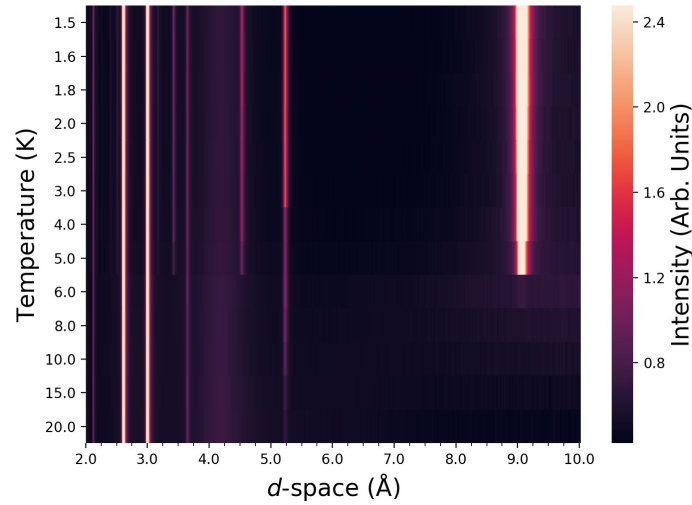
**Figure 6.4** Contour plot of bank 2/9 of WISH for Tb(DCO$_2$)$_3$ with respect to temperature, with a 0.1 T applied field. The weak peaks at $\approx$5.2 Å indicates the ferromagnetic phase, and the strong peaks at $\approx$9 Å indicates the TIA phase.

an applied magnetic field. Above this temperature diffuse scattering centred around $\approx$9.1 Å, indicating persistent short range order of the TIA phase, can be observed up to 40 K, as shown in Figure 6.5b. The diffuse scattering observed is qualitatively similar to that observed in previous studies, [4, 18, 194] and in the Ho(DCO$_2$)$_3$ short range ordered phases, and therefore can likely be attributed to short range 1D Ising correlations along the $c$-axis.



(a)          (b)
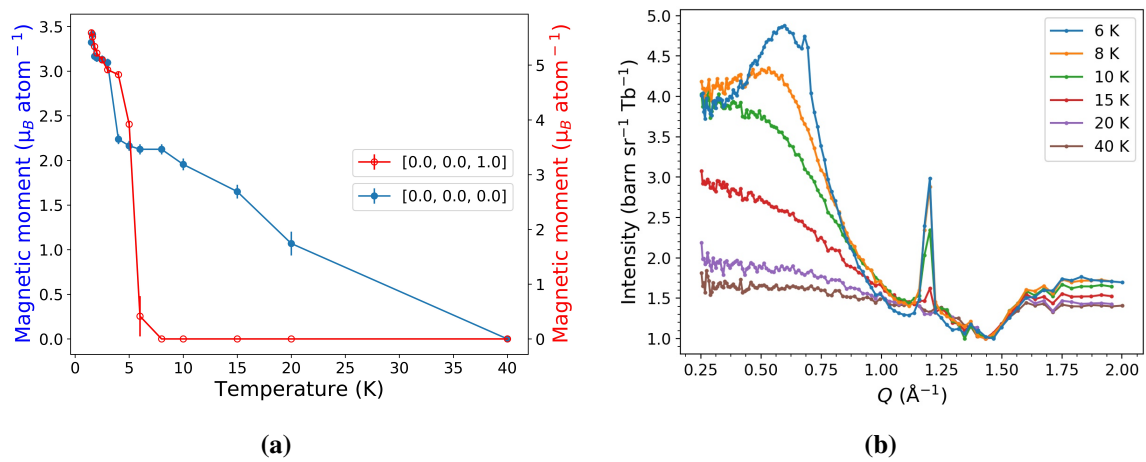
**Figure 6.5** (a) Evolution of the ordered magnetic moments associated with $\mathbf{k}_1$ and $\mathbf{k}_2$, in Tb(DCO$_2$)$_3$, with respect to temperature. (b) Evolution of the magnetic diffuse scattering associated with $\mathbf{k}_1$, in Tb(DCO$_2$)$_3$, with respect to temperature.

# 6.3 Neutron Diffraction of TbODCO$_3$ in Applied Fields

## 6.3.1 Field Sweep

TbODCO$_3$ was cooled in zero applied magnetic field to base temperature of T = 1.5 K and left to equilibrate for 1 hour. As in zero field measurements of TbODCO$_3$ strong magnetic diffuse scattering is observed at 1.5 K [5, 225] Field sweep measurements were taken between $\mu_0H$ = 0-3 T in variable steps with selected diffraction patterns shown in Figure 6.6 and a contour plot shown in Figure 6.7a. The clearest indication of the growing magnetic phases is shown by the Bragg peaks at 5.3, 7.1 and 8.5 Å, which increase with applied magnetic field.
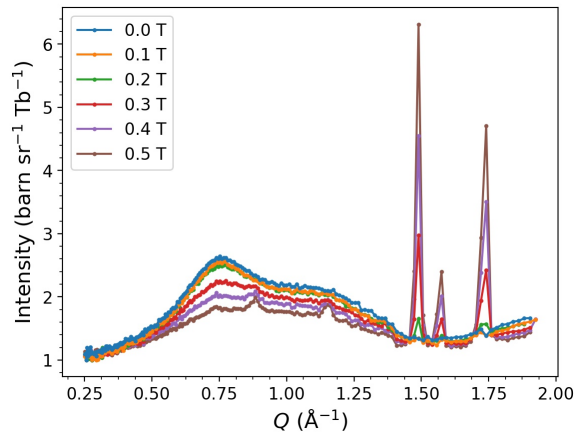


**Figure 6.6** The evolution of the Bragg peaks emerging from the magnetic diffuse scattering, indicating a transition from short to long rang order on application of a magnetic field, between 0 and 0.5 T.

The position of the Bragg reflections associated with the crystal structure do not change significantly under application of magnetic fields indicating there is no significant change in lattice parameters, which was confirmed by refinements. There was, however, a significant change in the features arising from magnetic scattering. In zero and small magnetic fields there is significant magnetic diffuse scattering and with the increase in applied magnetic field above 0.2 T the Bragg peaks associated with these phases evolve from this diffuse scattering, indicating a transition from short to long range order. This suggests more detailed studies should be performed in future to establish if there is a phase that can account for the sharp magnetic reflections and the magnetic diffuse scattering that accompanies it under higher applied magnetic fields. [81] The diffuse magnetic scattering observed in these studies is qualitatively similar to the scattering observed in the zero field studies of Section 5.4. Therefore, this diffuse scattering is likely due to the short range ferromagnetic Ising chain correlations.
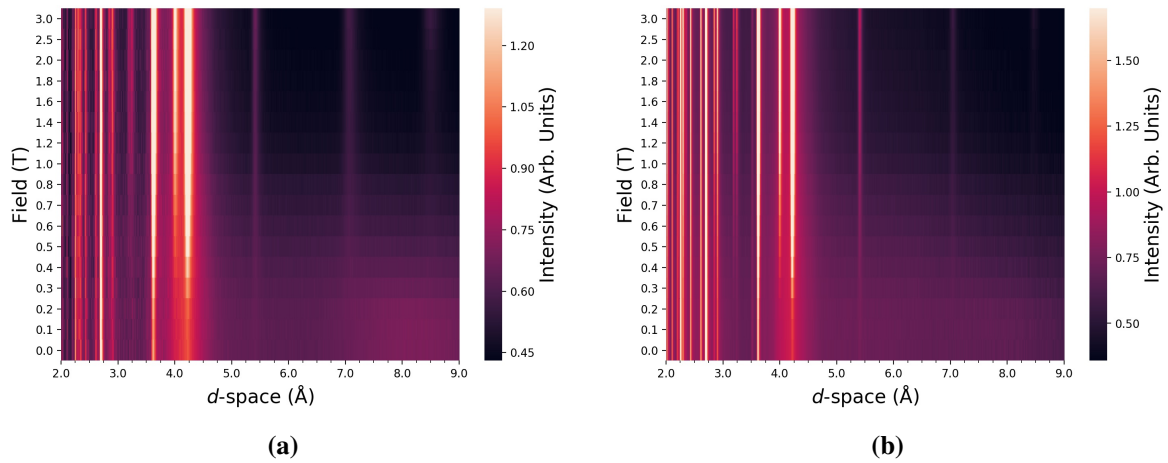
**Figure 6.7** Evolution of the ordered magnetic moments associated with the ferromagnetic phases of TbODCO$_3$ with respect to applied field. Growing peaks can be seen at 5.3, 7.1 and 8.5 Å with increasing applied magnetic field. (a) Bank 1/10 (b) Bank 2/9. There is significant magnetic diffuse scattering at higher $d$-space, from which the Bragg Peaks emerge.

In the long $d$-spacing banks, centred at 27° (1/10), all of these magnetic peaks above 5 Å are weak but clearly visible, at all field strengths at which they are present. However in banks 2/9 (centred at 56°) these peaks are not visible, leading to some initial analysis problems. This loss of these peaks in bank 2/9 can be attributed to the absorption from the sample. In banks 2/9 the reflection at 8.5 Å is likely using a lambda between 9-10 Å but in banks 1/10 a much shorter wavelength is responsible for these reflections, so the absorption will be significantly higher in banks 2/9. As a result of this and that Tb is moderately absorbing, when the reflection is small it cannot be observed in banks 2/9. The peak intensity of the [011], [010] and [001] reflections is further affected by the anisotropic broadening of these higher $d$-space reflections.

The magnetic reflections of this material, which are associated with the Γ-point cannot be fitted well by a single magnetic phase (see Figure 6.8). Symmetry analysis of the **k**=0 propagation vector acting on the $P2_12_12_1$ space group produces four symmetry allowed magnetic space groups, three with ferromagnetic components along the $a$, $b$ and $c$-axis and one with no ferromagnetic component. The space group with no ferromagnetic component was observed at low temperatures in HoODCO$_3$, but in the presence of a magnetic field this is not energetically favourable, and phases would be expected to contain a ferromagnetic moment. Inspection of the other three magnetic space groups reveals that only those with a ferromagnetic component along the $b$ and $c$ axes, produces a magnetic structure compatible

with the easy axes of the Tb$^{3+}$ moments, established from the local structure determined at higher temperatures in Section 5.4.
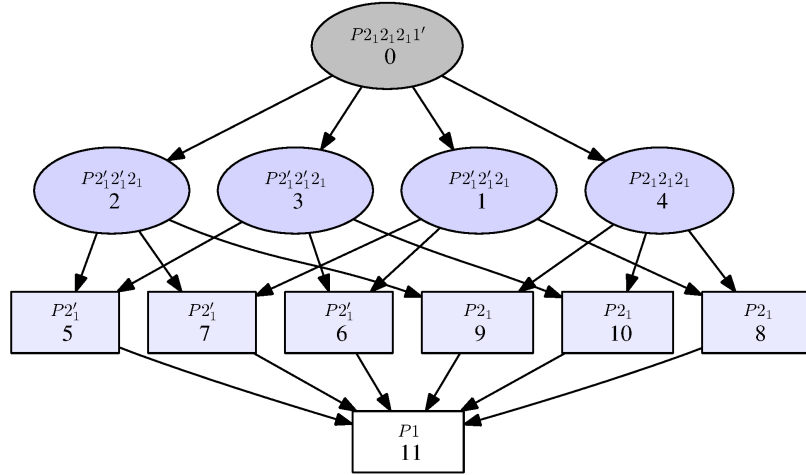


**Figure 6.8** TbODCO$_3$ group subgroup relationship for the $P2_12_12_1$ space group and a **k**=0 propagation vector.

Fitting the data with a model comprised of these two separate magnetic phases leads to excellent fits, as shown in Figure 6.9.
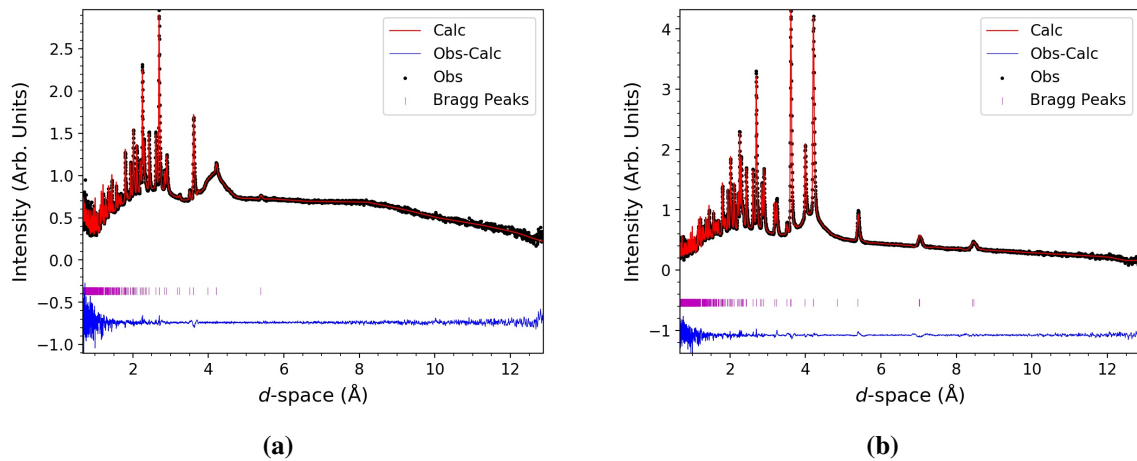


**Figure 6.9** Rietveld refinement fits to the neutron diffraction data of Banks 2/9 of TbODCO$_3$ at (a) 0.0 T and (b) 3.0 T, with the fitting statistics R$_p$: 3.85 %, R$_{wp}$: 1.62 % and R$_p$: 3.90 %, R$_{wp}$: 2.07 %, respectively.

These can be described as a ferromagnetic phase and a canted antiferromagnetic phase. The ferromagnetic phase and the canted antiferromagnetic phases are both expressed by the $P2_1'2_1'2_1$ space group but are differentiated by the presence of the $m\Gamma_4$ and $m\Gamma_2$ modes, respectively. Despite attempts, it was not possible to produce quality fits by lowering the

symmetry to $P2_1$ using any combinations of irreducible representations. This would produce magnetic moments orientations that differ from the easy axes determined in Section 5.4, and is therefore consistent with these previous results. It is also important to note that despite the changes in the magnetic scattering with applied field, the scattering from the crystal structure does not change indicating the crystal structure remains the same under all applied fields.

The ferromagnetic phase emerges in small magnetic fields (<0.1 T) with the canted antiferromagnetic phase forming at <0.2 T applied field, steadily rising with increasing magnetic field. The ferromagnetic phase shows the dominant ferro-magnetic component is along the $b$-axis (Figure 6.10), with non-collinear moments in agreement with the easy axis determined in Section 5.4.
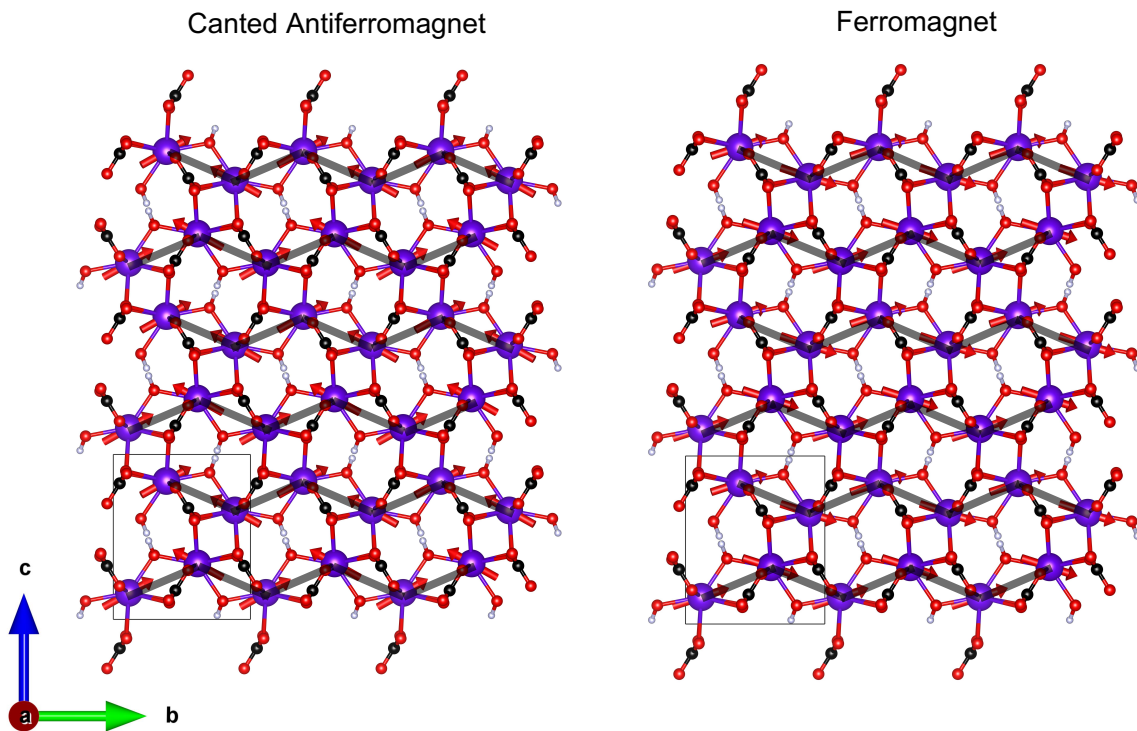


**Figure 6.10** The two magnetic structures of TbODCO$_3$ in an applied magnetic field at 3 T. Tb$^{3+}$ ions are shown in purple, carbon shown in black, oxygen shown in black and Deuterium shown in grey. Unit cell shown in black. Magnetic vectors shown as red arrows. The canted antiferromagnetic structure (left) still has a significant ferromagnetic component along the $c$-axis, and the ferromagnetic structure is purely ferromagnetic along the $b$-axis. Both structures agree with the Ising character and easy axis, inferred from previous measurements.

This reflects the non-collinear nature of the Ising-like short range ordered phase of TbODCO$_3$. In this long range ordered structure, however, not only are the magnetic cations within the

chains ferromagnetically coupled but they also have ferromagnetic inter-chain coupling. This indicates that the applied magnetic field has overcome the interchain antiferromagnetic coupling found in the short range ordered phase. Using the Bilbao Crystallographic Server [166] we have determined this magnetic phase can be described by the magnetic space group $P2_1'2_1'2_1$, with a single magnetic site.

The presence of a canted antiferromagnetic phase co-existing with a ferromagnetic phase in the presence of a magnetic field was initially peculiar. We can see that the refined canted antiferromagnetic phase has non-collinear spins oriented towards directions summarised in Table 6.1 and A.4 leading to a ferromagnetic component along the $c$-axis. The spin orientation in both phases is oriented essentially along the same easy axis, despite the changes in the orientation of the ferromagnetic component. This canted antiferromagnetic phase can also be described by the $P2_1'2_1'2_1$ magnetic space group, through a transformation, with antiferromagnetic intrachain coupling, which is also puzzling given ferromagnetic coupling is dominant within the chains of this compound in the short range correlated phase that forms in the absence of an applied field.

**Table 6.1** Summary of the *Ln*ODCO$_3$ applied field magnetic structures, showing the spin vectors of the canted antiferromagnetic (CAFM) and ferromagnetic (FM) structure at 3.0 T, given as unit vectors. The x, y and z fractional coordinates of Tb1-4 atomic sites are Tb1 = 0.00554(17), 0.11279(4), 0.161820(28); Tb2 = 0.49446(17), 0.88721(4), 0.661820(28); Tb3 = 0.99446(17), 0.61279(4), 0.338180(28) and Tb4 = 0.50554(17), 0.38721(4), 0.838180(28).

| Atomic Sites | CAFM | | | FM | | |
|---|---|---|---|---|---|---|
| *Atom* | u | v | w | u | v | w |
| Tb1 | 0.223(12) | 0.851(23) | 0.483(11) | 0.152(10) | 0.942(22) | 0.301(11) |
| Tb2 | −0.223(12) | −0.851(23) | 0.483(11) | 0.152(10) | 0.942(22) | −0.301(11) |
| Tb3 | 0.223(12) | −0.851(23) | 0.483(11) | −0.152(10) | 0.942(22) | −0.301(11) |
| Tb4 | −0.233(12) | 0.851(23) | 0.483(11) | −0.152(10) | 0.942(22) | 0.301(11) |

In order to rationalise the presence of two co-existing magnetic phases in variable applied fields, the applied field vector must be considered. The near random particle orientation distribution in powder samples produces suitable powder averaging to allow indexing and characterisation of the nuclear phase in these materials. However with highly anisotropic single ion moments, in the application of a magnetic field sufficient powder averaging is lost. Therefore, the applied magnetic field acting on the powder averaged sample forces the magnetic moments to align in the most favourable orientations that is symmetry allowed and with consideration to the local Ising easy axis. That is, if the magnetic field vector is applied

closer to the *b*-axis of the randomly oriented particle, the ferromagnetic component of the moments will be aligned along the *b*-axis producing the ferromagnetic phase, and while we hypothesis that the canted antiferromagnetic phase arises when the applied field is closer to the *c*-axis consisting the ferromagnetic component observed along the *c*-axis. Both structures produce moments with easy axes close to that determined from the RMC studies in Section 5.4 and the long range ordered **k**=0 state seen in HoODCO$_3$, but with the exception that they both have ferromagnetic components along the *b*, and *c* axes for the ferromagnetic and canted antiferromagnetic structures, respectively.

To properly understand the ground state of this material in moderate magnetic fields, neutron diffraction sized single crystals should be obtained since these will allow fields to be applied along particular directions of the crystal structure in a more controlled fashion. However, given the challenges in growing large single crystal under hydrothermal conditions this will require considerable synthetic optimisation. Additionally for highly anisotropic single ions such as Tb$^{3+}$, the magnetic moments refined from powder diffraction data must be considered tentatively. When a field is applied the moment are oriented along the easy axis vector as close to the applied field, but powder averaging fails to average the crystal field of the ions, and therefore the moments lengths are a approximation. Despite the lack of compensation in the FullProf suite (or any other Rietveld software), the magnetic structures and moments determined are sensible and therefore we are confident our model is close to the physical manifestation of these phenomena. The effect of the applied magnetic field on the evolution of the magnetic phases is in broad agreement with the magnetic susceptibility measurement, as shown in Figure 6.11, showing typical magnetisation behaviour and beginning to saturate below 2 T.

We note there is some discrepancy between the neutron diffraction measurements which were performed at 1.5 K, and the magnetisation measurements measured at 2 K. That is the magnetisation rises steeper than the neutron diffraction data, and so for comparison the neutron diffraction data has been compared with magnetisation measurements at 4 K. We hypothesis, however, that it is likely that the discrepancy is due to either the aforementioned issues with powder averaging in Ising like systems or the two experimental methods measuring magnetisation on an atomic and bulk scale. We cannot absolutely rule out that this is a result of poor thermal equilibration of the sample or by the trapped magnetic flux in the magnet. The co-existence of two **k**=0 magnetic phases additionally lead to the problem of have many overlapping reflections, with contributions from each phase difficult to de-convolute, leading to a noisy neutron magnetisation curve.
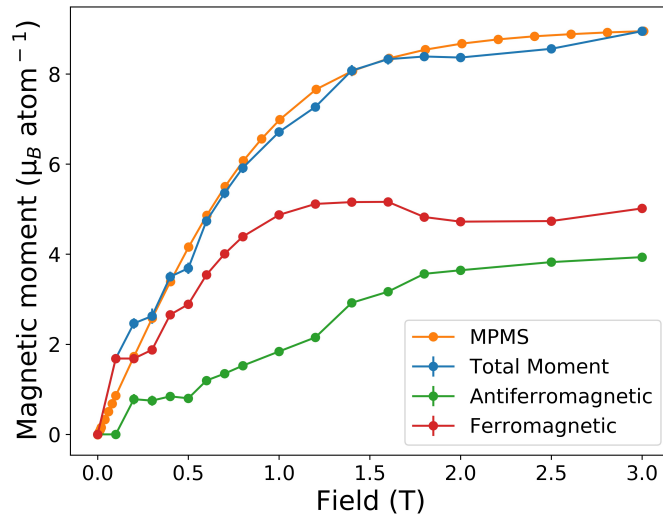
**Figure 6.11** Evolution of the ordered magnetic moments associated with the ferromagnetic phases of TbODCO$_3$ with respect to applied field. Shown in blue is the ordered magnetic moment as determined by Rietveld refinement of the diffraction pattern from neutron diffraction data. Shown in orange is the magnetic moment as determined by the SQUID MPMS. The magnetic moment determined from MPMS has been scaled appropriately for comparison, so that the largest magnetic moments are equal.

In a 3.0 T magnetic field, at 1.5 K, the ferromagnetic and canted antiferromagnetic phases have magnetic moments of 5.02(6) and 3.94(3) $\mu_B$, respectively. This indicates that the dominant phase is the ferromagnetic phase, which maintains the ferromagnetic chains observed in the short range ordered phase as discussed in Section 5.4, but with all ferromagnetic chains ferromagnetically coupled due to the field suppressing the interchain antiferromagnetic coupling. This indicates that only a small magnetic field along specific axis is required to suppress the interchain correlations and align the entire phase ferromagnetically along the *b*-axis. This may indicate that single crystal samples of TbODCO$_3$ magnetised along the *b*-axis may show a single ferromagnetic phase and therefore would have even better magnetocaloric performance in low applied magnetic fields, than the powder analogue. As discussed above the presence of this antiferromagnetic phase is likely due to the magnetic field vector applied along the *c*-axis in some particles, and requires higher magnetic fields to establish. This suggests that applying a magnetic field vector along the *c*-axis to a single crystal, of this phase, is likely to only display the canted antiferromagnetic structure described above. This could suggest that there is potential to recover the full entropy change of these materials in the adiabatic refrigeration cycle in smaller magnetic fields, by applied a magnetic field along the *b*-axis, such that the *Ln*ODCO$_3$ phases would provide even better magnetocaloric performance than its already impressive results. We therefore suggest that bulk magnetic

property studies and neutron scattering work on single crystals of these materials would likely shed further useful insight into the properties and interactions of these interesting materials.

## 6.4 Variable Temperature Measurements in a 1 T Magnetic Field

In order to determine the persistence of these magnetic phases to higher temperatures, variable temperature measurements have been performed in fixed magnetic fields. $TbODCO_3$ was warmed to 20 K, and the field was set to $\mu_0 H = 0$ T, in order to break down any short or long range magnetic order. The sample was then cooled to $T_{base} = 1.5$ K and a 1.0 T magnetic field was applied. A 1.0 T field was seen to be an appropriate field to apply due to the efficient magnetocaloric performance of $TbODCO_3$ in a 1.0 T field changes over a wide temperature range. In the presence of a 1.0 T magnetic field measurements were taken between 1.5 and 30 K in variable steps. At $T_{base}$ the magnetic peaks are clearly present indicating the presence of both the ferromagnetic and antiferromagnetic phases. The length of total moment is 7.31(12) $\mu_B$, consisting of ferromagnetic moments of 4.61(6) $\mu_B$, and antiferromagnetic moments of 2.70(6) $\mu_B$ (see Figure 6.12 for quality of the fit).



(a)  (b)
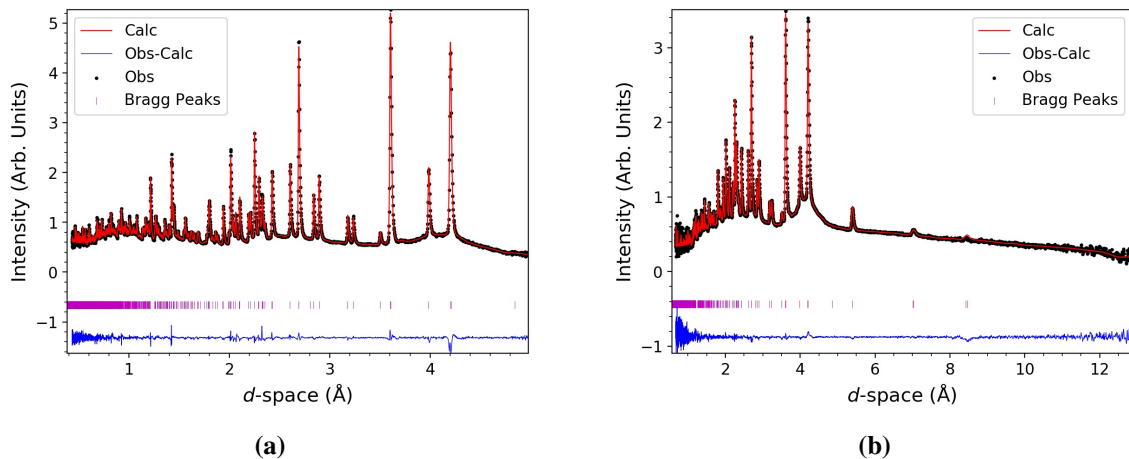
**Figure 6.12** Rietveld refinement fits to the neutron diffraction data of $TbODCO_3$ on banks (a) 5/6 at (b) 2/9 with the fitting statistics $R_p$: 2.59 %, $R_{wp}$: 2.82 % and $R_p$: 3.91 %, $R_{wp}$: 1.85 %, respectively.

Raising the temperature with the applied magnetic field resulted in a continuous reduction magnetic moment lengths of both phases, as can be seen in Figure 6.13. While the magnetic order of the canted antiferromagnetic phase is lost at 30 K there is still significant ordered

moment in the ferromagnetic phase (see Figure 6.13). The magnetic moment at these higher temperature must be considered tentatively, due to the small intensity of the magnetic peaks.
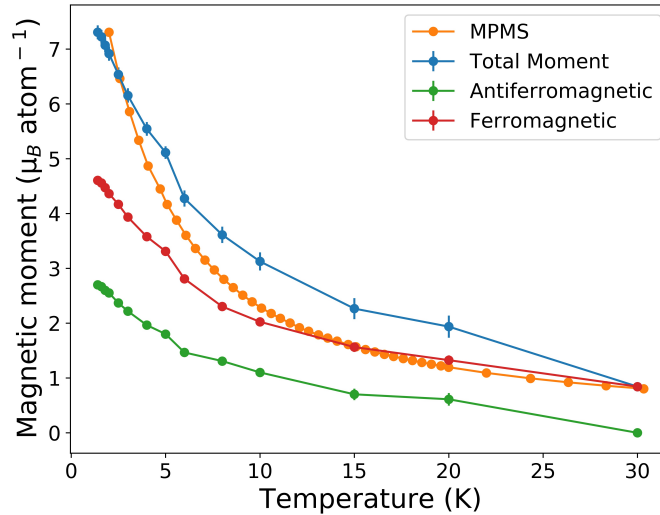


**Figure 6.13** Evolution of the ordered magnetic moments associated with the ferromagnetic phases of TbODCO$_3$ with respect to temperature in a 1 T applied field. Blue indicates the ordered magnetic moment as determined by Rietveld refinement of the diffraction pattern from neutron diffraction data. Orange indicates the magnetic moment as determined by the SQUID MPMS in a 0.1 T field scaled appropriately for comparison, so that the largest magnetic moments are equal.

The continued presence of this ferromagnetic phase in a magnetic field to high temperatures, and certainly through the temperature range where TbOHCO$_3$ has been found to have high magnetocaloric performance, indicates it readily forms under an applied magnetic field, which is beneficial to these physical properties.

As for Tb(DCO$_2$)$_3$ throughout the low applied field measurements there was still significant diffuse scattering, underneath the emergence of the Bragg peaks in TbODCO$_3$. This should encourage further studies utilising reverse Monte Carlo techniques, with considerations for both long and short range order. We have treated the presence of Bragg and diffuse scattering features as an indication of phase coexistence but could be an indication of a more complex magnetic phase exhibiting both.

## 6.5 Conclusions

We have shown that the magnetic structure of two excellently performing low temperature magnetocaloric materials, with applications in liquid helium refrigeration replacement, show

the transition from a high entropy short range ordered paramagnetic phase to a low entropy long range ordered phase under applied magnetic fields. In $Tb(DCO_2)_3$ short range order is initially present, before transitioning to a quasi long-range ordered phase (TIA) in small magnetic fields, and finally to a fully long range ordered ferromagnetic phase in moderate applied magnetic fields. Similarly $TbODCO_3$ shows short range order in zero and small magnetic fields which decreases as the magnetic field increases, as long range order emerges. In $TbODCO_3$ two ordered magnetic phases are found, one ferromagnetic and one canted antiferromagnetic phase, which we hypothesis as being a result of applying a magnetic field to a powder sample of an Ising system; this leads to different grains being exposed to fields from different orientations compared to the crystallographic structure stabilizing two different ground states.

It has been inferred previously in this thesis and in other works [5, 17, 225] that ferromagnetic chains in magnetocaloric materials are beneficial for allowing large changes in entropy with small applied magnetic fields. Here we have shown clearly that ferromagnetic Ising chains play a key role in the adiabatic refrigeration cycle of two promising materials, $Tb(DCO_2)_3$ and $TbODCO_3$. Specifically we suggest that the significant ferromagnetic correlations within these materials enable ordered magnetic states to emerge at low fields, once the frustrated antiferromagnetic interactions in both materials are suppressed. Such ordered states have much lower entropy than the short range ordered states, resulting in large magnetic entropy changes for relatively low applied magnetic field changes. Crucially we have shown that such ordered states persist to temperatures above which the peak magnetocaloric properties are observed, such they are likely to play a key role in this performance. This has great implications in the design of new magnetocaloric materials optimised for low temperature refrigeration, for liquid helium replacement. The hypothesised anisotropic response of $TbODCO_3$ to the applied magnetic field complicates this picture somewhat, since the canted antiferromagnetic state does not retain the ferromagnetic correlations from the short-range ordered structure. It is notable that this is the smaller phase fraction, particularly below 1 T, and may suggest better magnetocaloric performance could be obtained from single crystals of this sample.

# 7

# Conclusions

This thesis has primarily explored the magnetic structure and correlations of two families of magnetocaloric frameworks, the $Ln(DCO_2)_3$ (where $Ln$ = Gd-Er) and the $Ln$ODCO$_3$ series, and some magnetocaloric measurements of the $Ln$F$_3$. Through physical property measurements and diffraction experiments we have been able to understand the magnetic structure of these materials and how this relates to their exceptional magnetocaloric effect. The magnetocaloric effect in some of these materials has been shown to outperform the benchmark $Gd_3Ga_5O_{12}$ under the low applied magnetic fields, achievable with a permanent magnet and at temperatures more suited to liquid helium refrigeration replacement. The values determined from magnetisation measurements make these some of the best performing magnetocaloric materials in their class, promising a pathway towards magnetocaloric materials for a wider range of cryogenic applications.

These results have shown that the materials that display the largest changes in entropy in the smallest magnetic fields all have similar features in their magnetic lattices. Specifically in the paramagnetic phase these have chains of Ising-like lanthanide cations with short range ferromagnetic intrachain correlations and frustrated antiferromagnetic coupling between these chains. This short range order is present in the magnetocaloric operating temperatures of these materials, and the application of a moderate magnetic field enables these to be transformed into a long range ordered state. This is considered to be a result of the applied magnetic field suppressing the antiferromagnetic interactions between chains that prevent long range order from forming, while, in most cases, reinforcing the ferromagnetic coupling within the chain. This change between short range and long range correlated states enables a large change in magnetic entropy under relatively weak applied magnetic fields. In

short, ferromagnetic chains of Ising anisotropic spins, with competing antiferromagnetic interactions are a recipe for enhanced magnetocaloric materials - Figure 7.1. The conclusions from this thesis are set out in detail below.
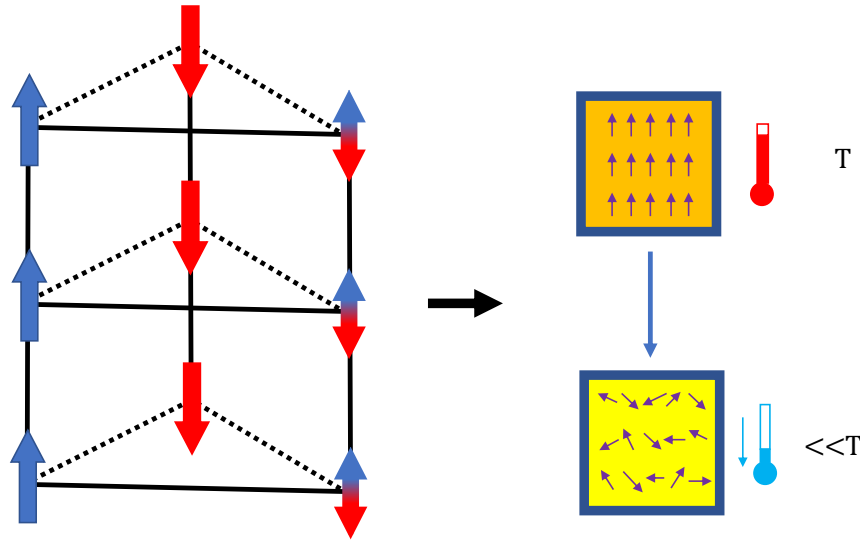


**Figure 7.1** A visual summary of the conclusion of this thesis. Ferromagnetic Ising chains, with competing antiferromagnetic interactions are a recipe for enhanced magnetocaloric materials.

## 7.1 The Magnetocaloric Effect

Inspired by the recent success of investigating non-gadolinium based magnetocaloric materials, [4, 72, 112] containing magnetic ions with significant single ion anisotropy, we have explored the magnetocaloric effect of the $Ln$OHCO$_3$ and the $Ln$F$_3$ material families. The peak entropy changes in some of these materials exceed that of Gd$_3$Ga$_5$O$_{12}$ in equivalent fields, making them suitable magnetic cooling materials for use at liquid helium temperatures using low applied magnetic fields. Magnetisation measurements suggest that all of these heavier lanthanide frameworks have magnetic ions with Ising-like anisotropy, which whilst reducing the total possible entropy change in powders, allows for easy alignment of the spins with applied field along the easy axis.

Of the materials $Ln$OHCO$_3$ frameworks TbOHCO$_3$, DyOHCO$_3$ and HoOHCO$_3$ were shown to have some improved magnetocaloric performance above 4 K in low applied magnetic fields (below 2 T), at the cost of reduced performance at lower temperatures. TbOHCO$_3$ and DyOHCO$_3$, which exhibit the highest MCE performance in this régime, have a greater $-\Delta S_m^{max}$ than the benchmark material Gd$_3$Ga$_5$O$_{12}$ with peak performance shifted to higher

temperatures. Of these DyOHCO$_3$ is the best performing compound maintaining a greater entropy change than $-\Delta S_m^{max}$ of Gd$_3$Ga$_5$O$_{12}$ to nearly 10 K.

In the *Ln*F$_3$ materials TbF$_3$ and HoF$_3$ have optimised performance for higher temperatures in low applied magnetic fields although this is inferior compared to the best of the *Ln*OHCO$_3$ phases. While both these compounds and DyF$_3$ and ErF$_3$ all show Ising-like magnetisation curves the magnetocaloric entropy change of DyF$_3$ and ErF$_3$ gradually increase to 2 K with inferior performance to GdF$_3$ which has a magnetisation curve consistent with Heisenberg spins. This indicates the high magnetocaloric effect cannot be described by the Ising-like anisotropy of the material alone, and that other factors must be taken into consideration to rationalise this improved performance. We show the particular high persistence of the magnetocaloric effect in HoF$_3$ may show promise in wide temperature magnetocaloric devices.

## 7.2   *Ln*(DCO$_2$)$_3$ **Magnetic Structure**

Prior to this work, the *Ln*(DCO$_2$)$_3$ frameworks had already been established to combine 1D magnetism with frustration leading to the triangular Ising antiferromagnetic (TIA) state in Tb(DCO$_2$)$_3$. This created the expectation there was more to be uncovered in these materials leading to the detailed neutron scattering studies presented in this thesis. We found that only the materials with magnetocaloric properties optimised for higher temperatures in low fields, Tb(DCO$_2$)$_3$, and Ho(DCO$_2$)$_3$, feature significant structured diffuse scattering above 1.5 K. This has been interpreted via reverse Monte Carlo methods to be a result of ferromagnetic 1D correlations with weaker frustrated antiferromagnetic coupling. This is in contrast to other Ising *Ln*(DCO$_2$)$_3$ phases, which lack such optimised magnetocaloric performance and diffuse scattering. The stronger 1D ferromagnetic correlations in Tb(DCO$_2$)$_3$ likely explain why this is the most efficient magnetocaloric material compared to Ho(DCO$_2$)$_3$.

Magnetic ordering of Tb(DCO$_2$)$_3$ changes below 1.2 K from a TIA state to one that appears to display emergent order, when interpreted via conventional crystallographic approaches. The broadness of the Bragg-like peaks and retention of the magnetic diffuse scattering is consistent with the retention of 1D order in the TIA phase of Tb(DCO$_2$)$_3$ in this lower temperature phase but only the average magnetic structure of this state has been refined in this thesis. The emergent charge ordered (ECO) state, likely the first example of such a state in a MOF, is robust to the two possible magnetic structures, which vary only in the phase of their scattering. Subsequently we show that Ho(DCO$_2$)$_3$ is likely the second example of a

MOF with an ECO state, with its short range ordered state directly evolving to give a similar combination of sharp and diffuse scattering as seen in $Tb(DCO_2)_3$, without the formation of the TIA phase in between. Using inelastic neutron scattering we confirm the presence of Ising anisotropy in $Tb(DCO_2)_3$ and directly determine the strength of its magnetic interactions by modelling its spin wave. Finally neutron measurements of $Er(DCO_2)_3$ reveal the emergence of an ordered state with antiferromagnetic intrachain coupling, which is likely linked to its poorer magnetocaloric properties since antiferromagnetic chains will not align as readily with an applied magnetic field.

Field studies further consolidate the hypothesis of 1D ferromagnetic chains improving the magnetocaloric effect in low applied fields. In $Tb(DCO_2)_3$ we directly observe a change from short range correlations in 1D ferromagnetic chains to the TIA state and finally to long range ferromagnetic order, all in fields under 1 T. This indicates that the application of the applied magnetic fields first strengthens the coupling within the chains before suppressing the antiferromagnetic correlations between them. The evolution of a ferromagnetic phase under a modest applied magnetic fields is consistent with our hypothesis that the 1D correlations in the short range ordered phase are clearly directly linked to the improved magnetocaloric effect. We see that these correlations persist well above $T_N$ in applied magnetic fields, and there is a clear route from high entropy short range ordered state, to a low entropy long range ordered phase.

## 7.3  *Ln*ODCO₃ **Magnetic Structure**

Inspired by the recent magnetostructural-property relationships of the $Ln(DCO_2)_3$, [4] and the efficient magnetocaloric effect of $GdOHCO_3$, [5, 77] we have explored the $Ln$ODCO₃ frameworks. These were found to show similar exotic magnetic states combining ferromagnetic chains with frustrated antiferromagnetic interchain coupling, which are directly responsible for the optimised magnetocaloric performance. We have shown that the magnetocaloric materials with properties optimised for applications above 4 K, $Tb$ODCO₃, $Dy$ODCO₃ and $Ho$ODCO₃, all display significant magnetic diffuse scattering. No short or long range order was observed in $Er$ODCO₃ which lacks such a magnetocaloric effect. Through reverse Monte Carlo techniques it has been shown that the magnetic diffuse scattering arises from short range ferromagnetically coupled spins on chains, with antiferromagnetic interchain interactions. Fits to the data with constrained spins indicate the spins have Ising-like anisotropy,

and fits to the temperature dependence of the correlations length indicate this evolve in the way consistent with isolated 1D Ising chains.

HoODCO$_3$ undergoes a transition from a short range ordered phase to an incommensurate magnetic phase at $\approx$1.3 K, as the correlations length grows from short range to quasi-long range order. This incommensurate magnetic phase can be described as a spin-density sine wave, which can be considered to be an average structure interpretation of a disordered magnetic structure. Cooling further causes a changed in the propagation vector eventually locking in to a $\mathbf{k} = 0$ antiferromagnetic phase, with a finite correlation length. Even at the lowest recorded temperature the correlation length of the magnetic interactions remains finite. Therefore, in its ground state the competing interactions prevent fully long range order from forming. All magnetic phases shown in HoODCO$_3$ contain the ferromagnetic Ising chains present in the short range ordered phase.

Field studies of TbODCO$_3$ indicate in the application of small magnetic fields, there is coexistence of short and long range order. With increasing magnetic fields the short range order diminishes in intensity as long range magnetic order becomes dominant. The long range magnetic order can be described by two magnetic phases, one with ferromagnetic intrachain correlations and one without. We attribute this dual magnetic phase to the application of a magnetic field to an anisotropic powder. In the application of moderate magnetic fields this long range order persist to temperatures well above $T_N$ , indicating these phases are directly responsible for the change from a high entropy short range order phase to the low entropy long range ordered magnetic phase.

## 7.4   Future Work

This thesis has explored the magnetocaloric behaviour and magnetic structure of the late lanthanides frameworks. In order to fully understand why these materials have greater MCE at higher temperatures and lower fields than the gadolinium analogues, despite lower total entropy we need to understand the magnetic structure of GdODCO$_3$ and Gd(DCO$_2$)$_3$. Of course this is not a trivial task through neutron diffraction techniques due to the high absorption cross section of naturally abundant gadolinium approximately 50x more absorbing than Dy and 2100x more absorbing than Tb. [223] In order to carry out such experiments, synthesis of these materials with enriched gadolinium will be required, and long count times. We would expect to see no frustration in these materials due to the lack of single ion anisotropy in Gd, and therefore no short range order and eventual long range order at

sufficiently low temperatures, as noted in $Er(DCO_2)_3$. Similar low temperature studies on all $Ln(DCO_2)_3$ and $LnODCO_3$ materials down to dilution refrigeration temperatures would also enable these to be probed for unique magnetic states.

In order to clarify why the Er materials behave so differently from the Tb and Ho materials, despite apparent Ising-like anisotropy, it would be necessary to probe any magnetic excitations through inelastic neutron spectroscopy of both $Ho(DCO_2)_3$ and $Er(DCO_2)_3$. Assuming magnetic excitations are present, we would expect to see a spin-wave similar to that seen in $Tb(DCO_2)_3$, in $Ho(DCO_2)_3$ while antiferromagnetic intrachain coupling in $Er(DCO_2)_3$ should lead to significantly different features. We have inferred the anisotropy of the $LnODCO_3$ through RMC techniques and magnetisation measurements, but it would be preferable to confirm the Ising mechanics of these materials directly.

Inelastic measurements of $Tb(DCO_2)_3$ revealed some interesting magnetic features, which we were unable to fully account for in the spectra fitting. It is possible the high temperature features were simply due to the persistence of the quasi-1D magnetism, as seen in other quasi 1D systems. [212] However these features also alluded to more exotic behaviour which would require more extensive variable temperature studies, and better fitting. For example fitting the structure factor of a bond valence solid to the feature that we saw in the high temperature phases. In the low temperature ECO phase the spin-wave excitation fit the feature quite well, however we are still unaware of whether this is a static or fluid state. Muon spin spectroscopy would be the ideal tool for probing the dynamics of these low temperatures phases, but the decay of the muon is directly related to the magnetic moment of the magnetic ion. [31, 226] Therefore, an instrument without very fast counting times, will miss the decay of the muon and measure no useful data. Therefore a sufficiently fast instrument, such as those at the Paul Sherrer Institut, Switzerland should be used to probe the dynamics and quasi-long range order seen in $Tb(DCO_2)_3$ and $Ho(DCO_2)_3$. The average structure approach we have applied to understanding the ECO phases of $Tb(DCO_2)_3$ and $Ho(DCO_2)_3$ are sufficient for an initial understanding of these materials, but further Monte Carlo studies are required to understand the precise nature of this state and how its combination of diffuse and sharp scattering arises.

The magnetocaloric behaviour of the $LnF_3$ was explored, but in some cases, in poorly crystalline impure materials. Synthesis of higher quality powders and/or single crystal should be attempted of these lanthanide compounds, and also of the solid solutions, which showed promising magnetocalorics in the $Ln(DCO_2)_3$. [4] Inspection of the nuclear and reported magnetic structure reveals they show properties required to show short range order and

ferromagnetic chains. Therefore, neutron diffraction studies should be performed on modern instruments on the $Ln$F$_3$, in order to probe the magnetic structure and correlations, including for the presence of short range ordered states.

GdPO$_4$ is another example of a framework material with a promising magnetocaloric effect at temperatures 2-10 K. [69] Given the success of substituting isotropic Gd for anisotropic Tb, Dy and Ho found in this work these member of the $Ln$PO$_4$ series of materials should be thoroughly investigated to determine their magnetocaloric properties and, using similar approaches to those presented in this thesis, probe the link to their magnetic interactions.

Our magnetocaloric measurements throughout this thesis have assumed that the Maxwell relations that calculate the magnetocaloric effect from magnetisation curves are accurate, as has shown to be the case for other materials. [77, 227, 228] In order to confirm the accuracy of the magnetocaloric measurements direct measurement of the magnetocaloric effect should be performed within an adiabatic refrigerator setup, measuring the change in temperature with changes in magnetic field. The priority here would be DyOHCO$_3$ which showed the greatest changes in entropy with applied magnetic field and is therefore the most likely to find applications in low temperature refrigeration. The suggestion that the direction of the applied field on TbODCO$_3$ play a role in which of two long range ordered states also highlights that the magnetocaloric performance of the $Ln$ODCO$_3$ phases could be improved by judicial application of magnetic fields to various directions of the single crystals of these materials. Accompanying neutron scattering studies of such single crystal samples would also provide a wealth of information.

# References

(1)   R. Moessner and A. P. Ramirez, *Physics Today*, 2006, **59**, 24–29.

(2)   R. L. Comstock, *Journal of Materials Science: Materials in Electronics*, 2002, **13**, 509–523.

(3)   F. S. Guo, B. M. Day, Y. C. Chen, M. L. Tong, A. Mansikkamäki and R. A. Layfield, *Science*, 2018, **362**, 1400–1403.

(4)   P. J. Saines, J. A. M. Paddison, P. M. M. Thygesen and M. G. Tucker, *Materials Horizons*, 2015, **2**, 528–535.

(5)   R. J. Dixey and P. J. Saines, *Inorganic Chemistry*, 2018, **57**, 12543–12551.

(6)   Y. D. Xiao, R. Paudel, J. Liu, C. Ma, Z. S. Zhang and S. K. Zhou, *International Journal of Molecular Medicine*, 2016, **38**, 1319–1326.

(7)   P. Wasilewski and G. Kletetschka, *Geophysical Research Letters*, 1999, **26**, 2275–2278.

(8)   P. Weiss, *Journal de Physique Théorique et Appliquée*, 1907, **6**, 661–690.

(9)   M. L. Néel, *Annales de Physique*, 1948, **12**, 137–198.

(10)  A. K. Cheetham and C. N. R. Rao, *Science*, 2007, **318**, 58–59.

(11)  A. M. Ganose, C. N. Savory and D. O. Scanlon, *Chemical Communications*, 2017, **53**, 20–44.

(12)  J. L. Minns, P. Zajdel, D. Chernyshov, W. Van Beek and M. A. Green, *Nature Communications*, 2017, **8**, 15152.

(13)  H. Li, M. Eddaoudi, M. O'Keeffe and O. M. Yaghi, *Nature*, 1999, **402**, 276–279.

(14)  J.-R. Li, R. J. Kuppler and H.-C. Zhou, *Chemical Society Reviews*, 2009, **38**, 1477–504.

(15)  L. E. Kreno, K. Leong, O. K. Farha, M. Allendorf, R. P. Van Duyne and J. T. Hupp, *Chemical Reviews*, 2012, **112**, 1105–1125.

(16)  P. Jain, V. Ramachandran, R. J. Clark, D. Z. Hai, B. H. Toby, N. S. Dalal, H. W. Kroto and A. K. Cheetham, *Journal of the American Chemical Society*, 2009, **131**, 13625–13627.

(17)  R. Li, P. Manuel, F. Orlandi and C. Greaves, *Journal of Materials Chemistry A*, 2018, **6**, 21149–21155.

(18)  D. R. Harcombe, P. G. Welch, P. Manuel, P. J. Saines and A. L. Goodwin, *Physical Review B*, 2016, **94**, 174429.

(19)  P. W. Atkins and J. De Paula, *Atkins' Physical chemistry*, Oxford University Press, 2010, p. 695.

(20)  *International Tables for Crystallography*, ed. M. I. Aroyo, International Union of Crystallography, Chester, England, 2016, vol. A.

(21)  P. J. Hall, *Synthese*, 1986, **69**, 267–272.

(22)  F. Hund, *Linienspektren und Periodisches System der Elemente*, J. Springer, 1927.

(23)  N. A. N. A. Spaldin, *Magnetic materials : fundamentals and applications*, Cambridge University Press, 2011, p. 274.

(24)  S. A. Cotton, *Lanthanide and actinide chemistry*, Wiley, 2006, p. 263.

(25)  H. N. Russell and F. A. Saunders, *The Astrophysical Journal*, 1925, **61**, 38–69.

(26)  C. G. Shull and J. S. Smart, *Physical Review*, 1949, **76**, 1256–1257.

(27)  E. Fawcett, H. L. Alberts, V. Y. Galkin, D. R. Noakes and J. V. Yakhmi, *Reviews of Modern Physics*, 1994, **66**, 25–127.

(28)  A. R. West, *Solid state chemistry and its applications*, Wiley, 1984.

(29)  L. Savary and L. Balents, *Quantum spin liquids: A review*, 2017.

(30)  J. R. Hook and H. E. Hall, *Solid state physics*, John Wiley and Sons, 2010, p. 474.

(31)  S. Blundell, *Magnetism in Condensed Matter*, Oxford University Press, 2001, vol. 71, p. 238.

(32) D. C. Jiles and D. L. Atherton, *Journal of Magnetism and Magnetic Materials*, 1986, **61**, 48–60.

(33) P. Mukherjee and S. E. Dutton, *Advanced Functional Materials*, 2017, **27**, 1701950.

(34) J. Filippi, F. Tcheou and J. Rossat-Mignod, *Solid State Communications*, 1980, **33**, 827–832.

(35) H. Kramers, *Physica*, 1934, **1**, 182–192.

(36) P. W. Anderson, *Physical Review*, 1950, **79**, 350–356.

(37) J. B. Goodenough, *Journal of Physics and Chemistry of Solids*, 1958, **6**, 287–297.

(38) J. Kanamori, *Journal of Physics and Chemistry of Solids*, 1959, **10**, 87–98.

(39) J. Goodenough, *Magnetism and the chemical bond.* Interscience Publishers, New York, 1963.

(40) E. Ising, *Zeitschrift für Physik*, 1925, **31**, 253–258.

(41) R. Peierls, *Mathematical Proceedings of the Cambridge Philosophical Society*, 1936, **32**, 477–481.

(42) A. Hellemans and B. H. Bunch, *The timetables of science : a chronology of the most important people and events in the history of science*, Simon and Schuster, 1988, p. 656.

(43) L. Landau, *Nature*, 1936, **138**, 840–841.

(44) Haan, Klaetke and Mütter, *Physical Review. B*, 1992, **46**, 5723–5726.

(45) J. Neirotti and M. de Oliveira, *Physical Review B*, 1996, **54**, 6351–6355.

(46) P. Fendley, *Modern Statistical Mechanics*, The University of Virginia, 2014, p. 98.

(47) F. Bloch, *Zeitschrift für Physik*, 1930, **61**, 206–219.

(48) J. C. Slater, *Physical Review*, 1930, **35**, 509–529.

(49) J. Van Kranendonk and J. H. Van Vleck, *Reviews of Modern Physics*, 1958, **30**, 1–23.

(50) S. Viola Kusminskiy, in *Quantum Magnetism, Spin Waves, and Optical Cavities*, 2019, pp. 45–59.

(51) C. Kittel, *Introduction to solid state physics*, Wiley, 2005, p. 680.

(52) A. Prabhakar and D. D. Stancil, *Spin waves: Theory and applications*, Springer US, Boston, MA, 2009, pp. 1–355.

(53)   A. Smith, *The European Physical Journal H*, 2013, **38**, 507–517.

(54)   E. Brück, *Journal of Physics D: Applied Physics*, 2005, **38**, R381–R391.

(55)   W. F. Giauque and D. P. MacDougall, *Physical Review*, 1933, **43**, 768–768.

(56)   F. J. Bruni, in, Springer, Berlin, Heidelberg, 1978, pp. 53–70.

(57)   T. J. Sato, D. Okuyama and H. Kimura, *Review of Scientific Instruments*, 2016, **87**, 123905.

(58)   Y. I. Spichkin, A. K. Zvezdin, S. P. Gubin, A. S. Mischenko and A. M. Tishin, *Journal of Physics D: Applied Physics*, 2001, **34**, 1162–1166.

(59)   M. Evangelisti, E. K. Brechin and M. Verdaguer, *Dalton Transactions*, 2010, **39**, 4672–4676.

(60)   Y.-Z. Zheng, G.-J. Zhou, Z. Zheng and R. E. P. Winpenny, *Chem. Soc. Rev.*, 2014, **43**, 1462–75.

(61)   J. W. Sharples and D. Collison, *Polyhedron*, 2013, **54**, 91–103.

(62)   G. Lorusso, J. W. Sharples, E. Palacios, O. Roubeau, E. K. Brechin, R. Sessoli, A. Rossin, F. Tuna, E. J. L. McInnes, D. Collison and M. Evangelisti, *Advanced Materials*, 2013, **25**, 4653–4656.

(63)   Y. Lvovsky, E. W. Stautner and T. Zhang, *Superconductor Science and Technology*, 2013, **26**, 93001.

(64)   R. Radebaugh, *Journal of Physics Condensed Matter*, 2009, **21**, 164219–164227.

(65)   Z. Gan, W. Dong, L. Qiu, X. Zhang, H. Sun, Y. He and R. Radebaugh, *Cryogenics*, 2009, **49**, 198–201.

(66)   L. Chen, H. Jin, J. Wang, Y. Zhou, W. Zhu and Q. Zhou, *Cryogenics*, 2013, **54**, 54–58.

(67)   J. A. Paddison, H. Jacobsen, O. A. Petrenko, M. T. Fernández-Díaz, P. P. Deen and A. L. Goodwin, *Science*, 2015, **350**, 179–181.

(68)   J. Barclay and W. Steyert, *Cryogenics*, 1982, **22**, 73–80.

(69)   E. Palacios, J. A. Rodríguez-Velamazán, M. Evangelisti, G. J. McIntyre, G. Lorusso, D. Visser, L. J. De Jongh and L. A. Boatner, *Physical Review B*, 2014, **90**, 214423.

(70)  R. S. Silva, P. Barrozo, N. O. Moreno and J. A. Aguiar, *Ceramics International*, 2016, **42**, 14499–14504.

(71)  T. Numazawa, K. Kamiya, T. Okano and K. Matsumoto, *Physica B: Condensed Matter*, 2003, **329-333**, 1656–1657.

(72)  P. Mukherjee, Y. Wu, G. I. Lampronti and S. E. Dutton, *Materials Research Bulletin*, 2018, **98**, 173–179.

(73)  Y.-C. Chen, J. Prokleška, W.-J. Xu, J.-L. Liu, J. Liu, W.-X. Zhang, J.-H. Jia, V. Sechovský and M.-L. Tong, *J. Mater. Chem. C*, 2015, **3**, 12206–12211.

(74)  B. Daudin, R. Lagnier and B. Salce, *Journal of Magnetism and Magnetic Materials*, 1982, **27**, 315–322.

(75)  S. Biswas, H. S. Jena, A. Adhikary and S. Konar, *Inorganic Chemistry*, 2014, **53**, 3926–3928.

(76)  K. Michiba, T. Tahara, I. Nakai, R. Miyawaki and S. Matsubara, *Zeitschrift für Kristallographie*, 2011, **226**, 518–530.

(77)  Y.-C. Chen, L. Qin, Z.-S. Meng, D.-F. Yang, C. Wu, Z. Fu, Y.-Z. Zheng, J.-L. Liu, R. Tarasenko, M. Orendáč, J. Prokleška, V. Sechovský and M.-L. Tong, *Journal of Materials Chemistry A*, 2014, **2**, 9851–9858.

(78)  G. H. Wannier, *Physical Review*, 1950, **79**, 357–364.

(79)  C. Castelnovo, R. Moessner and S. Sondhi, *Annual Review of Condensed Matter Physics*, 2012, **3**, 35–55.

(80)  C. Castelnovo, R. Moessner and S. L. Sondhi, *Nature*, 2008, **451**, 42–45.

(81)  J. A. Paddison, H. S. Ong, J. O. Hamp, P. Mukherjee, X. Bai, M. G. Tucker, N. P. Butch, C. Castelnovo, M. Mourigal and S. E. Dutton, *Nature Communications*, 2016, **7**, 13842.

(82)  H. Serrano-González, S. T. Bramwell, K. D. M. Harris, B. M. Kariuki, L. Nixon, I. P. Parkin and C. Ritter, *Physical Review B*, 1999, **59**, 14451–14460.

(83)  S. Kawamura, H. Miyashita, *Journal of the Physical Society of Japan*, 1985, **54**, 3385–3395.

(84)  D. A. Keen and A. L. Goodwin, *Nature*, 2015, **521**, 303–309.

(85) P. Mendels and F. Bert, *Comptes Rendus Physique*, 2016, **17**, 455–470.

(86) M. R. Norman, *Reviews of Modern Physics*, 2016, **88**, 041002.

(87) M. P. Shores, E. A. Nytko, B. M. Bartlett and D. G. Nocera, *Journal of the American Chemical Society*, 2005, **127**, 13462–13463.

(88) J. S. Helton, K. Matan, M. P. Shores, E. A. Nytko, B. M. Bartlett, Y. Yoshida, Y. Takano, A. Suslov, Y. Qiu, J. H. Chung, D. G. Nocera and Y. S. Lee, *Physical Review Letters*, 2007, **98**, 107204.

(89) A. Banerjee, C. A. Bridges, J. Q. Yan, A. A. Aczel, L. Li, M. B. Stone, G. E. Granroth, M. D. Lumsden, Y. Yiu, J. Knolle, S. Bhattacharjee, D. L. Kovrizhin, R. Moessner, D. A. Tennant, D. G. Mandrus and S. E. Nagler, *Nature Materials*, 2016, **15**, 733–740.

(90) E. Majorana, *Il Nuovo Cimento*, 1937, **14**, 171–184.

(91) J. A. Paddison, M. Daum, Z. Dun, G. Ehlers, Y. Liu, M. B. Stone, H. Zhou and M. Mourigal, *Nature Physics*, 2017, **13**, 117–122.

(92) C. Mitra, *Nature Physics*, 2015, **11**, 212–213.

(93) T. Koretsune and M. Ogata, *Physical Review Letters*, 2002, **89**, 116401.

(94) A. Vasiliev, O. Volkova, E. Zvereva and M. Markina, *npj Quantum Materials*, 2018, **3**, 18.

(95) H. Yoshizawa, W. Kozukue and K. Hirakawa, *Journal of the Physical Society of Japan*, 1980, **49**, 144–153.

(96) M Mekata, A. T. Sugino A Oohara and K. S. Ohara Yasuda Y Oohara H Yoshizawa, *Journal of Magnetism and Magnetic Materials*, 1995, **140-144**, 1987–1988.

(97) K Kakurai, R Pynn, B Dorner and M Steiner, *Journal of Physics C: Solid State Physics*, 1984, **17**, L123–L128.

(98) T. N. Nguyen, P. A. Lee and H. C. Zur Loye, *Science*, 1996, **271**, 489–491.

(99) A. Maignan, V. Hardy, S. Hébert, M. Drillon, M. R. Lees, O. Petrenko, D. M. K. Paul and D. Khomskii, *Journal of Materials Chemistry*, 2004, **14**, 1231–1234.

(100) J. A. Paddison, S. Agrestini, M. R. Lees, C. L. Fleck, P. P. Deen, A. L. Goodwin, J. R. Stewart and O. A. Petrenko, *Physical Review B*, 2014, **90**, 014411.

(101)   M. Nandi and P. Mandal, *Journal of Applied Physics*, 2016, **119**, 133904.

(102)   J. Chadwick, *Proceedings of the Royal Society A: Mathematical, Physical and Engineering Sciences*, 1932, **136**, 692–708.

(103)   C. G. Shull, W. A. Strauser and E. O. Wollan, *Physical Review*, 1951, **83**, 333–345.

(104)   K. Lonsdale and H. Smith, *Proceedings of the Royal Society A: Mathematical, Physical and Engineering Sciences*, 1941, **179**, 8–50.

(105)   T. R. Welberry, A. P. Heerdegen, D. C. Goldstone and I. A. Taylor, *Acta Crystallographica Section B: Structural Science*, 2011, **67**, 516–524.

(106)   S. B. Maisel, N. Schindzielorz, S. Müller, H. Reichert and A. Bosak, *Journal of Applied Crystallography*, 2013, **46**, 1211–1215.

(107)   J. A. M. Paddison and A. L. Goodwin, *Physical Review Letters*, 2012, **108**, 017204.

(108)   J. A. Paddison, J Ross Stewart and A. L. Goodwin, *Journal of Physics Condensed Matter*, 2013, **25**, 454220.

(109)   P. J. Saines and N. C. Bristowe, *Dalton Transactions*, 2018, **47**, 13257–13280.

(110)   S. O. H. Gutschke, M. Molinier, A. K. Powell and P. T. Wood, *Angewandte Chemie International Edition*, 1997, **36**, 991–992.

(111)   R. Feyerherm, A Loose and J. L. Manson, *Journal of Physics Condensed Matter*, 2003, **15**, 663–673.

(112)   P Mukherjee, A. C. Sackville Hamilton, H. F. J. Glass and S. E. Dutton, *Journal of Physics Condensed Matter*, 2017, **29**, 405808.

(113)   T. Tahara, I. Nakai, R. Miyawaki and S. Matsubara, *Zeitschrift fur Kristallographie*, 2007, **222**, 326–334.

(114)   H.-S. Sheu, W.-J. Shih, W.-T. Chuang, I.-F. Li and C.-S. Yeh, *Journal of the Chinese Chemical Society*, 2010, **57**, 938–945.

(115)   W. Clegg, *Crystal structure determination*, Oxford University Press, 1998, p. 84.

(116)   H. A. Hauptman, *Reports on Progress in Physics*, 1991, **54**, 1427–1454.

(117)   *Powder Diffraction: Theory and Practice*, ed. R. E. Dinnebier and S. J. L. Billinge, Royal Society of Chemistry, Cambridge, 2008, p. 570.

(118) G. M. Sheldrick, *Acta Crystallographica Section A Foundations of Crystallography*, 2008, **64**, 112–122.

(119) G. M. Sheldrick, *Acta Crystallographica Section C: Structural Chemistry*, 2015, **71**, 3–8.

(120) O. V. Dolomanov, L. J. Bourhis, R. J. Gildea, J. A. K. Howard and H. Puschmann, *Journal of Applied Crystallography*, 2009, **42**, 339–341.

(121) D. Altermatt and I. D. Brown, *Acta Crystallographica Section B*, 1985, **41**, 240–244.

(122) B. T. M. Willis and C. J. Carlile, *Experimental neutron scattering*, Oxford University Press, 2009, p. 325.

(123) J. W. Thomason, *Nuclear Instruments and Methods in Physics Research, Section A: Accelerators, Spectrometers, Detectors and Associated Equipment*, 2019, **917**, 61–67.

(124) L. C. Chapon, P. Manuel, P. G. Radaelli, C. Benson, L. Perrott, S. Ansell, N. J. Rhodes, D. Raspino, D. Duxbury, E. Spill and J. Norris, *Neutron News*, 2011, **22**, 22–25.

(125) *ISIS Wish, https://www.isis.stfc.ac.uk/Pages/Wish.aspx, (09/2019).*

(126) A. J. Studer, M. E. Hagen and T. J. Noakes, *Physica B: Condensed Matter*, 2006, **385-386**, 1013–1015.

(127) A. W. Hewat, *Nuclear Instruments and Methods*, 1975, **127**, 361–370.

(128) G. J. McIntyre and P. J. Holden, Journal of Physics: Conference Series, IOP Publishing, 2016, vol. 746, p. 012001.

(129) *Diamond light - Brighter Than The Sun, https://phys.org/news/2012-02-diamond-brighter-sun.html (09/2019).*

(130) C. Vettier, *Journal of Magnetism and Magnetic Materials*, 1994, **129**, 59–65.

(131) L. Paolasini, R. Caciuffo, A. Sollier, P. Ghigna and M. Altarelli, *Physical Review Letters*, 2002, **88**, 106403.

(132) S. W. Lovesey, *Theory of neutron scattering from condensed matter*, Clarendon Press, Oxford (UK), 1984.

(133) O. Halpern and M. H. Johnson, *Physical Review*, 1937, **51**, 992–992.

(134)   O. Halpern and M. H. Johnson, *Physical Review*, 1937, **52**, 52–53.

(135)   O. Halpern and M. H. Johnson, *Physical Review*, 1939, **55**, 898–923.

(136)   O. Halpern and T. Holstein, *Physical Review*, 1941, **59**, 960–981.

(137)   D. Sivia, *Elementary Scattering Theory*, Oxford University Press, 2011.

(138)   *International Tables for Crystallography*, ed. E. Prince, International Union of Crystallography, Chester, England, 2006, vol. C.

(139)   P.J. Brown, *Magnetic Form Factors*.

(140)   G. E. Bacon, *Neutron diffraction*, Clarendon Press, 1975, p. 145.

(141)   H. M. Rietveld, *Journal of Applied Crystallography*, 1969, **2**, 65–71.

(142)   T. J. Rivlin, *Chebyshev Polynomials: From Approximation Theory to Algebra and Number Theory*, John Wiley and Sons, 1990.

(143)   G. Caglioti, A. Paoletti and F. P. Ricci, *Nuclear Instruments*, 1958, **3**, 223–228.

(144)   S. Ikeda and J. M. Carpenter, *Nuclear Inst. and Methods in Physics Research, A*, 1985, **239**, 536–544.

(145)   J Rodriguez-Carvajal, M. T. Fernandez-Diaz and J. L. Martinez, *Journal of Physics: Condensed Matter*, 1991, **3**, 3215–3234.

(146)   J. Rodríguez-Carvajal, *Physica B: Physics of Condensed Matter*, 1993, **192**, 55–69.

(147)   B. Hunter, *Int. Union Crystallogr., Commission Powder Diffr. Newsletter*, 1998, **20**, 21.

(148)   A.C. Larson and R.B. Von Dreele, *Los Alamos National Laboratory Report LAUR*, 2000, 86–748.

(149)   B. H. Toby, S. Hall, F. Allen, I. Brown and H. Rietveld, *Journal of Applied Crystallography*, 2001, **34**, 210–213.

(150)   V. Petrícek, M. Dušek and L. Palatinus, *Zeitschrift fur Kristallographie*, 2014, **229**, 345–352.

(151)   A. I. Gusev, *Physics-Uspekhi*, 2014, **57**, 839–876.

(152)   D. H. Wojtas and R. P. Millane, *Physical Review E - Statistical, Nonlinear, and Soft Matter Physics*, 2009, **79**, 041123.

(153)   C. Yoon and R. P. Millane, *Journal of the Optical Society of America A*, 2014, **31**, 1416.

(154)   R. L. McGreevy and L. Pusztai, *Molecular Simulation*, 1988, **1**, 359–367.

(155)   R. L. McGreevy, *Journal of Physics Condensed Matter*, 2001, **13**, R877–R913.

(156)   M. G. Tucker, D. A. Keen, M. T. Dove, A. L. Goodwin and Q. Hui, *Journal of Physics Condensed Matter*, 2007, **19**, 335218.

(157)   G. L. Squires, *Introduction to the theory of thermal neutron scattering*, Cambridge University Press, Cambridge, 2012, vol. 9781107644, pp. 1–260.

(158)   H. Heesch, *Zeitschrift für Kristallographie - Crystalline Materials*, 1930, **73**, 325–345.

(159)   A. S. Wills, *Powder Diffraction*, 2017, **32**, 148–155.

(160)   S. van Smaalen, *Incommensurate Crystallography*, Oxford University Press, 2008, vol. 9780198570, pp. 1–288.

(161)   B. J. Campbell, H. T. Stokes, D. E. Tanner and D. M. Hatch, *Journal of Applied Crystallography*, 2006, **39**, 607–614.

(162)   E. F. Bertaut, *Acta Crystallographica Section A*, 1968, **24**, 217–231.

(163)   E. F. Bertaut, *Le Journal de Physique Colloques*, 1971, **32**, C1–462–C1–470.

(164)   F. A. Cotton, *Chemical Applications of Group Theory*, 1990.

(165)   T Roisnel and J. Rodriquez-Carvajal, Materials Science Forum, Trans Tech Publications, 2001, vol. 378, pp. 118–123.

(166)   J. Perez-Mato, S. Gallego, E. Tasci, L. Elcoro, G. de la Flor and M. Aroyo, *Annual Review of Materials Research*, 2015, **45**, 217–248.

(167)   A. Wills, *Physica B: Condensed Matter*, 2000, **276**, 680–681.

(168)   G. Shirane, S. M. Shapiro and J. M. Tranquada, *Neutron Scattering with a Triple-Axis Spectrometer*, Cambridge University Press, 2002, p. 273.

(169)   R. I. Bewley, J. W. Taylor and S. M. Bennington., *Nuclear Instruments and Methods in Physics Research, Section A: Accelerators, Spectrometers, Detectors and Associated Equipment*, 2011, **637**, 128–134.

(170) O. Arnold, J. C. Bilheux, J. M. Borreguero, A. Buts, S. I. Campbell, L. Chapon, M. Doucet, N. Draper, R. Ferraz Leal, M. A. Gigg, V. E. Lynch, A. Markvardsen, D. J. Mikkelson, R. L. Mikkelson, R. Miller, K. Palmen, P. Parker, G. Passos, T. G. Perring, P. F. Peterson, S. Ren, M. A. Reuter, A. T. Savici, J. W. Taylor, R. J. Taylor, R. Tolchenov, W. Zhou and J. Zikovsky, *Nuclear Instruments and Methods in Physics Research, Section A: Accelerators, Spectrometers, Detectors and Associated Equipment*, 2014, **764**, 156–166.

(171) S Toth and B Lake, *Journal of Physics Condensed Matter*, 2015, **27**, 166002.

(172) M. McElfresh, *Fundamentals of Magnetism and Magnetic Measurements*, Quantum Design, 1994, p. 34.

(173) B. D. Josephson, *Physics Letters*, 1962, **1**, 251–253.

(174) P. W. Anderson and J. M. Rowell, *Physical Review Letters*, 1963, **10**, 230–232.

(175) V. Khovaylo, *Journal of Alloys and Compounds*, 2013, **577**, S362–S366.

(176) J. D. Moore, K. P. Skokov, J. Liu and O. Gutfleisch, *Journal of Applied Physics*, 2012, **112**, 063920.

(177) Y. Yang, Q.-C. Zhang, Y.-Y. Pan, L.-S. Long and L.-S. Zheng, *Chem. Commun.*, 2015, **51**, 7317–7320.

(178) E. S. R. Gopal, in *Specific Heats at Low Temperatures*, Springer US, Boston, MA, 1966, pp. 20–54.

(179) T. L. Hill, *An introduction to statistical thermodynamics*, Dover Publications, 1986, p. 508.

(180) D. Smith and F. Fickett, *Journal of Research of the National Institute of Standards and Technology*, 1995, **100**, 119.

(181) P Mukherjee, E Suard and S. E. Dutton, *Journal of Physics Condensed Matter*, 2017, **29**, 405807.

(182) S. Cotton, *Lanthanide and Actinide Chemistry*, John Wiley and Sons, Ltd, Chichester, UK, 2006.

(183) J. H. Van Vleck, *The theory of electric and magnetic susceptibilities*, Oxford University Press, Oxford, 1965, p. 384.

(184) B. Reid, D. McMorrow, P. Mitchell, O. Prakash and A. Murani, *Physica B: Condensed Matter*, 1991, **174**, 51–55.

(185) J. Hammann and M. Ocio, *Physica B+C*, 1977, **86-88**, 1153–1155.

(186) C. P. Reshmi, S. Savitha Pillai, K. G. Suresh and M. R. Varma, *Journal of Magnetism and Magnetic Materials*, 2012, **324**, 1962–1966.

(187) N. F. Chilton, D. Collison, E. J. McInnes, R. E. Winpenny and A. Soncini, *Nature Communications*, 2013, **4**, 2551–2557.

(188) L. Holmes and H. J. Guggenheim, *Le Journal de Physique Colloques*, 1971, **32**, C1–501–C1–502.

(189) B Bleaney, J. F. Gregg, R. W. Gregg, M Lazzouni, M. J. Leask and M. R. Wells, *Journal of Physics C: Solid State Physics*, 1988, **21**, 2721–2734.

(190) P. J. Brown, J. B. Forsyth, P. C. Hansen, M. J. Leask, R. C. Ward and M. R. Wells, *Journal of Physics: Condensed Matter*, 1990, **2**, 4471–4484.

(191) J. Brinkmann, R. Courths, S. Hüfner and H. J. Guggenheim, *Journal of Magnetism and Magnetic Materials*, 1977, **6**, 279–282.

(192) M. Piotrowski and A. Murasik, *physica status solidi (a)*, 1985, **89**, 571–580.

(193) K. Krämer, H. Romstedt, H. U. Güdel, P. Fischer, A. Murasik and M. T. Fernandez-Diaz, *European Journal of Solid State and Inorganic Chemistry*, 1996, **33**, 273–283.

(194) R. J. C. Dixey, F. Orlandi, P. Manuel, P. Mukherjee, S. E. Dutton and P. Saines, *Philosophical Transactions of the Royal Society A: Mathematical, Physical and Engineering Sciences*, 2019, **377**, 20190007.

(195) A. A. Tari, *The specific heat of matter at low temperatures*, Imperial College Press, London, 2003, pp. 211–276.

(196) M. Steiner, J. Villain and C. G. Windsor, *Advances in Physics*, 1976, **25**, 87–209.

(197) H. J. Mikeska and M. Steiner, *Advances in Physics*, 1991, **40**, 191–356.

(198) K. Sasaki and T. Tsuzuki, *Journal of Magnetism and Magnetic Materials*, 1983, **31-34**, 1283–1284.

(199) T. Schneider and E. Stoll, *Physical Review B*, 1980, **22**, 5317–5338.

(200) Y. Shirata, H. Tanaka, A. Matsuo and K. Kindo, *Physical Review Letters*, 2012, **108**, 057205.

(201) Y. Li, H. Liao, Z. Zhang, S. Li, F. Jin, L. Ling, L. Zhang, Y. Zou, L. Pi, Z. Yang, J. Wang, Z. Wu and Q. Zhang, *Scientific Reports*, 2015, **5**, 16419.

(202) A. Kurbakov, J. Rodriquez-Carvajal, V. Trounov and N. Starostina, *Materials Science Forum*, 2000, **321-324**, 971–975.

(203) B. E. Warren, *Physical Review*, 1941, **59**, 693–698.

(204) A. S. Wills, G. S. Oakley, D. Visser, J. Frunzke, A. Harrison and K. H. Andersen, *Physical Review B*, 2001, **64**, 094436.

(205) T. Fennell, S. T. Bramwell, D. F. McMorrow, P. Manuel and A. R. Wildes, *Nature Physics*, 2007, **3**, 566–572.

(206) B. Canals, I. A. Chioar, V. D. Nguyen, M. Hehn, D. Lacour, F. Montaigne, A. Locatelli, T. O. Menteş, B. S. Burgos and N. Rougemaille, *Nature Communications*, 2016, **7**, 11446.

(207) N. E. Brese, M. O'Keeffe and IUCr, *Acta Crystallographica Section B Structural Science*, 1991, **47**, 192–197.

(208) L. Clark, G. Sala, D. D. Maharaj, M. B. Stone, K. S. Knight, M. T. Telling, X. Wang, X. Xu, J. Kim, Y. Li, S. W. Cheong and B. D. Gaulin, *Nature Physics*, 2019, **15**, 262–268.

(209) R. A. Mole, J. A. Stride, T. Unruh and P. T. Wood, *Journal of Physics Condensed Matter*, 2009, **21**, 076003.

(210) S. Sachdev, *Quantum magnetism and criticality*, 2008.

(211) I. Kimchi, A. Nahum and T Senthil, *Physical Review X*, 2018, **8**, 031028.

(212) S. Toth, W. Wu, D. T. Adroja, S. Rayaprol and E. V. Sampathkumaran, *Physical Review B*, 2016, **93**, 174422.

(213) H. W. Capel, *Physica*, 1965, **31**, 1152–1176.

(214) J. Felsteiner and S. K. Misra, *Physical Review B*, 1981, **24**, 2627–2633.

(215) H. D. Zhou, C. R. Wiebe, L. Balicas, Y. J. Yo, Y. Qiu, J. R. Copley and J. S. Gardner, *Physical Review B - Condensed Matter and Materials Physics*, 2008, **78**, 140406.

(216) S. H. Curnoe, *Physical Review B - Condensed Matter and Materials Physics*, 2013, **88**, 014429.

(217) D. R. Harcombe, P. G. Welch, P. Manuel, P. J. Saines and A. L. Goodwin, *Physical Review B*, 2016, **94**, 174429.

(218) S. T. Bramwell and M. J. P. Gingras, *Science*, 2001, **294**, 1495–1501.

(219) M. R. Moura, A. P. Ayala, J. Mendes Filho, I. Guedes, C. W. A. Paschoal, A. G. Leyva, G. I. Polla, D. R. Vega, P. K. de Perazzo, H. Lanza and J. Mendes-Filho, *Journal of Raman Spectroscopy*, 2004, **35**, 159–164.

(220) P. Schiffer, A. P. Ramirez, D. A. Huse, P. L. Gammel, U. Yaron, D. J. Bishop and A. J. Valentino, *Physical Review Letters*, 1995, **74**, 2379–2382.

(221) D. Y. Wei and Y. Q. Zheng, *Zeitschrift fur Kristallographie - New Crystal Structures*, 2003, **218**, 23–24.

(222) Y.-C. Chen, L. Qin, Z.-S. Meng, D.-F. Yang, C. Wu, Z. Fu, Y.-Z. Zheng, J.-L. Liu, R. Tarasenko, M. Orendáč, J. Prokleška, V. Sechovský, M.-L. Tong, E. K. Brechin and E. J. L. McInnes, *J. Mater. Chem. A*, 2014, **2**, 9851–9858.

(223) V. F. Sears, *Neutron News*, 1992, **3**, 29–37.

(224) R. J. Baxter FRS, H. Brace Jovanovich and P. London San Diego New York Berkeley Boston Sydney Tokyo Toronto, *Exactly Solved Models in Statistical Mechanics*, Academic Press, 1982.

(225) R. Dixey, G. Stenning, P. Manuel, F. Orlandi and P. Saines, *Journal of Materials Chemistry C*, 2019, **7**, 13111–13119.

(226) A. Le Yaouanc and P. D. Reotier, *Muon spin rotation, relaxation, and resonance: applications to condensed matter*, Oxford University Press, 2011, p. 486.

(227) I. K. Kamilov, A. G. Gamzatov, A. M. Aliev, A. B. Batdalov, A. A. Aliverdiev, S. B. Abdulvagidov, O. V. Melnikov, O. Y. Gorbenko and A. R. Kaul, *Journal of Physics D: Applied Physics*, 2007, **40**, 4413–4417.

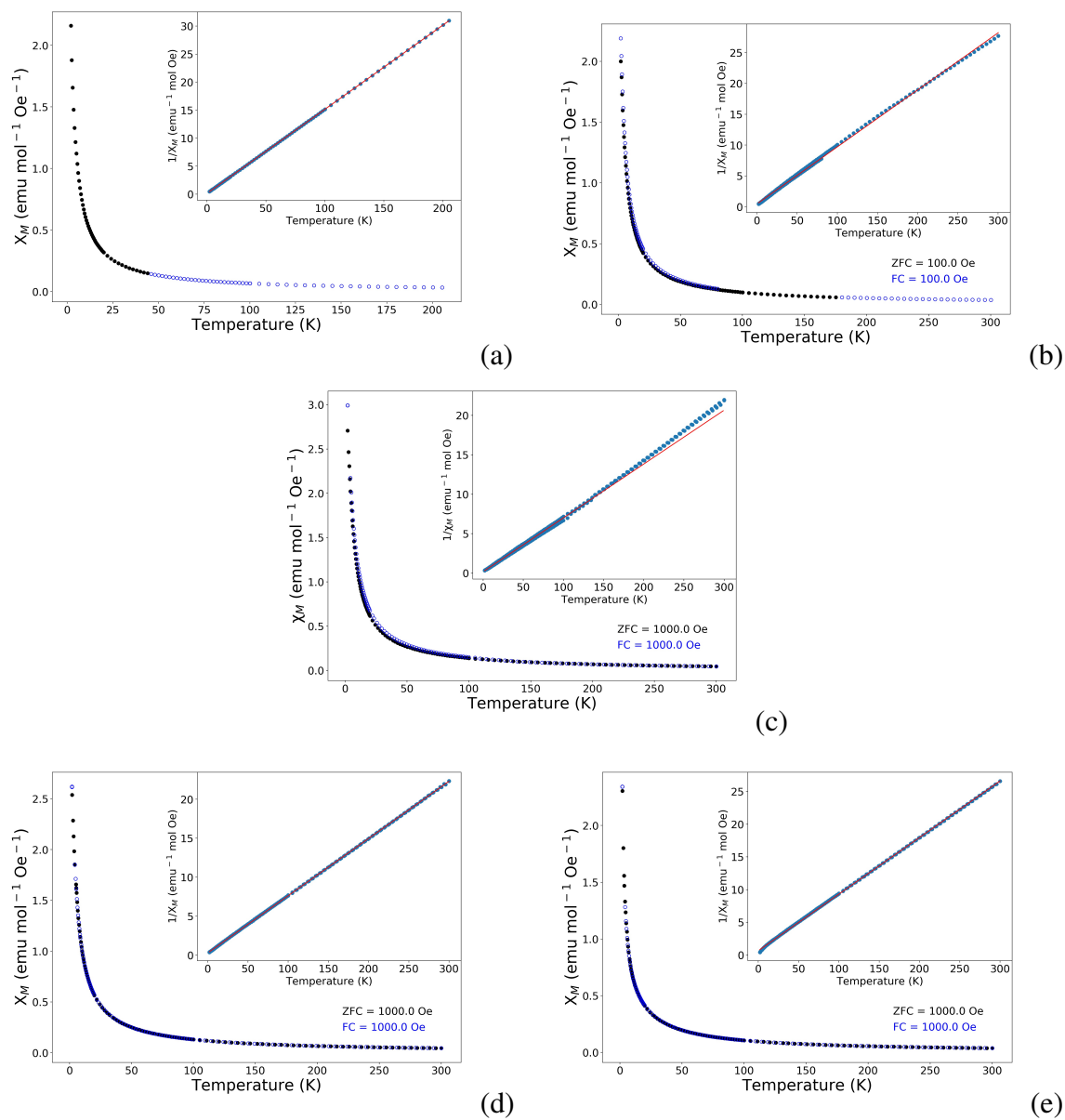(228) V. K. Pecharsky and K. A. Gschneidner, *Journal of Magnetism and Magnetic Materials*, 1999, **200**, 44–56.

# Appendix A

# Supplementary Information

For a complete collection of all data, refinements, calculations and figures: see the included USB drive.
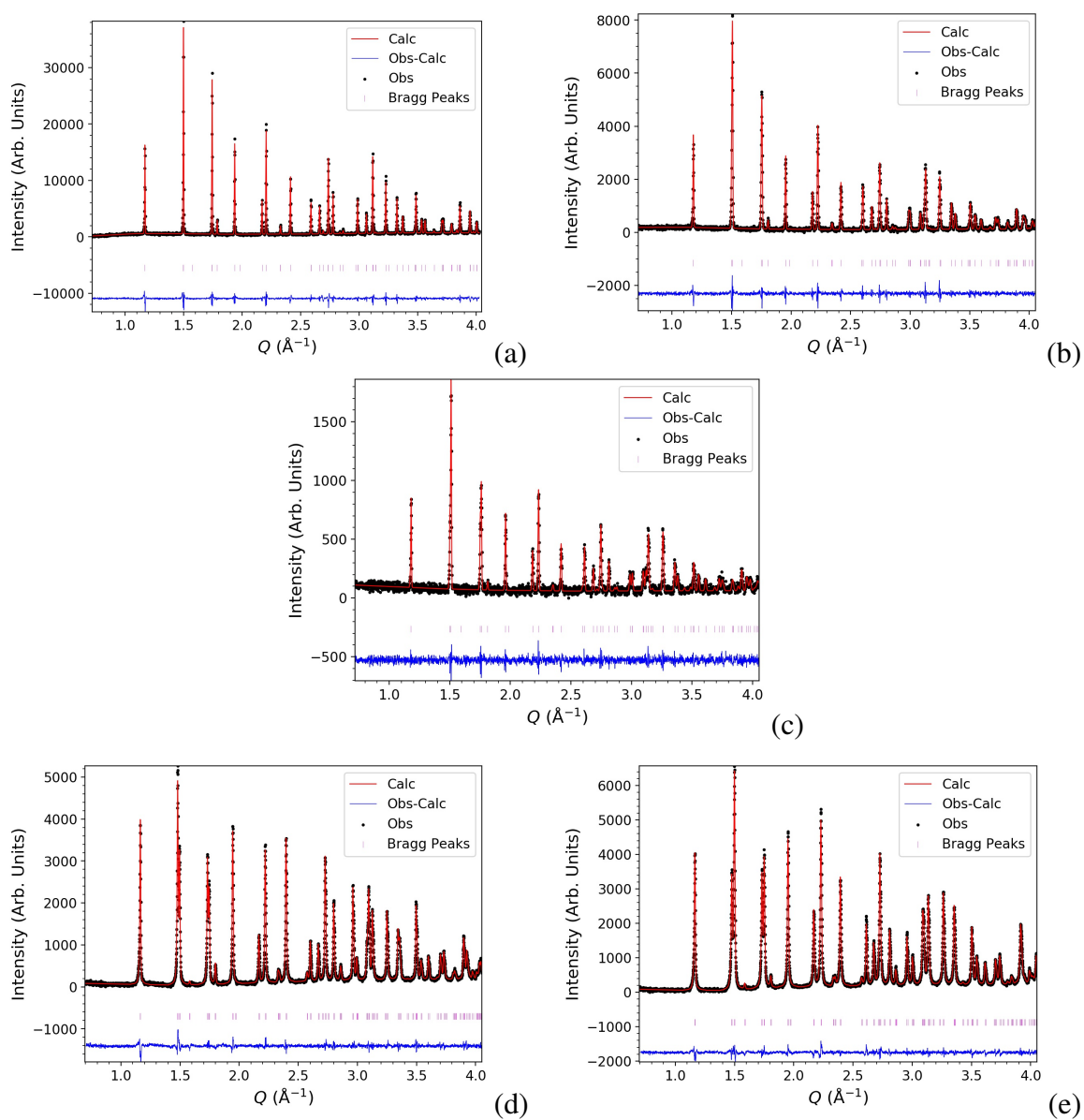
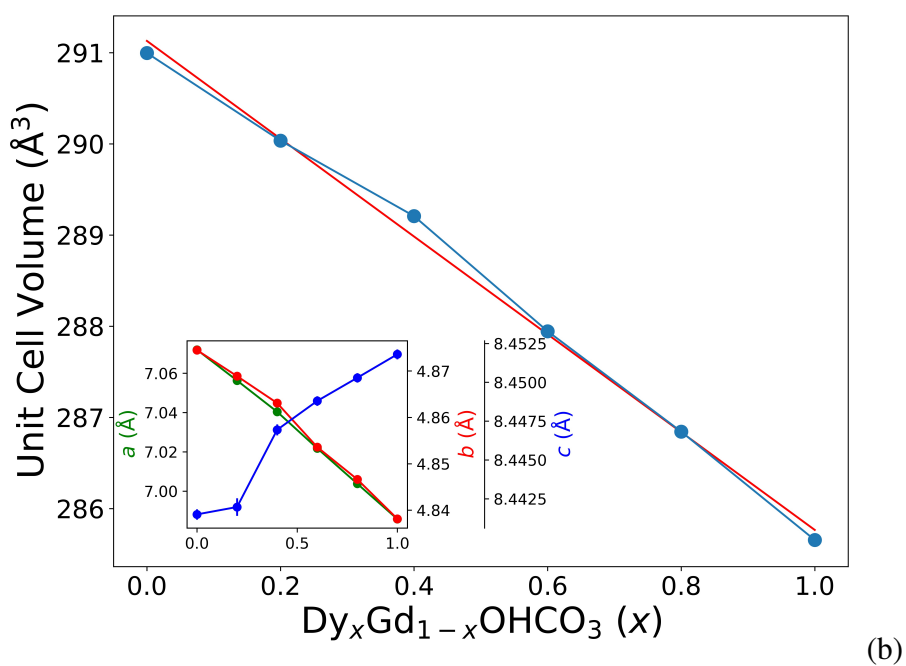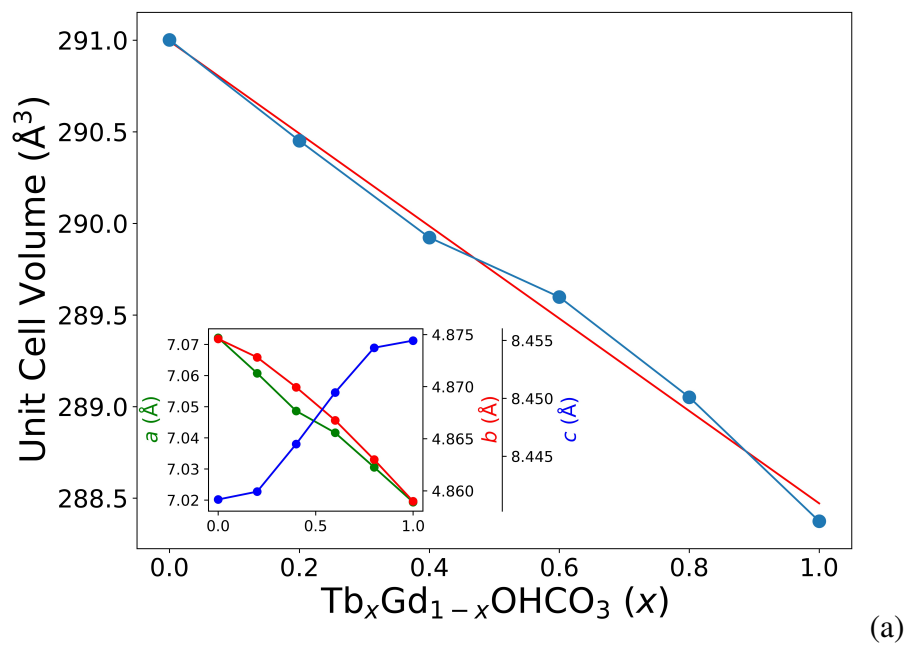**Figure A.1** Le Bail refinements of the *Ln*OHCO$_3$ frameworks (a) GdOHCO$_3$, (b) TbOHCO$_3$, (c) DyOHCO$_3$, (d) HoOHCO$_3$ and (e) ErOHCO$_3$ at 300 K.
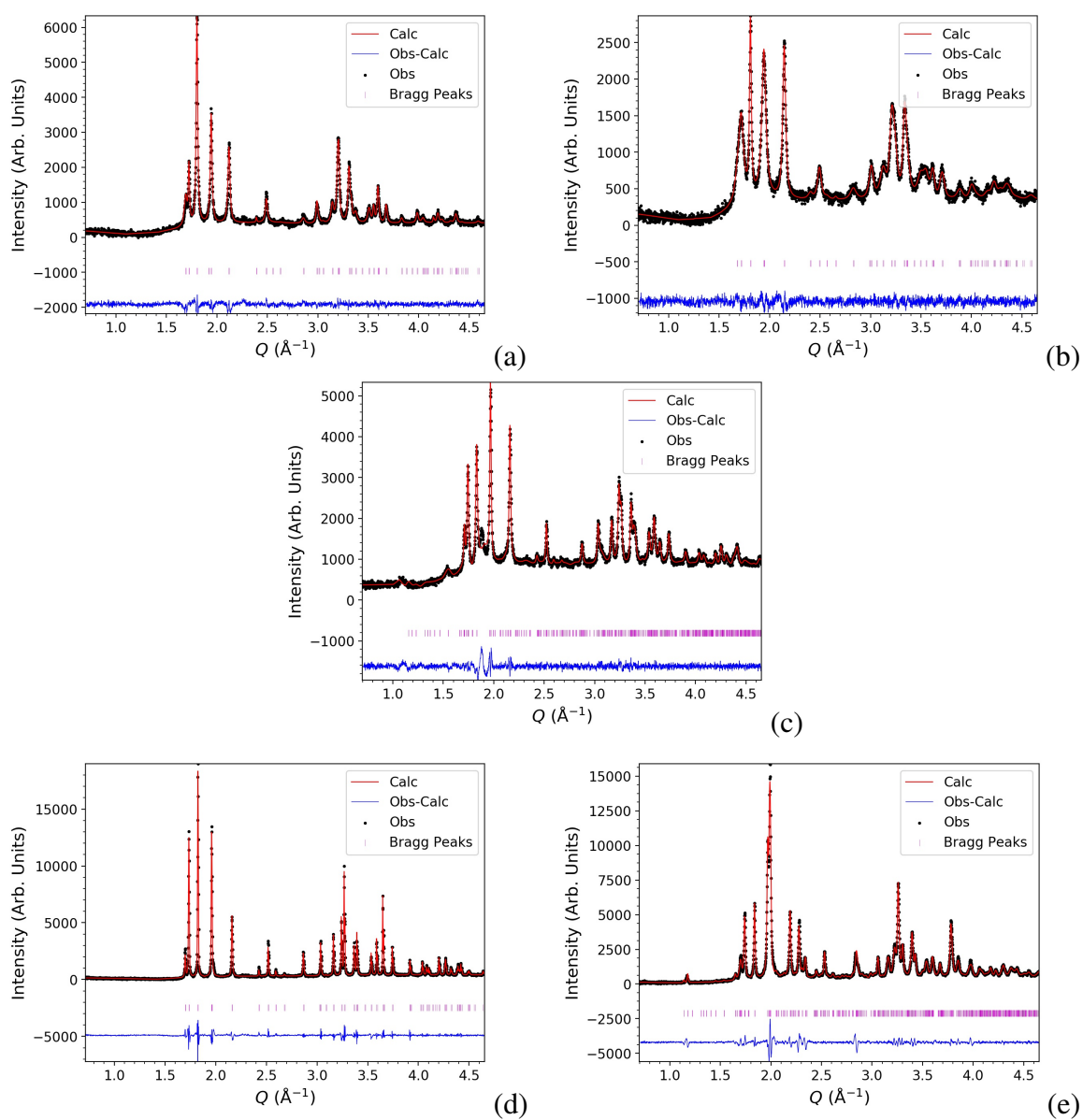
**Figure A.2** FC and ZFC measurements in a 1000 Oe field, the insert shows a Curie-Weiss fit to the inverse magnetic susceptibility measurements for (a) GdOHCO$_3$, (b) TbOHCO$_3$, (c) DyOHCO$_3$, (d) HoOHCO$_3$ and (e) ErOHCO$_3$. Curie-Weiss behaviour fit between 2-300 K, with the exception of DyOHCO$_3$ which was fit below 150 K and extrapolated to higher temperature.
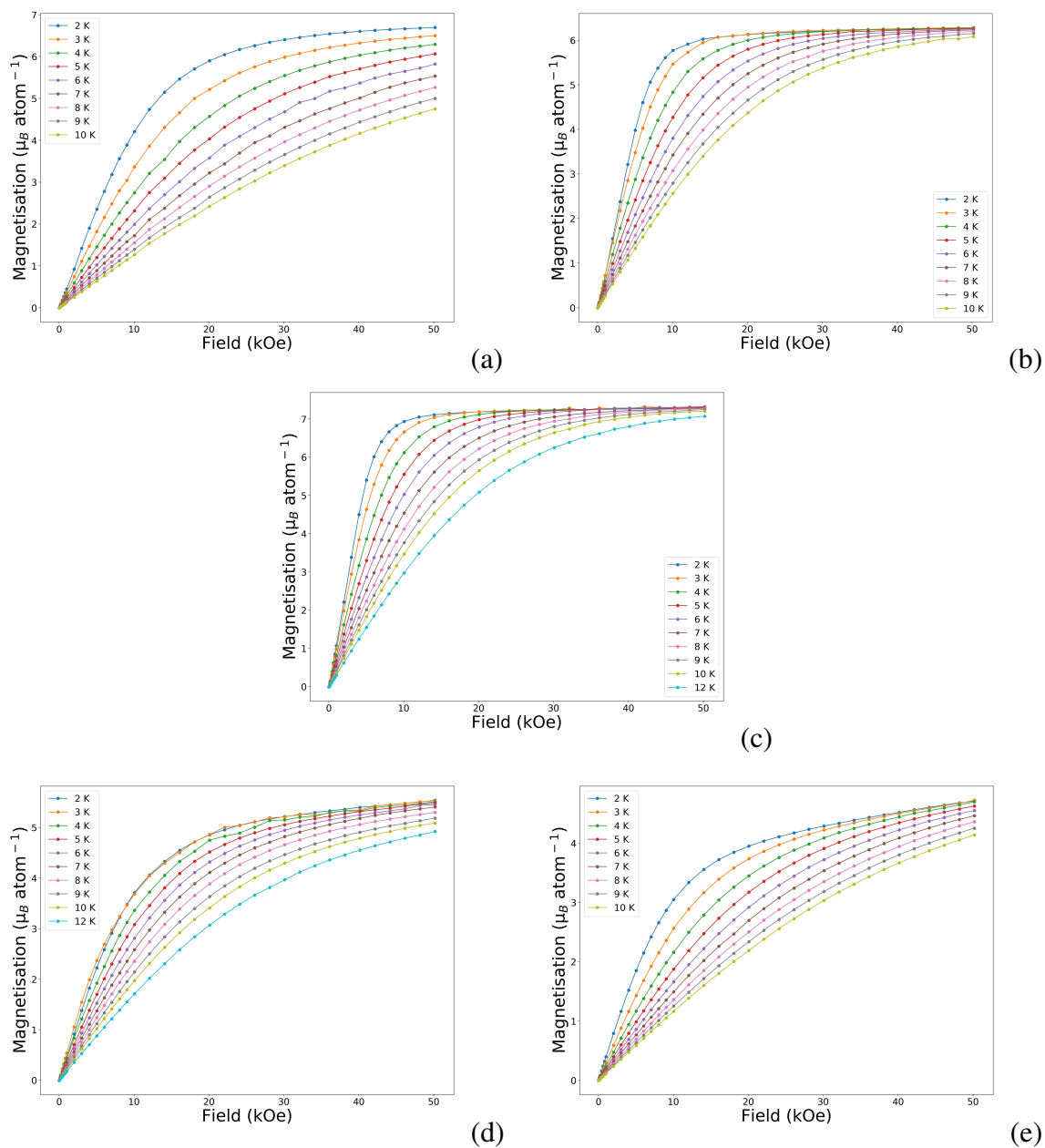
**Figure A.3** Magnetisation measurements of the *Ln*OHCO$_3$ frameworks at variable temperatures for (a) GdOHCO$_3$, (b) TbOHCO$_3$, (c) DyOHCO$_3$, (d) HoOHCO$_3$ and (e) ErOHCO$_3$

**Figure A.4** Vegard's law of doped *Ln*OHCO$_3$ showing the reduction of the unit cell volume with fraction of (a) Tb and (b) Dy doped into GdOHCO$_3$. Error bars are shown but smaller than the graph points.

**Figure A.5** Le Bail refinements of the *Ln*F$_3$ frameworks (a) GdF$_3$, (b) TbF$_3$, (c) DyF$_3$, (d) HoF$_3$ and (e) ErF$_3$
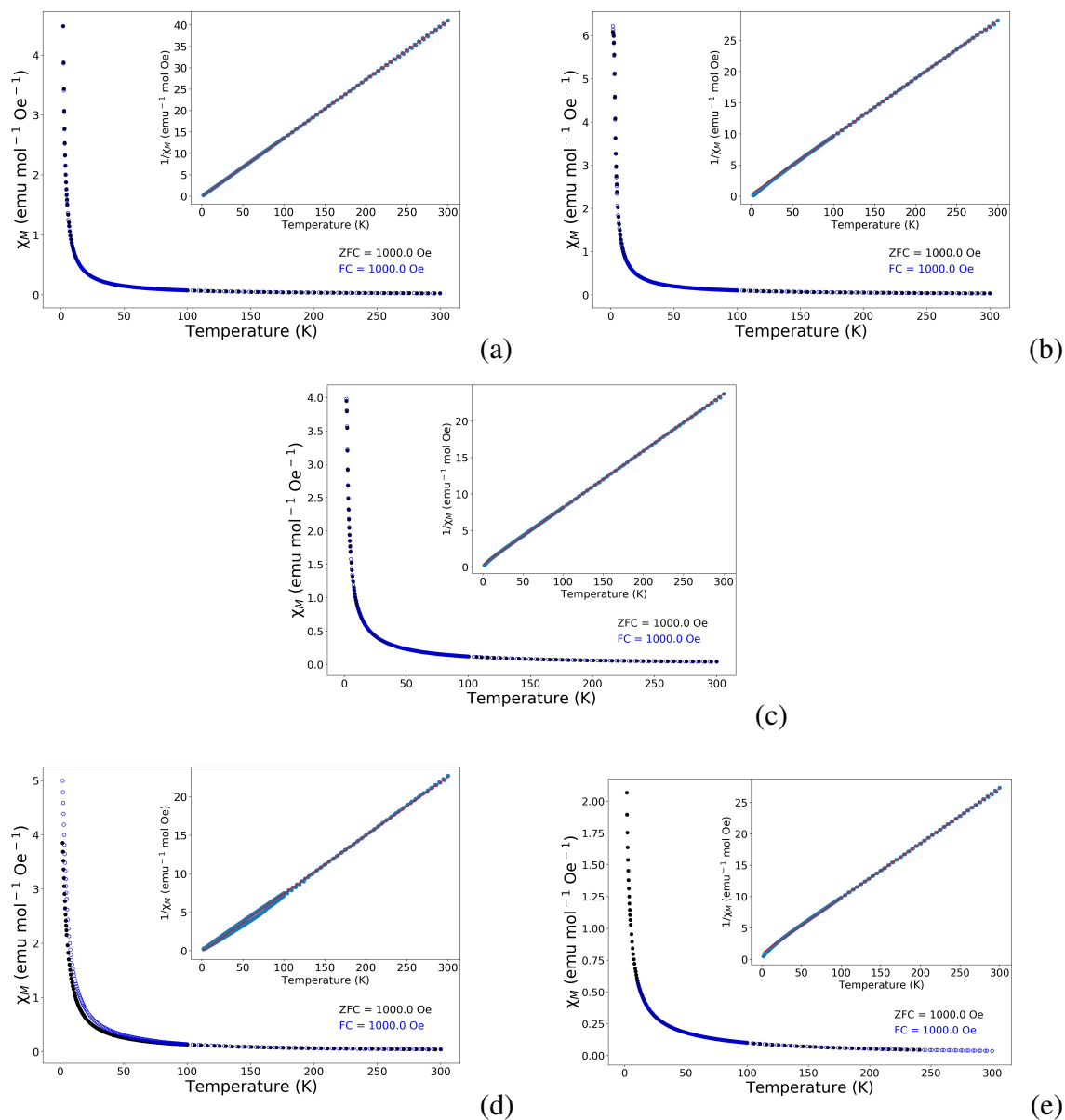
**Figure A.6** FC and ZFC measurements in a 1000 Oe field, the insert shows a Curie-Weiss fit to the inverse magnetic susceptibility measurements for (a) $GdF_3$, (b) $TbF_3$, (c) $DyF_3$, (d) $HoF_3$ and (e) $ErF_3$. Curie-Weiss behaviour fit between 50-300 K.
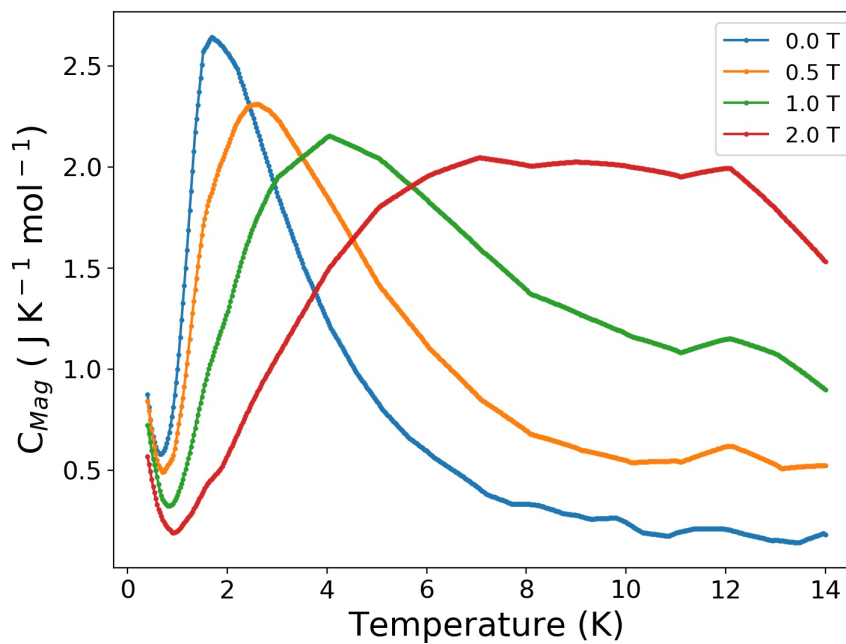
**Figure A.7** $C_{mag}$ of Tb(HCO$_2$)$_3$ in variable fields between 400 mK and 14 K.
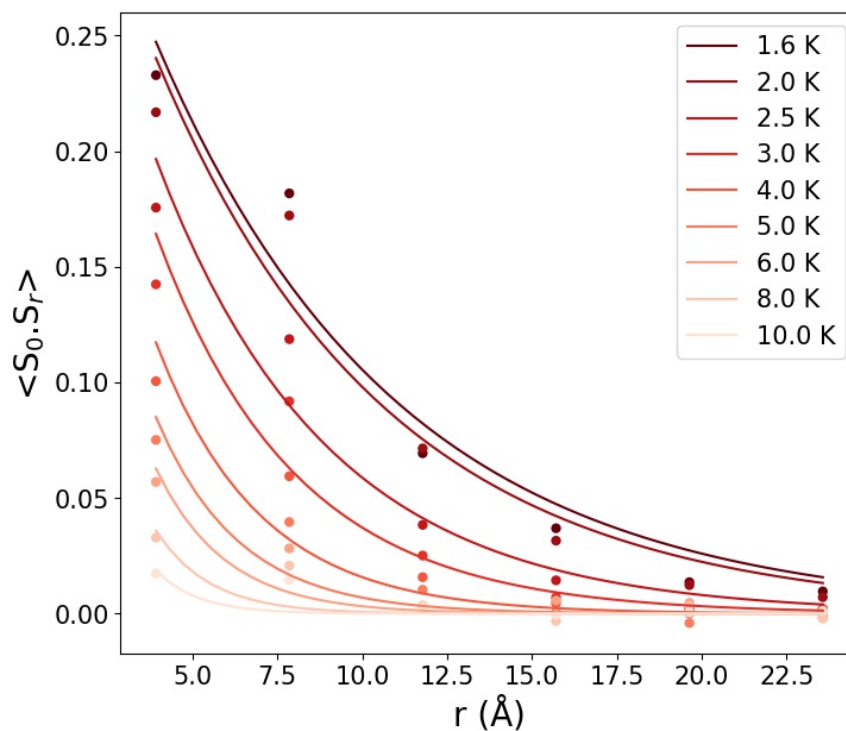


**Figure A.8** Evolution of the correlation lengths of the 1D Ising chains in Ho(DCO$_2$)$_3$, with respect to temperature.

**Table A.1** A table summarising the atomic information of the non-magnetically ordering $Ln(DCO_2)_3$ frameworks at 1.5 K, using the $R3m$ space group.

| Atom | x | y | z | $U_{iso}$ x 100 Å$^2$ | Occupancy |
|------|---|---|---|-----------------------|-----------|
| **Ce(DCO$_2$)$_3$** | | | | | |
| Ce | 0.33333 | 0.66667 | 0.000 | 0.738(18) | 1.000 |
| C | 0.51394(24) | 0.48605(24) | 0.20643(12) | 0.814(73) | 1.000 |
| D | 0.49505(18) | 0.50494(18) | 0.46622(3) | 1.90(16) | 0.974(18) |
| O1 | 0.46808(23) | 0.53190(23) | -0.01130(4) | 0.72(8) | 1.000 |
| O2 | 0.58271(16) | 0.41729(16) | 0.17198(22) | 0.55(7) | 1.000 |
| **Pr(DCO$_2$)$_3$** | | | | | |
| Pr | 0.33333 | 0.66667 | 0.000 | 0.944(17) | 1.000 |
| C | 0.51393(20) | 0.48606(20) | 0.20519(4) | 1.06(7) | 1.000 |
| D | 0.49473(16) | 0.50526(16) | 0.46429(7) | 2.59(12) | 0.991(2) |
| O1 | 0.46778(21) | 0.53220(21) | -0.00922(23) | 1.015(68) | 1.000 |
| O2 | 0.58214(14) | 0.41784(14) | 0.17250(7) | 0.811(62) | 1.000 |
| **Nd(DCO$_2$)$_3$** | | | | | |
| Nd | 0.33333 | 0.66667 | 0.000 | 0.76(9) | 1.000 |
| C | 0.51290(19) | 0.48709(19) | 0.20395(14) | 1.01(7) | 1.000 |
| D | 0.49414(17) | 0.50585(17) | 0.46362(16) | 1.49(1) | 0.972(12) |
| O1 | 0.46747(20) | 0.53252(20) | -0.01661(22) | 0.71(6) | 1.000 |
| O2 | 0.58271(15) | 0.41729(15) | 0.16569(12) | 0.59(6) | 1.000 |
| **Dy(DCO$_2$)$_3$** | | | | | |
| Dy | 0.33333 | 0.66667 | 0.000 | 0.82(6) | 1.000 |
| C | 0.51152(19) | 0.48847(19) | 0.24120(5) | 0.93(7) | 1.000 |
| D | 0.49420(18) | 0.50581(18) | 0.50725(5) | 2.656(12) | 0.973(2) |
| O1 | 0.46502(18) | 0.53497(18) | 0.00951(4) | 0.58(7) | 1.000 |
| O2 | 0.58263(16) | 0.41737(16) | 0.19604(23) | 0.71(7) | 1.000 |
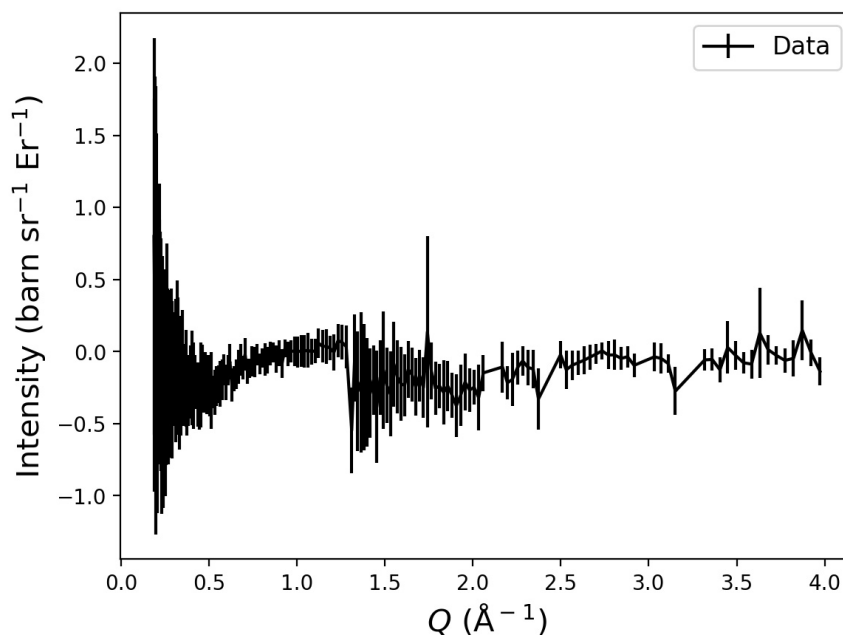
**Figure A.9** Temperature subtracted data of $T_{low}$ - $T_{high}$, where $T_{low}$ = 1.6 K and $T_{high}$ = 20 K.

**Table A.2** Table summarising bond lengths of $Ln$ODCO$_3$ (where $Ln$ = Tb, Dy, Ho and Er) determined from neutron diffraction measurements taken at 100 K. Bond lengths are given in angstroms (Å)

| Bond | Length ($Ln$ = Tb) | Length ($Ln$ = Dy) | Length ($Ln$ = Ho) | Length ($Ln$ = Er) |
|---|---|---|---|---|
| $Ln$1_O1 | 2.2909(10) | 2.2774(16) | 2.2581(9) | 2.2446(14) |
| $Ln$1_O1 | 2.2773(13) | 2.2730(20) | 2.2627(12) | 2.2259(17) |
| $Ln$1_O2 | 2.4689(25) | 2.446(4) | 2.4376(19) | 2.4240(23) |
| $Ln$1_O2 | 2.4840(23) | 2.4374(28) | 2.4190(17) | 2.3852(22) |
| $Ln$1_O2 | 2.8555(24) | 2.8938(3) | 2.9243(17) | 2.9631(20) |
| $Ln$1_O3 | 2.5034(22) | 2.473(3) | 2.4905(17) | 2.4791(20) |
| $Ln$1_O3 | 2.5842(22) | 2.6382(26) | 2.6338(18) | 2.6366(23) |
| $Ln$1_O3 | 2.6768(23) | 2.6133(30) | 2.6041(18) | 2.5858(22) |
| $Ln$1_O4 | 2.4691(29) | 2.4320(5) | 2.3828(22) | 2.3473(28) |
| $Ln$1_O4 | 2.5095(28) | 2.5230(4) | 2.5593(22) | 2.5647(28) |
| C1_O1 | 1.2752(25) | 1.3010(4) | 1.2991(23) | 1.3158(34) |
| C1_O2 | 1.2811(22) | 1.27000(4) | 1.2764(23) | 1.2700(32) |
| C1_O3 | 1.2591(11) | 1.2721(27) | 1.2699(15) | 1.2807(19) |
| O4_D1 | 0.9714(17) | 0.939(3) | 0.9798(17) | 0.9792(24) |
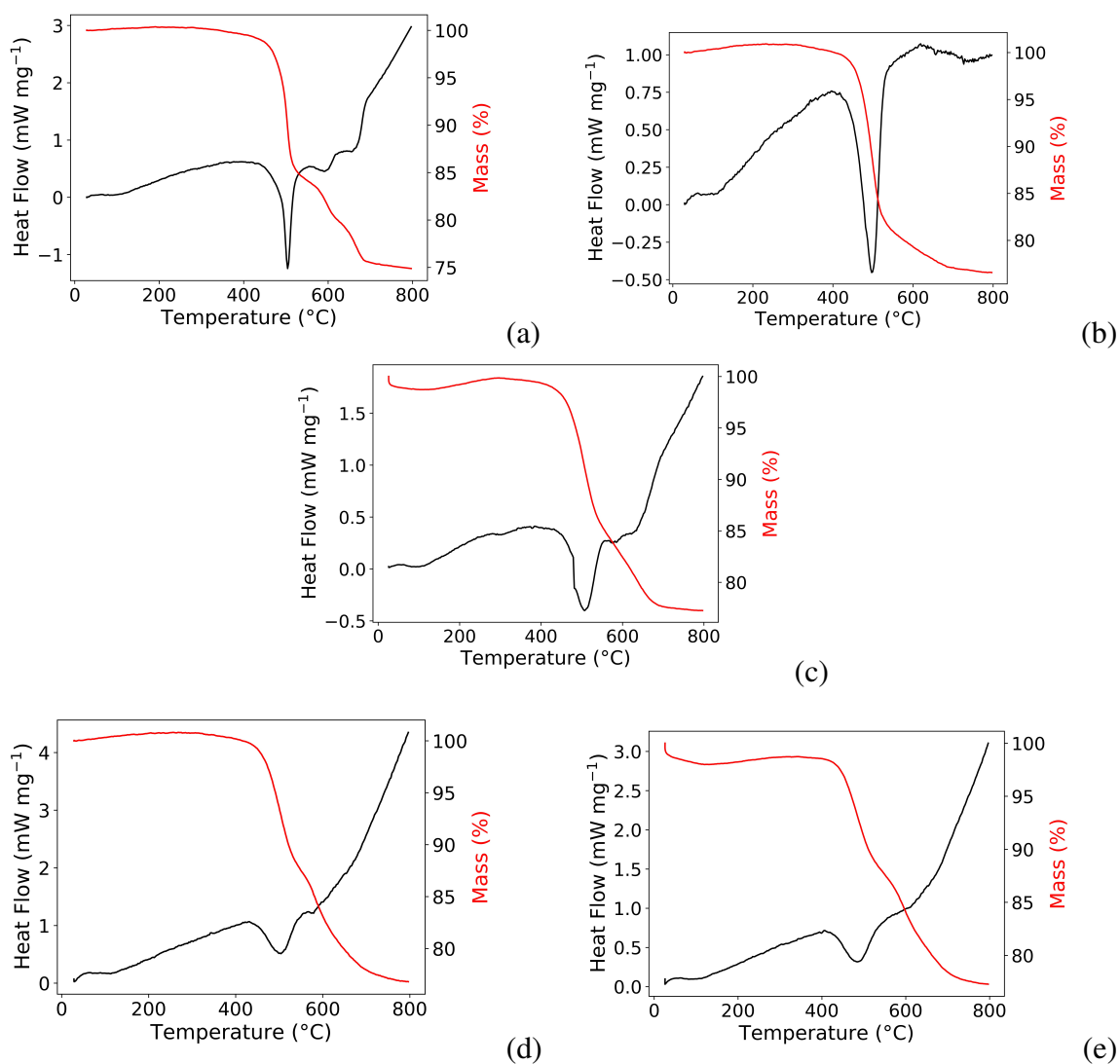
**Figure A.10** Changes in the mass and heat flow of (a) GdOHCO$_3$, (b) TbOHCO$_3$, (c) DyOHCO$_3$, (d) HoOHCO$_3$, and (e) ErOHCO$_3$, with respect to temperature, the sample is heated at $10°C$ min$^{-1}$ between 30-800$°C$.
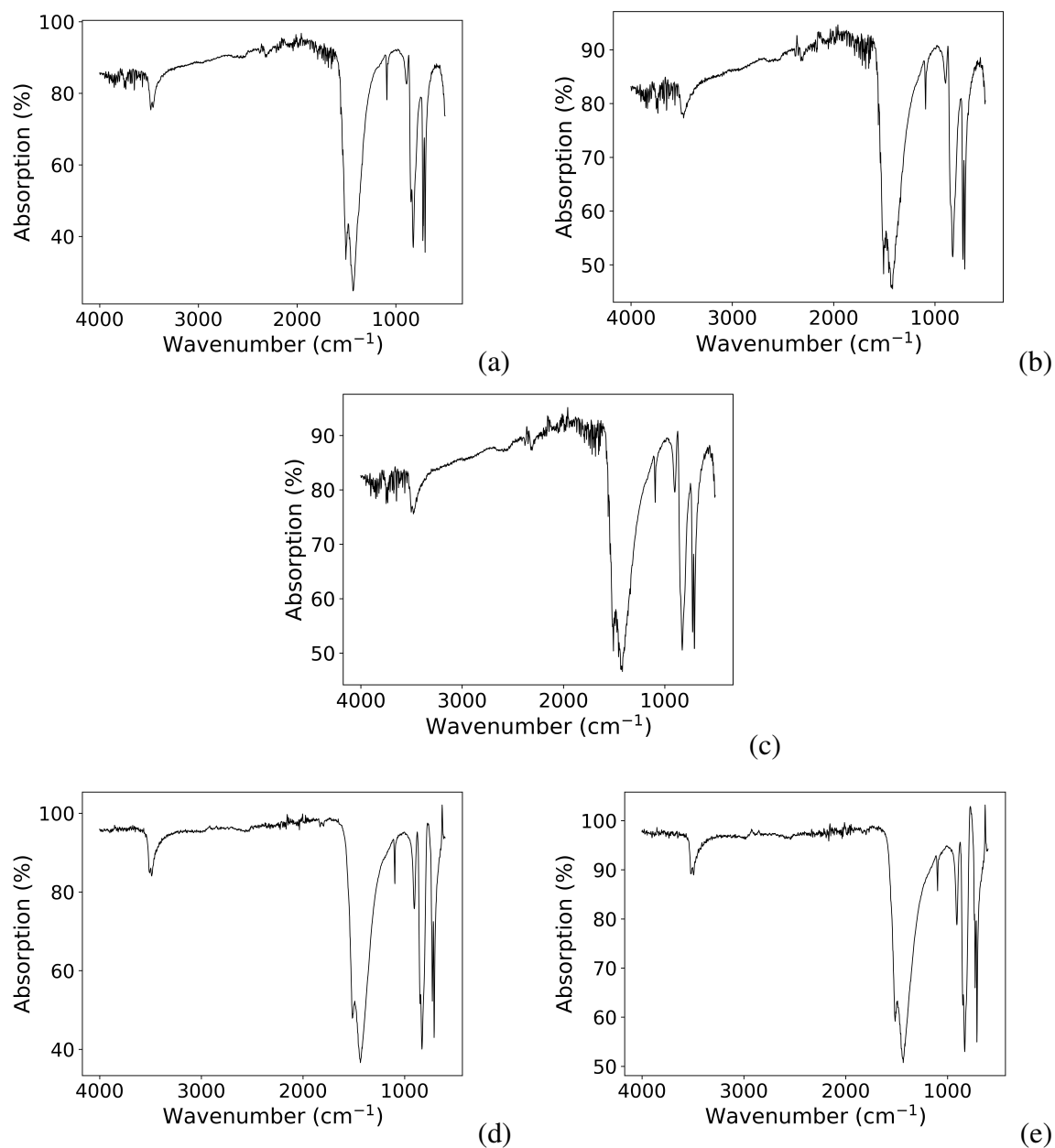
**Figure A.11** Infrared spectroscopy measurements of (a) $GdOHCO_3$, (b) $TbOHCO_3$, (c) $DyOHCO_3$, (d) $HoOHCO_3$, and (e) $ErOHCO_3$, between 500 and 4000 $cm^{-1}$.
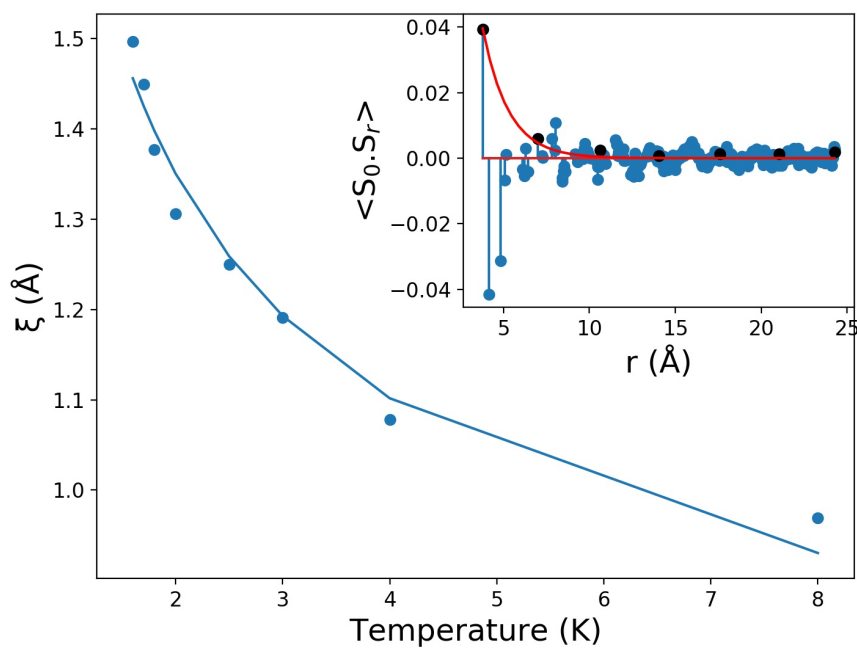
**Figure A.12** Fit to the chain correlation length of $DyODCO_3$ using a Heisenberg model. The fit to the base temperature at 1.5 K in the insert.

**Table A.3** Summary of the bond distances of $HoODCO_3$ at 0.25 K, determined from Rietveld refinement.

| Atom 1 | Atom 2 | Distance (Å) |
| --- | --- | --- |
| Ho | O1 | 2.554(12) |
| Ho | O1 | 2.563(11) |
| Ho | O2 | 2.270(13) |
| Ho | O3 | 2.224(7) |
| Ho | O3 | 2.262(7) |
| Ho | O4 | 2.405(10) |
| Ho | O4 | 2.415(10) |
| C | O1 | 1.082(13) |
| C | O2 | 1.381(8) |
| C | O4 | 1.383(13) |
| D | O3 | 1.037(11) |
| O1 | O2 | 2.143(12) |
| O1 | O4 | 2.218(14) |
| O2 | O4 | 2.287(11) |
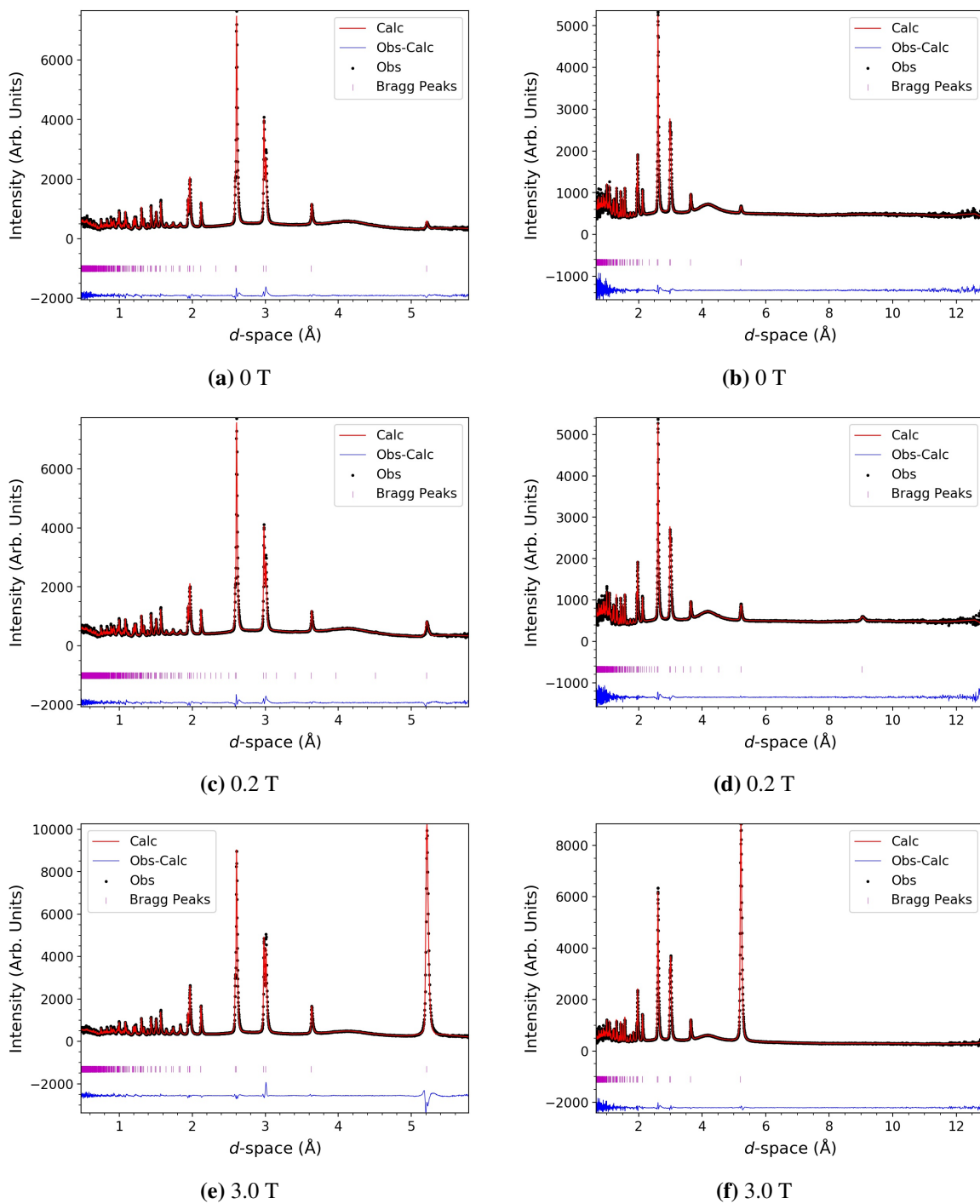
**Figure A.13** Rietveld fits to applied field neutron diffraction patterns of Tb(DCO$_2$)$_3$ at variable fields from (left) bank 4/8 and (right) 2/9 of WISH along with the fitting statistics (a) R$_p$ = 3.46 %, R$_{wp}$ = 3.72 %, (b) R$_p$ = 3.63 %, R$_{wp}$ = 2.16 %, (c) R$_p$ = 3.38 %, R$_{wp}$ = 3.53 %, (d) R$_p$ = 3.64 %, R$_{wp}$ = 2.14 %, (e) R$_p$ = 3.91 %, R$_{wp}$ = 3.78 %, (f) R$_p$ = 4.00 %, R$_{wp}$ = 2.73 %.

**Table A.4** Summary of the *Ln*OHCO$_3$ applied field magnetic structures, showing the spin vectors of the canted antiferromagnetic (CAFM) and ferromagnetic (FM) structure at 3.0 T.

| | Atomic Sites | | | CAFM | | | FM | | |
|---|---|---|---|---|---|---|---|---|---|
| *Atom* | x | y | z | u | v | w | u | v | w |
| Tb1 | 0.0113(18) | 0.1131(3) | 0.16084(28) | 1.17 | 4.48 | 2.51 | 1.02 | 6.32 | 2.04 |
| Tb2 | 0.4886(18) | 0.8868(3) | 0.66084(28) | -1.17 | -4.48 | 2.51 | 1.02 | 6.32 | -2.04 |
| Tb3 | 0.9886(18) | 0.6131(3) | 0.33916(28) | 1.17 | -4.48 | 2.51 | -1.02 | 6.32 | -2.04 |
| Tb4 | 0.5113(18) | 0.3868(3) | 0.83916(28) | -1.17 | 4.48 | 2.51 | -1.02 | 6.32 | 2.04 |